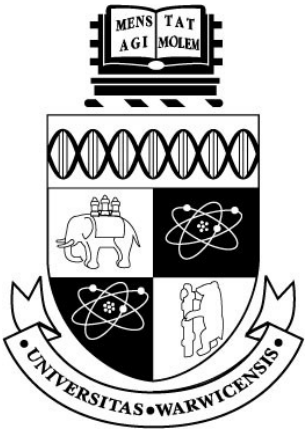

Growth and characterisation of dilute nitride antimonide layers by plasma-assisted molecular beam epitaxy

J. J. Bomphrey

A thesis submitted in fulfilment of the requirements for the degree of Doctor of Philosophy in Chemistry

Department of Chemistry, University of Warwick

May 2011

Table of Contents

Acknowledgments

I wish to thank my supervisor Tim Jones for providing me with the opportunity to undertake a PhD in his research group. Gratitude is extended to Tomasz Krzyzewski and Raffaello da Campo for their contributions, both academic and otherwise. I am further indebted to Mark Ashwin for his tuition and support, often in the face of adverse circumstances. I gratefully recognise David Josey, Julie Macpherson, Vas Stavros and Martin Wills who have spared no effort to assist me in achieving my goal.

I owe a tremendous debt of gratitude to my family for their love and ceaseless support. In particular, I thank my parents, without whom I would not be where I am today – my achievements are as much yours as they are mine.

To Sarah and all those who I am proud to call my friends, your companionship and support has been extraordinary – I am very lucky to have met such good people.

To my colleagues and the characters of the department of Chemistry, I thank you all for making my time at Warwick so much more than a course of study.

"In everyone's life, at some time, our inner fire goes out. It is then burst into flame by an encounter with another human being. We should all be thankful for those people who rekindle the inner spirit." - Albert Schweitzer (1875-1965)

Declaration

I confirm that this document, or any part thereof, has not been submitted for the consideration of any other degree, at any institution. I declare the work described herein to have been undertaken by me, except where acknowledged and in the cases of X-ray characterisation (Iain Dunn, Warwick) and SIMS analysis (Eng Soon Tok, Singapore). TEM images were supplied by Ana Sanchez (Warwick).

I believe this thesis to meet the standards required for the achievement of the degree of doctor of philosophy (Chemistry) by research.

_____

Candidate: John Bomphrey

I have read this thesis and believe it meet the standards required for the achievement of the degree of doctor of philosophy (Chemistry) by research.

_____

Supervisor: Professor Tim Jones

Related Publications

M. J. Ashwin, T. D. Veal, J. J. Bomphrey, I. R. Dunn, D. Walker, P. A. Thomas, T. S. Jones, *Controlled nitrogen incorporation in GaNSb Alloys,* Applied Physics Letters (Submitted)

M. J. Ashwin, T. D. Veal, J. J. Bomphrey, I. R. Dunn, D. Walker, P. A. Thomas, T. S. Jones, *Probing the measured saturation level of nitrogen in GaNSb alloys,* Applied Physics Letters (To be submitted)

Abstract

The work presented in this thesis is concerned with the growth and characterisation of III-NSb films by plasma-assisted molecular beam epitaxy (PA-MBE). The research was motivated by their application in technologically important regions of the IR spectrum.

Homoepitaxial growth of GaSb films was conducted and characterised as a function of V:III ratio and growth temperature, permitting observation of morphology changes with growth conditions, also providing insight into surfaces of the ternary dilute nitride. Heteroepitaxial GaSb/GaAs growth has highlighted defect formation and propagation arising from lattice mismatched deposition.

Films of GaN_xSb_{1-x}, a material of interest for device applications in the 2-5 μm spectral range, have been grown on GaSb(001) substrates. The results demonstrate the degree to which substitutional N content may be controlled through variation of the temperature and rate of deposition. Models based upon kinetic and thermodynamic principles and previously applied to GaN_xAs_{1-x} have been evaluated for N content of GaN_xSb_{1-x} films as a function of the rate and temperature used for growth.

The growth of InN_xSb_{1-x}, an alloy of significance in the technologically important wavelength region of 8-12 μm, upon InSb(001) substrates is described. There is qualitative agreement with the temperature dependence of N content. Analysis of the substitutional N content as a function of growth rate, however, suggests a difference between GaN_xSb_{1-x} and GaN_xAs_{1-x}. An explanation is presented for the trend in the level of substitutional N uptake across III-V-N materials.

Further experiments are proposed to extend the parameter space sampled in the investigation of GaN_xSb_{1-x} and InN_xSb_{1-x} films, with regard to the Sb:III ratio employed during growth. Initial results are reported from measurements undertaken with a pyrometer operating at 1.6 μm, suggesting that growth can be conducted at lower temperatures. Additional preliminary results are presented for the growth of $Ga_xIn_{1-x}N_ySb_{1-y}$ films, demonstrating a tuneable band gap quaternary material, lattice matched to GaSb is possible.

Chapter 1

"Nothing is too wonderful to be true if it be consistent with the laws of nature."

Michael Faraday (1791 - 1867)

In this chapter, there follows an overview of semiconductor behaviour, growth and structure. In particular, III-V materials are discussed, with attention given to the dilute nitride alloys. Also discussed is the motivation for research into narrow band gap materials.

1.1 Introduction to Semiconductors:

Semiconductor technology plays an enormous role in almost every facet of modern living, providing dynamic electrical properties unavailable with traditional materials. Since the first documented observations of semiconductor properties by Michael Faraday in 1833, research in the field has led from the "extraordinary case" of silver sulphide crystals to increasingly complex devices.

The term "semiconductor" has been defined in the Oxford English Dictionary as

"a material whose capacity to conduct electricity is intermediate between that of a good conductor and an insulator."

It is the case that this description makes no allusion to the remarkable properties and versatility exhibited by semiconductor materials, as well as neglecting materials such as diamond and GaN which are widely regarded as wide band gap semiconductors.

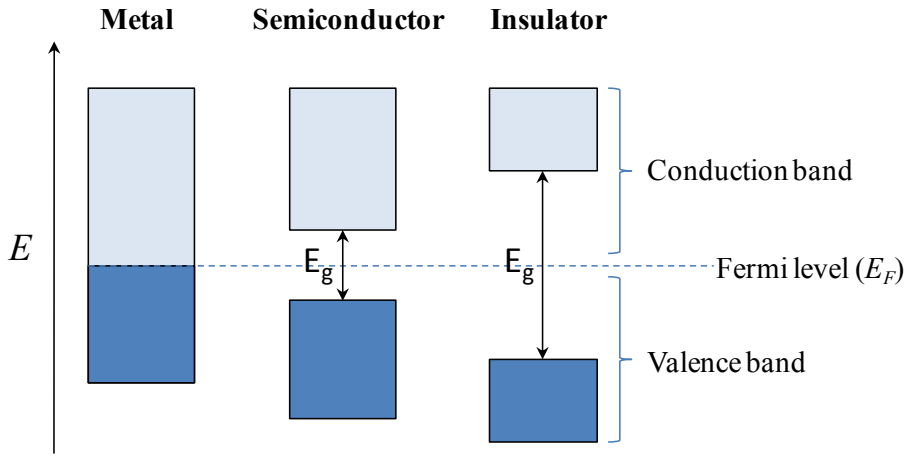

Figure 1.1: A metal is characterised by unoccupied states existing within the same continuum as occupied states. Semiconductors and insulators exhibit regions in which electron occupation is forbidden. It is the magnitude of this zone that defines whether the material in question is semiconducting or insulating in practical application.

The properties of a semiconductor arise from the nature of its band structure (Figure 1.1). In a metal, the highest occupied energy band is partially filled, which allows conduction without the need to overcome an inter-band energy barrier. For semiconductors and insulators, the highest occupied bands are completely filled, with the next unoccupied band being at a higher energy. The band gap (E_g) is the energy difference between these two bands.

At a temperature of 0K, the Fermi level (E_F) in a metal is at the maximum energy at which there is electron population, following filling of states with the available electrons. For T > 0K, E_F is defined as the energy at which there is a 50% chance of finding an electron, as described by Fermi-Dirac statistics and given by

———————, (1.1)

where *F(E)* is the probability of an electron populating a state of energy E, k_B is the Boltzmann constant and T is the temperature in Kelvin.

While this is relatively straightforward to visualise in the case of a metal, for semiconductors and insulators E_F falls within an energy range where electron occupation is forbidden and is derived from applying eq. (1.1) to the number density of population in the allowed regions (Figure 1.2).

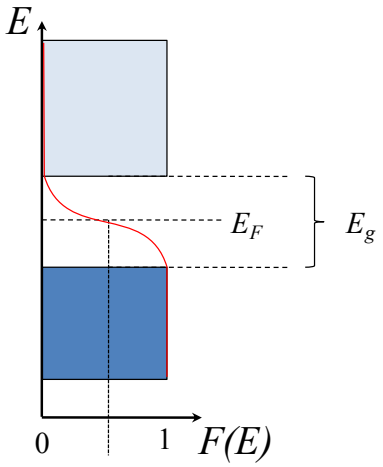

Figure 1.2: The Fermi level in an intrinsic semiconductor is between the edges of the valence and conduction bands, despite there being no chance of electron population in that region for a pure semiconductor. The distribution arising from the Fermi function is shown in red, with the Fermi level appearing at E_F, where $F(E) = 0.5$. Changes in carrier population of the bands can result in E_F being closer to either the conduction or valence band.

In the case of a semiconductor, one may imagine a scenario analogous to an electronic transition in an atom, with the gap between bands being equivalent to the energy required for the promotion of the electron from one state to the next. As the number of contributing atomic orbitals increases, the energy transitions that are discrete in the case of atomic species form continua of energy in the bulk (Figure 1.3).

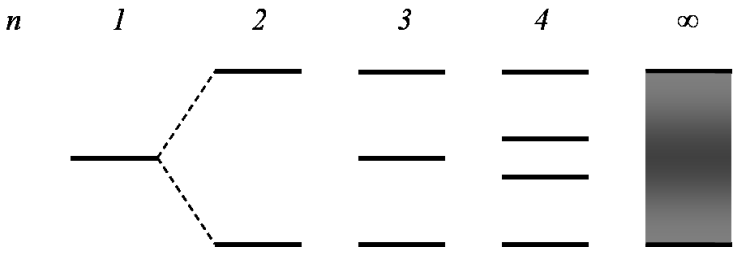

Figure 1.3: As the number of *s* orbitals, *n*, in a one-dimensional chain of atoms is increased, the discrete energy levels undergo splitting. As $n \rightarrow \infty$, a continuum forms. While a useful insight into the origin of energy bands as opposed to levels, this model does not consider all the permutations relevant in a "real" system. This approximation is based on the tight binding (TB) model.

By analogy with transitions between atomic energy levels, the region between the bands may not be occupied and is referred to as the band gap. As a matter of general agreement, the upper bound for the band gap of a semiconductor lies within the region of 3-4 eV, after which point the material is considered to be an insulator within the limits of practical application.[1] Of the species under the label of semiconductors, there are two main sub-categories – intrinsic and extrinsic semiconductors. The former definition refers to a material in which the carrier concentration arising from any impurity species are negligible and the thermally generated carriers of the bulk material are dominant. Extrinsic semiconductors are those which have had their electronic properties modified by impurities which have a different number of valence electrons, either enriching (*n*-type) or depleting (*p*-type) the number of electrons in the conduction band, hence resulting in a change in the carrier population of the band structure. Such doping may be intentional or, as in the case of GaSb grown by molecular beam epitaxy (MBE), an unintentional consequence of defects.[2]

When the first transistor was demonstrated in 1947, the intrinsic semiconductor used was Ge. Despite not being as suited for the application as Si, Ge remained the element of choice until the late 1960s, when advances in technology allowed Si to be purified effectively. The requirement for ultra-high purity in the field of semiconductor development is only one of the hurdles that must be overcome in order to access the unique properties these materials offer, as any impurities at interfaces will interfere with the local band structure, whilst undesirable species in the bulk may act as the centres of dislocations, defects and crystal imperfections.[3] Such effects lead to another crucially important consideration, one of structure - both

electronic and physical. In the case of electronic structure, the basic model (Figure 1.1) fails to provide a basis for two further categories of semiconductor - direct and indirect band gap semiconductors. To adequately explain this difference, a more complex band structure based on the nearly free electron (NFE) model that takes account of how inter-band transitions occur must be considered (Figure 1.4).

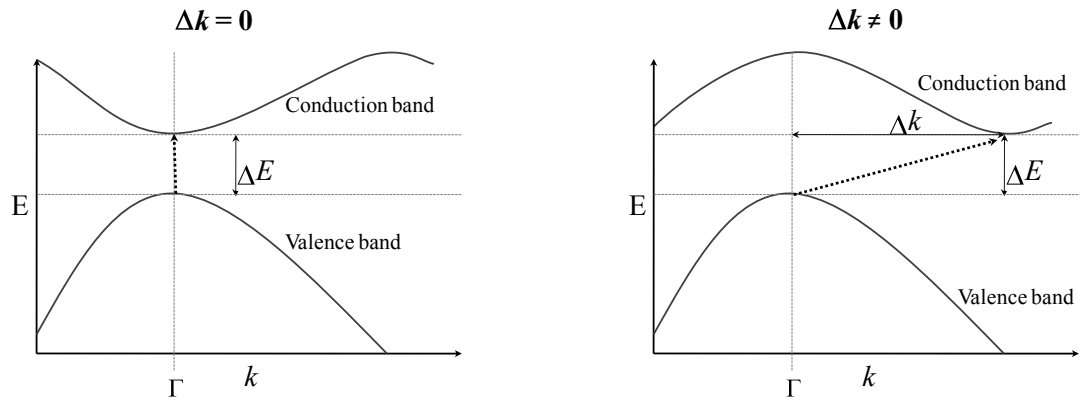

Figure 1.4: Depiction of band structures exhibiting direct (left) and indirect (right) band gaps. The change in the momentum wavevector, k, may be achieved through a phonon transition.

In the case of direct band gap semiconductors, the transition from the valence band to the conduction band requires no change in the wavevector associated with transition, i.e. $\Delta k = 0$. For indirect band gap semiconductors, there is an off-set in terms of wavevector between the point highest in energy of the valence band and the energy minimum of the conduction band. For a transition to occur, the wavevector magnitude must change which may be achieved through electron interaction with a phonon.[4]

The distinction between direct and indirect band gaps is important when considering materials for use in the field of optoelectronics, as the requirement for the involvement of a phonon in electronic transitions reduces the probability of their

occurrence. This explains the relatively low near band-edge absorption coefficients of Si and Ge and suggests that, in order to have a device that efficiently allows conversion between electrical and optical energy, semiconductors with direct band gaps are preferred. Probably the most familiar example of a direct band gap semiconductor can be found in the majority of consumer electronics – red indicator light emitting diodes (LEDs) are based on a series of doped GaAs layers. The basic requirements for fabrication of the active layers of such devices are strict: there must be an absolute minimum of impurities, the substrate temperature must be maintained within appropriate limits and it must be possible to control or monitor the rate of film growth.

Such requirements are satisfied by several growth techniques, including molecular beam epitaxy (MBE). In conjunction with in situ monitoring techniques such as reflection high-energy electron diffraction (RHEED), these techniques allow manipulation of the chemical composition and thickness of the films grown under ultrahigh vacuum (UHV) conditions. It should be noted that, while UHV conditions are prerequisites for some epitaxial growth techniques, metal organic vapour phase epitaxy (MOVPE) is undertaken in higher pressure regimes.[5]

1.2 Narrow Band Gap Semiconductors:

The band gap of a semiconductor is of key importance when considering which materials are used in different applications. The term narrow band gap has been applied either to materials exhibiting a lower band gap than that of Si (E_g = 1.1 eV)

or materials for which $E_g < 0.5$ eV.[6] To permit the inclusion of GaSb ($E_g = 0.72$ eV)[7] in this category, the former definition will be used for this investigation.

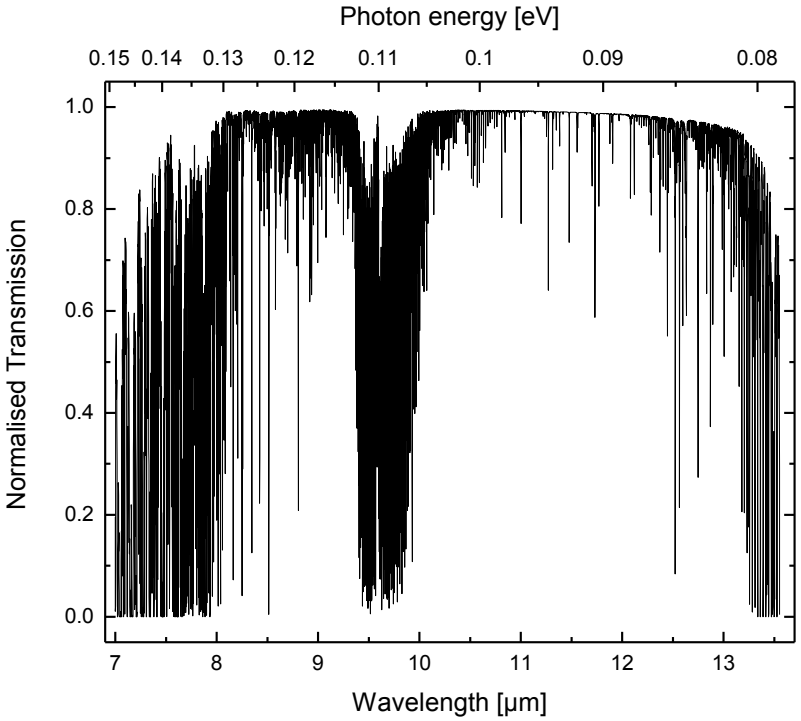

Figure 1.5: A normalised transmission spectrum of the atmosphere demonstrates large regions of low absorption in the infrared spectrum. These regions are of significant interest in the fields of communications and imaging technology. (Data collected at the Gemini Observatory, Lord, 1992)

It is often the case that materials undergo significant research and development to fulfil a need, rather than a use being found after thorough investigation. The same is now true of narrow band gap semiconductors, which are of particular interest for infrared emitters and detectors. Applications for such devices include data communication technology, sensor systems and imaging solutions for use in medical, military and commercial fields, where the wavelengths of operation coincide with the regions of maximum atmospheric transmission (Figure 1.5).[8]

Narrow band gap semiconductors can also produce electricity in thermophotovoltaic (TPV) systems.[9]

1.3 III-V Semiconductors:

These have elements from groups III and V of the periodic table in a 1:1 stoichiometric ratio (Figure 1.6).[*] Systems such as GaN_xAs_{1-x} and $In_xGa_{1-x}N_yAs_{1-y}$ also exist in this category, providing that the components (excluding those at typical dopant concentrations) are solely from groups III and V.

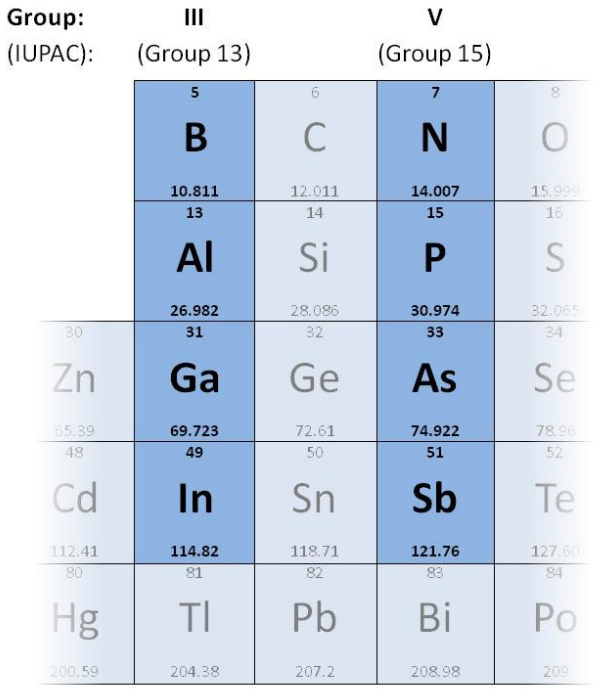

Figure 1.6: The constituents of the most common III-V materials are highlighted above. These elements may combine in a large number of permutations to produce alloys that exhibit vastly different properties.

[*] Although now superseded by the IUPAC nomenclature, traditional group names remain in common usage.

Exhibiting a wide range of lattice parameters and band gaps, III-V materials have been the focus of intense interest for a large range of diverse applications including blue LEDs, TPV devices, imaging in the mid-far infrared (IR) spectrum for military and medical systems, high frequency transistors and lasing media.[7,10,11]

There are applications of boron-containing III-Vs, particularly BN, although these are considered insulators and are not discussed further. Also omitted in this thesis are alloys of thallium and bismuth which, although falling within the III-V category, are less studied. Technological interest in each is increasing, however, with thallium alloys used for long wave IR and temperature-independent band gap materials.[12-14] Although III-Bi binaries semi-metallic, ternary alloys containing a few percent of bismuth have temperature-independent band gaps.[15] MBE growth of GaNAs and liquid phase epitaxy (LPE) of GaN have been improved with the use of Bi as a surfactant.[16,17]

Many III-V compounds have direct band gaps, making them usable for optoelectronic devices, including the materials grown, characterised and discussed in this thesis.

1.4 Dilute Nitride Alloys:

The introduction of nitrogen to III-V materials such as GaAs, GaSb, InAs and InSb has been of particular interest,[8,10,18-24] due to the effect of reducing the band gap of the host binary. The addition of nitrogen also results in a reduction in lattice parameter from that of the binary material.[25] This offers the opportunity, by using quaternary alloys, to vary both the composition and lattice spacing independently.

1.4.1 The Band Anticrossing (BAC) Model:

The qualitative description of band gap reduction upon addition of nitrogen to the lattice originates from the band anticrossing (BAC) model. First applied to the $Ga_xIn_{1-x}N_xAs_{1-x}$ system,[26] it describes the manner in which the band structure from that of the host lattice is altered by the introduction of a resonant nitrogen level.

The assumptions present in the simplest implementation are that the nitrogen content is sufficiently low that each interaction between nitrogen atoms is negligible and that only one nitrogen state, E_N, is considered. As such, nitrogen clusters are not considered. An additional assumption employed is that the presence of nitrogen does not perturb the valence band structure of the host lattice.

The host conduction band, E_c, is modelled by

$$\text{——}, \qquad (1.2)$$

where $E_c(k)$ is the conduction band energy at wavevector k, $\hbar$ is the reduced Planck constant and m^* denotes the effective electron mass of the host matrix (Figure 1.7). The bands resulting from the interaction of E_c and E_N, E_+ and E_-, are provided as the solutions of

$$- \qquad \text{——————}, \qquad (1.3)$$

where V_{cN} is an interaction parameter given by

$$\text{—}, \qquad (1.4)$$

Here, β is a constant and x is the substitutional N mole fraction. As a function of k, one may model the change in band structure (Figure 1.8).

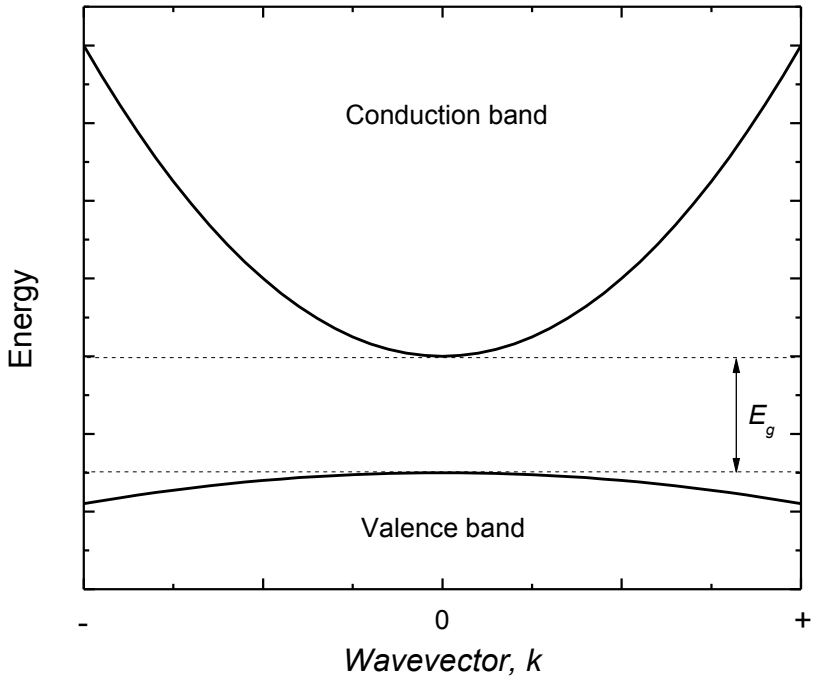

Figure 1.7: A representation of the lowest conduction band and uppermost valence band of a III-V compound.

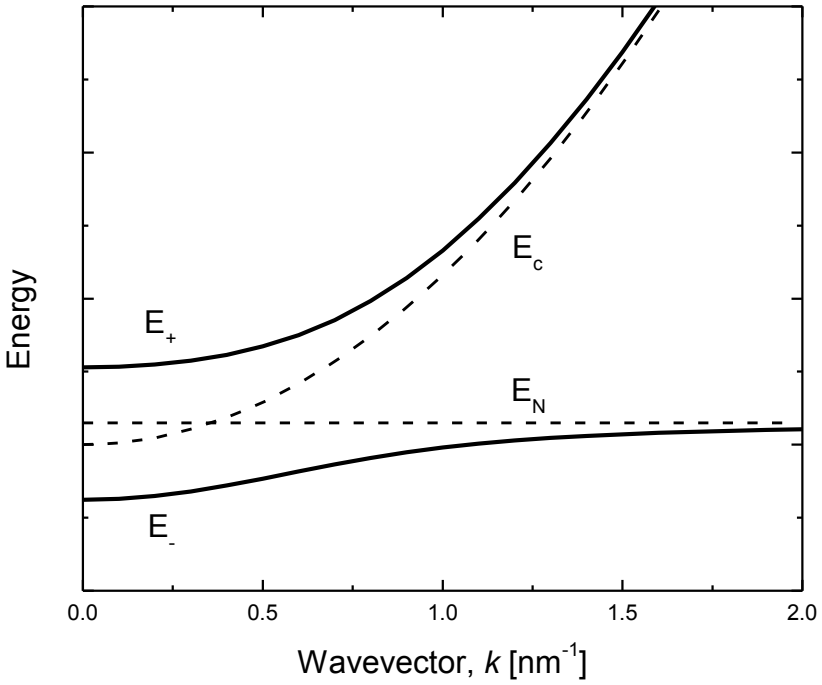

Figure 1.8: A representation of the change in band structure resulting from the introduction of a resonant nitrogen level, for a fixed nitrogen content. The original host conduction band (E_c) and the resonant nitrogen level (E_N) are shown as dashed lines, with the resulting E_+ and E_- bands shown as solid lines. It can be seen that the new E_- band has decreased in energy at $k = 0$, resulting in a decrease in the effective band gap.

The effect of the creation of the E_- band is to reduce the conduction band minimum (CBM). Since the valence band structure is assumed to remain unaffected by the addition of the atomic nitrogen state, this results in an effective reduction in band gap.

As can be seen from eq. (1.4), the level of interaction between E_c and E_N scales as the square root of nitrogen content, permitting a simulation of the E_+ and E_- levels as a function of nitrogen content (Figure 1.9).

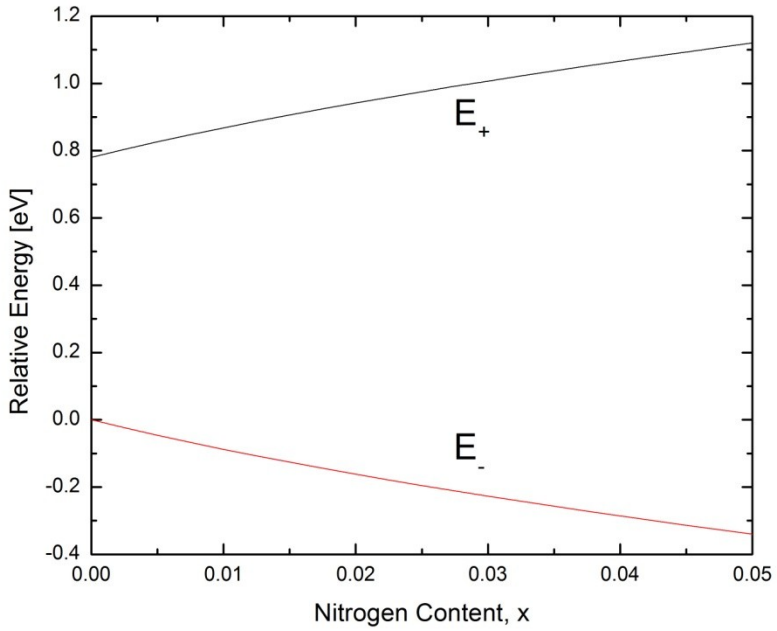

Figure 1.9: A simulation, at $k = 0$, depicting the energy level of the E_+ and E_- bands in GaN_xSb_{1-x} as a function of nitrogen content, x. Under the assumption that the valence band structure is independent of nitrogen content, the decrease in the energy of the E_- band with increasing nitrogen correlates with the amount of band gap reduction.

Limitations of this model arise in situations where the implicit assumptions do not remain valid. For example, at sufficiently high nitrogen concentration, nitrogen

atoms no longer exist in total isolation from one another, resulting in interaction of the electronic states. Furthermore, the model does not take into account interstitial N species or nitrogen clusters, the presence of which would further perturb the band structure of the host matrix.

1.5 Crystal Structure:

Periodicity is the primary requirement of a simple crystal structure. Knowledge of the crystal system is also fundamental to the understanding of diffractive analytical processes, such as reflection high-energy electron diffraction (RHEED) and X-ray diffraction (XRD). Deviations from a perfect periodicity are also required to rationalise the behaviour of real semiconductor systems.

1.5.1 The Crystal Lattice:

There are a finite number of arrangements of atoms in a crystal, described by the 14 unique three-dimensional crystal structures, or Bravais lattices. These are sub-types of the 7 principal crystal systems and made distinct from those primitive lattice (where lattice points appear only on the lattice vertices) by the addition of lattice points to the unit cell.

The simple cubic (SC) unit cell is the most conceptually simple, with one atom repeated with every distance a in the x, y and z directions, with every unit cell containing 8 x (1/8) atoms. It should, however, be noted that the cubic structures are unique, where the lattice vectors are all orthogonal and equal in magnitude.

1.5.1.1 Lattice parameters:

A complete set of lattice parameters comprises three lengths and three angles (Figure 1.10). These describe the translation required from a given point to the next identical point in an ideal crystal and, in some of the crystal structures, two or more of these lengths and/or angles may be equivalent.

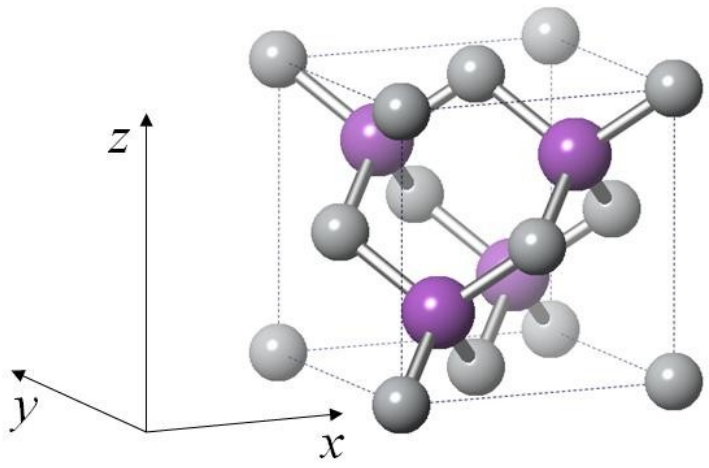

Figure 1.10: The lattice parameters (also referred to as constants) are the three lengths and the angles between them. In the cubic systems, of which the zinc blende structure is one, it can readily be established that these lengths are all equivalent and that the angles between them are 90°.

1.5.2 Crystal Imperfections:

In many situations, it would be ideal to form a perfect crystal. In practice however, there are always imperfections in the structure. Such features may arise as a result of the incorporation of contaminants during the growth process, imperfections present in the substrate or the failure of deposited species to "settle" in the correct location, resulting from sub-optimal growth conditions. Since, in terms of electronic and physical properties, the effects of each of these phenomena extend over a

comparatively large range in the crystal structure, it is of benefit to understand the main types of defects and dislocations.

1.5.2.1 Defects:

The term defect is a generic label for any imperfection, in a crystal structure it is more properly used to describe point irregularities in the lattice. The most conceptually simple, for a structure consisting of a single element, are the exclusion of an atom from the lattice, a vacancy defect (Figure 1.11a), or the inclusion of an extra atom where there would not normally be one, an interstitial defect (Figure 1.11b).

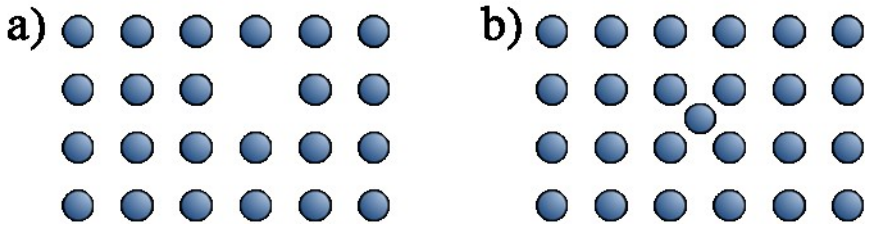

Figure 1.11: 2D representations of crystal structure with a) a vacancy defect and b) an interstitial defect in a cubic crystal consisting of a single atom type. Interstitial defects may also occur due to the inclusion of contaminants in the structure.

Point defects such as those described above are unavoidable and are, within limits, energetically favoured (Figure 1.12). Point defects increase the disorder of the system, thus they are entropically favoured and offset the adverse enthalpic contribution according to

$$\Delta G = H - T\Delta S \tag{1.5}$$

where ΔG is the change in Gibbs free energy, H denotes enthalpy, T is the temperature and ΔS is the change in entropy afforded by the inclusion of defects.[27]

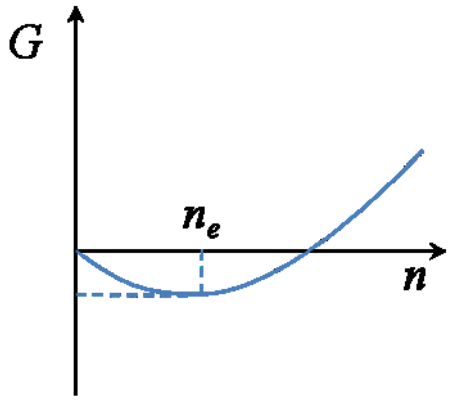

Figure 1.12: Initially, the Gibbs free energy of a crystal is observed to decrease as a function of the number of point defects, n. At a minimum of Gibbs free energy, the number of such defects is n_e. This results from increased entropic contribution in eq. (1.5)

When impurities are incorporated into the lattice, each may occupy either an interstitial site or a site that would ordinarily be filled by native species, a substitutional defect. The term "impurity" in this context is somewhat erroneous however. In consideration of a binary crystal, comprising elements A and B, there may be the inclusion of an atom of B where one would ordinarily expect an atom of type A to be situated. In this instance, the defect is referred to as an antisite defect and denoted B_A.[28]

The intentional introduction of non-native material to the lattice is used to alter the physical and/or electronic properties of the crystal. In semiconductor fabrication, utilising such impurities, or dopants, is a method by which extrinsic semiconductors may be formed.

1.5.2.2 Dislocations:

Dislocation is the term used to describe a line defect in a lattice and is characterised in terms of the Burgers vector, *b*, which describes the propagation of distortion through the lattice and can be visualised by considering the effect of an introduced dislocation on a closed loop of lattice points around the dislocation origin (Figure 1.13). Where the Burger's vector is normal to the dislocation line, it is considered an edge dislocation, while a Burger's vector occurring parallel to the dislocation line describes a screw dislocation. However, these represent extreme examples and, in practice, the angle between the Burger's vector and dislocation line may take any value to give mixed dislocations. In an edge dislocation, an incomplete row of lattice points is present, causing a deformation in the lattice.

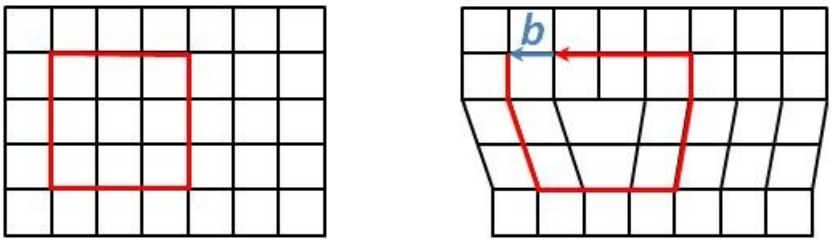

Figure 1.13: The introduction of an edge dislocation in a simple cubic lattice, where an incomplete row of atoms causes deformation. In a 3-dimensional model, the lattice may be considered to extend perpendicular to the plane of the page. For an edge dislocation, the Burger's vector, *b*, is normal to the dislocation line.

Occurring where there is a mismatch in lattice parameter, edge dislocations are commonly referred to as misfit dislocations forming when the energetic cost of formation may be overcome by the strain energy in the film.

Screw dislocations are the result of the partial shearing of a plane (Figure 1.14). While the long range effects of an edge dislocation may be diminished with distance

from the end of the incomplete row of atoms, under perfect growth, the screw dislocation persists with each subsequent layer grown upon it.

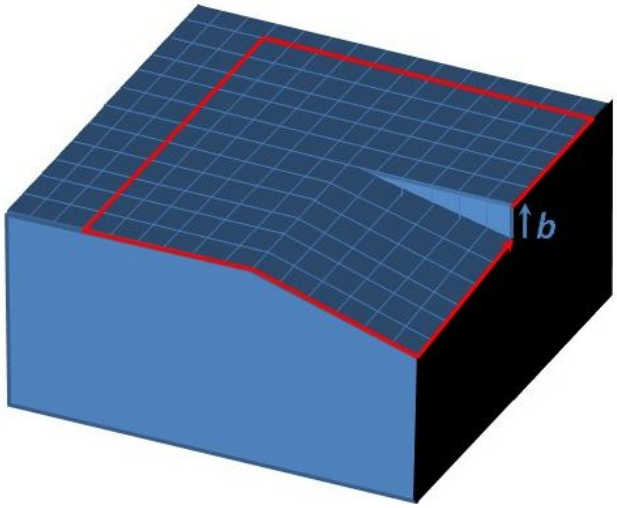

Figure 1.14: A representation of a screw dislocation. The Burger's vector is parallel to the dislocation line.

1.6 Epitaxial Growth of Thin Films:

In its broadest sense, there are many means through which a deposited layer may be added to a substrate, including spin-coating and sputtering. For the manufacture of effective semiconductor device structures however, it is essential to control the thickness, morphology and crystal quality of the deposition. For this reason, the discussion of thin film growth shall focus on epitaxial growth. Epitaxy takes its name from the Greek words *epi*, ("above") and *taxis*, ("in ordered manner") and describes a process whereby ordered layers may be formed on an existing substrate from incident atomic or molecular species.[29]

There are three main mechanisms of epitaxial film growth.[30] The Frank-van der Merwe mechanism is the simplest, where the growth sequence is layer-by-layer. In

the idealised case in this mode of growth, one layer is completed before another is started. The surface coverage, θ, is analogous to Langmuir surface coverage, with the modification that allowed values may extend such that $\theta > 1$ to describe coverage extending beyond monolayer thickness.

Frank-van der Merwe (FdM) growth does not occur when the aggregation of the deposited material is more energetically favourable, however. In this instance, an island growth mechanism described as being Volmer-Weber (VM) growth dominates, allowing complete coverage of the substrate only as the 3D islands broaden and coalesce.

Under the conditions employed in epitaxial growth, the evolution of the surface morphology is thermodynamically driven. As a result, the consideration of the relative surface energies of the two materials (γ_A and γ_B, where $\gamma_A < \gamma_B$) in combination with the interfacial energy, γ^*, produces a qualitative picture of the mechanism likely to dominate. Considering the case of deposition of material *A* on *B*, with $\gamma_A + \gamma^* < \gamma_B$, and the growth will favour the formation of 2D layers. If the reverse situation is the case however, with deposition of *B* on a substrate of material *A*, then $\gamma_B + \gamma^* > \gamma_A$ and 3D island growth is preferred.

Where strain is present in the system, the interfacial energy may increase with deposition thickness, causing a transition between the growth modes, as in the Stranski-Krastanov (SK) mechanism.

It is important to make the distinction between initial (VM) island growth, where the formation of islands is driven by energetic factors, and growth that proceeds with island-like structures, such as that in the latter stage of SK growth. In the second

scenario, film morphology is dominated by the existing roughness resulting from the formation of islands.

Whilst not strictly a mode of growth in the same way as those described above, step-flow growth is nevertheless a phenomenon to take into consideration. Briefly, the ability of species to migrate across the surface is a result of sufficient thermal energy allowing atoms to move through formation and cleavage of bonds and contributes to the prevention of surface roughening.[31] The distance over which this may occur, or diffusion length, allows species to find a local energy minimum within that range. Step edges provide a sink for diffusing species thus, where species have sufficient energy but do not desorb, growth will preferentially evolve at these sites. In the simplest case, an adatom with a sufficient diffusion length will be able to reach either the step edge of that terrace or the next step edge down. The result is a situation where step edges migrate across the surface, resulting in no net change in roughness (Figure 1.15).

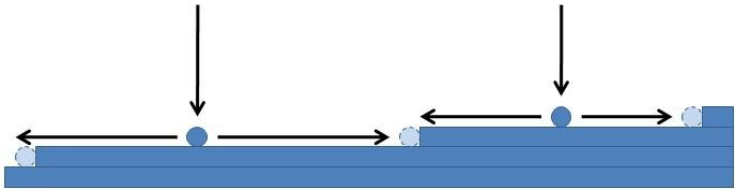

Figure 1.15: During step-flow growth, surface roughness does not change significantly, as species have diffusion lengths sufficient to reach the more energetically favourable step edge sites. This results in step edges migrating, rather than being eliminated, causing a lack of observed RHEED oscillations as a function of time. RHEED is discussed more thoroughly in Chapter 2.

When using an epitaxial method for film growth, there are many factors which must be taken into account, depending on the proposed film thickness. The first of these is the similarity between selected physical characteristics of the substrate and those

of the film to be grown.[32] The most important of these is the lattice constant associated with each. During the first few monolayers of layer-by-layer growth, the deposited material adopts the same lattice parameters of the substrate, introducing an inherent strain in the growing layer. Such growth is referred to as being pseudomorphic and persists while elastic strain energy may be accommodated. Should the growth proceed past the critical thickness, the layer may relax by the formation of dislocations as the energy requirement for the accommodation of strain exceeds the energetic cost of forming dislocations. For the growth of films with a low density of defects, lattice mismatch is a prime concern. Where lattice mismatch is present between the intended film and the substrate, buffer layers of intermediate lattice parameter may be utilised. In the simplest case, the strain in films of the material under investigation is reduced by the introduction of layers of another intermediate material, the lattice constants of which are between those of the substrate and the film to be grown thereon. Successive buffer layers result in a staggered reduction of the lattice constant, hence a reduction in the strain of the final grown film. An alternate method is to grow a single buffer layer of, for example, a ternary system with graduated composition.

1.7 Crystallography of the GaSb(001) Surface:

Upon first inspection, the (001) surface of a zinc blende unit cell (Figure 1.10) appears to have four-fold rotational symmetry. However, examination of the whole unit cell reveals a two-fold rotational symmetry, due to the alternating directions of the bonds.

Growth of GaSb is generally conducted under an excess of antimony, causing the surface to be Sb-terminated. For III-V (001) surfaces, dimeric group V species are common,[33-35] with the upper layers of the GaSb(001) surface thought to consist of at least two layers of antimony, with the uppermost layer formed from rows of dimers which extend along the [10] direction.[33] Figure 1.16 demonstrates that the antimony-rich GaSb(001) surface exhibits anisotropy for both major reconstructions.

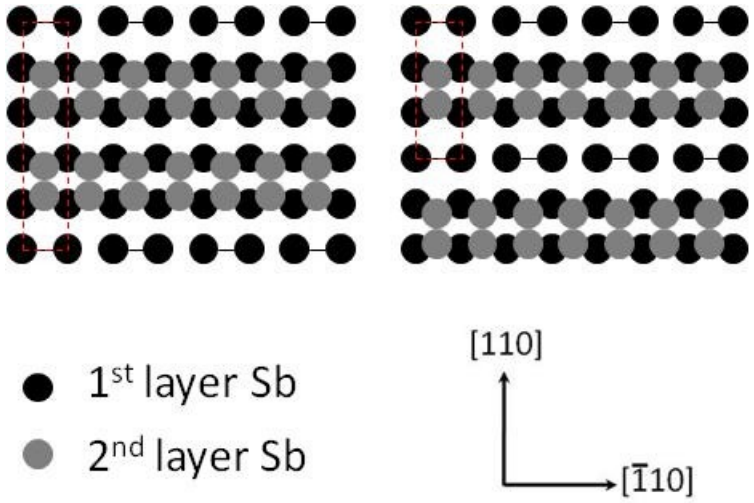

Figure 1.16: Possible arrangements for the Sb-terminated GaSb(001) surface, giving a (1x5) symmetry (left) and a (1x3) surface reconstruction (right). Reconstruction unit cells are highlighted in each case.

The structure of a surface has an effect on the mobility of species. In particular, the symmetry of a surface can give rise to anisotropy in growth, with the ability of species to diffuse in one direction differing significantly from diffusion in another direction.[36] As such, it is expected that the III-V surfaces grown in this study may exhibit anisotropy in the surface features observed.

[1] Peter Y. Yu and Manuel Cardona, *Fundamentals of Semiconductors* (Springer-Verlag, Heidelberg, 2010).

[2] T. D. Veal, Surface Science **499**, 251-260 (2002).

[3] S. W. King, J. P. Barnak, M. D. Bremser, K. M. Tracy, C. Ronning, R. F. Davis, and R. J. Nemanich, Journal Of Applied Physics **84**, 5248 (1998).

[4] E. O'Reilly, *Quantum Theory of Solids* (Taylor & Francis, London, 2002).

[5] W. Richter, Vacuum **41**, 963-964 (1990).

[6] S. Misra, G. S. Tripathi, and P. K. Misra, Journal of Physics C: Solid State Physics **20**, 277 (1987).

[7] I. Vurgaftman, J. R. Meyer, and L. R. Ram-Mohan, Journal of Applied Physics **89**, 5815 (2001).

[8] P. H. Jefferson, L. Buckle, D. Walker, T. D. Veal, S. Coomber, P. A. Thomas, T. Ashley, and C. F. McConville, Physica Status Solidi (RRL) – Rapid Research Letters **1**, 104-106 (2007).

[9] K.J. Cheetham, P.J. Carrington, N.B. Cook, and a. Krier, Solar Energy Materials and Solar Cells **95**, 534-537 (2011).

[10] T. D. Veal, L. F. J. Piper, S. Jollands, B. R. Bennett, P. H. Jefferson, P. A. Thomas, C. F. McConville, B. N. Murdin, G. W. Smith, and L. Buckle, Applied Physics Letters **87**, 132101 (2005).

[11] E. Michel, G. Singh, S. Slivken, C. Besikci, P. Bove, I. Ferguson, and M. Razeghi, Applied Physics Letters **65**, 3338 (1994).

[12] H. Asahi, M. Fushida, K. Yamamoto, K. Iwata, H. Koh, K. Asami, S. Gonda, and K. Oe, Journal of Crystal Growth **175-176**, 1195-1199 (1997).

[13] R. Beneyton, B. Canut, P. Regreny, M. Gendry, G. Grenet, and G. Hollinger, Journal of Crystal Growth **275**, e1171-e1175 (2005).

[14] M. Takushima, N. Kobayashi, Y. Yamashita, Y. Kajikawa, Y. Satou, Y. Tanaka, and N. Sumida, Journal of Crystal Growth **301-302**, 117-120 (2007).

[15] G. Feng, K. Oe, and M. Yoshimoto, Physica Status Solidi (a) **203**, 2670-2673 (2006).

[16] E. Young, S. Tixier, and T. Tiedje, Journal of Crystal Growth **279**, 316-320 (2005).

[17] C. T. Foxon, Journal of Crystal Growth **251**, 510-514 (2003).

[18] Y. Lin, Thin Solid Films **368**, 249-252 (2000).

[19] M. Kondow, K. Uomi, A. Niwa, T. Kitatani, S. Watahiki, Y. Yazawa, K. Hosomi, and T. Mozume, Solid-State Electronics **41**, 209–212 (1997).

[20] Q. X. Zhao, S. M. Wang, M. Sadeghi, a. Larsson, M. Friesel, and M. Willander, Applied Physics Letters **89**, 031907 (2006).

[21] A. Lindsay, E. O'Reilly, A. Andreev, and T. Ashley, Physical Review B **77**, 1-10 (2008).

[22] S. Sakai, Journal of Crystal Growth **189-190**, 471-475 (1998).

[23] M. Hao, Journal of Crystal Growth **189-190**, 481-484 (1998).

[24] Y. H. Zhang, P. P. Chen, H. Yin, T. X. Li, and W. Lu, Journal of Physics D: Applied Physics **43**, 305405 (2010).

[25] L. Buckle, S. D. Coomber, T. Ashley, P. H. Jefferson, D. Walker, T. D. Veal, C. F. McConville, and P. A. Thomas, Microelectronics Journal **40**, 399-402 (2009).

[26] W. Shan, W. Walukiewicz, J. Ager, E. Haller, J. Geisz, D. Friedman, J. Olson, and S. Kurtz, Physical Review Letters **82**, 1221-1224 (1999).

[27] A. R. West, *Solid State Chemistry and Its Applications* (John Wiley & Sons, 1987), p. 319.

[28] R. J. D. Tilley, *Defects In Solids* (John Wiley & Sons, 2008), p. 29.

[29] B. A. Joyce, Rep. Prog. Phys. **48**, 1637-1697 (1985).

[30] D. J. Eaglesham and M. Cerullo, Physical Review Letters **64**, 1943–1946 (1990).

[31] M. Biehl, W. Kinzel, and S. Schinzer, Europhysics Letters (EPL) **41**, 443-448 (1998).

[32] R. Enderlein and N. J. Horing, *Fundamentals of Semiconductor Physics and Devices* (World Scientific Books, 1996), pp. 396-403.

[33] P. M. Thibado, B. R. Bennett, M. E. Twigg, B. V. Shanabrook, L. J. Whitman, 14, 885-889 (1996).

[34] A.R. Avery, D. M. Holmes, J. Sudijono, T. S. Jones, B. A. Joyce. Surface Science, **323**, 91-101, (1994)

[35] C. F. McConville, T. S. Jones, F. M. Leibsle, S. M. Driver, T. C. Q. Noakes, M. O. Schweitzer, and N. V. Richardson, Physical Review B 50, 14965 (1994).

[36] V. Ivanov, A. Boudza, N. Kutt, N. Ledentsov, S. Ruvimov, V. Shaposhnikov, S. Kop, Journal of Crystal Growth **156**, 191-205 (1995).

Chapter 2

"Some say opportunity knocks only once. That is not true. Opportunity knocks all the time, but you have to be ready for it. If the chance comes, you must have the equipment to take advantage of it."

Louis L'Amour (1908 - 1988)

In this chapter are details of the experimental equipment and techniques used during this study. Sample-specific operating parameters are described in their respective chapters.

2.1 Molecular Beam Epitaxy (MBE):

MBE imposes stringent requirements upon equipment and operating conditions.[1] The growth of samples was conducted in a GEN II (Varian) MBE system with sources capable of supplying Ga, In, As_n (n=2,4), Sb_n (n=2,4), N, Be and Si. This section details the construction and function of the chamber and sources.

2.1.1 Equipment construction:

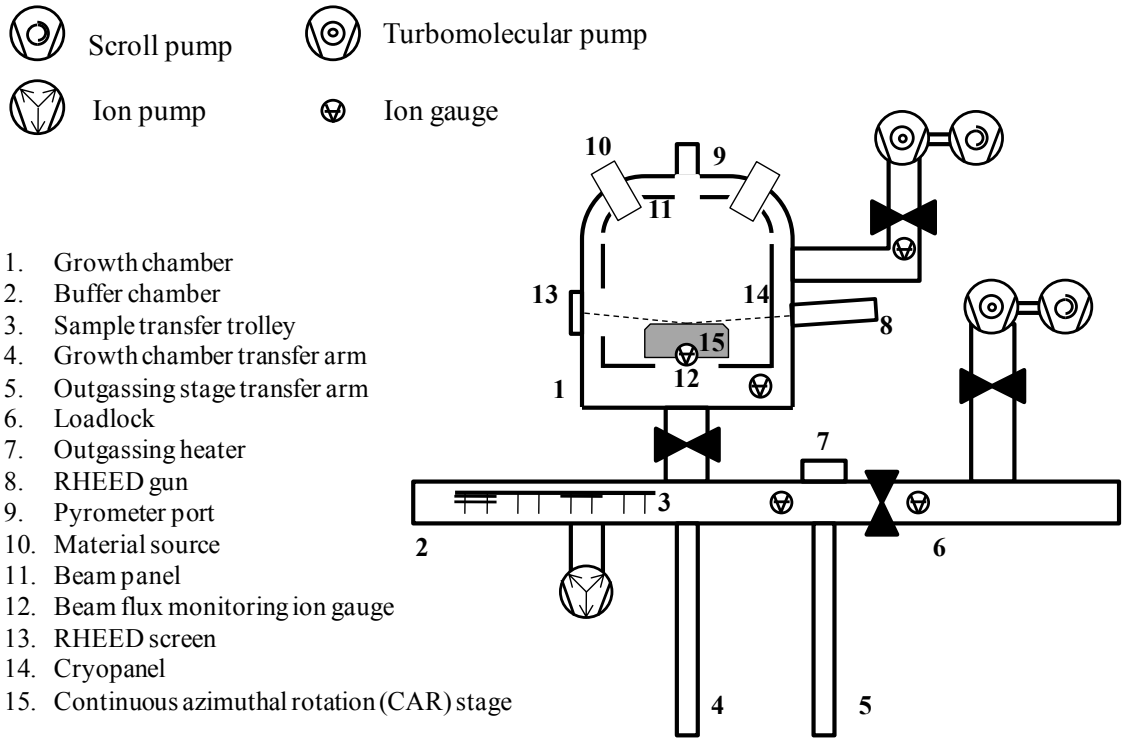

Figure 2.1: A reduced schematic representation of the GEN II equipment used in this study. For clarity, only two sources are displayed.

The GEN II modular system (Figure 2.1) is designed to be used for the epitaxial growth of material on wafers up to 3" in diameter. The chamber consists of the outer

walls, within which the cryoshroud is situated. This is a thin stainless steel reservoir through which liquid nitrogen is pumped, which provides effective pumping for contaminants such as water vapour as well as reducing undesirable material flux from hotspots such as ion gauges.[2] Where the sources protrude into the chamber, they are segregated by the beam panel and a reservoir, cooled to -25°C by a re-circulated water/polyethylene glycol mixture. The effects of the beam panel are to reduce the severity of thermal gradients, to mitigate liquid nitrogen boil-off from the cryoshroud and to suppress the migration of material from one source aperture to another. In addition, the beam panel provides a degree of thermal isolation between sources.

2.1.2 Ultra-High Vacuum (UHV) Environment:

To limit as far as possible the incorporation of contaminants into the grown layers, the growth chamber must operate in ultra-high vacuum (UHV) conditions ($< 10^{-9}$ mbar). To achieve this, the system used for this study utilises several different pumps to achieve a base pressure better than 1×10^{-10} mbar.

In order to decrease the pressure of the system to ca. 10^{-3} mbar, scroll pumps are employed. In contrast with the other commonly used option, rotary pumps, scroll pumps are oil-free and negate the risk of organic contaminants leaching back into the growth chamber. Turbomolecular pumps may then be activated to reduce the pressure as far as ca. 10^{-10} mbar. To achieve pressures as low as this, it is necessary to bake the system, to facilitate the removal of adsorbed water. The active components of a turbomolecular pump are a series of turbine fan blades which rotate,

causing the deflection of gaseous species into the backing line, where they are removed by scroll pumps.[3] Turbomolecular pumps are most effective when utilised in a molecular flow regime, and where the turbine blade velocity is comparable to the thermal velocity of the species to be pumped.[4] Once the chamber has achieved a pressure of 10^{-5} mbar or better, ion pumps may be used. This upper limit on pressure regime is chosen in order to reduce the potential for arcing and to prolong the life of the trapping electrodes. Fully encased in a vacuum-tight housing, ion pumps contain no moving parts, thus may be switched off at any time without causing the system to vent. Diode pumps represent the most conceptually simple type of ion pump where, through the application of a potential difference (ca. 5-6 kV) between large surface area titanium electrodes, gaseous species may be ionised and subsequently trapped on the charged plates. This may be facilitated by the sputtering of titanium atoms/clusters which act to trap the collected species. Triode pumps, as the nomenclature suggests have three electrodes, as opposed to the two present in a diode pump. In this arrangement, gaseous species undergo ionisation at the anode prior to acceleration through the primary cathode to a collection cathode situated behind the primary. The primary benefit of the triode arrangement over the diode pump is the ability to trap noble gas species.[5]

Cryopumps may also be employed for the effective removal of H_2, H_2O and CO. In the GEN II apparatus, helium is compressed through an expansion system, causing the temperature of the active surface inside the vacuum to fall within the range 4-15K, facilitating adsorption of incident species. An alternative to the compression/expansion method is heat exchange between the active surface and cryogen liquid circulation system. It is the latter means by which the cryoshroud

(which is essentially a rudimentary cryopump that surrounds the inside of the growth chamber) performs its function.

In common with many other pumping systems, helium is not readily removed by cryopump apparatus,[6] which may present difficulties when it is employed as a leak-detection agent. Unlike ion pumps, a power interruption will cause an increase in temperature in a cryopump, leading to desorption of contaminants and partial regeneration of the system.

2.1.3 The growth chamber

Growth chambers with more than one source do not permit the molecular beams to be normal with respect to the plane of the sample (Figure 2.2). As a result, the beam flux experienced by the sample varies across its surface. If the sample is sufficiently small, relative to the rate of change of effective flux with lateral distance, this variance is negligible. In the case of larger samples, such as those used in this study, rotation of the wafer during growth is necessary to encourage a homogenous flux exposure.[7]

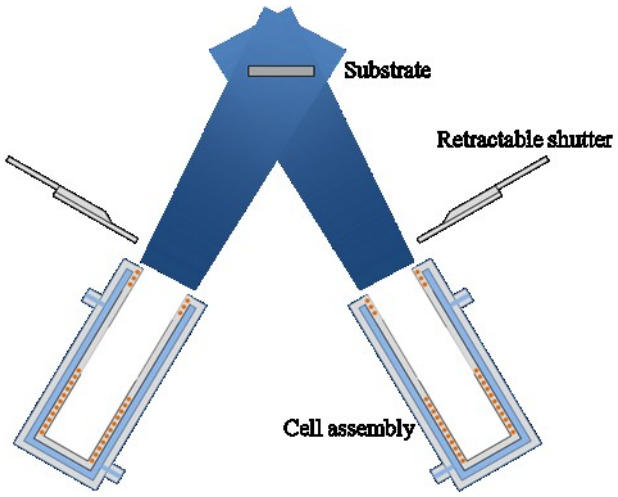

Figure 2.2: A depiction of the cell position and orientation, relative to the substrate. This is not considered to adversely affect the growth, providing that the sample is of sufficient temperature and, in the case of a large substrate, sample rotation is employed.[7]

Substrates are mounted on the CAR using Mo platens, bound with either indium solder or secured with molybdenum cover slides, held in place with a circlip. Behind this assembly, the heater unit comprises a ceramic disc inside which is affixed a resistive element. A small aperture in the heater assembly allows the positioning of a thermocouple for feedback temperature control to be positioned ca. 3 mm from the back of the platen/wafer (Figure 2.3).

2.1.4 Sample Mounting:

Sample mounting is a crucial aspect of growth, having an effect not just on substrate fixation, but the mechanisms of heating/cooling and the types of technique may be employed during and after growth. Amongst many conditions that a mounting solution must satisfy are the requirements that it provide good stability over a large

range of temperature, must not affect the composition of the growing layer and must permit removal of the sample under conditions that will not alter the sample, either mechanically or chemically. There are two basic methods of affixing a sample for growth, one employing a solder or eutectic and the other relying on a mechanical arrangement that may hold a wafer without the need for any additional bonding agent. While there is a range of materials that may be employed in the former case, below are discussed only the methods employed in this investigation.

2.1.4.1 Indium Bonding:

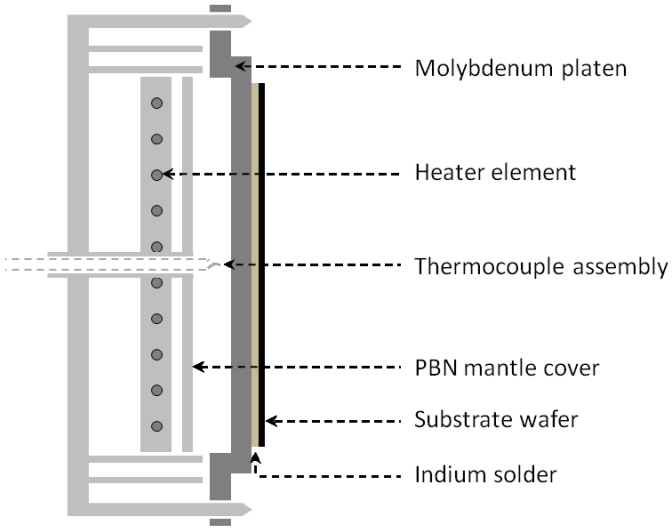

Figure 2.3: A schematic representation of a molybdenum platen supporting a wafer bound with indium solder.

Historically, indium solder has been used extensively to bond substrates to the sample holder. Due to the relatively low melting point of indium metal (ca. 157°C) wafers may be affixed to the platen with a thin film of indium and, despite epitaxial growth invariably occurring in a temperature regime where the solder is in liquid

phase, the sample tends to be held in place. The sample may be removed from the platen after growth by placing the assembly on a hotplate. After growth involving indium bonded substrates in the GEN II apparatus, there was noticeably less liquid solder in the case of each sample. This, in conjunction with pitting of soldered surfaces suggests that there is some ingress of indium into both the platen and wafer, although the exact nature of bonding remains undetermined.

Aside from ease of application, indium solder has been widely utilised with the aim of ensuring good thermal contact throughout the mounting assembly. However, there is literature to suggest that sample quality may be affected where temperature gradients, unintentional indium incorporation or mechanical strain are present.[8,9] Additionally, where samples have been affixed for a sufficient amount of time, they may be difficult to remove without risking damage to the wafer.

There is clearly a strong drawback of using indium solder in instances where the grown sample is to be characterised by transmission optical measurements, although such characterisation is possible after mechanical abrasion and polishing processes. A layer of solder, however, does offer the potential for heating which is both uniform and conductive.

2.1.4.2 Indium-free Substrates:

An alternative method of substrate fixation relies upon a wafer being placed in a bespoke holder. Held between two flat rings, both sides of the substrate remain uncovered, allowing radiation from the heater to fall directly on the rear of the wafer. As such, this changes the mechanism of substrate heating from a process dominated

by conduction from the platen/solder to one primarily of absorption of energy radiated by the heater assembly. For situations where growth on a cleaved wafer sample is required, the substrate retaining plates may be replaced with ones featuring an aperture of the required dimensions.

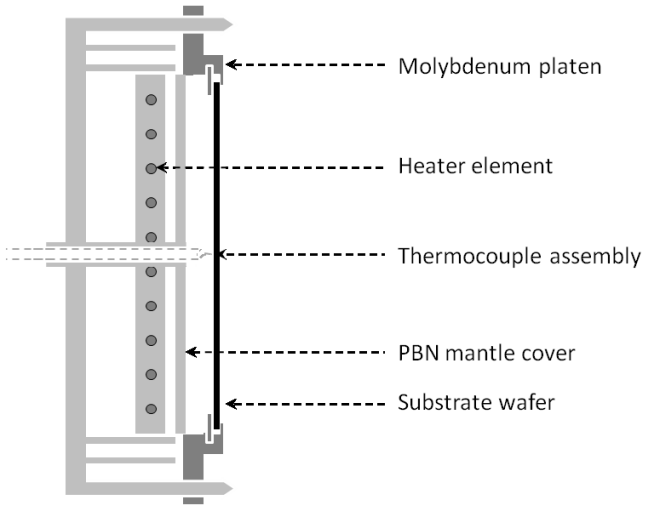

Figure 2.4: A schematic representation of an indium-free substrate platen, affixed to the sample heater assembly. The wafer is held against an opening in the front face with a retaining ring. Radiant heat from the diffuser plate is incident directly on the reverse of the substrate.

2.1.5 Material Sources

Advances in material sources allow the inclusion of an expanding variety of species for use in epitaxial growth. There are numerous means by which the species required for growth may be admitted to the chamber, which may provide either pure material for growth, or precursors designed to decompose upon the surface with the remainder of the compound desorbing from the substrate and taking no further part in the growth process. In the latter case, species may be provided from the evaporation/sublimation of a liquid/solid or, as in the case of phosphine and arsine, supplied in gaseous form.

There follows a description, covering the modes of operation of the types of cell employed on the GEN II system used in this study:

2.1.5.1 Effusion Cells

For effusion from solid or liquid source materials, the cell ordinarily consists of a heated pyrolytic boron nitride (PBN) crucible containing the material to be deposited. Where evaporation occurs from a free surface, it may be described as Langmuir evaporation. However, in effusion sources such as those employed in the GEN II apparatus, this is not the case. Instead, a near equilibrium vapour pressure is maintained inside the source, resulting in evaporation predominantly of the Knudsen type.[10] Hence, such sources are commonly referred to as Knudsen or K-cells (Figure 2.5). The operating temperature of the crucible is dependent upon the material used and the flux required.

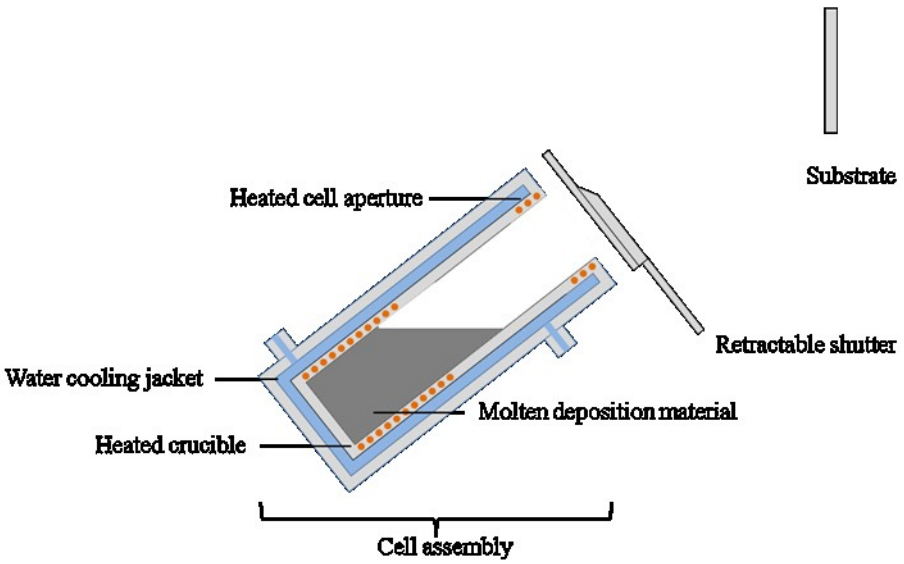

Figure 2.5: A simplified representation of an effusive cell and shutter assembly. Omitted for clarity are the heat shield and thermocouple. The water cooling facility is not present on all sources.

A variation of this design is the SUMO® cell (Veeco), which features a narrowed aperture (Figure 2.6).

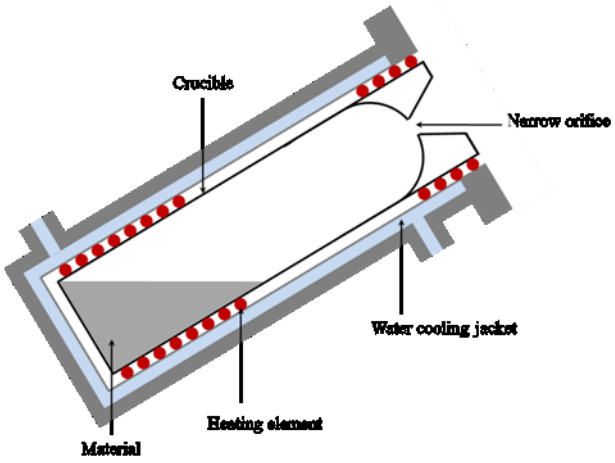

Figure 2.6: A schematic of a SUMO® cell designed, showing the heated, narrow orifice that provides an increased crucible pressure, leading to greater flux uniformity. Omitted for clarity are the heat shields and thermocouples.

This design has been proven to enhance uniformity of deposition in elements which exhibit a high vapour pressure, through increasing the pressure in the crucible stage.[11] It also offers a second advantage of reducing the likelihood of cross-contamination.

2.1.5.2 Valved Cracker Sources

While it is possible to supply a flux from solid group V elements such as antimony and arsenic using the type of source described above, there is very little flexibility. For example, sublimation of As and Sb produces a majority tetramer flux in each case. It is desirable in some cases to perform growth with monomers or dimers of

group V elements and, while an increase in temperature may be employed to provide dimer or monomer species, the beam equivalent pressure will also be affected.[12]

In order to achieve control of both the degree of cracking and the flux density, a source utilising separate evaporation and cracking regions is necessary (Figure 2.7). To provide additional control, a valve following the sublimation stage permits the flux to be varied without requiring any change in operating parameters.

An additional benefit of valved over non-valved sources includes an extended source lifetime that results from less material loss during the time taken to reach operating temperature, thus reducing the frequency with which the source must be refilled with often toxic materials.

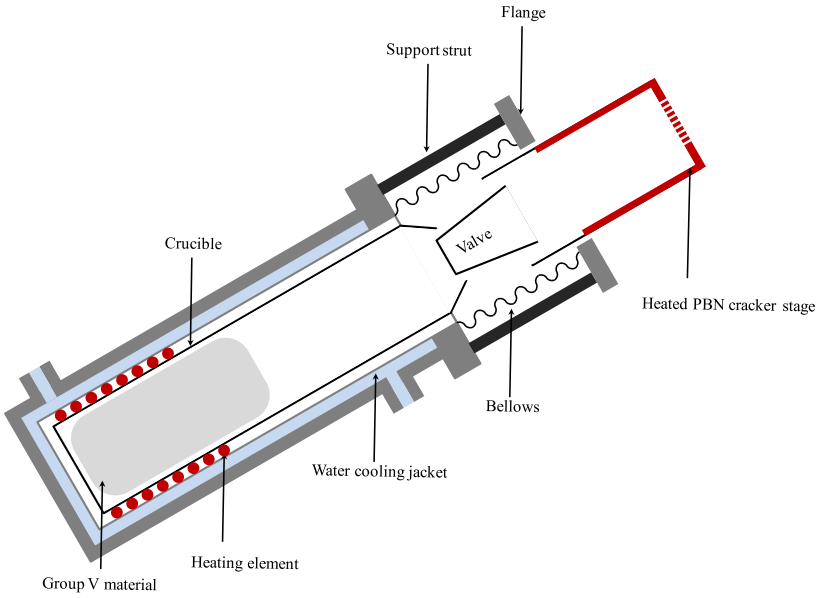

Figure 2.7: A schematic representation of the antimony valved cracker cell used on the GEN II chamber. Omitted for clarity are the two thermocouples and the heat shields. The cracker stage consists of a heated PBN shroud with fine apertures in the tip, maximising collisions of species yet to undergo bond fission. The cell body position moves relative to the PBN valve stopper, facilitated by the bellows.

The Sb cell on the GEN II instrument is not suitable for operation in a downward-pointing orientation. Where a source is required to operate at such an angle, there are available sources designed for this purpose, with the material reservoir positioned with the aperture pointing up. The sublimed species then negotiate an elbow, entering the cracker tube assembly which points toward the substrate. The arsenic cracker source attached to the GEN II apparatus has this design.

2.1.5.3 Radio frequency (RF) plasma Source:

The atoms of molecular nitrogen are bridged by an extremely strong bond (ca. 945 kJ mol^{-1}) and consequently thermal cracking of N_2 into active species is impractical for MBE applications. To supply atomic nitrogen, a radio-frequency (RF) plasma source is employed, using a microwave cavity to provide the energy required for bond fission.

As well as excited neutral molecules, generated species consist of radicals, monatomic and diatomic ions that are likely to result in substrate damage. To limit the incidence of the ionic components upon the substrate, deflection plates with a ~200 V potential difference are utilised after the microwave cavity, allowing only neutral species to enter the chamber.[13]

The plasma is monitored with a silicon photodiode sensitive in the region surrounding ca. 820 nm, the voltage reading from which is used as an indication of plasma presence and intensity. Emission in this region corresponds to the production of atomic nitrogen species.[14]

Another method by which nitrogen may be introduced to the growth chamber, is by supplying a flux of ammonia. At a sufficiently hot surface, the N-H bonds undergo thermal fission, leaving active nitrogen species.

2.2 Characterisation Equipment & Techniques

Reproducible growth of samples and systematic refinement of growth parameters are reliant upon characterisation of grown films. Such characterisation may be *in situ*, where growth may be monitored and evaluated during the growth process. *Ex situ* techniques require the conclusion, or at least interruption, of growth prior to execution. While the latter may provide more detailed information regarding sample quality and composition, there is necessarily a delay inherent in sample extraction, preparation and analysis that prevents growth parameters being altered *ex tempore.*

There follows a description of each analysis technique, both *in* and *ex situ* used during this investigation, and what information may be obtained from them.

2.2.1 Reflection High Energy Electron Diffraction (RHEED):

The most common method of probing surface quality during the growth process is by electron diffraction. Of the available techniques, the one most commonly applied to MBE is RHEED.

Due to the glancing angle of electron beam incidence (Figure 2.8) and the strong interactions between electrons and matter, the information gathered from RHEED is surface sensitive, ensuring that elastic scatting contributions from the bulk are small.

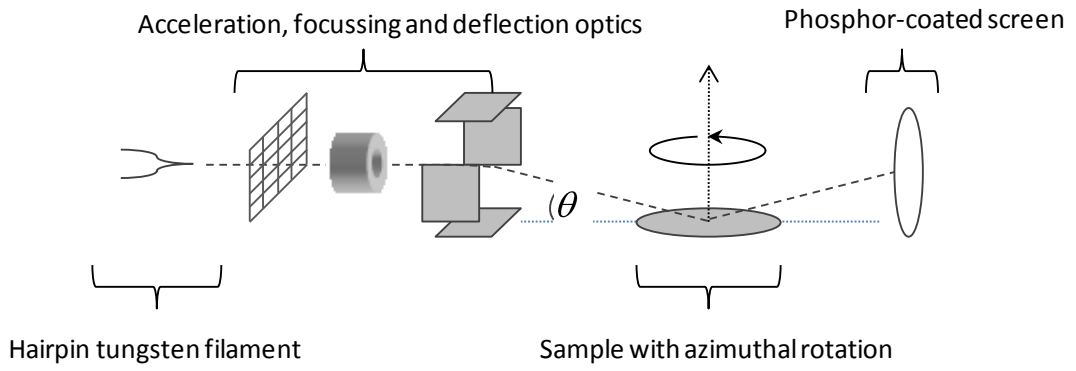

Figure 2.8: A simplified representation of a RHEED experimental setup. Typically, the angle of beam incidence, θ, is 1-5°. The RHEED screen consists of a phosphor-coated window, where diffracted electron beams may be observed.

Diffraction is a product of the wave-like properties of electrons which, under the correct conditions, permit coherent interference from atomic-scale features. The wavelength of an electron, λ_e, is given by the de Broglie equation (2.1):

$$\lambda = \frac{h}{\rho} \qquad (2.1)$$

where h is Planck's constant and ρ is the momentum of the electron. The electron momentum is dependent on its mass and velocity, m_e and υ respectively:

$$\rho = m_e \upsilon \qquad (2.2)$$

The velocity is a function of the electron mass, its charge, q, and the accelerating potential applied, V:

$$\upsilon = \sqrt{\frac{2qV}{m_e}} \qquad (2.3)$$

Substituting the into (2.1) gives:

(2.4)

Due to the fact that an electron accelerated by a 15 kV potential may achieve a velocity that is approximately 24 % the speed of light, a relativistic correction factor may be added to (2.4):

(2.5)

While this is negligible at low electron velocities, at an accelerating voltage of 15 kV, it accounts for a difference in the calculated wavelength of ca. -1.4 %.

2.2.1.1 The Reciprocal Lattice:

The patterns produced by the RHEED apparatus are a function of the reciprocal lattice, which is constructed from the set of vectors, K, that satisfy

(2.6)

over all lattice point positions, R. The primitive vectors, *a', b'* and *c',* of the reciprocal lattice can be derived from the primitive vectors of the original real-space lattice, *a, b* and *c:*

(2.7)

(2.8)

(2.9)

In a system where the primitive vectors are orthogonal, from (2.7-9), it follows that the magnitude of *a'* would correspond to a value of . This becomes more problematic when the "real space" lattice vectors are *not* orthogonal, such as in the case of the hexagonal Bravais system.

2.2.1.2 Requirements for Diffraction Events:

When the wavelength of the incident radiation is comparable to the scale of features under investigation, there are two requirements that must be fulfilled in order to form a diffraction feature. Firstly, the interference must be constructive. This is referred to as the Laue condition and is expressed as

(2.10)

where K is a reciprocal lattice vector, k is the incident beam wave vector and k' denotes the wave vector of the diffracted beam.[15] The second requirement is that the scattering is elastic, the case where

(2.11)

due to the requirement for conservation of energy.

In real space, coherent scattering conditions may be described by Bragg's law of diffraction:

(2.12)

where n is an integer, θ is the angle of the incident beam, λ_e is the wavelength of the incident radiation and d_{hkl} is the spacing of features from which diffraction occurs.

Diffracted electrons are scattered through all angles and directions – in order to visualise which are likely to appear as maxima, an Ewald sphere may be constructed (Figure 2.9).

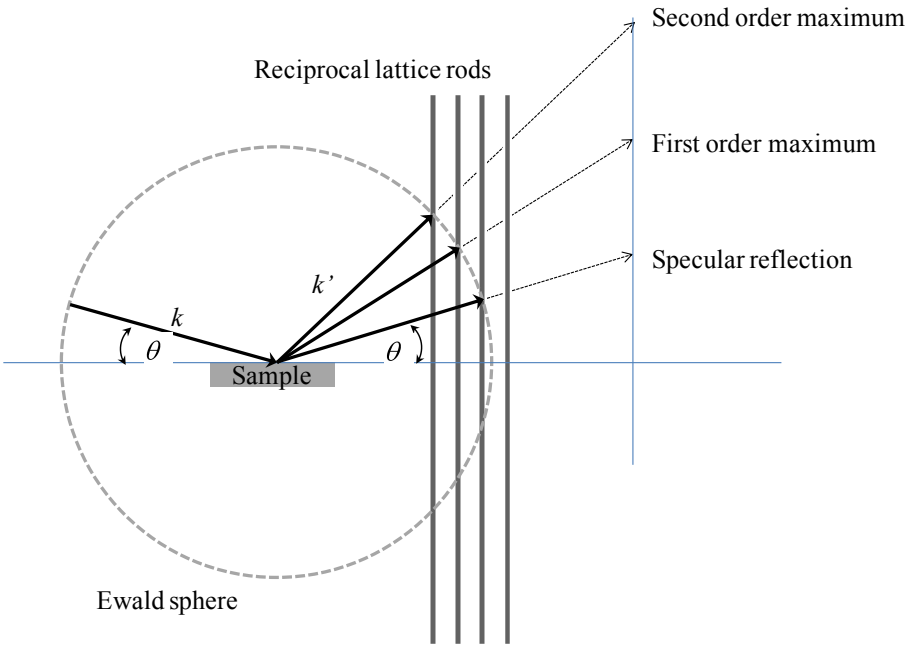

Figure 2.9: The construction of an Ewald sphere for diffraction events, as viewed from the direction bisecting the incident and diffracted wave vectors.

A sphere of radius k (necessarily also k'), represents the surface in space that satisfies the Laue condition and originates at the point of incidence of the electron. From the conditions set in (2.10) and (2.11), the diffracted electron wave vector, k', must be of the same magnitude as k and their difference must be equal to an integer

number of reciprocal lattice vectors. Combined with this, the fact that reciprocal lattice rods represent space where the Bragg diffraction condition is satisfied means that diffraction maxima are obtained where the lattice rod intersects the surface of the constructed sphere. The rods arise from the surface specificity of RHEED, which effectively samples 2D lattice. This causes a lengthening of the finite lattice points that exist in real space to rods in reciprocal space. Although the sphere may be imposed anywhere on the reciprocal lattice, simple rotation or translation show that all locations for the sphere in a perfect lattice are equivalent.

Although diffraction maxima would theoretically be seen as points with a perfectly focussed beam incident upon a regular lattice, streaks are most commonly seen. This is due to disorder and thermal motion inherent in the surface and the fluctuations in electron beam energy which affect the wave vector *k,* and hence the radius of the Ewald Sphere.

2.2.1.3 Interpretation of RHEED observations:

As an *in situ* analysis tool, RHEED may be used to obtain details of surface morphology (Figure 2.10), growth mode and, under certain conditions, the rate at which growth proceeds.

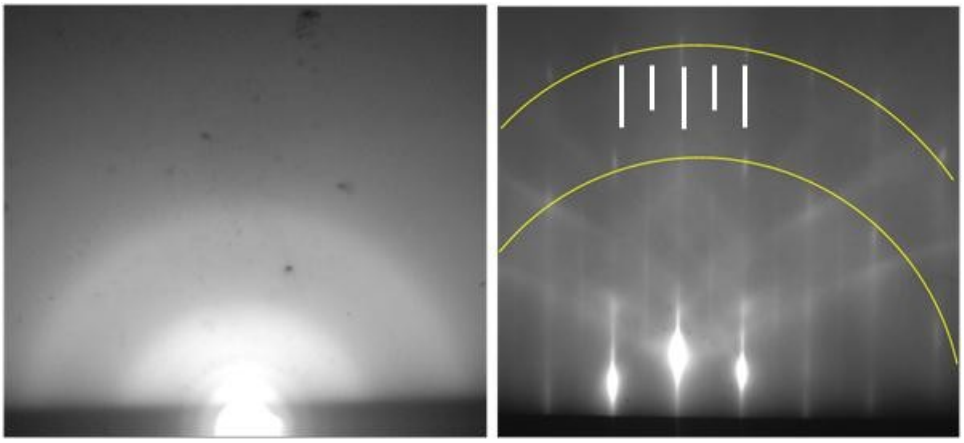

Figure 2.10: RHEED images produced from a ~13 kV electron beam performed on an amorphous/polycrystalline oxide layer (left) and a GaSb (001) surface with the electron beam incident in the [110] direction. In the case of the polycrystalline sample, the specular spot is visible. For the ordered surface, it is possible to observe first and second order patterns (highlighted) as well as Kikuchi lines. The integer and fractional order streaks are marked for clarity (right).

Due to the grazing angle of incidence, RHEED exhibits high surface specificity, with the resultant patterns displaying surface periodicity very clearly. Where there is a repeating surface feature for every five units of the underlying structure, for example, the RHEED pattern has five fractional order diffraction features between the streaks of the zeroth-order (1 x 1) substrate pattern (Figure 2.11).

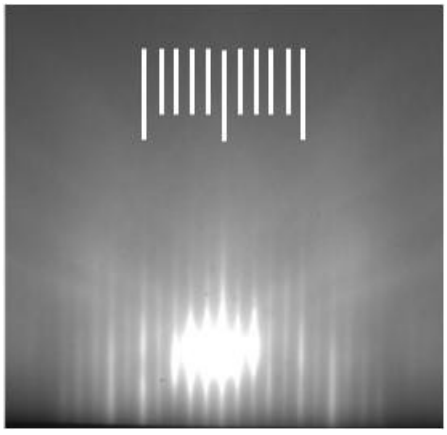

Figure 2.11: A 5x pattern generated by a ~13 kV electron beam, incident upon a GaSb (001) surface and electron beam incident in the [10] direction. RHEED can only describe the periodicity of surface structure, while atomic positions are better obtained by a complimentary technique such as scanning tunnelling microscopy (STM).

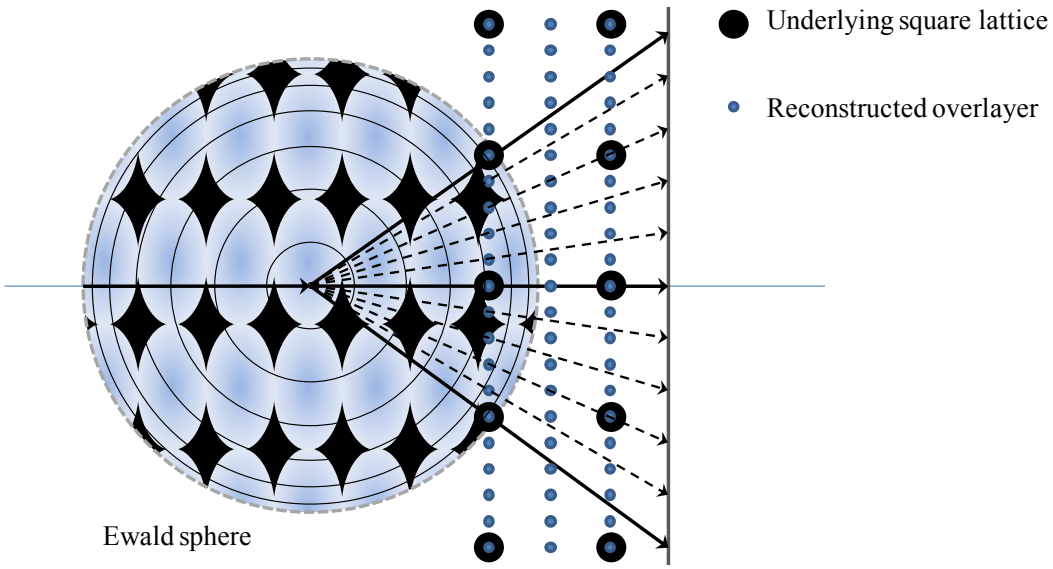

Figure 2.12: A flattened representation of a (2 x 5) surface reconstruction, depicted in reciprocal space. The contours present on the Ewald sphere display the curvature of its surface, demonstrating that all reciprocal lattice rods shown to contribute to the pattern satisfy the Laue condition. A two-fold periodicity would result, were the sample rotated in the plane of the page by 90°.

The former pattern results from diffraction occurring due to the structure of the uppermost layer, and appears superimposed over diffraction from the bulk material within the penetration depth of the RHEED beam (Figure 2.12).

In growth dominated by Frank-van de Merwe characteristics, described in Chapter 1, RHEED intensity oscillations as a function of time are used to obtain the rate of epitaxial layer formation.[16] They are caused by the periodic change in surface order (as described in chapter 1) with a period corresponding to the time taken to complete each layer. They can provide information on temperature and flux dependencies of film growth. This is of use when calibrating a material source, where the time

evolution of a particular diffraction feature is monitored at different substrate temperatures incident fluxes (Figure 2.13).

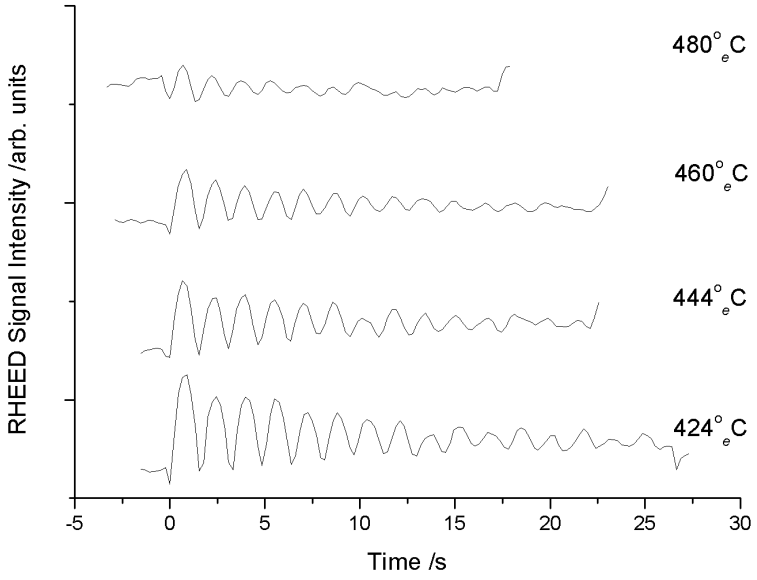

Figure 2.13: Group-III limited oscillations in the growth of GaSb with the electron beam incident in the [010] direction. It can be seen that the amplitude decreases with increasing temperature in this instance, but this is not universal.[17]

Growth rates, obtained from the oscillation period, can be functions of the impinging fluxes. From these, regimes of group III-limited growth can be determined. Furthermore, when conducting measurements at a fixed antimony flux, it is possible to observe a plateau region when the supplied antimony is insufficient to permit more rapid growth. By this method, it is possible to establish reliable flux ratios for growth that are directly observed and independent of differences between growth systems. Where a series of measurements is performed over a range of substrate temperature, this method also permits the elucidation of incorporation kinetics, as has been determined for GaAs.[18]

Where a surface does not have an oscillatory change in roughness, time-resolved growth information is inaccessible by RHEED. Such a situation may arise in a regime dominated by step-flow growth due to increased mobility of species as a function of growth temperature, or where the surface on which RHEED oscillation experiments are conducted is already rough due to a poor substrate or degradation in preceding preparatory stages.

2.2.2 X-Ray Diffraction (XRD):

With a wavelength of 50-250 pm, X-rays may be used to probe layer thickness, composition, strain, mismatch and structure on the scale of lattice spacing through the interaction of photons (< 100 keV) with a sample. Such interaction may result in inelastic and incoherent Compton scattering or Rayleigh scattering, which is both coherent and elastic. It is the latter type from which diffraction occurs. Diffraction intensity maxima in XRD are present when Bragg's law of diffraction (2.12) is satisfied and when the bisector of the angle between the incident and diffracted beams is parallel to the plane normal.[19] A simplified XRD setup (Figure 2.14) is similar to the RHEED arrangement described in section 2.2.1, with the exception that the angles of incidence and diffraction are varied, as opposed to the fixed angles and varied azimuth in RHEED.

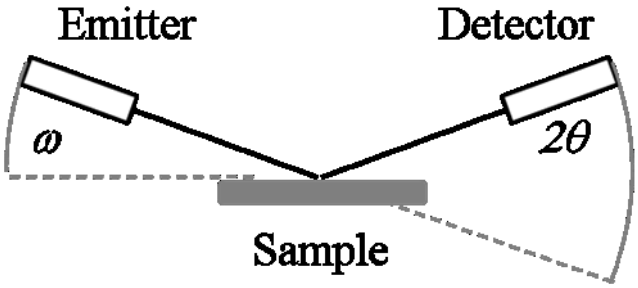

Figure 2.14: A representation of an XRD experimental arrangement. In practice, omega (ω) is varied by rotating both the sample and detector to change the incident angle of the beam. For the production of a reciprocal space map (RSM), omega scans and 2theta (2θ) are scanned over a range of parameter space to display diffraction maxima.

Scans performed may be symmetric or asymmetric: In the former case, the periodicity is probed normal to the sample surface, with the latter case applying to all other accessible planar spacings.

Through mapping of inter-planar spacing in both symmetric and asymmetric directions (in the case of this investigation, the probing of (004) and (224) plane normals respectively) as a function of omega and omega 2θ, a reciprocal space map (RSM) is produced for each plane, allowing elucidation of layer strain, orientation and composition. Since compositional change of a matrix is detected in XRD by a comparison of lattice spacing, this is essential in establishing accurate values for elemental ratios.[20]

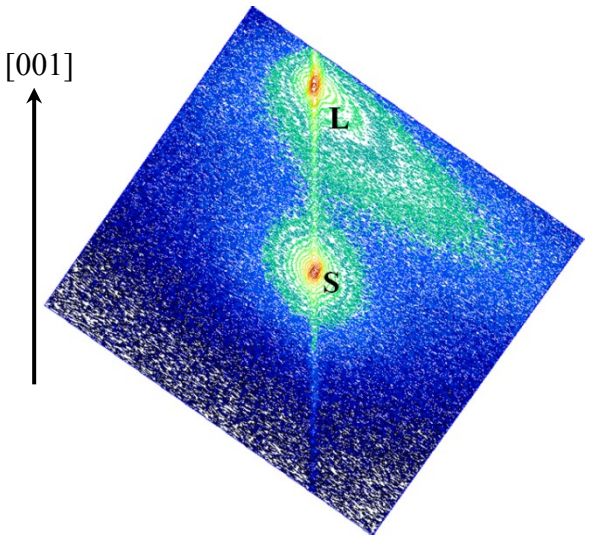

Figure 2.15: The (224) RSM for a GaNSb/GaSb(001) sample provides information on layer strain. In reciprocal space, a coincidence of substrate and layer peaks along the (001) plane normal indicates a fully strained layer.

In addition to compositional data, XRD can be used as a measure of crystal quality through examination of the full-width at half maximum (FWHM) peak widths, as defects and strain lead to peak broadening.[19]

2.2.3 Atomic Force Microscopy (AFM):

While diffraction techniques are extremely helpful in evaluating crystal quality and surface characteristics exhibiting periodicity, it is also advantageous to be able to examine the film morphology in real space, where individual imperfections may be observed directly.

AFM is one means by which this information may be gathered, with the MFP-3D (Asylum Research) apparatus (Figure 2.16) used in this study allowing topography

to be probed in linear *x* and *y* ranges of 0.5-90 μm and delivering *z* resolution sufficient to distinguish monolayer terraces (Figure 2.18).

1. *z* – piezo
2. Laser
3. Mirror
4. Spatial photodetector
5. Cantilever & probe assembly
6. Sample
7. Sample stage with independent *x* and *y* piezo stages

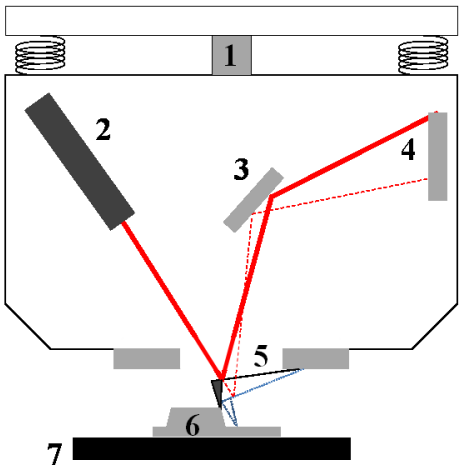

Figure 2.16: A simplified diagram of the MFP-3D scanning head. In contrast to other scanning probe microscope (SPM) systems, the piezoelectric actuators are mounted separately to avoid cross-talk.

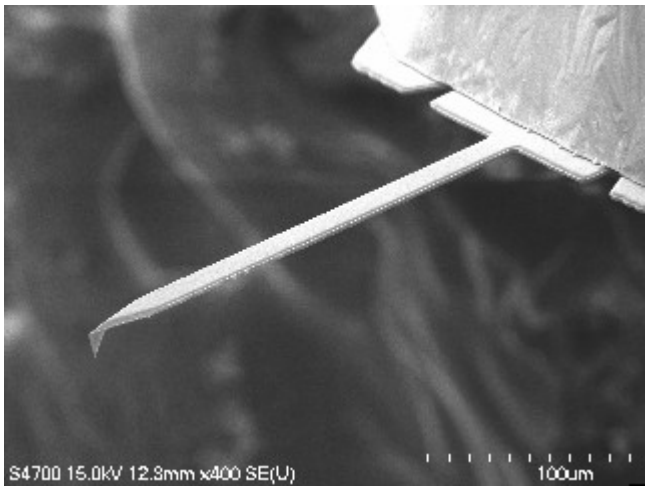

Figure 2.17: *A* scanning electron microscope (SEM) image of an Olympus AC240-TS W2 microscopy probe of the type used for AFM measurements throughout this investigation. Image reproduced with kind permission of Olympus, Japan.

In the MFP-3D instrument, the *z* piezo is isolated from the *x* and *y* stages, which in turn are separate from one another. As a consequence, this arrangement minimises

interference, or cross-talk, between the stages and reduces the need for post-processing of the data which may result in the elimination of real features recorded. Unlike scanning tunnelling microscopy (STM), there is no requirement to ensure good sample conductivity, as imaging occurs through physical interaction rather than quantum tunnelling.

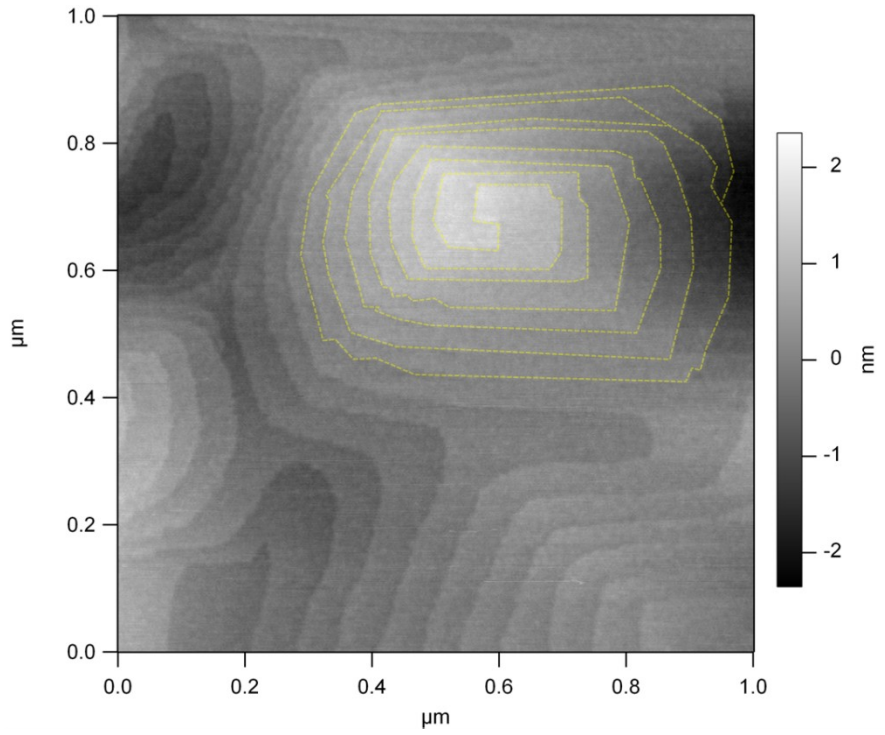

Figure 2.18: A 1 µm x 1 µm topograph of a spiral defect (highlighted) observed in the growth of an epitaxial layer of GaSb grown on GaAs (001). An analysis of the change in height over a range of the steps allowed confirmation of monolayer terrace height.

AFM measures the forces of interaction between the probe tip and the specimen under examination. These can vary from no net force, through a region of attraction to a range over which a strong repulsive force is experienced (Figure 2.19).[21]

Imaging is best performed in the region of repulsion, where the change in force is larger than in the attractive region, for the same net displacement.*

While sub nanometer resolution in the z direction is routine, lateral resolution (*x*,*y*) is universally limited by the effective tip dimensions.[22]

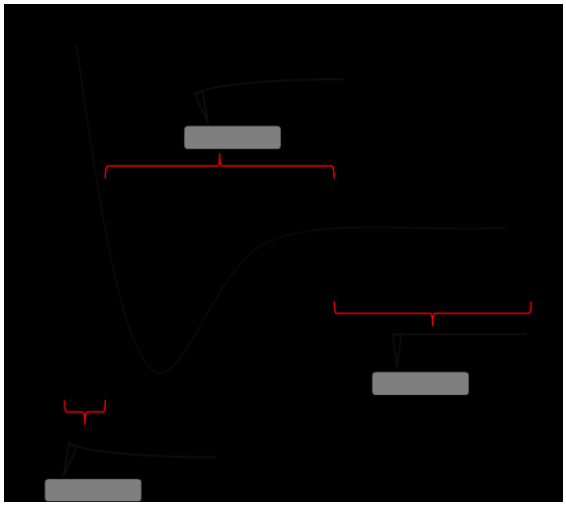

Figure 2.19: As inter-nuclear separation decreases, the net force experienced is first attractive before becoming strongly repulsive. It is in the latter region that topography measurements are preferentially conducted, due to the increased force gradient which allows better resolution and a lower susceptibility to noise.

Both of the two imaging modes discussed here are reliant upon measurement of the *z* piezo voltage required to maintain the constant position of a reflected laser spot on a photodiode array.

2.2.3.1 Contact Mode:

Contact mode AFM is so named, as the tip remains in contact with the surface throughout the scanning procedure. Briefly, a sharp tip mounted on a cantilever is

* Private communication with Mick Phillips, Asylum UK

moved across the surface by separate *x* and *y* piezo stages. A laser spot is deflected by movement in the cantilever resulting from changing interaction with the surface. This change in deflection is minimised by means of a feedback loop adjusting the potential on the *z* piezo and recorded as a function of *x* and *y* positions.

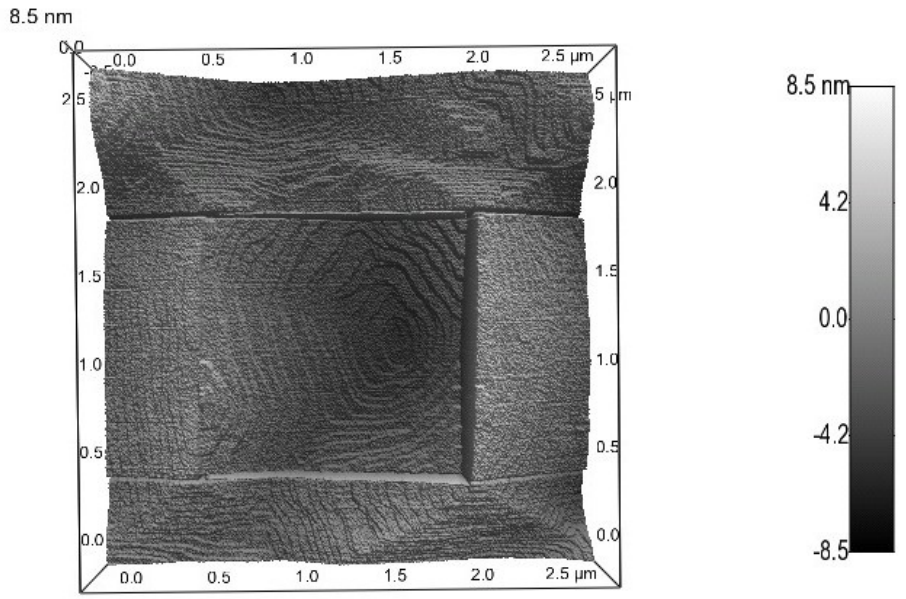

Figure 2.20: Contact mode may result in mechanical sample damage such as that seen above. The pit is thought to be the result of a previous 1.5 µm x 1.5 µm scan performed on a GaSb/GaAs(001) sample.

A disadvantage of contact mode is the prospect of surface damage (Figure 2.20). Where surface features are sufficiently prominent, damage may also be sustained by the tip.

2.2.3.2 Tapping (AC) Mode:

In situations where damage to a delicate sample is a concern, or where the tip may snag on significant surface protrusion, tapping mode can be used as an alternative to

contact mode. In tapping mode, the cantilever undergoes an off-resonant, oscillatory excitation driven by a piezo. The *z* stage is then extended until the motion of the probe is damped by the repulsive forces and lateral scanning may commence. Damage is thus avoided by each point measurement effectively consisting of an approach/withdraw cycle. During the scan, the feedback control adjusts the *z* piezo in order to maintain constant oscillation amplitude, which is recorded as a function of *x* and *y* position to provide spatially resolved topographic information. The phase of interference in the damping caused by sample-tip interaction can be used to infer changes in composition (Figure 2.21), although chemical-specific information may not be obtained in this manner.

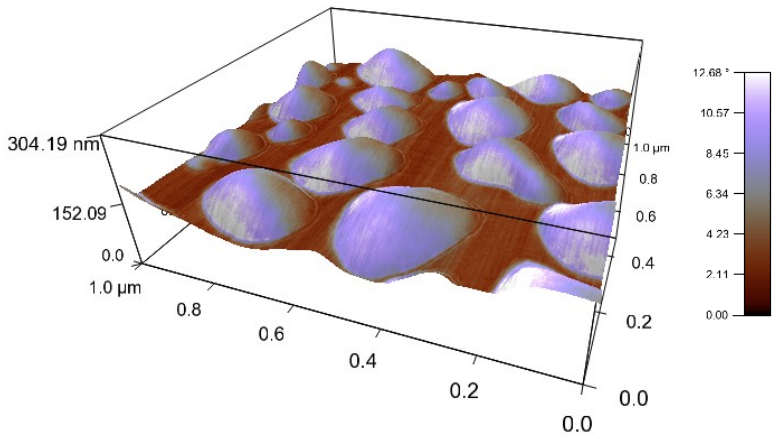

Figure 2.21: A 1µm x 1µm AFM topograph taken in tapping mode. Clearly visible are droplets on the GaSb surface. The colour represents the phase of interference with oscillatory motion, and indicates a varying tip-sample interaction. It was initially considered that the droplets consisted of gallium, although they transpired to be a condensation of volatile organic matter from the sample fixative.

2.2.4 Transmission electron microscopy (TEM):

AFM can provide a great deal of information about a sample, including threading dislocation density and morphology at the surface, but gives no information on the

properties of the bulk material. TEM is a technique that may be applied to examine surface layers and cross-sectional samples, allowing the propagation of dislocations and interface quality to be examined (Figure 2.22).

Sample thicknesses must be kept to a minimum (of the order of the mean free path of an electron in that material), as an electron beam will be attenuated by the sample more significantly than would x-ray radiation. This can be of benefit in imaging, as the degree to which such attenuation occurs, or mass thickness contrast, is proportional to the square of the atomic number, thus resulting in varying degrees of intensity between layers of differing composition.[23]

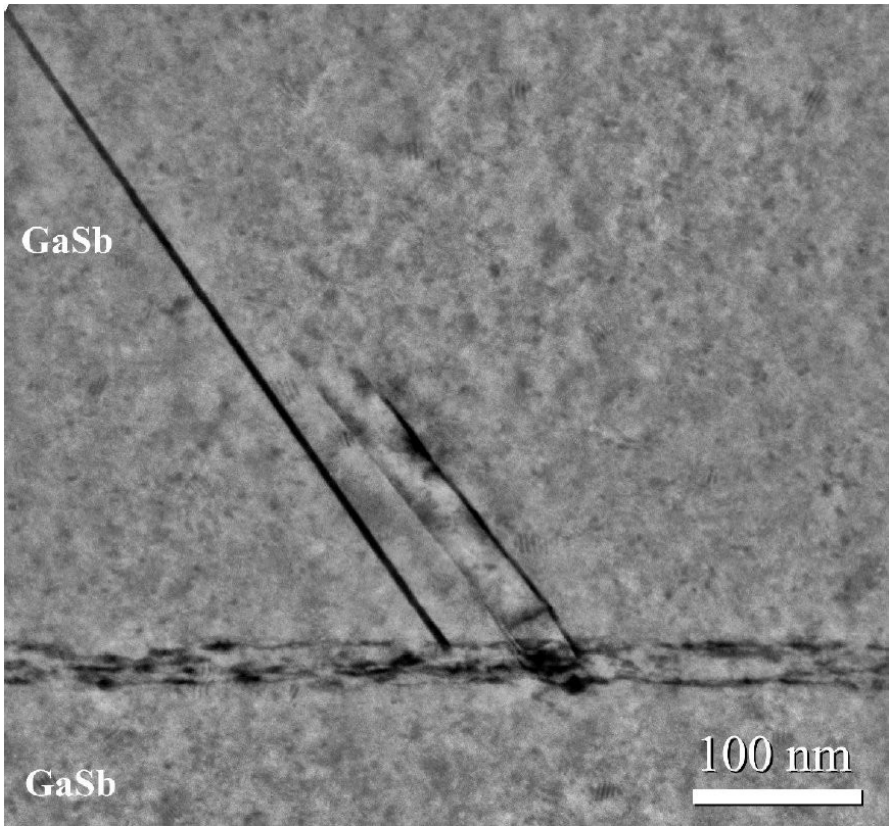

Figure 2.22: A micrograph taken of a GaSb buffer layer grown on GaSb (001) under 220 bright field conditions. From the use of TEM, it is apparent that the dislocations observed originate from the interface, rather than from within the substrate wafer. Additional dislocations are observed in both the substrate and epilayer.

There are two modes in which TEM may be conducted: bright field and dark field imaging. The former relies on the transmission of electrons through a sample for detection to occur subsequently at a point lying to the axis of the incident electron beam. For dark field imaging, the image is created only from electrons collected off-axis from the incident beam – that is to say, those electrons that have undergone diffraction.[24] Where an index is supplied, it denotes the family of planes from which the strong diffracted signal was collected e.g. "220 dark field" conditions.

Dual beam measurements may also be undertaken, where a combination of both modes results in an image comprising the bright field component and a contribution of diffracted electrons.

2.2.5 Secondary Ion Mass Spectrometry (SIMS)

Secondary ion mass spectrometry (SIMS) is a valuable tool for establishing concentration profiles in the direction of growth. Briefly, an ion beam which, in the case of this investigation, is formed of Cs^+ species and directed at the sample, causing the sputtering from the surface of secondary ions and neutral species. The ionic species are directed into a mass spectrometer, where their composition is determined. The depth sensitivity arises from control of the kinetic energy of the primary ions, and hence their penetration depth into the investigated medium. A depth profile emerges when the sputter time, which at constant energy is proportional to the depth achieved, is correlated with ion signal intensity from the mass spectrometer.[25] The pit depth may be measured by means of a profilometer, or by the inclusion of marker layers grown into the film. However, care must be taken

to ensure that the beam energy is optimised, as too high an energy results in a roughening of the channel in the material through a larger degree of ablation, while too low a value results in insufficient ion signal for compositional determination.

To avoid interference with the beam resulting from collisions prior to impact with the sample and to prevent generation of spurious secondary ions from ambient species, SIMS experiments are best conducted *in vacuo*.

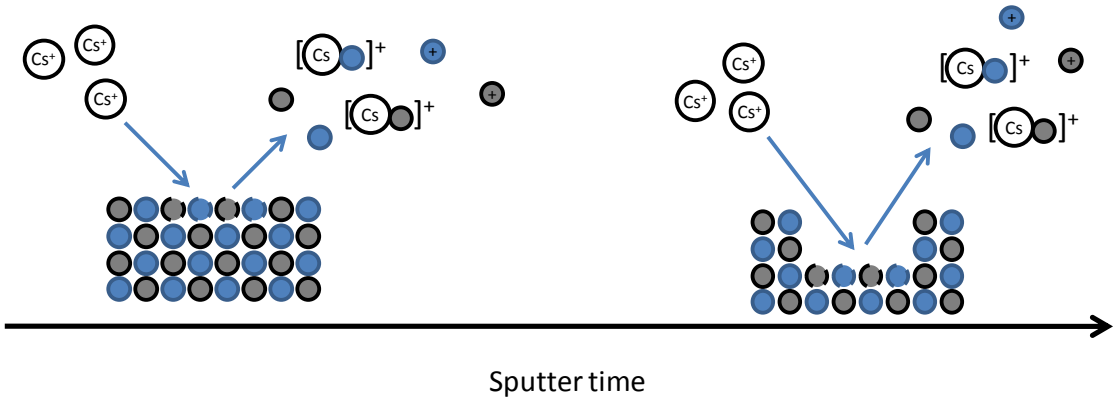

Figure 2.23: A simplified representation of a depth-resolved SIMS experiment. Secondary ions are created from primary ion impact and corresponding collision cascade, which produces both neutral and ionic species. The energy of the incident ion beam and the material under investigation govern the penetration depth and, hence, the rate of change of depth with sputter time.

As a qualitative tool, SIMS can be used to highlight changes in composition that have occurred during growth. However, quantitative SIMS analysis for cross-sample comparison is more complex, requiring careful calibration to known standards. This is necessary due to the element-specific sensitivity factors and the matrix effect, a phenomenon in which local environmental factors cause large variation in secondary ion production.[26] Due to the different processes involved in XRD and SIMS, where quantitative analyses by both methods are undertaken the proportion of the total concentration of an element present that is incorporated substitutionally can be

found. In the case of nitrogen in GaNAs, this shows that there may be a comparatively large amount of nitrogen that is not substitutional.[27]

[1] A. Cho, J. Arthur, Progress in Solid State Chemistry **10**, 157-191 (1975).

[2] R. F. C. Farrow, *Molecular Beam Epitaxy: Applications to Key Materials* (Noyes Publications, New Jersey, 1995), p. 24.

[3] J. F. O'Hanlon, *A User's Guide To Vacuum Technology*, 3rd ed. (2003).

[4] D. J. Hucknall, A. Morris, *Vacuum Technology Calculations In Chemistry* (The Royal Society of Chemistry, Cambridge, 2003), p. 85.

[5] K. M. Welch, *Capture Pumping Technology*, 2nd ed. (Elsevier Science B.V., Amsterdam, 2001), pp. 102-112.

[6] D. J. Hucknall, A. Morris, *Vacuum Technology Calculations in Chemistry* (The Royal Society of Chemistry, Cambridge, 2003), p. 92.

[7] B. A. Joyce, Rep. Prog. Phys. **48**, 1637-1697 (1985).

[8] J. M. Reifsnider, D. W. Gotthold, A. L. Holmes, B. G. Streetman, Journal of Vacuum Science & Technology B: Microelectronics and Nanometer Structures **16**, 1278 (1998).

[9] G. M. Williams, I. M. Young, Journal of Crystal Growth **62**, 219–224 (1983).

[10] M. A. Herman, W. Richter, H. Sitter, *Epitaxy: Physical Principles and Technical Implementation* (Springer-Verlag, Berlin, 2004), p. 85.

[11] J. W. Cook, Journal of Vacuum Science & Technology B: Microelectronics and Nanometer Structures **8**, 196 (1990).

[12] Y Rouillard, B Lambert, Y Toudic, M Baudet, M. Gauneau, Journal of Crystal Growth **156**, 30–38 (1995).

[13] M. Uchiyama, F. Ishikawa, M. Kondow, Japanese Journal Of Applied Physics **48**, 081102 (2009).

[14] R. Vaudo, J. Cook Jr., J. Schetzina, Journal of Crystal Growth **138**, 430-436 (1994).

[15] W. Braun, *Applied RHEED: Reflection High-Energy Electron Diffraction During Crystal Growth* (Springer-Verlag, Berlin, 1999), p. 13.

[16] E. Michel, G. Singh, S. Slivken, C. Besikci, P. Bove, I. Ferguson, M. Razeghi, Applied Physics Letters **65**, 3338 (1994).

[17] P. Steans, Surface Science **459**, 277-286 (2000).

[18] E. S. Tok, J. H. Neave, M. R. Fahy, F. E. Allegretti, J. Zhang, T. S. Jones, B. A. Joyce, Microelectronics Journal **28**, 833–839 (1997).

[19] B. Cullity, *Elements of X-ray Diffraction* (1956).

[20] L. Buckle, S. D. Coomber, T. Ashley, P. H. Jefferson, D. Walker, T. D. Veal, C. F. McConville, P. A. Thomas, Microelectronics Journal **40**, 399-402 (2009).

[21] Y. Seo and W. Jhe, Reports On Progress In Physics **71**, 016101 (2008).

[22] W. Zhong, G. Overney, D. Tománek, Europhysics Letters (EPL) **15**, 49-54 (1991).

[23] B. Fultz, J. Howe, *Transmission Electron Microscopy and Diffractometry of Materials*, 3rd ed. (Springer, 2007).

[24] M. De Graef, *Introduction to Conventional Transmission Electron Microscopy* (Cambridge University Press, Cambridge, 2003), pp. 262-264.

[25] H. J. Butt, K. Graf, M. Kappl, *Physics and Chemistry Of Interfaces* (Wiley-VCH, Weinheim, 2003), p. 175.

[26] J. W. Niemantsverdriet, *Spectroscopy in Catalysis* (Wiley-VCH, Weinheim, 2000), pp. 80-81.

[27] Q. X. Zhao, S. M. Wang, M. Sadeghi, a. Larsson, M. Friesel, M. Willander, Applied Physics Letters **89**, 031907 (2006).

Chapter 3

"There are known knowns. These are things we know that we know. There are known unknowns. That is to say, there are things that we know we don't know. But there are also unknown unknowns. There are things we don't know we don't know."

Donald Rumsfeld (1932 -)

Various methods of substrate temperature determination have been examined with respect to their consistency and suitability for growth of III-(N)-Sb alloys. Both indium-bonded and indium-free substrate mounting methods have been investigated, particularly in relation to accessing temperatures below the specified minimum of the pyrometer available.

3.1 Introduction

Accurate control of temperature is an important aspect of high quality epitaxial growth. The temperature of the growing surface governs the sticking and incorporation of the incident species, while also affecting the surface mobility of adsorbed atoms and molecules. Too high a growth temperature may result in decomposition and desorption, while too low a temperature is likely to result in poor epitaxy and reduced film quality. Even in growth regimes where the surface temperature lies between these extremes, the surface mobility, sticking probability or incorporation coefficient of species may change dramatically. Potential manifestations of this are the transition in growth mode from a terrace growth process to step-flow growth[1*] and compositional variation.[2,3] Furthermore, accurate knowledge of temperature is crucial in studies performed to measure desorption fluxes and energies.

The same reasoning applies to precise knowledge of the temperature when transferring growth conditions between reactors. While internal consistency in one laboratory can yield satisfactory growth in one range of measured growth parameters, the values published may differ markedly from those collected on other apparatus.[4] A somewhat contradictory, but equally valid, assertion in terms of consistent growth of high quality films, is that the *true* surface temperature is less relevant, providing that values gathered and reported may be reproduced between experimental systems.

[*] On a non-vicinal surface

Despite the importance of substrate temperature in the routine production of epitaxial thin film material, it is often difficult to measure, giving rise to intense scientific interest in its research. Temperature control is particularly demanding for III-Sb compounds and alloys, due to the lower growth temperatures required and the greater prospect for material degradation than in the case of GaAs, for example.

This chapter describes the comparison of different methods of temperature determination for the growth of Sb-based narrow gap semiconductor materials and how best to quantify the surface temperature in a reproducible and transferrable manner.

3.1.1 Temperature Measurement Techniques:

Due to the nature of the vacuum apparatus and the conditions of growth, there are limitations to the technology that may be employed. The types of thermometry that may be applied fall into three broad categories: (i) those that are conducted inside the system by use of a probe; (ii) methods that use the optical properties of a material to conduct measurements on radiation passing through a window in the chamber; and (iii) observation of temperature-specific phenomena exhibited by species on the surface. The means of quantifying temperature during this investigation are outlined in this section, along with details of experiments conducted to establish best practice for temperature determination in III-Sb film growth.

3.1.1.1 Thermocouple Probes

When the ends of two different metals are joined, a thermocouple junction is formed from which an electromotive force is generated.[5] This produces a voltage as a function of the temperature differential of two junctions in a circuit, but the temperature measurement provided is relative rather than absolute, requiring a comparison with a junction of known temperature. This is known as a reference junction and older instruments tend to rely on a separate thermocouple junction held in an ice bath, although in modern devices such as those used in the GEN II instrument, the reference junction refers to a thermistor. This requires less calibration, but introduces some error in measurement due to changes in ambient temperature, which change the environment of the reference sensor and affect the reported values of temperature inside the instrument.

Thermocouple junctions provide an inexpensive measurement solution, with junctions incorporating different metal pairs allowing access to a large range of temperatures. While it is relatively simple to position thermocouples inside a vacuum system, the disadvantage in MBE is that they may not be affixed to the film during growth. This is a problem not confined solely to rotating samples, as used in the GEN II chamber, as such an arrangement could introduce contaminants in the growing surface, disrupt uniform growth and potentially also hinder observations by RHEED.

Thermocouples are often positioned behind and not in direct contact with the substrate, and readings do not represent a true value of the surface temperature, due to poor coupling between the environment of the thermocouple and the sample surface.[6] Nevertheless, thermocouples remain an intrinsic part of MBE growth due

to their ease of use, versatility and the wide ranges of temperature that may be measured by a single junction type.

3.1.1.2 Pyrometry

An optical pyrometer detects incident radiation within one or more wavelength bands. Pyrometry as a means of non-contact temperature measurement is based upon the Stefan-Boltzmann law, which states that the energy flux density, j^*, emitted by an object is related to the temperature, T, by the relationship

$$j^* = \sigma T^4, \tag{3.1}$$

where σ is the Stefan-Boltzmann constant. The frequency distribution of radiation of j^* is given by Planck's law of black-body radiation:

$$\frac{\quad}{\quad} \tag{3.2}$$

where ν is the frequency of emitted radiation, T is the temperature of the black body, h denotes Planck's constant, c represents the speed of light and k_B is the Boltzmann constant.

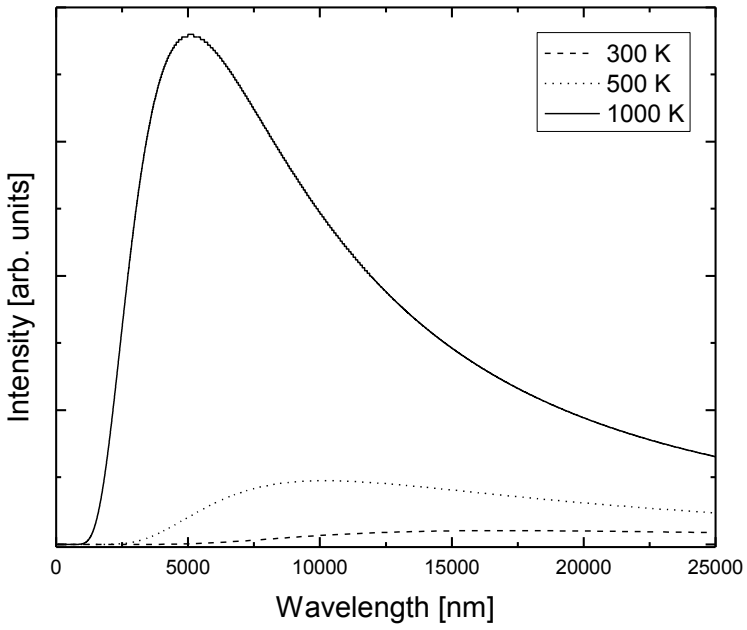

Figure 3.1: Simulations of the energy distributions of a black body at 300 K, 500 K and 1000 K. The maximum of each peak decreases in both intensity and energy, shifting to shorter wavelengths as the temperature increases.

Eq. (3.1) applies only to perfect black-bodies. The factor differentiating the theoretical behaviour of a black body from the emission characteristics of a real entity is the emissivity. Defined as the ratio of energy emitted by an object compared to that emitted by a black body at the same temperature, the emissivity is given as

——— (3.3)

where and denote the energy flux densities at a frequency ν and temperature T, for an object and black-body respectively. Since the black-body is a theoretical construct that exhibits perfect emission ($\varepsilon = 1$), values for the emissivity of real objects necessarily fall within the range $0 < \varepsilon < 1$. For practical applications,

the grey body case may be used, with insertion of the fractional emissivity coefficient into eq. (3.1):

$$j^* = \varepsilon \sigma T^4 \tag{3.4}$$

On this basis, pyrometers may be used to calculate the temperature from the intensity of the radiation measured over a narrow range of wavelengths (such as the single colour pyrometer), or take ratios of intensities measured over two or more bands, allowing the radiation profile to be better established.

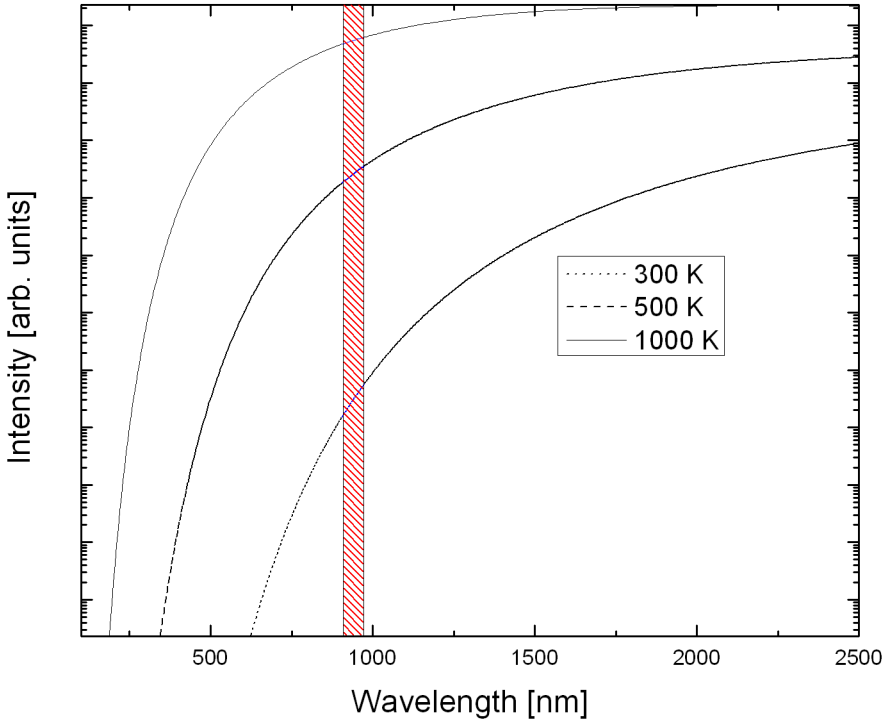

Figure 3.2: Viewing the simulations from Figure 3.1 with a log *y*-axis for clarity, the difference in intensities emitted by a black body at a selection of temperatures in the spectral range of the pyrometer (hatched) is evident.

Due to the combination of the fixed wavelength band(s) used by these instruments and the profile of Planck's distribution, there are finite ranges of temperature that may be evaluated with any degree of accuracy. For the Modline 3V pyrometer used in this study (λ = 0.91-0.97 μm), the intensity of radiation emitted in the detected region decreases by approximately six orders of magnitude as the temperature decreases from 1000 K to 500 K (Figure 3.2).

It is evident that a single colour pyrometer operating in this region will be adversely affected, if the incident radiation in this region falls sufficiently low that instrument sensitivity or signal-to-noise ratio become limiting factors. Readings from instruments using two bands will also be affected, should either band coincide with a region where this is the case.

The Modline 3V pyrometer was selected for use on the GEN II apparatus, as its spectral range was designed to permit temperature measurements on GaAs substrates. GaAs is transparent to infrared radiation in the 0.91-0.97 μm range at room temperature, but the energy of the GaAs band edge decreases sufficiently with an increase in temperature that it becomes opaque in the operating wavelength range above ca. 400°C. This is discussed further in section (3.1.1.4). In addition, given the lower band gaps of both GaSb and InSb in comparison to GaAs, the Modline 3V apparatus was considered a suitable choice of instrument for this investigation.

Even within the ideal operating range, these modes of operation can both be greatly affected by a number of factors, including variation of window transmittance over the spectral ranges sampled, variation of emissivity as a function of time, which occurs during epitaxial growth and deposited species on the pyrometer viewport.

The last factor has been observed in the GEN II instrument, with differences in temperatures found to be caused by the absorption of radiation in the region measured by the pyrometer.[7]

Additional issues may arise from assuming ε is constant, rather than a function of thickness, wavelength, angle of emission, structural morphology, chemical composition and temperature.[8]

Problems may also occur if the pyrometer operates in a region in which the substrate is not optically opaque. This is caused by the band gap of a semiconductor wafer being at a shorter wavelength than one or both of the pyrometer bands, and results in the transmission of a proportion of the radiation from the substrate heater, or from the sample platen.[7] This occurs more frequently in long-wavelength pyrometers, which have a larger intensity signal at low photon energies and permit lower temperatures to be determined. The detection of radiation not originating from the sample also means that reflections emanating from the cell heaters, for example, cause variations in the measured temperature.[9]

Despite these problems, pyrometry is a technique that is simple to set up, allows rapid acquisition of a temperature value, allows a "hot-swap" capability for changing detectors, and permits real-time monitoring of the infrared signal received. In addition, where adverse factors may be systematically eliminated or remain constant, it is possible to achieve reproducible growth even if the temperatures recorded may not be readily transferred between experimental equipment.

3.1.1.3 Surface Reconstructions:

Historically, epitaxial growth has occurred under conditions where there is thought to be little temperature dependence. Alternatively, *in situ* temperature calibrations can be made from observation of the different surface reconstructions exhibited by the material under investigation or by observation of a well defined phase change, such as the melting of an indium droplet. With only these methods of measurement available, research in several alloy systems was hampered, as transitions between surface reconstructions take place over a range of temperatures, rather than any single value. Even with *in situ* temperature measurement techniques, such as thermocouple junctions and pyrometry devices, discrepancies between the readings provided by each method have been widely reported.[6,7,9-11] Furthermore, where only one or two points are established, obtaining a reliable temperature scale is problematic. However, where temperatures can be assigned to a transition at known group V flux, a temperature scale can be made by interpolation (Figure 3.3).

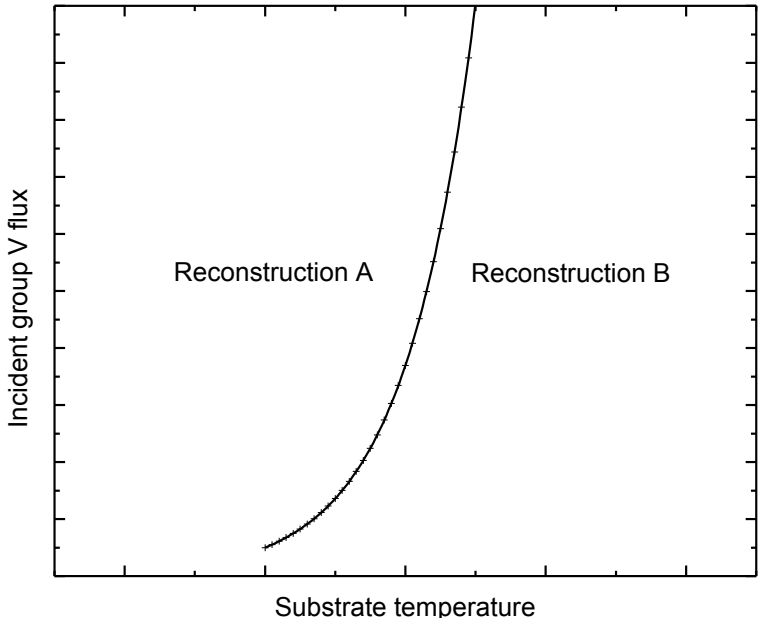

Figure 3.3: A plot depicting a theoretical phase boundary, in terms of the incident flux at which a transition is observed as a function of substrate temperature. Where the flux value is known, the substrate temperature may be derived.

The assumptions are that the temperature used for calibration is the true surface temperature and that the chemical composition of the fluxes used for calibration and measurement are identical, as observed transition temperatures are a function of whether, for example, a dimer or tetramer group V flux is supplied.[12]

3.1.1.4 Band Edge Thermometry

A relatively recent advance in non-contact thermometry of semiconductors uses the established temperature dependence of the band edge, given by the Varshni equation:

—, (3.5)

where $E_g(T)$ denotes the band gap at temperature T, $E_g(0)$ is the band gap at 0K and α and β are constants specific to the sample.[13] This equation shows that the reduction in band gap changes from being proportional to T^2 at low temperatures to a linear trend with T at higher temperature.[14]

The device is a wide band infrared spectrophotometer and software processing package, which scans a range of wavelengths in order to calculate a value for the onset of the band edge. Using known values α and β for the wafer under investigation, equation (3.5) is to determine the temperature. The values of α and β are obtained from temperature measurements with a thermocouple placed between wafers of the material subject to calibration.* While the technique may generally be referred to as band edge thermometry, it may also be named more specifically as diffuse reflectance spectroscopy or infrared transmission thermometry, depending on the mode in which it operates, as shown in Figure 3.4.[15] For the former implementation, a light source irradiates the sample and the characteristic absorption profile is deduced from the reflected signal. In transmission mode, broadband radiation from behind the substrate (either from a fibre optic light-pipe, or the heater) is collected at the detector, permitting the spectral absorption of the sample to be obtained. In some respects, the reflection geometry is preferable to transmission measurements, as the signal cannot be attenuated by increasing deposition thickness and is more likely to provide a temperature value that has a lesser degree of coupling to the characteristics of the substrate. Where there are no viewports to allow illumination of the wafer face, a period of downtime is required, which means venting the growth chamber to atmospheric pressure, followed by time for baking

* Private communication: Jeff Harris, k-Space Associates.

the system, as well as time to accommodate viewport installation. This procedure also introduces the risk of contamination to the growth chamber and material sources and is conducted as infrequently as possible.

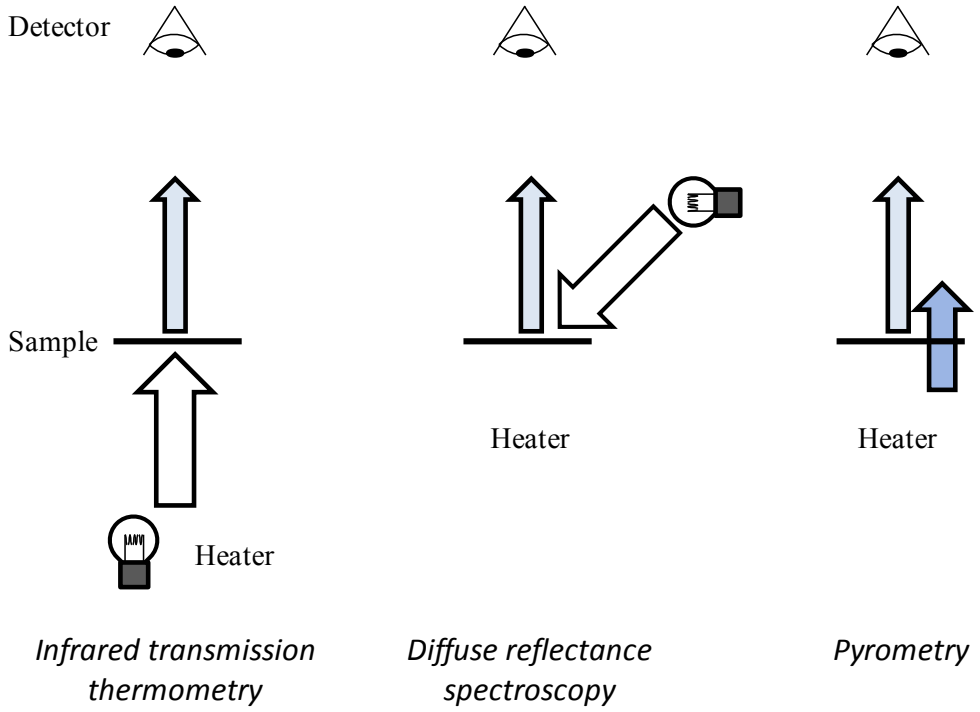

Figure 3.4: A series of simplified schematic representations depicting the operating modes offered by use of a broadband spectrophotometer. Whether or not heater radiation is detected in any case, it is possible to restrict the bands detected to exclude undesirable signals.

In some circumstances, a band gap is not accessible within the dynamic range of the instrument, or it may be obscured by the absorption profile of a grown layer. The spectrophotometer can perform as a multi-colour pyrometer, by measuring the intensity of incident radiation and obtaining a value for the temperature as described by (3.4). Due to the large bandwidth of such equipment in comparison with pyrometer detection bands, the regions used to calculate the grey body curve characteristics can better defined, to give a more accurate determination of the

temperature. This method of operation is dependent upon a sufficient wavelength range of the grey body signal of the substrate falling within the spectral band of the spectrophotometer, but overcomes the problems suffered by single and dual colour pyrometers at low temperatures. It also allows the filtering out wavelength bands in which the sample is transparent to heater radiation and permits interpolation in these regions to calculate a more accurate temperature. Furthermore, with correct calibration, the contribution of stray light sources may be eliminated from calculation of the temperature, although care must be taken where sample rotation is employed, as there is the potential to induce a periodic variation in detected radiation.

Further details about how such systems calculate the temperature are difficult to ascertain, due to their proprietary nature. However, it is evident that in an accurate temperature determination system, there must be some compensation for emissivity, for example using the relationship between absorptivity and emissivity as given by Kirchhoff's law:

$$A(\nu) = \varepsilon(\nu), \tag{3.6}$$

where A is the absorptivity with respect to incident radiation of frequency ν. There must also be a standard point of band edge determination, which is complicated by the presence of the band tail (Figure 3.5).

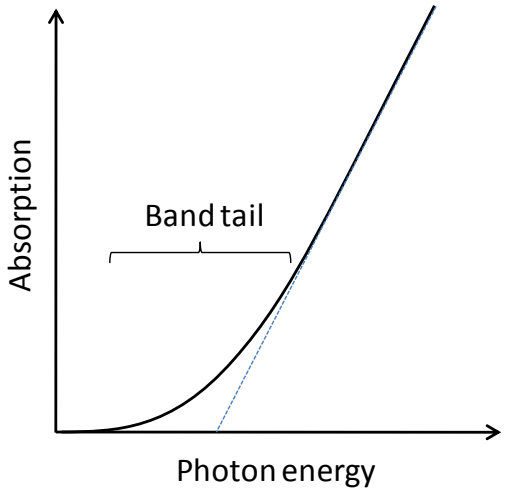

Figure 3.5: Representation of the absorption profile of a semiconductor in the region of the band edge. The band tail makes a definitive value for the band edge difficult to obtain, although a linear extrapolation (dashed line) may be employed to provide a more consistent value.

Using linear extrapolation of the above to zero absorption to obtain an energy value is one way in which this may be achieved, although literature reports indicate that first (and higher) order derivatives may also be employed.[6,8]

While such systems offer three methods by which temperature is determined, this flexibility is reflected in the cost and, due to the limitations described above, do not provide a universal solution to the issue of temperature determination.

3.1.2 Surface specificity:

Prior to any investigative work, it is important to establish the distinction between substrate and thin film temperatures. The lack of such a distinction assumes that their values are equal, and discounts potentially significant differences due to thermal gradients through the substrate/film and any difference in absorption profiles with respect to incident thermal energy.

Of the techniques employed in the GEN II, the thermocouple junction is the only absolute measure of temperature, but is also the least likely to provide the true film temperature. This apparent contradiction arises from the position of the thermocouple junction in relation to the wafer (Figure 2.3, Figure 2.4). While the readings gathered may describe with precision the temperature of the thermocouple junction and that of its immediate environment, the positioning of the junction is such that its surroundings are different from those of the growing film surface. In this situation, there is potentially a significant difference between the temperature reported by the thermocouple and the actual film temperature. This may lead to poor growth, a lack of reproducibility and, in extreme cases, destruction of the substrate and/or film.

When using pyrometers for temperature measurement, it is crucial to determine the contributions from the different heat sources present. Considering a bare wafer mounted either with or without indium bonding, different heat sources are apparent (Figure 3.6). In the case of an indium-bonded substrate, the dominant heat transport mechanism is conduction, via the molybdenum platen and the indium solder. Where indium-free mounting is employed, radiative heating and loss are the major processes at the centre of the wafer, with conductive heating/cooling becoming significant only at the edges, where a platen-substrate contact is present. As well as heat loss through conduction, it has been demonstrated that lower radiative heating, due to a lack of spatial uniformity in the radiation distribution from the heater or shielding of radiation by the platen, may contribute to lower temperatures at the edge of the wafer in an indium-free bonding arrangement.[16]

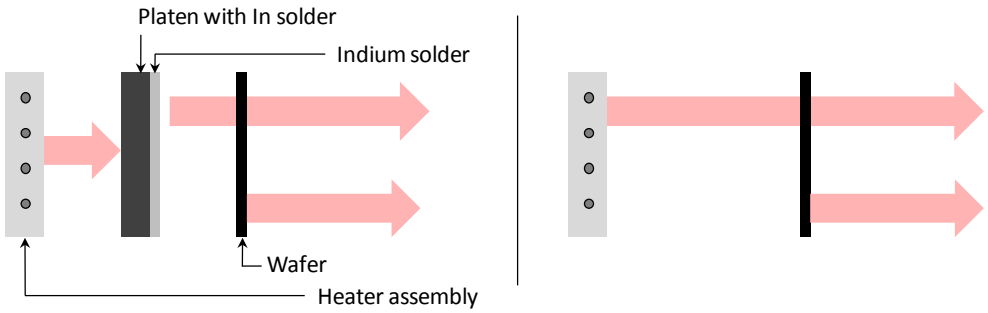

Figure 3.6: Two sample mounting arrangements, with different overall transmission characteristics: Indium bonded (left) and indium-free (right). In each case, it is the radiation emanating from the surface of the wafer which is of most use in determining the temperature. The top arrow in the schematic denotes the heating provided by the heater or solder. It is important to note the major mechanisms are conduction for indium-bonded and radiative heating for indium-free mounting.

Disregarding the issues inherent in pyrometry discussed previously, the accuracy of such measurements depends largely on the position of the detection band of the pyrometer relative to the onset of the band edges of the film and the substrate. Limitations arising from with a large substrate band gap are seen in temperature measurements conducted with the Modline 3V equipment on a sapphire substrate. With a wide transmission window (ca. 0.2 – 5 μm), sapphire is an extreme example of a substance exhibiting transparency in the operating region of the pyrometer. Therefore, any measurements made prior to growth on a naked sapphire substrate would be dominated by the infrared emission of the heater or platen immediately behind the wafer, with any radiation from the film being much smaller (Figure 3.8)

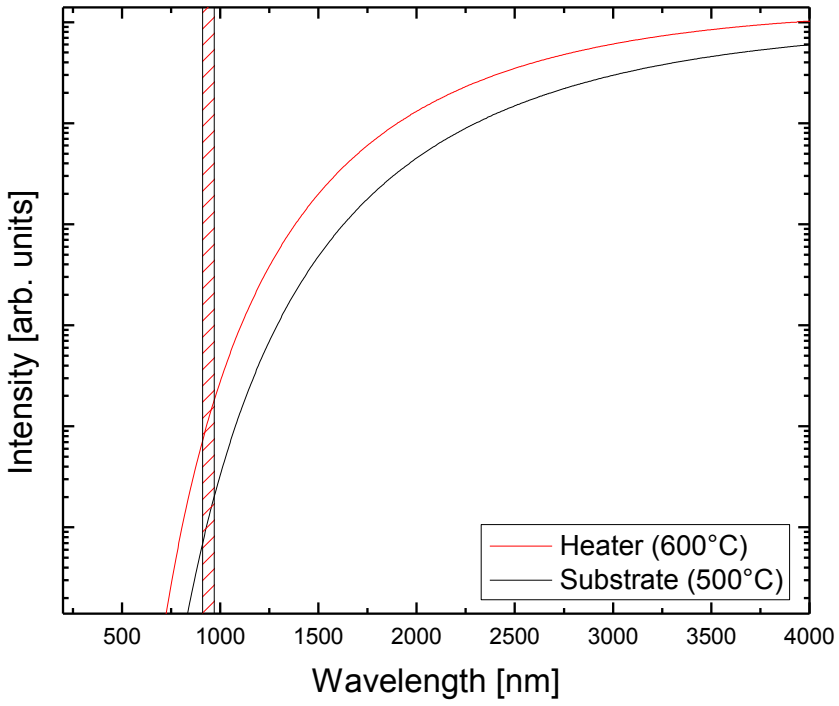

Figure 3.7: A simulation showing the differences in intensity for a heater at 600°C and a substrate at 500°C. No account of the emissivity differences or absorbance by the substrate has been taken. Each curve assumes black body behaviour.

With the onset of growth of material that absorbs radiation within the measurement region of the pyrometer on a substrate such as sapphire, the recorded temperature will change as a function of epilayer thickness until a critical layer thickness is achieved. At this point, there is no radiation transmitted by the wafer/film ensemble and the temperature measured corresponds to emission, rather than transmission. While sapphire has been chosen to illustrate this point due to its large band gap, the principle holds for other substrates.

When a material with a smaller band gap is deposited on a substrate which has a larger band gap, absorption of infrared radiation by the film can further disrupt precise temperature determination. With the use of band edge thermometry, Shanabrook *et al.* report that the deposition of a smaller band gap material on a

substrate leads to surface heating, as radiation transmitted by the substrate is absorbed by the film (Figure 3.8).[6] However, Hall *et al.* have proposed an explanation for the phenomenon that also takes into consideration the effects of absorption due to phonons and free carriers.[6]

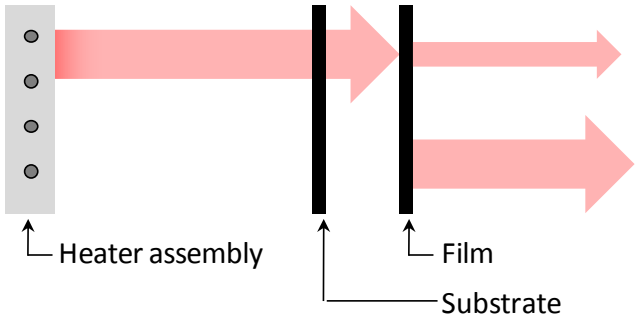

Figure 3.8: A diagram illustrating how radiation emitted by the heater may pass through a substrate such as GaAs, before being absorbed in a narrow band gap film. In absorbing this radiation, the temperature of the surface increases as a function of film thickness until some critical value is reached.

Taking the example of GaSb grown on GaAs, the substrate temperature and heater value can be fixed at a constant value prior to growth and increase during deposition due to the strong absorption of infrared radiation by the growing material.[11]

The incorporation of nitrogen into GaAs, for example, has been shown to have a strong dependence on temperature.[2] In such a system where there is no feedback from the film with respect to temperature control, this process may result in a film being grown over a range of temperatures.

As well as deposition potentially resulting in a change in temperature, one must consider the effect of the absorption of the film on the measured signal for

transmission band edge thermometry. At the point of growth where further temperature rise has ceased, it is possible that the signal received by the spectrophotometer is insufficient for substrate temperature determination, due to the total absorption of the infrared radiation used for band edge determination.

It is impossible to generalise with respect to the magnitude of these effects, as they depend also on the individual mounting arrangement, the rate of growth and the thickness and type of film and substrate. Considering such phenomena is important when comparing different temperature determination techniques.

For clarity, temperatures quoted have a subscript of the form $^{\circ}{}_{a}C$ to denote the method used to obtain the value. In place of *a*, *p* indicates a pyrometer reading, *e* a measurement taken from the Eurotherm controller, *r* a temperature derived from reconstruction transitions, and *b* a temperature determined from band edge measurements.

3.2 Overview of Experimental Work:

The aim of these experiments was to establish a method of best practice, with which temperature values could be determined with the highest degree of reproducibility possible. Preliminary measurements focussed on the relationship between pyrometer reading and the setpoint of the Eurotherm controller and any factors observed to affect measured values. Experiments were conducted with both indium bonded and indium free mounted samples, with the aim of establishing the degree of reproducibility of pyrometer measurements as a function of the temperature, as determined using the thermocouple probe. The effect of stray radiation reaching the

pyrometer was measured and the degree to which pyrometer viewport coating could have an impact upon measured readings.

Further work was undertaken to establish whether the temperature-dependent surface reconstruction transitions reported for GaSb could be used for temperatures below that which the pyrometer was capable of measuring. For a short period, band edge thermometry equipment in the form of BandiT (k-Space Associates) was available for use in conjunction with the GEN II apparatus. BandiT was evaluated for temperature determination in the growth of (Ga,In)Sb alloys and the corresponding dilute nitride derivatives.

3.2.1 The Effect of Pyrometer Viewport Fouling:

Since temperature measurements made by pyrometry depend upon radiation emanating from the substrate, any obstruction occurring between the sample and detector lowers the temperature reading. There is evidence in the literature to support this, with viewport coating cited as being likely to affect temperature determination by pyrometry.[7] The GEN II used here has previously been used for the growth of As-containing material, providing a long-lasting memory effect, which may cause a build up of arsenic on unheated surfaces.[17] Additionally, material can desorb from an As-containing sample, in the direction of the viewport. Temperature measurements were taken before and after cleaning to determine whether arsenic had been deposited on the viewport.

3.2.1.1 Experimental:

A cleaved quarter piece of a GaAs(001) semi-insulating wafer was mounted with indium solder and outgassed (400°$_e$C, > 60 minutes). It was then transferred to the growth chamber and the oxide removed under a stabilising Sb_2 flux (~1 x 10^{-6} torr). Prior to measurements being taken, the viewport was inspected and appeared clear to the naked eye.

The substrate temperature was set by the Eurotherm controller and allowed to equilibrate. Following acquisition of a stable pyrometer reading, two further temperatures were recorded in the same manner. The pyrometer viewport was then heated by a hot air gun (~ 5 minutes), during which time the window appeared to clear slightly. The viewport was then allowed to cool before the measurement process was repeated.

3.2.1.2 Results and Discussion:

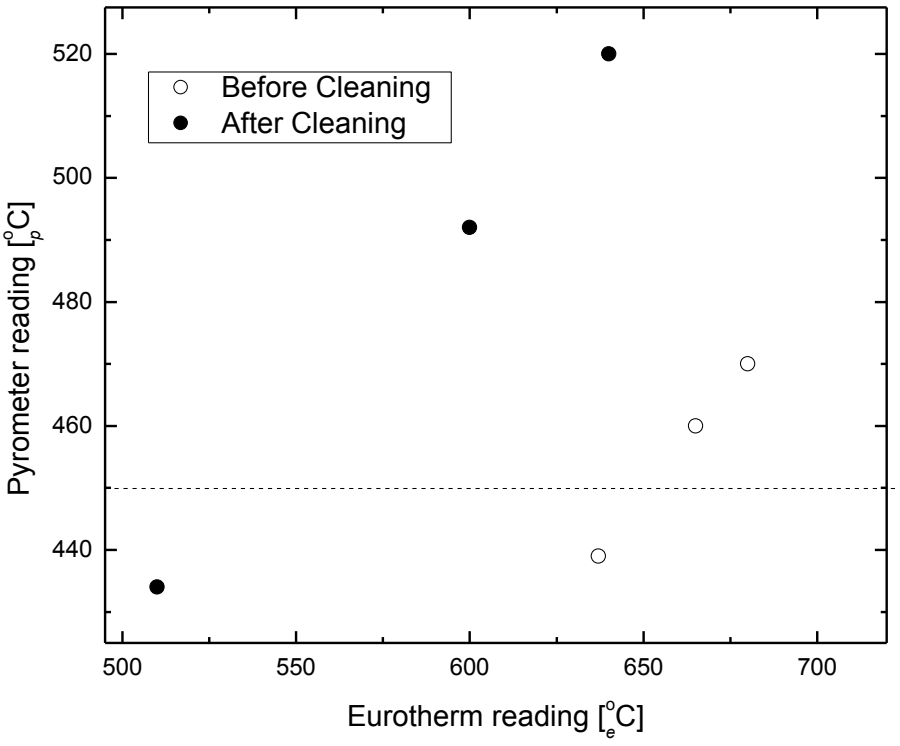

Figure 3.9: Pyrometer readings collected as a function of Eurotherm values indicate that the viewport coating has a marked effect upon the pyrometer substrate temperature. The dashed line indicates the specified minimum temperature of the pyrometer.

The data gathered by the pyrometer as a function of Eurotherm controller value before and after viewport cleaning showed a consistent shift, corresponding to an offset in the pyrometer readings of ca. 80°$_p$C (Figure 3.9). While visual inspection of the viewport did not reveal any obvious coating, the measurements indicate that the thin film present had a large effect on the transmission of infrared radiation within the detection region of the pyrometer.

Without either regular cleaning or a method of preventing the adsorption of species to the viewport, this coating may not be recognised until recorded pyrometer temperatures are significantly affected, while causing the potential for increasingly

inconsistent temperature measurements in the intervening period. A solution to this problem was identified, involving installation of a heated viewport (Veeco). Following the cleaning, it was discovered that the apparent temperature of the ion gauge, as measured by the pyrometer, had increased over 100°$_p$C to 1004°$_p$C. In the period until the heated viewport was fitted, the recorded ion gauge temperature was used as a means to assess whether species had accumulated on the viewport.

3.2.2 Indium free vs. indium soldered substrates:

During this investigation substrates were mounted with and without the use of indium solder. Other bonding agents were not investigated in this study. Available literature describes the benefits and drawbacks of each approach,[16,18,19] thus experiments were conducted to assess the consistency of both indium-bonded and indium free substrates in the GEN II apparatus.

3.2.2.1 Experimental:

Measurements were conducted on cleaved quarter pieces of unintentionally doped p-type GaSb(001) substrate (originally 2", WaferTech). In the case of wafers mounted with indium solder, the samples were bonded to a molybdenum platen using a minimum of indium solder on a hotplate held at ca. 170°C. Excess liquid indium was removed with a razor blade prior to wafer mounting. For indium free mounting, the wafers were secured as detailed in Chapter 2. Prior to admission to the growth chamber, the wafers were outgassed (300°$_e$C, ~60 minutes) and the oxide layer removed under an antimony flux (~1 x 10^{-6} torr). The substrate surface was then

planarised by the growth of a GaSb layer (T_g = 500°$_p$C, 0.5 µm h^{-1}, Sb_2:Ga = 5:1), until the RHEED pattern indicated a smooth, 2D surface. For both types of sample, pyrometer readings were collected as a function of the temperature displayed by the Eurotherm controller, which was used to increase the temperature at a rate of 2°$_e$C min^{-1}.

As reflections from source furnaces can contribute to pyrometer readings, all non-essential sources were set at idle temperatures of 400°C in order to reduce reflected radiation disturbing the measurements. The antimony source (T_{cell} = 560°C, $T_{cracker}$ = 800°C) provided a stabilising group V flux (~1 x 10^{-6} torr) to prevent Sb sublimation from the surface. On cooling, the antimony flux was removed when the temperature decreased to ca. 300°$_e$C. Upon re-heating, the Sb flux was applied above 300°$_e$C.

Over the days during which these data were taken, no arsenic was used and the ion gauge temperature measured by pyrometer to determine whether a viewport coating was present.

3.2.2.2 Results and Discussion:

The results gathered from the pyrometer as a function of Eurotherm reading indicate no trend as a function of time (Figure 3.10).

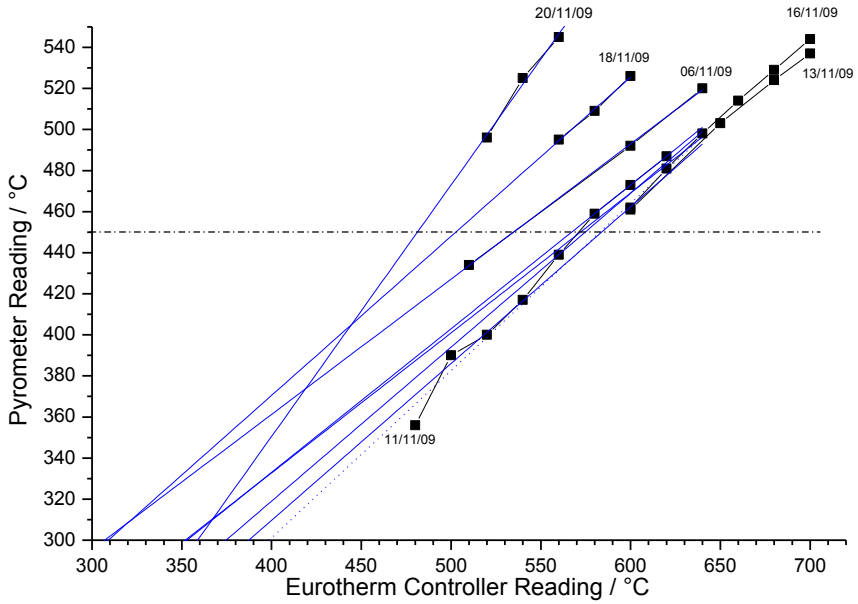

Figure 3.10: Data showing the variation encountered in temperatures measured on the same substrate and platen assembly over six days of experiments, after cleaning of the pyrometer window. Any systematic real-time trend is not observed and it is suggested that changes to the indium bonding may occur due to repeated heat cycling and subsequently affect the temperatures measured. The dashed line shows the stated minimum limit of the Modline 3V pyrometer used.

It can be concluded that any arsenic fouling accumulated over the period of these experiments had a negligible contribution to the variation in results and that other factors must be dominant. It is of note that the Eurotherm temperature was significantly higher than the measured pyrometer reading, indicating a degree of inefficient thermal coupling to the sample in comparison to the thermocouple environment. This demonstrates how each of the measurement techniques report readings in different ways and there is no straightforward conversion from $°_pC$ to $°_eC$. Of particular note is a lack of consistency in the gradient, as well as the absolute temperature values. These factors together are observed to result in a spread of ca. $120°_pC$ and $150°_eC$ at the extremes.

While there is not enough evidence to determine a definite cause of the wide spread of data, the two most likely causes are a change in emissivity resulting from a change in surface roughness, or some physical change in the nature of the indium solder that was used for bonding, such as melting and solidifying cycles or interaction with the wafer changing the degree of thermal contact.

The former case appears unlikely, as the RHEED pattern was examined frequently and was not observed to undergo significant change. One might also expect, if the emissivity of the were substrate undergoing significant change, that there might be a correlation with time as the surface continued to evolve. If the spread of data resulted from a variation in solder characteristics, then even if the pyrometer did measure the surface temperature precisely, the lack of any feedback from the pyrometer to the Eurotherm controller means that the temperature cannot be corrected to accommodate changes in the solder, such as those described above.

A smaller spread of temperature trends was observed for substrates mounted without indium, where pyrometer readings were correlated with those gathered from the Eurotherm controller (Figure 3.11). The spread of data was observed to be < 20°C in respect to both pyrometer and Eurotherm values and the data series did not show any trend as a function of time. There was much less variation in the gradients of the data series, in comparison to the measurements conducted using indium solder.

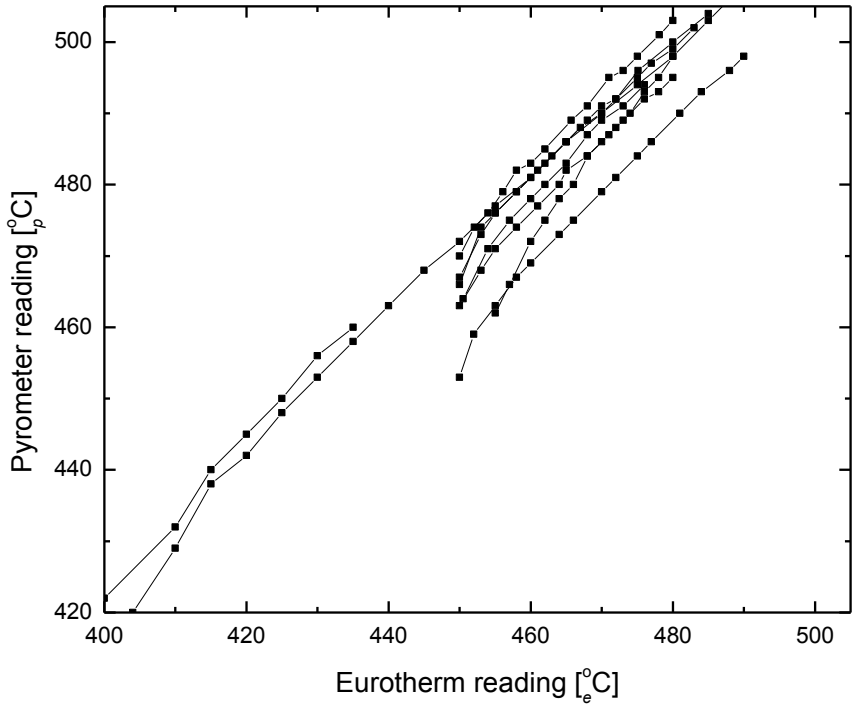

Figure 3.11: Compared with measurements performed on indium-bonded substrates, the spread of data gathered from indium-free mounted substrates is markedly smaller (ca. 20°C with respect to each axis). These data, collected from ten different samples, resulted from increasing the Eurotherm temperature of a quarter GaSb (001) wafer at 2°$_e$C min^{-1}.

The data gathered from samples mounted both with and without indium solder clearly indicate that temperature may not simply be determined by the Eurotherm controller, due to factors that can vary between (and potentially during) experiments. Such variables include surface emissivity, reflected radiation from source furnaces, film composition, thickness of deposited material and in the case of indium-bonded substrates, any physical changes in the mounting. Each of these contributes to the measured values and, considered together, couple the pyrometer readings to properties that may not be measured *in situ* with the available equipment.

While samples mounted neither with nor without indium solder provided wholly consistent results, indium-free mounting demonstrated better consistency, without

the potential for the erratic changes in measured values resulting from changes of the indium solder over the course of a growth process. In consideration of these data, it was decided to utilise indium-free mounting for future sample growth.

3.2.3 The effect of other radiation soures upon measured temperature values:

Temperature determination by pyrometric methods may be affected by reflections of radiation inside the growth system.[9] Such effects can lead to large inaccuracies in growth temperature, giving poor results. The influence of radiation from sources other than the substrate upon the measured pyrometer reading was investigated to determine best practice for future growth.

Following installation of the heated viewport, measurements were also conducted to ascertain whether there was any radiative contribution by the viewport to the measured pyrometer signal.

3.2.3.1 Experimental:

To measure the error in readings taken during growth, pyrometer measurements were taken at a number of temperature values set on the Eurotherm controller. After first achieving the target temperature, there followed a delay of ca. 5 minutes to allow thermal equilibrium to be attained. Data were then collected with the shutter to the gallium cell in both the open and closed positions. During the course of these measurements, the gallium cell was held at normal operating temperature for a group III-limited growth rate of 0.5 μm h^{-1} (T_{cell} = 918.2ºC, T_{lip} = 920°C). A stabilising

antimony flux was provided while the sample was at elevated temperatures, with the antimony cell set to 560°C and the cracker tip to 800°C.

To determine whether the heated viewport had an effect on temperature determination, a series of temperature increases were undertaken at different viewport power levels. The measurements were taken on a quarter wafer of GaSb (001) (Wafertech), following thermal oxide removal and deposition of a planarising GaSb layer (~50 nm). The antimony source was held at 560°C, the cracker tip at 800°C and the valve set to provide a stabilising flux (ca. 1.6×10^{-6} torr) at all times. The pyrometer value recorded as a function of measured Eurotherm value. The rate of increase of temperature was set at $2°_e C\ min^{-1}$.

3.2.3.2 Results and Discussion:

The substrate temperature measurements made by the pyrometer differed according to whether the gallium shutter was open or closed. It is clear from a plot of pyrometer reading as a function Eurotherm temperature that the difference in readings between shutter states decreased as the substrate temperature increased (Figure 3.12).

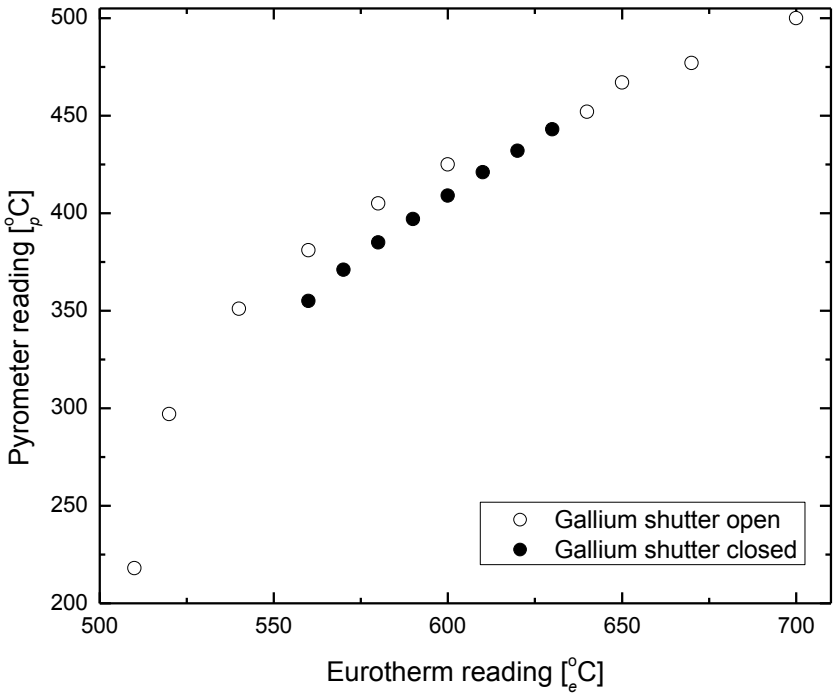

Figure 3.12: The variation in measured temperature as a function of gallium shutter state was observed to be more significant at lower temperatures. It is possible that this is a function of reflected radiation making a proportionally larger contribution to the detected signal at lower wafer temperatures.

One possible explanation for this arises from the wafer having an emissivity < 1. From (3.6), it follows that the absorptivity must also be < 1. In this case, the wafer will reflect some of the radiation incident upon it, with any reflected radiation falling within the detection range of the pyrometer contributing to the recorded value. At lower wafer temperatures, any reflected radiation in the detection range of the pyrometer contributes to a larger extent than at higher temperatures, when the radiation of the sample is more significant than any reflection. Since the gallium shutter must be open for growth of Ga:V films, Figure 3.12 clearly demonstrates that in a substrate temperature regime of 350-450°$_p$C, the impact of reflected radiation (< 25°$_p$C) on the measured values is substantial. These measurements were made to determine the effect of reflections from the gallium source, but other sources

necessarily operate over different ranges. As such, the effect of reflected radiation upon the measured values will vary, depending on operating temperature, any deviation of the substrate normal from the pyrometer axis and the sources employed in the growth.

The series of pyrometer measurements as a function of Eurotherm reading, made with different heated viewport settings, indicate that the pyrometer reading varied as a function of the power supplied to the viewport heater (Figure 3.13).

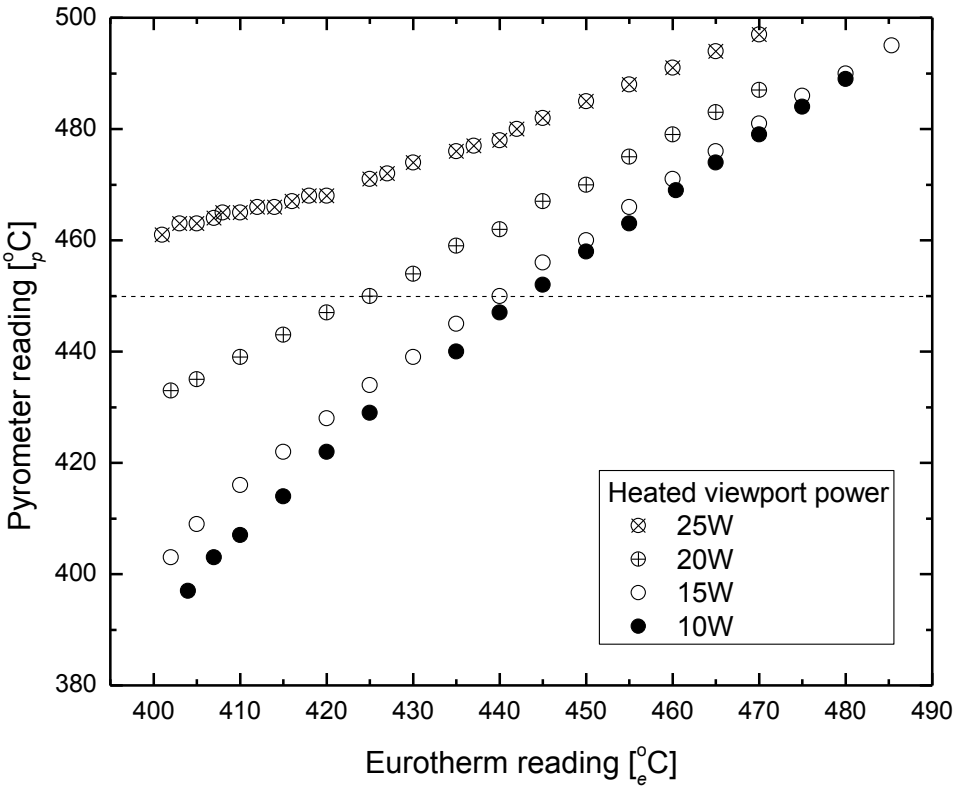

Figure 3.13: A plot displaying the pyrometer readings collected as a function of Eurotherm temperature, for different levels of power supplied to the heated viewport. At high power levels, there is a significant contribution to the pyrometer reading by the heated viewport. The dashed line indicates the specified minimum limit of the pyrometer.

The correlation of increased pyrometer reading with higher power provided to the viewport demonstrates that some radiation from the heated viewport assembly is able

to reach the pyrometer detector. In the range 10-15W, there was a maximum difference of ~5°$_p$C within the specified range of the pyrometer. The spread of pyrometer readings for all series was less at higher Eurotherm readings. Assuming consistent Eurotherm values, this indicates that the contribution by the heated viewport to the pyrometer temperature dominates where there is comparatively little radiation from the substrate and becomes negligible when the signal from the substrate is sufficiently large. Indeed, when used to measure the temperature of the ion gauge (> 1000°$_p$C), the heated viewport setting appeared to have little impact.

Other factors have been observed to provide similar interference with the pyrometer, including the use of a halogen lamp to inspect the inside of the growth chamber and the hot antimony cracker tip. Each of these factors has an effect with a reported substrate temperature of 500°$_p$C. Furthermore, rotation of the sample has often been observed to produce oscillations in pyrometer readings in the GEN II. This suggests that, where the wafer surface is not completely normal to the axis of the pyrometer, at certain angles stray radiation reaches the pyrometer.

For reproducible future growth, it was decided that temperature measurements by the pyrometer should be taken where there was the least stray light to influence the reading. To this end, the heated viewport was set to 10 W during growth, with the pyrometer reading permitted to stabilise as the viewport cooled. In this way the effect upon pyrometer signal could be minimised, while still reducing adsorption on the inner viewport surface. When pyrometer measurements were required, the sample was rotated to a position giving the lowest pyrometer reading and all source shutters closed. This was extended to momentary closure of the antimony source shutter, even when a stabilising flux was required. Due to the short interruption of

Sb_2 flux, this was not believed to have a detrimental effect upon the sample, which was supported by observations by RHEED.

3.2.4 Temperature-dependant surface reconstructions of GaSb:

The surface reconstructions of GaSb (001) have been studied extensively, with an antimony-stabilised surface exhibiting apparent 3 or 5-fold periodicity phases in the [110] direction of the surface (Figure 3.14).[20]

It has been reported that the phase change between reconstructions depends on both incident Sb_n flux and substrate temperature and provides an absolute measure of the surface temperature. Bracker *et al.*, measured the [(2 x 5) → (1 x 3)] boundary temperature directly by band edge thermometry and correlated it with flux values of both dimeric and tetrameric group V species.[12] For both GaSb and GaAs substrates, the published data suggests a means of determining the film temperature in the absence of band edge thermometry or pyrometry equipment, using a known beam equivalent pressure of antimony and the relationship derived by Bracker *et al.* to extract the temperature of the surface.

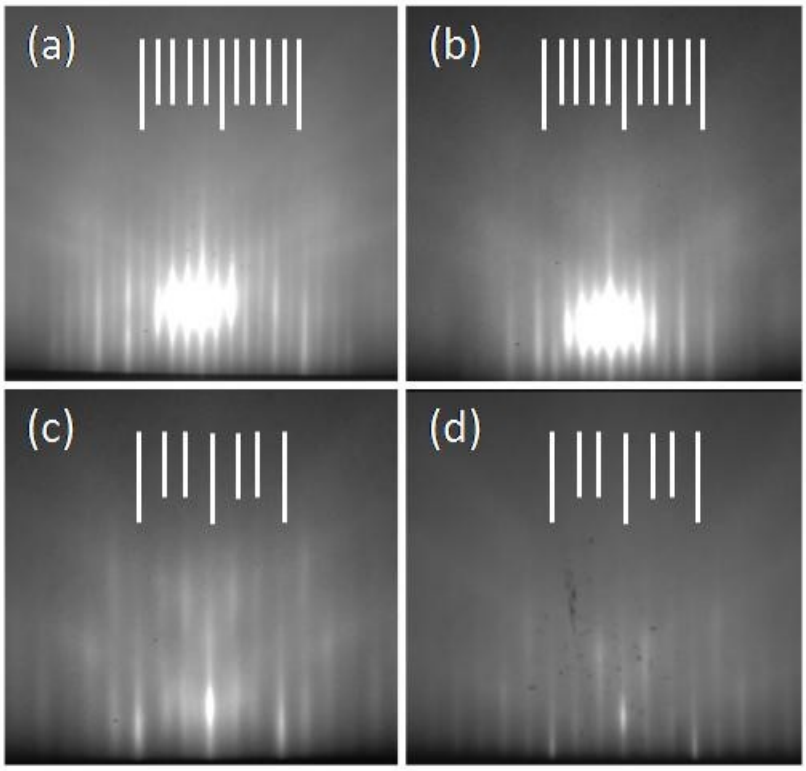

Figure 3.14: A sequence of RHEED images detailing the [(2 x 5) → (1 x 3)] transition with a ~13 kV beam incident in the [10] direction, as a function of temperature increase from (a) to (d). In contrast to the description given by Bracker *et al*,[12] an asymmetric transformation was observed: (b) shows the 4/5 order streaks diminishing prior to the 1/5 streaks, which are seen to merge with the 1/3 or 2/5 streak in (c). The final and symmetric (1 x 3) pattern is shown in (d).

The phase boundaries of the surface reconstructions exhibited by GaSb depend strongly upon temperature and incident antimony flux.[21] The experiments conducted were motivated by the prospect of calibrating the thermocouple probe according to temperatures extracted from the relationship between antimony flux and substrate temperature.[12] The primary advantage in using this method is that, assuming a fixed incident Sb_n flux, the surface reconstruction depends on the temperature of the surface and thermal gradients across the layer may be disregarded. Using this work as a guide, RHEED observations were made to determine whether surface

reconstruction phase changes could be used to provide information on the temperature of a GaSb(001) surface.

3.2.4.1 Experimental

Due to the design of the GEN II apparatus, beam equivalent pressure (BEP) readings may not be taken without changing the orientation of the substrate from that used for growth. Since a stabilising antimony flux is required to avoid surface damage at temperatures above ca. 300°C and the change in orientation of the CAR takes 30-40 seconds to complete, it was necessary to establish a means of determining the antimony BEP which could be employed without moving the sample.

BEP readings were taken as a function of valve position before use on each day of experiments, or whenever the valve had been closed for any reason (Figure 3.15). The antimony cell was held at a temperature of 560°C, with the cracker tip held at 800°C.

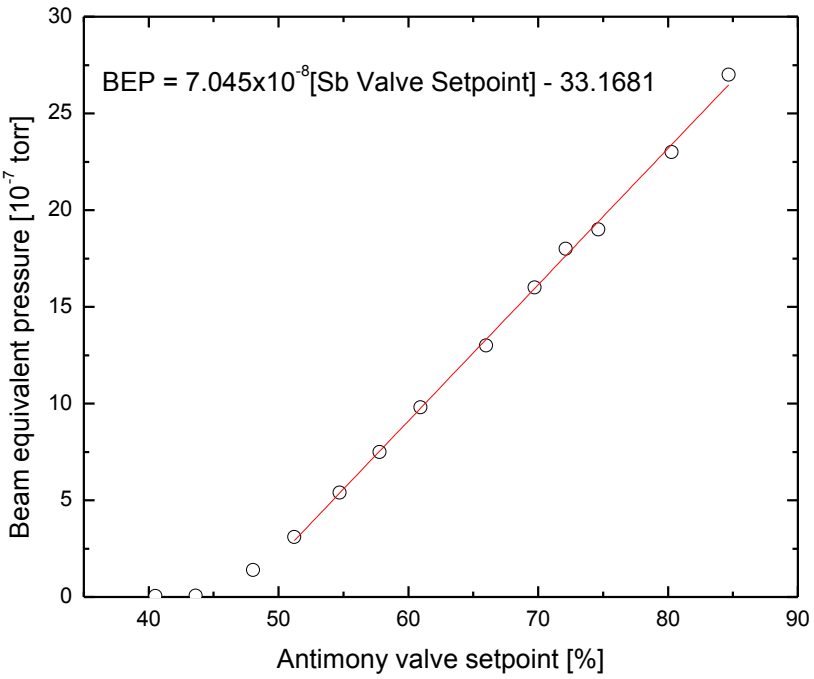

Figure 3.15: A plot of measured antimony BEP as a function of the antimony valve setpoint. A linear relationship in the fitting region shown permitted conversion between BEP and valve values.

All measurements of the Sb flux were made while opening the valve to minimise valve hysteresis and were observed to be largely consistent until valve closure. In cases where a decrease in flux was required, the valve value was set below the target value, before being increased to the desired level.

Preliminary examination of the surface with RHEED confirmed the observation by Bracker *et al.* of the (2 x 5) surface reconstruction (Figure 3.16).

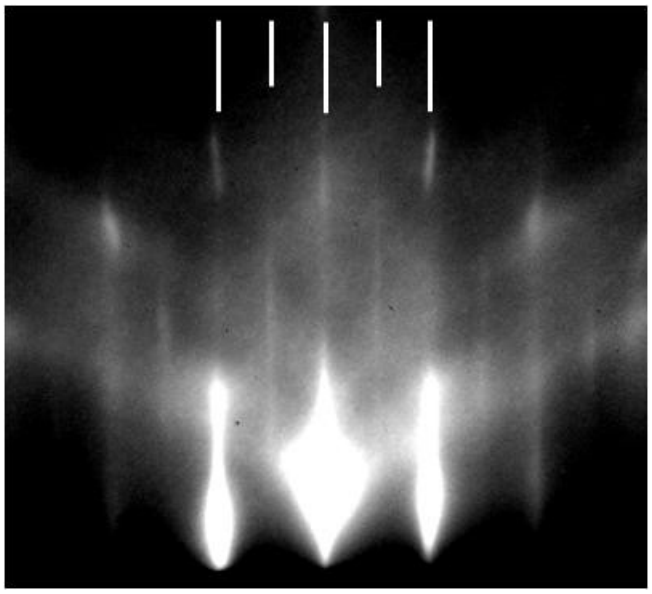

Figure 3.16: Although faint, the ½ order streaks were observed with a ~13 kV beam incident in the [110] direction. While these were visible on occasion in previous observations, the installation of a new RHEED screen provided clearer images, allowing a positive assignment.

From the experiments conducted previously, the most consistent measurements were observed with indium-free substrates. As a result, the investigation into surface reconstruction transition temperatures was carried out using this method of substrate fixation. While Bracker *et al.* report phase boundaries for fluxes containing a majority of dimeric and tetrameric antimony, thermal coupling between the cell and cracker tip of the antimony source did not permit a sufficiently low cracker temperature for the production of a majority tetramer flux.[17]

An "epi-ready" 2" GaAs (001) semi-insulating substrate (AXT) was affixed to an indium-free platen and outgassed (ca. 400°$_e$C, ~60 minutes). After admission to the growth chamber, the oxide layer was removed (600°$_e$C, 590°$_p$C) under a stabilising Sb_2 flux (ca. 1 x 10^{-6} torr) and a GaSb layer deposited (T_g = 500°$_p$C, 0.5 μm h^{-1}, Sb_2:Ga = 5:1), until the RHEED pattern indicated a planar surface.

The incident antimony flux was set prior to each experimental run, and the substrate temperature set to a value where a complete 5 x reconstruction was visible. The substrate temperature was then increased at a ramp rate of 2.0°$_e$C min^{-1}, to provide time for thermal equilibrium to be achieved. During the temperature ramp, the RHEED pattern was observed until the specified end point of the transition was reached. At this point, the antimony flux was increased to the next value and the substrate temperature adjusted to recover the 5x reconstruction pattern. This sequence was repeated until the end of the experimental process.

To preserve the GaSb surface, the antimony flux was maintained during substrate cooling, until the thermocouple value reached ca. 300°$_e$C. The choice of this range was based upon the lower of the published guidelines for antimony stabilisation as a function of temperature,[22] although the true surface temperature was unknown.

Despite the temperature range being below the specified minimum of the Modline 3V pyrometer, readings were taken at each transition point in order to establish whether the pyrometer demonstrated any correlation below this value. Prior to closure of the antimony valve, the Sb shutter was closed briefly while observing the RHEED pattern. No evidence of a change in the pattern was observed, suggesting that no significant loss of antimony occurred. During this investigation, however, it has been observed that the change from one reconstruction to the other may take place on the order of minutes, as the net loss of antimony from the surface is relatively low.

3.2.4.2 Results and Discussion:

In each of the experiments reported here, the observed evolution of the phase transition differed from that reported by Bracker *et al.*[12] This was reported as a symmetric transformation, with the coalescence of the 1/5 and 2/5 order streaks occurring simultaneously with the merging of the 3/5 and 4/5 order streaks. Bracker *et al* define the point of transition as the pattern observed half way through the transition. During this study, an asymmetric transformation was observed, in which the 1/5 order streak remained visible after the disappearance of the 4/5 order streak (Figure 3.17).

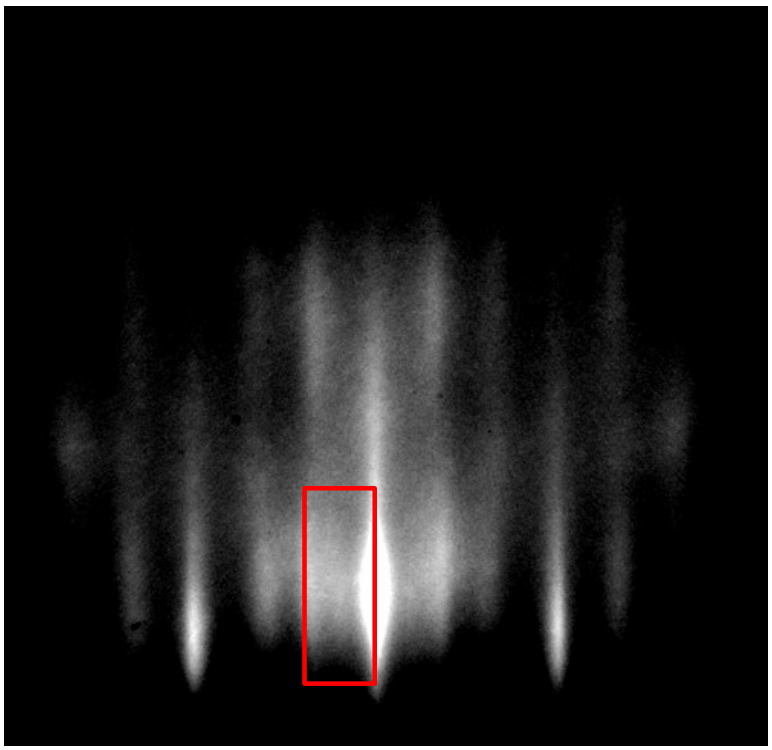

Figure 3.17: An image of a RHEED diffraction pattern, produced with a ~13 kV beam incident in the [10] direction and captured during the transition of surface reconstruction from five-fold to three-fold perodicity. Although faint, the 1/5 order streak (indicated) was observed to remain past the point at which the 4/5 order streak was no longer visible. While determination was made clearly with the naked eye, the image has been enhanced for the benefit of the reader.

Due to the variable quality of RHEED images and the observed asymmetry of the pattern transformation, the endpoint of the transition in the study conducted on the GEN II was defined as occurring when the 1/5 fractional streak became fully incorporated into the 1/3 streak of the (1 x 3) pattern. This point was chosen as it was easier to observe visually, thus minimising the associated. Over the temperature ranges employed, there was no observable change in transition width as a function of temperature (ca. 15°$_e$C). As such any systematic deviation from the observations of Bracker *et al.* should appear as a constant offset in a plot of transition temperature as a function of antimony flux.

The transition occurs over a range of temperature values, lacking any well-defined feature at which a definitive end point could be assigned, giving a reported uncertainty in the literature of ± 5°C.[2] A related issue is that the electron beam was moved away from the sample on a regular basis, in order to prevent destructive etching of surface and the phosphor-coated observation screen. This resulted in different regions of the surface being sampled. This may have introduced a source of error if there were temperature gradients across the surface of the type described in (3.2.4.2), or as detailed for GaAs in the literature.[16]

To remove any effect of ion gauge calibration issues, Bracker *et al* used a correction factor that converts from the measured BEP values (torr) to a flux-equivalent growth rate (ML s^{-1}). This factor is obtained by dividing the Group V BEP by the Group V-limited growth rate.[12]

Since both the correction factor and the relationship between the measured flux and transition temperature are laboratory-specific, this method is reported to produce data that is independent of the equipment used.

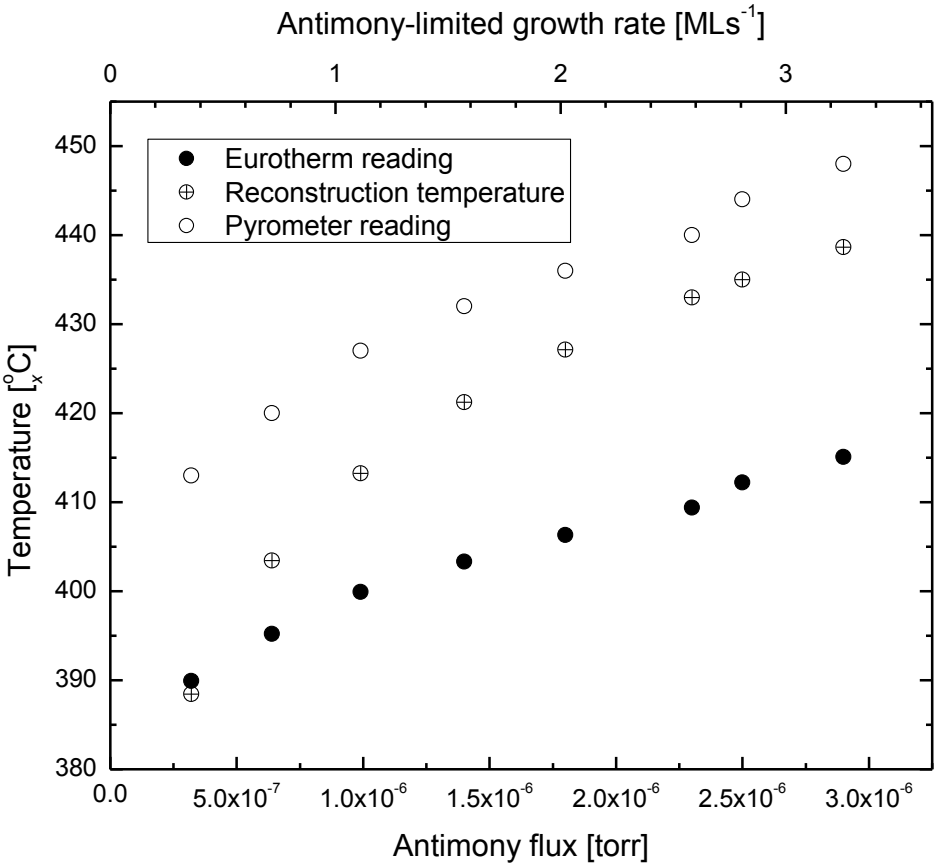

Figure 3.18: A plot of the transition temperature (as determined by pyrometer, Eurotherm controller and the theoretical temperature of transition) as a function of the incident antimony flux. All readings gathered are below the specified minimum operating temperature of the pyrometer, as reconstructions at higher temperature were inaccessible due to the limits of the antimony valved source.

Comparing the data collected by the Eurotherm controller and pyrometer with the theoretical reconstruction temperature given by Bracker *et al.*, there is seen to be little agreement (Figure 3.18).

Due to the limitations of the antimony source, higher levels of Sb flux could not be provided to the sample, thus precluding investigation of reconstruction transitions at higher temperatures, at which the pyrometer may have been more accurate.

On the evidence gathered, there could not be a reliable correlation drawn between the observed transition between surface reconstructions and any of the methods available for temperature determination available for use with the GEN II.

3.2.5 Temperature dependant surface reconstructions of InSb:

While reports are available detailing the phase boundaries of reconstructions for the growing InSb(001) surface,[22,23] there is little discussion of the transitions on a surface under Sb-stabilised conditions. The motivation for investigating the "static" surface was to ascertain which reconstructions could be observed and whether the conditions under which the transition occurred were likely to be of use in temperature determination.

3.2.6 Experimental:

A 2" GaAs(001) semi-insulating wafer (AXT) was outgassed at 400°$_p$C (> 60 minutes), prior to admission to the growth chamber and subsequent thermal oxide desorption under a stabilising Sb_2 flux (~1.6 x 10^{-6} torr). A buffer layer of GaSb (0.5 µm) was deposited (0.5 µm h^{-1}, T_g = 500°$_p$C, Sb_2:Ga = 5:1), followed by a 0.5 µm InSb film (0.5 µm h^{-1}, T_g = 400°$_p$C, Sb_2:In = 2:1), to produce a relaxed InSb(001) surface. The relatively thick layers grown were intended to absorb the majority of

infrared radiation passing through the GaAs wafer, such that temperature deviations arising from any further growth could be largely discounted.

The substrate temperature was ramped ($dT/dt = 2.0°_e C\ min^{-1}$) at different antimony valve positions until the transition between the reconstructions was complete. Using the method of calibrating the Sb_2 BEP as a function of valve setpoint, Sb_2 pressures were then extracted. In this way, a survey of reconstructions was made as a function of substrate temperature and Sb_2 flux. While (1 x 1), c(4 x 4) and asymmetric (1 x 3) [a(1 x 3)] reconstructions were observed, access to the (1 x 1) region was limited by Sb condensation on the surface. The reported c(8 x 2) and (4 x 3) reconstructions appear to result from In-rich conditions,[22] thus could not be reliably probed without risking irreversible damage to the surface. As such, the transition between the c(4 x 4) and a(1 x 3) was chosen for investigation.

3.2.7 Results and Discussion:

Preliminary experiments on the InSb(001) surface elucidated the transition boundary between the c(4 x 4) and the a(1 x 3) reconstructions, over which the change in reconstruction was observed to be relatively sharp, in comparison with that described for the GaSb(001) surface in chapter 3 (Figure 3.19).

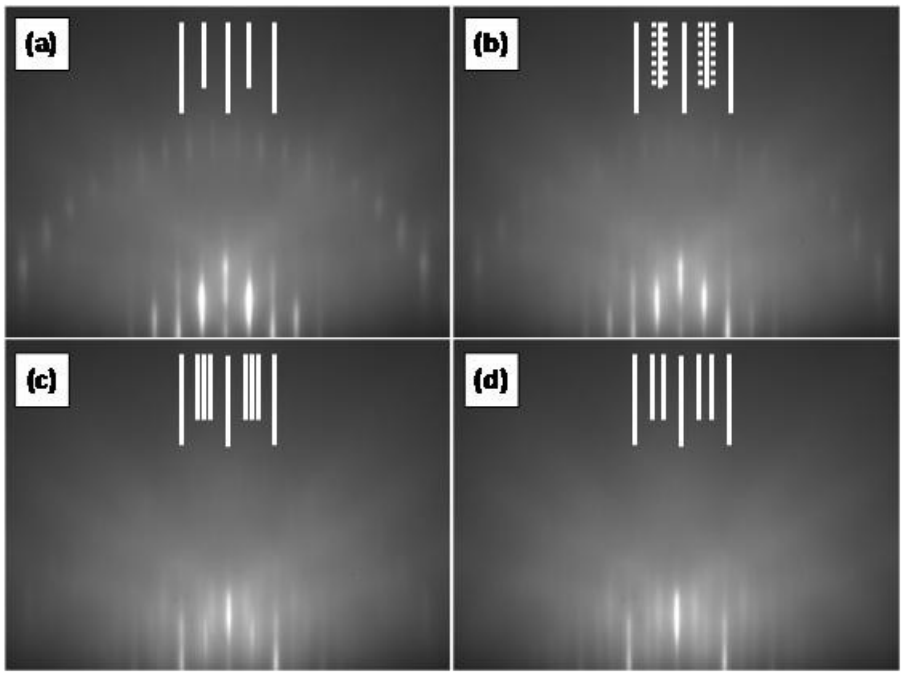

Figure 3.19: A series of ~13 keV RHEED images depicting the transition from the c(4 x 4) reconstruction to the a(1 x 3) resulting from increasing substrate temperature at a fixed antimony flux. The transition was observed to be sharp, occurring over ~5°$_e$C, with the c(4 x 4) yielding more defined and brighter streaks.

Examination of the data reveals a phase boundary with exponential character (Figure 3.20), consistent qualitatively with that described in the literature for a growing InSb(001) surface.[22,23] The Arrhenius plot in (Figure 3.21) indicates an activation energy for the transition of ca. 3.76 eV. The discussion in chapter 3 demonstrates that thermocouple readings alone are unlikely to provide the most accurate means of establishing the true surface temperature, suggesting that this figure in itself does not represent a reliable value. Of interest is the proximity of this value with the total bond energy of three Sb-Sb bonds, which is reported as 3.762 eV,[24] although without a calibrated temperature measurement, no firm conclusions may be drawn from this.

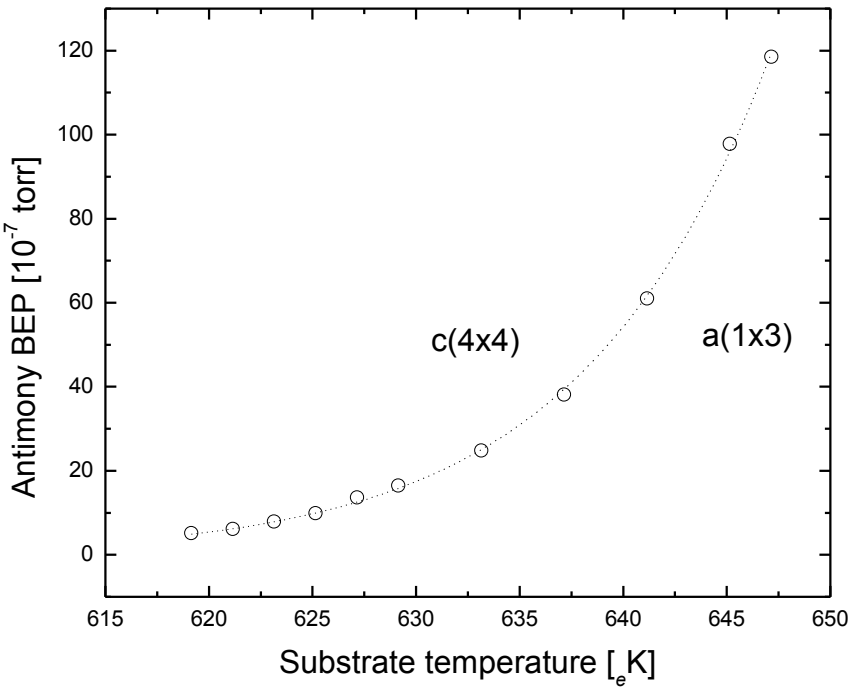

Figure 3.20: A plot depicting the phase boundary between the c(4 x 4) and a(1 x 3) reconstructions determined in this study. The subscript *e* appended to the temperature denotes a measurement in Kelvin, as determined by the Eurotherm controller.

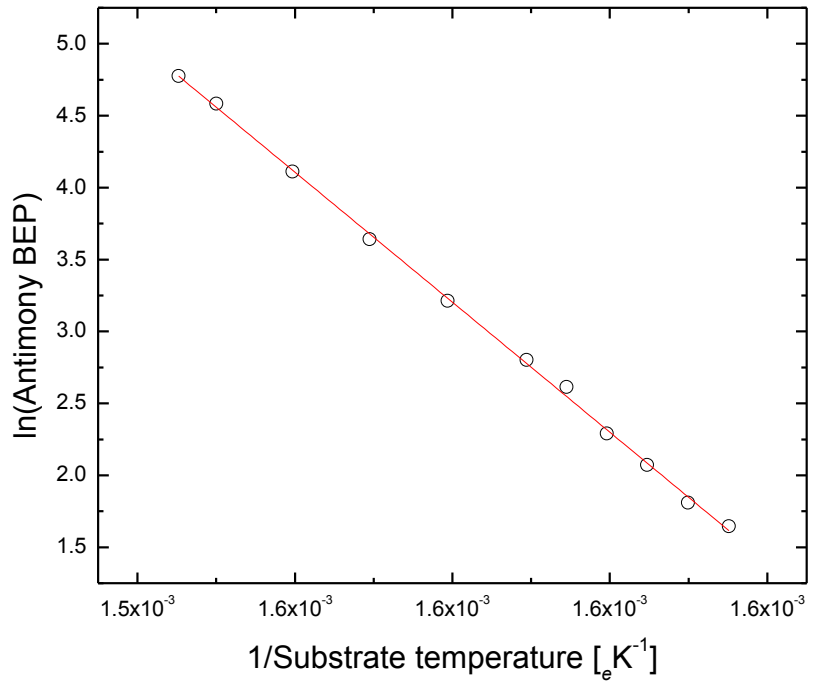

Figure 3.21: Arrhenius plot of the data displayed in Figure 3.20, from which the energy of activation was determined to be 3.76 eV.

As such, the value for activation energy is of less significance than the linearity of the Arrhenius plot, which provides an indication that the measured temperature scale was linear with respect to the surface temperature, over the values probed.

Droopad *et al*. report that the c(4 x 4) → a(1 x 3) transition occurs at ~370°C for a growing InSb(001) surface with an Sb_4:In ratio of 1.75:1 and at a rate of 0.77 ML s^{-1}.[25] Using the calibration method described in chapter 6 and the transition conditions provided by Droopad *et al.*, it is estimated that the measured substrate temperature is ~26°C lower than the estimate in the literature.[25] However, this is necessarily based on consideration of a single transition point, and discounts any differences between dimeric and tetrameric fluxes. This suggests that, if the surface temperature may be established for the transitions and corresponding conditions under which they were observed, a temperature scale may be established to allow growth at temperatures upwards of ~370°C.

For the static surface probed, the inability to access the reconstructions attributed to an In-rich surface is most likely due to difficulty in establishing a stable In-rich surface. For the dynamic case, this may theoretically be achieved through variation of the Sb_x:In ratio for any Sb_x flux value, providing that sufficient In is supplied.

3.2.8 Assessment of Band Edge Thermometry:

For a short period, the BandiT band edge thermometry apparatus (*k*-Space Associates) was made available for use on the GEN II. The spectrophotometer unit supplied was designed for use on GaAs substrates and measurements to determine band edges of other substrates were not possible, due to the spectral sensitivity limits

of the system. Although the apparatus was limited to operation in the transmission mode, due to the lack of an available viewport for illumination of the growing surface, this was not a problem, owing to the band gap of GaSb lying outside the spectral window of the spectrophotometer. The pyrometer and blackbody thermometry functions were briefly investigated, but investigation was discontinued, following the discovery that they both required calibration at temperatures above which GaSb and InSb alloys are likely to degrade.*

3.2.8.1 Experimental:

An experiment similar to that described previously for GaSb/GaAs was undertaken with the growth of InSb on a GaAs(001) semi-insulating substrate. The detector head replaced the pyrometer. Radiation from the heater was used for transmission band edge thermometry, due to the light-pipe behind the substrate not functioning.

Growth was conducted with a V:III ratio of 1.5:1 and at a group III limited rate of 1.0 μm h^{-1}. The initial growth temperature was set at 300 ± 10°$_b$C and was recorded as a function of deposition time. At the end of the experiment, the measured signal had decayed significantly and the heater power was increased momentarily to maximum output, to obtain some transmission, in an attempt to determine the final temperature.

* Private communication: Jeff Harris, *k*-Space Associates

3.2.8.2 Results and Discussion:

The signal received by the spectrophotometer was generally of a relatively low intensity and the temperature reading provided exhibited a high degree of noise throughout. This was found to be due to the substrate heater not providing sufficient radiation for the GaAs band edge to be clearly and consistently observed at the temperature chosen for growth. During deposition, a rise in temperature was recorded by the band edge thermometry equipment (Figure 3.22). The heater power was observed to remain constant throughout deposition.

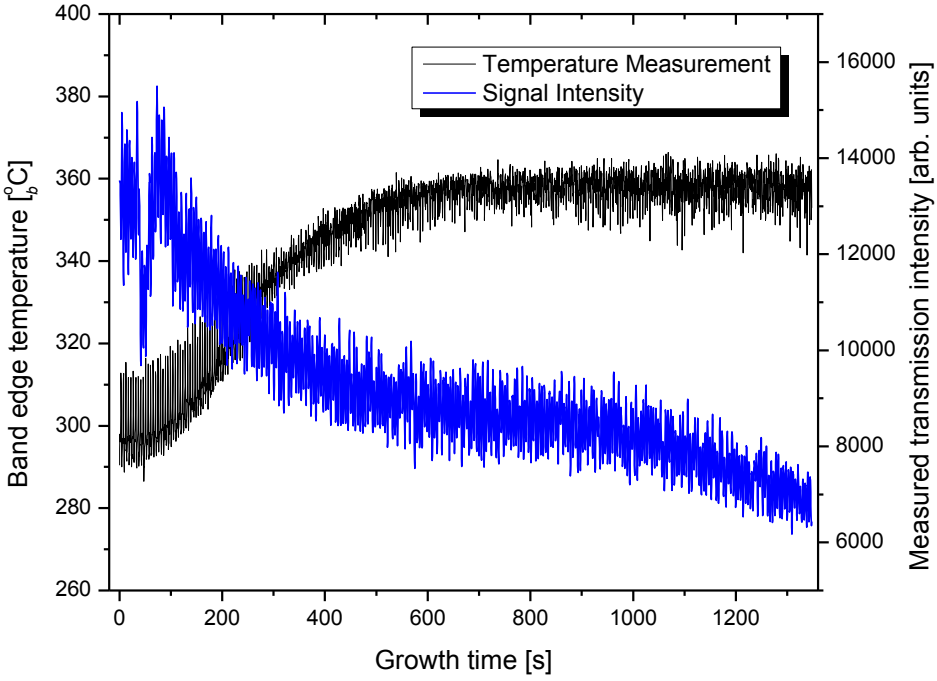

Figure 3.22: A plot of the measured temperature, as extracted from the GaAs band edge, and the signal acquired by the spectrophotometer as a function of deposition time. From the start of growth, a rise in temperature is accompanied by a loss in signal. After ca. 700s, the temperature rise stopped. This corresponds to a deposited InSb thickness of ~194 nm.

With the spectrophotometer signal being insufficient for temperature determination to ±10°$_b$C, the attempt to increase its magnitude by temporarily using full heater power resulted in significant damage to the film (Figure 3.23).

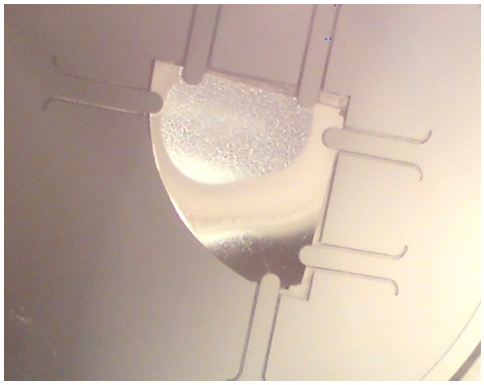

Figure 3.23: Following the illumination of the substrate by increasing the heater power to a maximum (ca. 1s), it was discovered that the resultant radiation had led to a large rise in temperature of the film. While the signal remained insufficient for an accurate temperature reading to be made, the gradients present over the sample are evident.

This shows clearly that band edge temperature measurements are not appropriate for reproducible growth of InSb on GaAs, due to the large temperature rise observed and the loss of signal that would limit detection of the GaAs band edge in the case of thicker films.

These findings also highlight the temperature gradients present, shown by the varied degree of damage to the film, ranging from none to a surface which was observed by the naked eye to be rough and covered with metallic droplets. It seems likely that the fingers of the platen which hold the sample in place, cause some conductive cooling, although the damage also suggests a spatial variation in heater power, due to the epicentre of damage appearing away from the centre of the wafer. If the composition of the epilayer is a function of V:III ratio or temperature then the region of the wafer sampled for temperature measurement should be the same region as is characterised.

3.2.9 Investigation into the Effect of Sample Heat Cycling:

It is not unusual for a buffer layer to be grown at a different temperature than the final epitaxial layer, or that the temperature may be required to change for different stages of growth. Temperature measurements made before such a change should be the same as those made afterwards. To determine the effect of a heating cycle, an experiment was conducted to detect any difference between two consecutive series of temperature measurements. After comparing measurements from substrates affixed with and without indium solder, an indium-free mounting arrangement was employed to minimise the errors.

3.2.9.1 Experimental:

A 2" GaAs (001) semi-insulating wafer (AXT) was mounted on an indium-free platen and outgassed at 400°$_e$C (~ 70 minutes), prior to oxide removal (T_{sub} = 610°$_e$C, 595°$_p$C) under a stabilising antimony flux (8.1 x 10^{-7} torr). A layer of GaSb (~0.27 μm) was then deposited at a Group III limited growth rate of 0.5 μm h^{-1} (T_{sub} = 530°$_e$C, 480°$_p$C). A pyrometer temperature measurement was made at the end of the growth of this layer. A further deposition of gallium antimonide was then undertaken (0.57 μm). In order to increase the quality of the observed RHEED pattern, an additional layer of GaSb (0.57 μm) was grown (T_{sub} = 500°$_e$C, 525°$_p$C) with an antimony beam equivalent pressure of ~1.6 x 10^{-6} torr.

The sample was cooled to 430°$_e$C and the substrate temperature increased at a rate of 2.0°$_e$C min^{-1}. Pyrometer measurements were taken at regular intervals as a function of the Eurotherm temperature controller reading. During each measurement, the

antimony shutter was closed momentarily, to avoid contribution to the pyrometer reading by radiation from the cracker tip. Following cooling under a stabilising antimony flux (~$1.6x10^{-6}$ torr), the sample was heated at the same rate and the measurement process repeated.

3.2.9.2 Results and Discussion:

Following two cycles of successive heating and cooling, the temperatures measured from the second run were observed to be higher than those collected in the first (Figure 3.24). At no time between the measurement sequences had the sample been exposed to atmosphere, or intentionally altered in any way. Comparison of the data sets did not show a constant offset in the measurements taken from the Eurotherm controller, but fitted well when the pyrometer values were multiplied by a constant (1.058), which is consistent with a ca. 6% increase in sample emissivity.

This change may occur during the cooling/heating sequence, possibly as a result of the stabilising antimony flux being too large during substrate cooling, resulting in antimony condensation.[22] This is thought to be an unlikely explanation however, as it is expected that the temperature range covered would allow the loss of excess antimony from the surface,[20] and the two series should converge with increasing temperature.

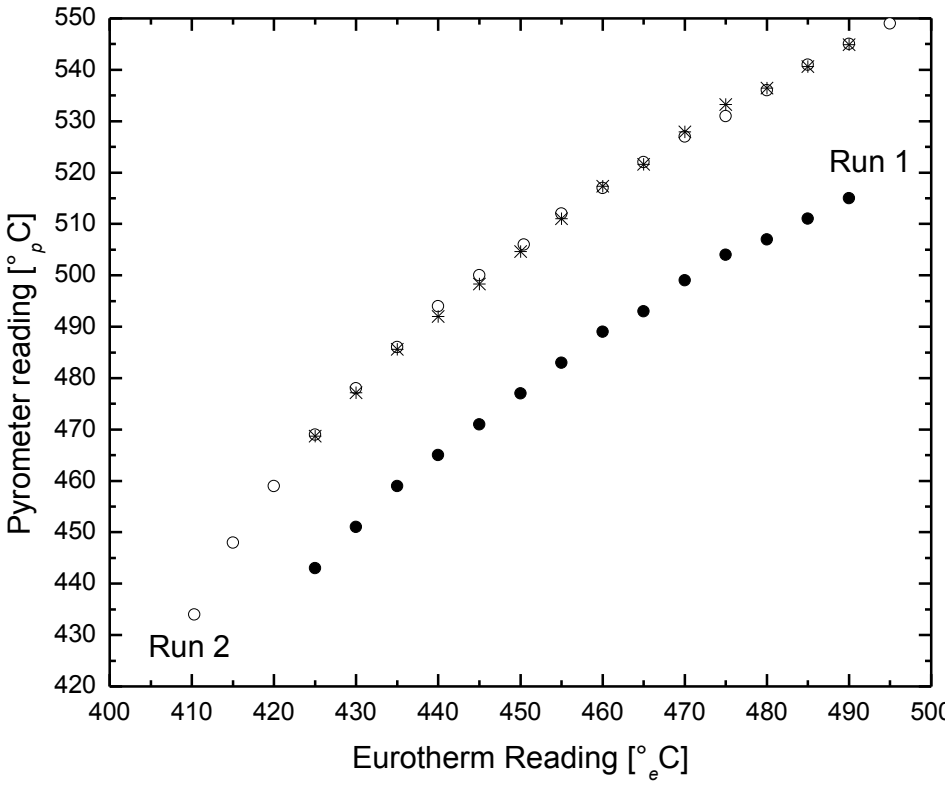

Figure 3.24: Data gathered from two consecutive experimental runs show an increase in the temperature as measured by the pyrometer. Between the first run (full circles) and the second run (empty circles), no intentional changes had been made to the sample or platen. The stars indicate the data gathered from Run 1 when multiplied by a constant (1.058).

This effect could also result from changes occurring to the rear of the wafer. Without a stabilising flux on the side of the wafer facing the heater, one would expect degradation of the wafer at elevated temperatures, owing to group V loss. Although no signs of damage or roughening of the surface were observed, an increase in observed substrate temperature has been seen previously resulting from thermally-induced changes affecting the rear wafer face.[6]

3.3 Comparison and Discussion of the Available Techniques:

The experiments conducted have highlighted areas in which pyrometric temperature measurement may be affected by reflections and the manner in which a substrate is affixed to the platen. With the results gathered from indium bonded substrates displaying significant inconsistency, the use of indium-free platens appears to constitute a course of best practice. After finding material adsorbed on the pyrometer viewport, a heated viewport was installed and a method of best practice established for its use.

The investigation into surface reconstructions of the GaSb(001) surface did not result in a sufficiently accurate method by which surface temperatures may be determined or set. Furthermore, calibration of existing equipment using this method was not possible, due to the limitations of the minimum operational pyrometer temperature and the maximum flux that could be delivered by the antimony valved source. Following this investigation, the Sb source was modified such that the valve range was improved, thus permitting a larger range of flux values.

Examination of the InSb(001) surface reconstruction transition from a c(4x4) to a(1x3) pattern gave better results, with the Arrhenius plot indicating a linear correlation between the Eurotherm controller and true surface temperature. However, the lack of a reliable calibration from either literature or pyrometer measurements does not allow calibration of this phase boundary with respect to temperature. Furthermore, the Eurotherm controller values recorded are not thought to be transferrable to other substrate/platen arrangements, due to the variation between samples observed in (3.2.2.2).

The suitability of band edge thermometry was investigated and it was found that the equipment used was not appropriate for the homoepitaxial growth of GaSb or InSb films in the available configuration. Furthermore, the signal from the heater received by the spectrophotometer was insufficient for accurate temperature determination. The pyrometer and blackbody methods of thermometry were investigated, but were found not to provide reliable measurements, requiring calibration at temperatures beyond the range sustainable by GaSb or InSb.

It was established that growth of narrow band gap material on a gallium arsenide wafer led to a rise in recorded temperature as a function of deposition time. For this reason, combined with the reported temperature sensitivity of nitrogen incorporation to III-V alloys,[2,23-25] it was decided that growth of GaN_xSb_{1-x} and InN_xSb_{1-x} should take place on gallium antimonide and indium antimonide wafers respectively. While the technology exists to employ band edge thermometry upon such substrates, it was not available during this investigation.

Evidence was found for temperature gradients across the surface, highlighting the need for care and consistency in selecting the region of the sample utilised for compositional and morphological analyses.

3.4 Conclusion:

It has been determined that the most suitable method for measuring growth temperatures above 450°C is by direct use of pyrometer readings. Access to lower temperatures is likely to be required, due to the envisaged lower growth temperatures required for nitrogen-containing alloys and InSb films. Where a target temperature

falls below 450°$_p$C, a linear extrapolation from pyrometer measurements at higher temperatures appears to be the best practice available. While not regarded as an ideal solution and assuming that the pyrometer reading is based largely upon the surface temperature, such a method allows consistency with the observed measurements of each sample, with little variation arising from any inconsistencies in substrate mounting, for example. Taking into account the effect of stray radiation, each datum, both for direct and extrapolated measurements, should be collected during momentary closure of all material source shutters and from a sample azimuth that provides the lowest pyrometer value.

Based on the evidence indicating the potential for temperature gradients across the sample, the favoured method appears to be to ensure that characterisation of all samples produced in this investigation is conducted as close as possible to the centre of the wafer, coinciding with the region sampled by the pyrometer.

[1] T. Nishinaga, S. Naritsuka, *Crystal Growth Technology* (Springer-Verlag, Berlin, Heidelberg, New York, n.d.), p. 61.

[2] V. A. Odnoblyudov, A. R. Kovsh, A. E. Zhukov, N. A. Maleev, Semiconductor **35**, 554-559 (2001).

[3] Y. Lin, Thin Solid Films **368**, 249-252 (2000).

[4] M. J. Yang, W. J. Moore, C. H. Yang, R. A. Wilson, B. R. Bennett, B. V. Shanabrook, Journal of Applied Physics **85**, 6632 (1999).

[5] D. D. Pollock, *The Theory and Properties of Thermocouple Elements* (American Society for Testing and Materials, 1971), p. 1.

[6] B. Shanabrook, J. Waterman, J. Davis, R. Wagner, Applied Physics Letters **61**, 2338–2340 (2009).

[7] M. Nouaoura, L. Lassabatere, N. Bertru, J Bonnet, **13**, 83-87 (1995).

[8] J. L. Hall, A. J. Kent, C. T. Foxon, and R. P. Campion, Journal of Crystal Growth **312**, 2083-2088 (2010).

[9] D. Katzer, B. Shanabrook, Journal Of Vacuum Science & Technology B: Microelectronics and Nanometer Structures **11**, 1003–1006 (2009).

[10] S. L. Wright, Journal of Vacuum Science & Technology B: Microelectronics and Nanometer Structures **4**, 505 (1986).

[11] S. L. Wright, Journal of Vacuum Science & Technology B: Microelectronics and Nanometer Structures **8**, 288 (1990).

[12] A. S. Bracker, M. J. Yang, B. R. Bennett, J. C. Culbertson, W. J. Moore, Journal of Crystal Growth **220**, 384–392 (2000).

[13] Y. Varshni, Physica **34**, 149-154 (1967).

[14] P. Pichler, *Intrinsic Point Defects, Impurities and their Diffusion In Silicon* (Springer-Verlag, Wien, 2004), p. 23.

[15] I. Farrer, J. Harris, R. Thomson, D. Barlett, C. Taylor, D. Ritchie, Journal of Crystal Growth **301-302**, 88-92 (2007).

[16] D. E. Mars, J. N. Miller, Journal of Vacuum Science & Technology B: Microelectronics and Nanometer Structures **4**, 571 (1986).

[17] Y. Rouillard, B. Lambert, Y. Toudic, M. Baudet, M. Gauneau, Journal of Crystal Growth **156**, 30–38 (1995).

[18] G. M. Williams, I. M. Young, Journal of Crystal Growth **62**, 219–224 (1983).

[19] J. M. Reifsnider, D. W. Gotthold, A. L. Holmes, B. G. Streetman, Journal of Vacuum Science & Technology B: Microelectronics and Nanometer Structures **16**, 1278 (1998).

[20] C. Goletti, U. Resch-Esser, J. Foeller, N. Esser, W. Richter, B. Brar, H. Kroemer, Surface Science **352**, 771–775 (1996).

[21] P. Thibado, Journal of Crystal Growth **175-176**, 317-322 (1997).

[22] C. F. McConville, T. S. Jones, F. M. Leibsle, S. M. Driver, T. C. Q. Noakes, M. O. Schweitzer, and N. V. Richardson, Physical Review B 50, 14965 (1994).

[23] A. J. Noreika, M. H. Francombe, C. E. C. Wood, Journal of Applied Physics 52, 7416–7420 (1981).

[24] Gary Wulfsberg, Inorganic Chemistry (University Science Books, Sausalito, 2000), p. 93.

[25] R. Droopad, R. L. Williams, S. D. Parker, Semiconductor Science and Technology 4, 111 (1989).

[26] E.J. Koerperick, L.M. Murray, D.T. Norton, T.F. Boggess, J.P. Prineas, Journal Of Crystal Growth **312**, 185-191 (2010).

[27] , R. J. Hauenstein, M. L. O'Steen, T. C. McGill, Applied Physics Letters **68**, 1510 (1996).

[28] L. Buckle, B. Bennett, S. Jollands, T. D. Veal, N. R. Wilson, B. Murdin, C. F. Mcconville, T. Ashley, Journal of Crystal Growth **278**, 188-192 (2005).

[29] Z. Pan, L. H. Li, W. Zhang, Y. W. Lin, and R. H. Wu, Applied Physics Letters **77**, 214 (2000).

Chapter 4

"Make everything as simple as possible, but not simpler."

Albert Einstein (1879 – 1955)

Various growth conditions have been utilised for the homoepitaxial growth of GaSb films. Following characterisation by means of atomic force microscopy (AFM), reflection high energy electron diffraction (RHEED) and circular-polarised differential interference contrast (C-DIC) microscopy, heteroepitaxial GaSb/GaAs layers were then produced to establish the dependence of film quality on growth rate and deposition thickness.

4.1 Introduction

The interest in GaSb as a substrate (or metamorphic buffer layer) stems primarily from the proximity of its lattice constant (6.095 Å) with those of ternary and quaternary III-V alloys which exhibit a wide spectral range of band gaps (ca. 0.3-1.58 eV).[1,2] As such, GaSb shows promise in the manufacture and development of devices operating in the regions of 2-5 and 8-14 μm, which include wavelength ranges useful for low loss fibre optic technology and long-wave infra red sensors for military and medical diagnostic applications.[2-4] High-quality films are fundamental to optimise optoelectronic performance and it is desirable to establish growth parameters for the binary compound for use as a buffer layer and prior to investigation of the corresponding ternary and quaternary systems.

Preliminary investigation of GaSb growth was motivated by the requirement to understand the dependence of film quality on the choice of growth temperature, rate of deposition, incident flux ratios and choice of substrate. Such information gathered from the binary compound is useful when establishing the cause of differing surface morphologies or growth problems that may occur in GaN_xSb_{1-x} samples, providing insight into whether they are common to both binary and ternary materials under certain conditions, or result from the addition of nitrogen and appear only in the ternary system.

4.2 Literature discussion of GaSb Growth by MBE

Prior to epitaxial growth of a high quality film, it is necessary to have a clean surface.[5-8] Of the methods available, there are two principle categories: *in situ* and

ex situ treatments. While *ex situ* chemical treatments are simple to implement and have been reported to be successful in thinning the oxide layer that forms on a GaSb surface, contaminants are likely to persist on the wafer, either from the original oxide layer, or those introduced by solution processing. In the case of complete removal of the oxide layer, exposure to anything other than an inert atmosphere upon removal from solution will lead to further oxide formation. This assertion is supported by Kodama *et al.*, who report that a 20-30 Å oxide layer remains after a CH_3COOH:HNO_3:HF etch, citing high surface reactivity as the cause.[9]

In situ techniques are preferable as they do not require exposure to the atmosphere after cleaning, prevent particulates alighting upon the substrate during movement inside or outside the growth system. Of these methods, thermal desorption has been widely used on GaSb,[10-13] as well as other substrates.[14-18] As a technique, it has the benefits that it lacks the requirement of any additional equipment and may be performed over a timescale of minutes. Baba *et al*. report, however, that carbon species may persist following thermal treatment of substrates, indicated by depletion of carrier concentration.[19] Furthermore, it has been reported that thermal oxide desorption can result in roughening of a GaAs surface,[20] suggesting that care must be taken with the less resilient antimonide. However, where a buffer layer is to be applied, it may be possible to recover the surface.

In the case of GaSb, substrate temperatures exceeding 300°C are sufficient to alter the stoichiometry and morphology of the (100) surface, although the oxide layer persists at higher temperatures.[21] As such, thermal oxide removal under an overpressure of antimony may present a viable option, analogous to oxide removal from the GaAs (001) surface.[22]

As a result of damage resulting from thermal cleaning, there has been investigation into other *in situ* cleaning, involving ion, radical or plasma processes, including H-plasma, H-gas and H-radical cleaning.[19] Compared to thermal desorption alone, each of the hydrogen methods are cited as providing a cleaner surface, although radiation damage is evident in the sample exposed to plasma. Ion sputtering may also be employed as a cleaning technique, although this induces surface patterning and morphological changes.[23,24] However, ion bombardment conducted at a glancing angle with respect to the substrate has demonstrated promise in application on GaAs, resulting in a flat surface.[25]

RHEED observations have resulted in reports detailing a number of surface reconstructions for the oxide-free GaSb (001) surface, with the following having been confirmed by STM studies: (1 x 5), (2 x 5), c(2 x 10), c(2 x 6) and (1 x 3).[13,26] While there are conflicting reports as to the boundary conditions for the transitions between these reconstructions, there are two aspects on which there is consensus. The first is that the (*n* x 5) and c(2 x 10) reconstructions are observed in a more antimony-rich regime, whereas the c(2 x 6) and (1 x 3) result from a lower density of surface antimony species.* The second point is that transitions between these surface phases have strong dependence on both the incident antimony flux and surface temperature,[27] although the experiments conducted in chapter 3 illustrate the difficulties that may be encountered with respect to accurate and reproducible determination of temperature.

* Although both surfaces are Sb-rich in terms of stoichiometry.

Among III-V films, the (*n* x 5) reconstructions are thought to be unique to GaSb, due to the near equivalence of the unit cell size of gallium antimonide with the lattice parameter of trigonally-bonded Sb.[13]

Reconstructions are reported as occurring under different fluxes and substrate temperatures. These are likely to arise from the measurement inconsistencies endemic in inter-laboratory comparison, as discussed in chapter 3. It is not always clear how the V:III ratios have been determined, which increases difficulties associated with translating parameters from one growth system to another. It is generally considered that expressing material fluxes as a function of limiting growth rates instead of beam equivalent pressures provides a more consistent means of quantifying the supply of material to the substrate. Furthermore, the clarity of the RHEED image is also affected by the apparatus with which it is observed, the quality of the camera used for acquisition, and the presence of any adsorbed species on the interior of the phosphor-coated window.

GaSb has been grown on a number of substrates, including Si, GaAs and GaSb.[2,28-33] The substrates used for growth each have associated benefits and drawbacks: while GaAs and Si are relatively inexpensive and can be produced with a lower density of inherent defects than GaSb, their lattice constants differ significantly (5.430Å and 5.653Å respectively) from that of GaSb, resulting in dislocations that propagate through the grown film.[29]

In terms of MBE growth, antimony has been described as a "nuisance" element, due to its low vapour pressure.[1,2,32] There is a tendency of antimony atoms to aggregate, causing Sb vacancies and Ga_{Sb} defects.[2,30,34] This process is cited as the reason for the invariably *p*-type nature of MBE grown GaSb.[2,21,30,35] To counter this, it is

reported that epitaxial growth of GaSb, regardless of substrate, must be conducted under an excess of antimony.[2] As an aside, it should be noted that *n*-type GaSb layers have been reportedly formed by liquid phase epitaxy (LPE) at temperatures > 400°C.[2,36]

When Ga-rich flux ratios are used, Lee *et al.* report a progressive decline in the intensity and clarity of the (1 x 3) RHEED pattern associated with an antimony-stabilised GaSb surface above 400°C, until there is no observable pattern.[28] This suggests formation of an amorphous surface with gallium aggregation, which is supported by reports in the same publication of rough surfaces with a metallic lustre. While an antimony rich flux is required, Lee *et al.* refer in the same publication to the near minimum excess of antimony, reporting a decrease in PL efficiency for Sb_4:Ga ratios above this value.

Upon sublimation, antimony is generally produced as Sb_4. Epitaxial growth may proceed also with monomeric or dimeric Sb by means of a cracker, though the populations of the different species are often assumed from the cracker temperature regime or inferred from published data,[36] rather than directly measured.[27] The latter method is hindered by the difference in ion gauge sensitivity between the diatomic nitrogen most commonly used for calibration and antimony. Additionally, the hot filament common to all ion gauges can cause thermal cracking of both Sb_2 and Sb_4 species. It is reported that growth with Sb_4 proceeds with a second-order dependency upon antimony flux.[12] This is in common with growth of GaAs with As_4 species, where the second-order characteristics are caused by a two-body dissociative process.[15]

As with reported observations of surface reconstructions, published growth conditions vary, especially with respect to measurements of antimony beam equivalent pressure and substrate temperature. The former results from the variation between experimental systems and the inclusion (or absence) of relative sensitivity factors in flux calculations, which is rarely stated explicitly in the literature. It has been demonstrated in chapter 3 that values resulting from temperature measurement may vary according to the method of determination. With these factors in mind, it was considered important to establish lab-dependent parameters, using published data only as a guide.

In the case of MBE growth undertaken in a chamber in which arsenic has been used, it is possible that some As incorporation will occur.[37] This has been reported where arsenic has been deposited on a heat-cycled piece of apparatus, such as the antimony cracker. Upon heating, sublimation may effectively create a secondary As source. However, this may decrease as a function of time of operation of the antimony cracker and is less likely to be present at significant levels where the antimony cracker tip is kept at elevated temperatures when not in use.[36]

For GaSb growth temperatures of 550°C, which is the optimum recorded by Lee *et al.*, and a group III limited growth rate of 1 μm h^{-1}, the minimum excess in terms of Sb_4:Ga flux is reported to be ca. 2.2:1. Lee *et al.* state that the free exciton transition at 810 meV was not observed in any PL experiments, suggesting that the optical quality of the films grown was relatively poor.

There are reports that native defect concentrations may be decreased by use of Sb_2 in conjunction with lower growth temperatures.[36] The rationale is that Sb_2 species

undergo incorporation with first-order dependence and do not need the larger atomisation energy of Sb_4 from the surface, thus allowing both a lower growth temperature and enhancing the reaction with surface gallium species. There is no significant difference in hole concentration or mobility between films grown using Sb and Sb_2 species.[38]

Of the growth schemes for GaSb/GaAs and GaSb/GaSb reported the key facts are summarised below:

Substrate	**T_{Sub} (°C)**	**Sb_x:Ga Ratio**	**Growth Rate**	**Ref.**
Te-GaSb	500-600	-	0.6-2.5 μm h^{-1}	[32]
Cr-GaAs	500-600	-	0.6-2.5 μm h^{-1}	
-	500-600	-	0.6-1.5 μm h^{-1}	[2]
GaAs (001)	480-620	0.7-6.5:1	1.0 μm h^{-1}	[28]
GaSb (001)	550	2.5:1	1.0 μm h^{-1}	
Cr-GaAs SI (001)	500	2:1 (x = 4)	0.5 μm h^{-1}	[31]
GaSb	470-550	1.56-4.52:1 (x = 2,4)	0.8 μm h^{-1}	[37]
GaSb (001)	380-550	1.2-4 (x = 1,2)	1.1 μm h^{-1}	[33]

Ignoring the different methods that have been used to measure the conditions, particularly in the case of V:III ratios, the literature indicates that the oxide layer may be removed by thermal cleaning, although a stabilising antimony flux would be required to prevent degradation of the surface. Furthermore, it appears that successful growth must employ some excess of antimony, relative to the gallium flux supplied to the substrate.

4.3 Overview of Experimental Growth:

With a view to the production of GaN_xSb_{1-x} films, it was desirable to examine growth of the binary alloy. While a given set of growth conditions may result in a high level of incorporated nitrogen, for example, they may also be sub-optimal for binary alloy growth, to the detriment of film quality. This is of particular interest in GaN_xSb_{1-x}, due to the large difference between the optimum growth temperature employed by Lee *et al.* and temperatures at which appreciable levels of nitrogen ($x <$ 1.8%) have been incorporated.[39]

The controllable parameters routinely varied are the growth temperature (T_g), the growth rate, the ratio of materials supplied and the substrate. Each of these has been demonstrated for other materials to affect growth quality.[40]

Experiments were conducted to determine the effects of growth temperature and V:III flux ratios with respect to GaSb growth on GaSb(001) substrates. Further growth was conducted in order to ascertain what effects would result from the choice of GaAs(001) as a substrate.

4.3.1 Preparatory Work:

Here are described the procedures undertaken to ascertain the consistency of the antimony valved source and calibrate the gallium and antimony sources.

4.3.1.1 Assessment of the Stability of the Sb Valved Source:

The valved antimony source was examined, as varying V:III ratios can cause differences in quality between growths. On each day (or after closure of the antimony valve), the antimony beam-equivalent pressure was recorded as a function of valve position (Figure 4.1).

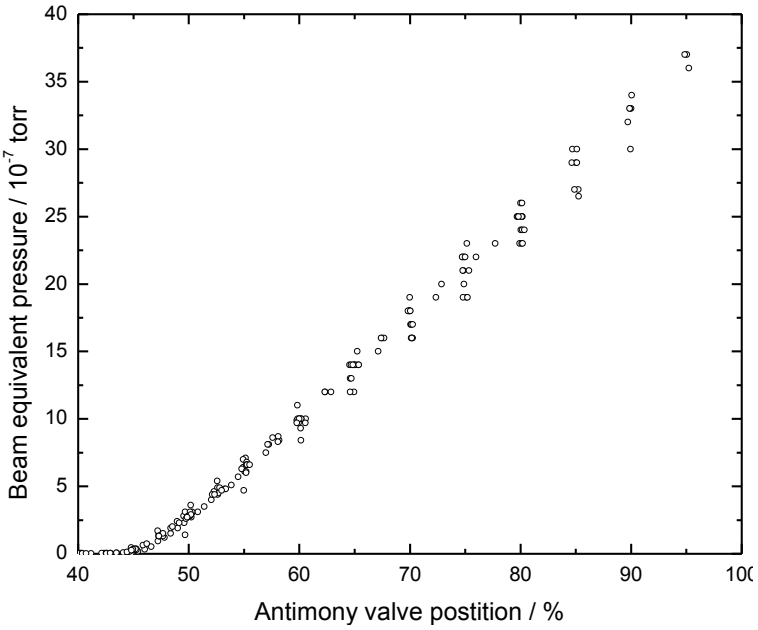

Figure 4.1: The pressure recorded on the Beam Monitoring Ion (BMI) gauge was plotted as a function of valve position. Data was collected on each day of growth, due to the observed variation in valve response.

Practical experience of this source indicated that the valve had a tendency to stick slightly upon opening the valve, resulting in an increase in BEP when the force provided became sufficient to free the valve. In order to minimise any effects of this on the measured values, the valve position was set to ca. 50%, before being reduced again for increasing readings to be taken. Valve hysteresis had been observed with this equipment previously and, so readings were only taken when opening the valve. Data from several days revealed a spread of BEP values as a function of valve

position, although the plots were observed to have much closer values where two measurements were conducted on the same day. While there was observed to be curvature to each of the series at a valve setting of ca. 47%, each plot was linear after this. Accordingly, it was possible for each day of measurements to produce a plot of BEP as a function of valve position in order obtain the desired V:III ratio.

4.3.1.2 Calibration of Material Sources:

For system-independent data, it is preferable to express the rates of deposition of both the group III and group V species in terms of growth rate. To achieve this, the technique of analysing time-resolved RHEED intensity oscillations discussed in Chapter 2 was employed, in order to ascertain the rate-limiting fluxes of both gallium and antimony.

Briefly, a GaAs(001) semi-insulating wafer was outgassed at 400°$_e$C (> 60 minutes) and the oxide removed under a stabilising antimony flux (~1.6 x 10^{-6} torr). A layer of GaSb was then grown under antimony rich conditions, until the RHEED pattern indicated a flat, ordered surface. For the measurements to determine the gallium flux, the substrate was held at 440°$_p$C and the antimony valve set at a fixed value. The gallium source temperature was varied over a range and with nominal group III fluxes determined from previous calibration undertaken on the GEN II. The antimony valve was set at a value, sufficient to produce a flux that was large in comparison with the envisaged range of gallium flux. This flux was supplied to the sample continuously, while that of the gallium was supplied only during the recording sequence. The intensity of a diffraction streak (Figure 4.2) was monitored

by a camera and selected in the RHEED software (kSA, k-Space Associates), with care taken to avoid contributions to the recorded region by Kikuchi lines or areas of the screen which appeared to exhibit an anomalous background signal.

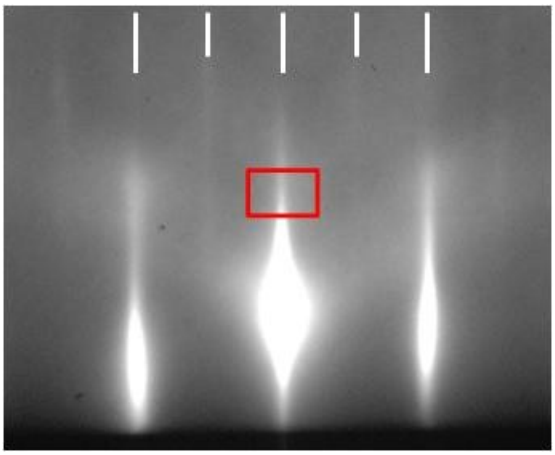

Figure 4.2: The region of the streak selected was chosen to avoid saturation of the signal received from the camera. Care was also taken to avoid the inclusion of Kikuchi lines in the selected area. The streak was observed to oscillate in brightness and apparent length while growth of GaSb was underway.

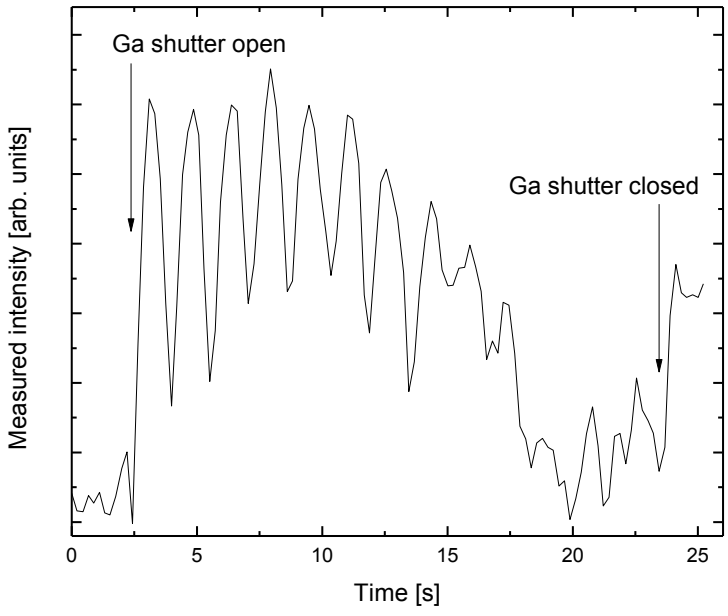

Figure 4.3: A typical plot of recorded data, depicting the intensity of the selected region of the diffraction pattern as a function of time. It was observed that the magnitude of the oscillations tended to damp with increasing time, until no clear periodicity could be observed.

Shortly after recording was commenced, the gallium shutter was opened and the change in diffraction fringe intensity monitored. After sufficient oscillations had been measured, or when the surface showed signs of gallium-rich conditions characterised by four-fold reconstruction periodicity, the gallium shutter was closed and the recording halted (Figure 4.3). At each temperature value of the gallium source, the procedure was conducted at least twice, to determine reproducibility

For determination of the antimony-limited regime, the valved source was set to a particular value and the gallium source temperature increased until the increase was not accompanied by a corresponding increase in the rate of oscillation (Figure 4.4). At this point, further measurements were attempted in order to better characterise the plateau, although care was taken during gallium-rich growth in order that the surface morphology was subjected to a minimum of adverse growth conditions. During higher growth rates at the lower temperature values investigated, very few oscillations were observed before the RHEED pattern exhibited four-fold periodicity associated with gallium-rich surfaces (Figure 4.5). Following these observations, the gallium growth rate was not increased further, in order to prevent irreparable surface deterioration.

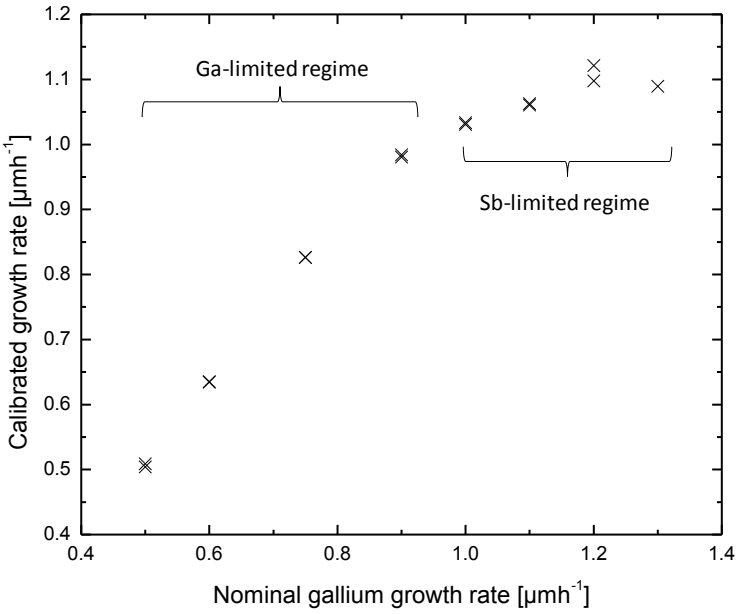

Figure 4.4: A plot depicting data gathered by varying the gallium flux at a fixed antimony valve value. The different regimes present are clearly visible. Each series provides additional confirmation of the gallium calibration factor and a single datum for the antimony-limited growth rate.

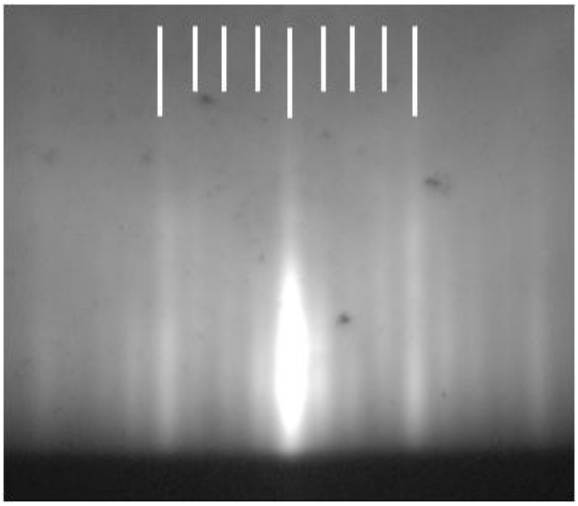

Figure 4.5: RHEED diffraction pattern formed from a ~13 kV beam, incident in the [010] direction towards the end of gallium oscillations performed under an antimony flux. The four-fold periodicity is observed as the result of a depletion of antimony producing a gallium-rich surface.

After one plateau had been identified, the BEP of antimony was increased and the procedure repeated, producing a linear relationship between limiting growth rate and antimony BEP (Figure 4.6).

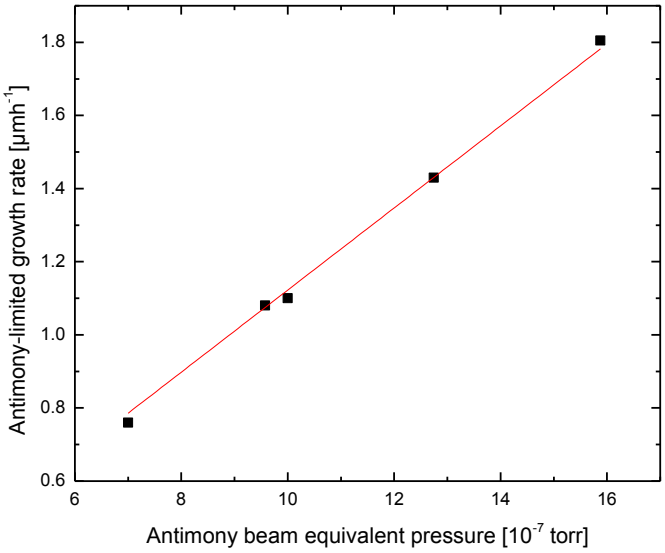

Figure 4.6: Plot of the antimony-limited growth rate as a function of antimony BEP. From this and, in combination with the calibration of the gallium cell, it was possible to determine V:III ratios as a function of growth rate.

From the experiments described above, both the gallium and antimony sources were calibrated as a function of easily determined variables, permitting growth to be expressed in terms of a ratio of fluxes as opposed to measured pressures.

Typically, experiments at lower substrate temperatures produced larger oscillations, although no difference in oscillatory period could be discerned over the temperature range studied (440-460°$_p$C). At higher temperatures, oscillations were not observed, precluding investigation into antimony incorporation kinetics of the type reported by Tok *et al.* for GaAs.[41] It is thought that the disappearance of oscillations at elevated temperature resulted from increased surface mobility of adsorbed species, causing a change in growth mechanism to one dominated by step-flow growth.

4.3.2 GaSb Homoepitaxial Growth:

Where possible, homoepitaxy is the preferred starting point for the investigation of epitaxial growth, as it reduces the number of problems associated with epitaxial growth, for example the strain that results from a lattice mismatch, mismatch dislocations and the consideration of critical thickness. The disadvantages of GaSb substrates include the relatively high cost in comparison with GaAs identical absorption profiles resulting from homoepitaxial growth. However, since infrared characterisation of the grown films was not required, this did not present an issue. Furthermore, the choice of GaSb(001) substrates meant the growth temperature did not change throughout deposition, as occurred for InSb/GaAs heteroepitaxy, discussed in chapter 3.

4.3.2.1 Experimental:

Cleaved quarter pieces of GaSb(001) substrates (Wafertech) were outgassed at 300°$_e$C (> 60 minutes) before admission to the growth chamber, after which the oxide layer was removed by thermal desorption (530-560°$_p$C) under a stabilising Sb_2 flux (~1.6 x 10^{-6} torr).

GaSb films were deposited to a thickness of 0.4 μm at 400°$_p$C, 460°$_p$C and 500°$_p$C, at V:III ratios of 1.5, 2 and 5 at each temperature. For temperature determination at 400°$_p$C, a planarising layer was grown until the RHEED pattern indicated a flat, ordered surface. For samples grown at 500°$_p$C, pyrometer readings were taken with the Sb shutter closed momentarily (1-2s). No degradation in the diffraction pattern was observed during this time. For samples grown at temperatures < 450°$_p$C, the

temperature of each substrate and buffer layer ensemble was ramped from 460-500°$_p$C (=2°$_e$C min^{-1}) and a linear extrapolation made to a corresponding thermocouple reading, used as the setpoint applied to the Eurotherm controller for each sample.

For consistency, the oxide layer of each sample was removed under the same stabilising flux (~1.6 x 10^{-6} torr), in the temperature range 530-560°$_p$C. Post-growth cooling was conducted with a stabilising Sb flux (~1 x 10^{-6} torr). Below ca. 300°$_e$C, the antimony flux was stopped under observation by RHEED.

A temperature previously used to grow GaN_xSb_{1-x} is 350°$_p$C.[39] Three further samples were grown at this temperature, using the same method as described above. In this case, the V:III ratios used were 1.1:1, 1.5:1 and 2:1.

Samples were then transferred to the buffer chamber, prior to removal and cleaving for analysis. From the observations in chapter 3, concerning the variation of temperature over the wafer, the centre of each sample was chosen to ensure that the region of the sample characterised corresponded to the area sampled by the pyrometer. Characterisation was undertaken using C-DIC microscopy, TEM, AFM and XRD.

4.3.2.2 Results and Discussion:

As the oxide layer thinned, the RHEED showed a polycrystalline pattern which then changed to one indicative of a regular and ordered lattice structure with a (1 x 3) surface reconstruction (Figure 4.7). This reconstruction is consistent with an antimony stable surface with a lower surface concentration of Sb species than in the

5 x reconstruction discussed previously.[27] This was expected for the range of temperatures employed during oxide removal, with the supplied level of antimony flux. The absence of a transition to a reconstruction of four-fold periodicity suggested that, in each case, the antimony flux was sufficient to maintain Sb-rich conditions. Although literature reports have suggested that gallium-rich growth conditions result in the disappearance of the (1 x 3) diffraction pattern,[42] a (4 x 3) pattern was observed during RHEED intensity oscillations and has been observed elsewhere.[43]

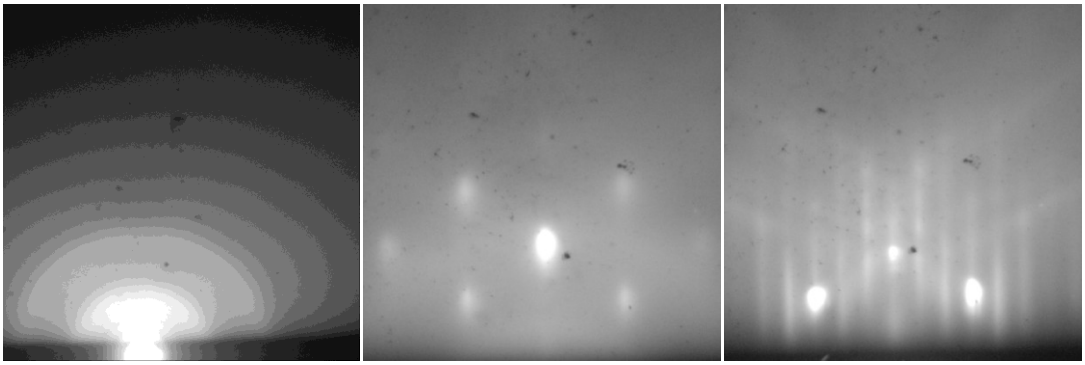

Figure 4.7: ~13 kV RHEED patterns recorded during oxide removal from a GaSb(001) wafer, under stabilising Sb flux. The semicircular halos in (a) are indicative of an over-layer that lacks lateral periodicity. Image (b) is the result of a rough surface that immediately follows thermal oxide desorption. The (1 x 3) reconstruction is clearly visible in (c), with the beam incident in the [10] direction, suggesting formation of a smoother, more ordered surface.

Cross-sectional TEM images were taken to examine the nature of the interface resulting from the homoepitaxial growth of GaSb (Figure 4.8). While RHEED observations suggested that the oxide layer had been removed, TEM analysis indicates that this was not always the case.

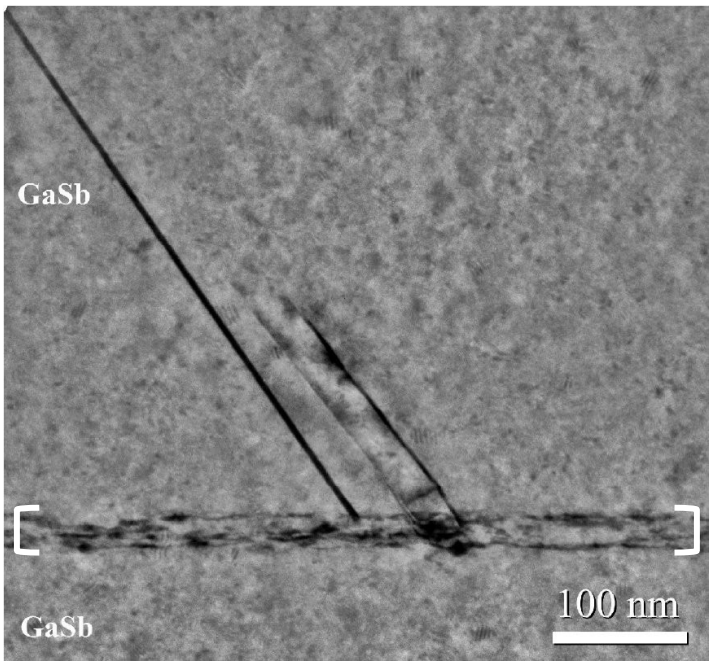

Figure 4.8: A TEM image, acquired under bright field 220 conditions. Brackets indicate the interface between substrate and epitaxial layer. Defects are observed to originate at the interface, suggesting incomplete thermal cleaning prior to growth. Dislocations are visible in both substrate and grown material, with the wafer exhibiting a relatively rough surface.

There is inherent difficulty in determining completion of oxide removal by RHEED alone; where a surface contains regions of both amorphous oxide layer and bare GaSb, reconstructions from the GaSb would be observed, but with an accompanying increase in background signal resulting from the oxide. This can be difficult to distinguish between growth runs, requiring a technique such as Auger electron spectroscopy (AES) to be used to ensure complete oxide removal. Closer examination of the TEM image (Figure 4.8) suggests the presence of dislocations in both the substrate and the epitaxially-grown material. It seems likely that these are artefacts resulting from sample preparation, however, as their density appears unchanged between the substrate and grown material.

XRD analysis of the homoepitaxial GaSb samples yielded a relatively consistent full-width at half maximum (FWHM) peak value (18-20 arc s), implying that crystal quality did not differ significantly over the parameter space investigated. This assumes that the substrate exhibited a lower FWHM value than the deposited film in each case. There were two anomalous results, however, where the peak width was approximately double that of all other samples (39.9 arc s). There was no apparent correlation with growth conditions, although some GaSb substrates have exhibited poor crystal quality during this investigation. Since, in the case of homoepitaxy, the substrate peak coincides with that of the deposited film, it was not possible to ascertain the degree to which either may contribute to peak broadening.

Samples were examined using C-DIC microscopy, revealing no definitive trend in morphology as a function of the parameters used for growth (Figure 4.9). The samples grown at 460°$_p$C were observed to exhibit anomalously rough surfaces, with an apparent improvement for the sample grown with a V:III ratio of 5:1. The sample grown at 500°$_p$C and with a V:III ratio of 2:1, and that grown at 400°$_p$C with a V:III ratio of 5:1 were both observed to have surface structures, absent from the other samples.

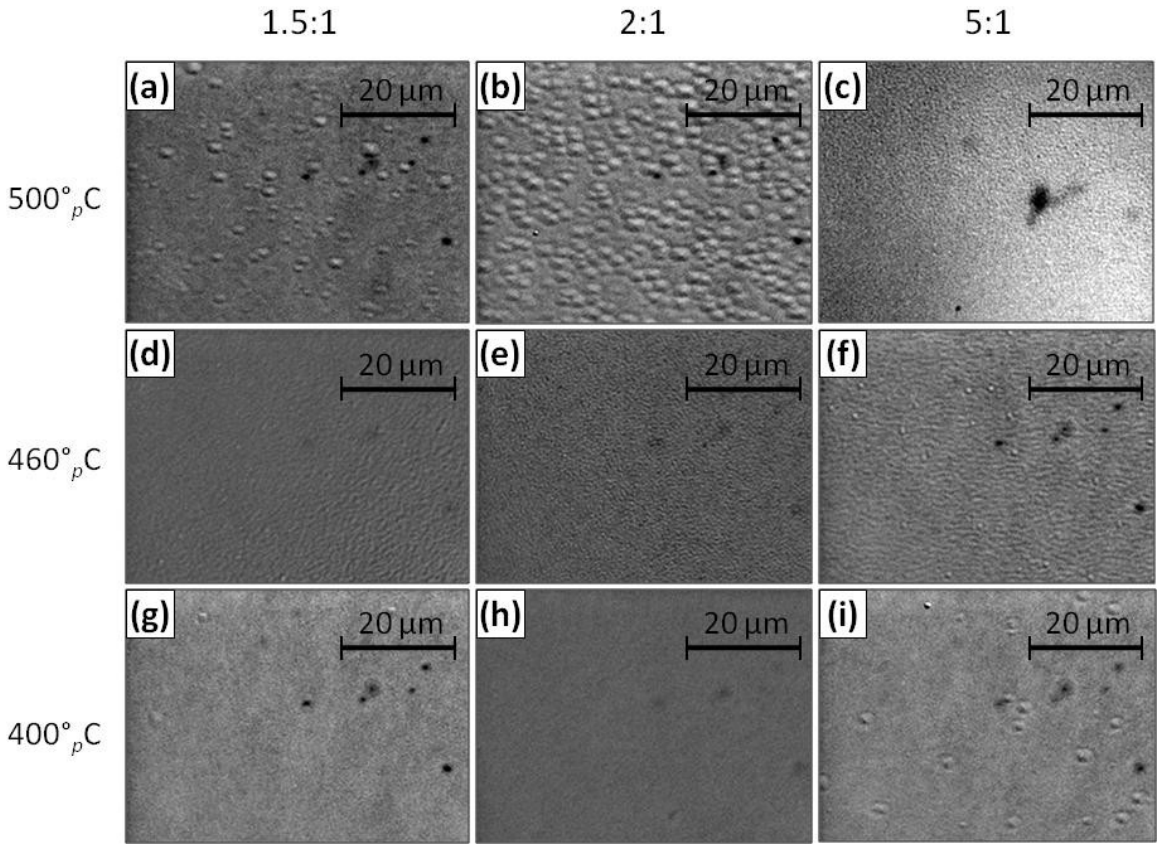

Figure 4.9: C-DIC images of GaSb samples grown at the temperatures and V:III ratios indicated. The majority of samples were observed to be relatively flat, with samples (b) and (i) exhibiting structures on the surface. Samples (d), (e) and (f) were observed to be comparatively rough.

AFM was used to assess RMS roughness and examine the surface morphology in more detail, although initial analysis was hampered by erroneous results (Figure 4.10). Initially, it was thought that the samples grown at V:III ratios of 1.5:1 and 2:1 exhibited gallium droplet formation, resulting from an insufficient antimony flux during growth. This phenomenon has previously been reported with GaSb growth.[42]

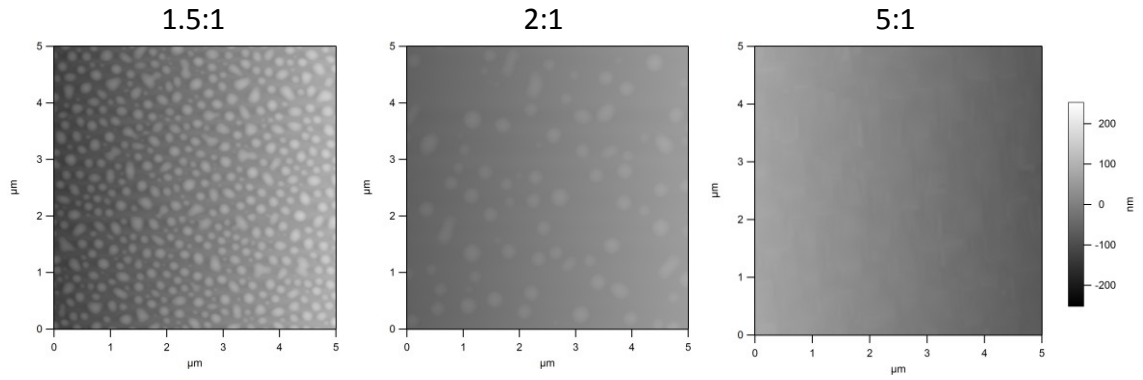

Figure 4.10: AFM topographs of samples grown at 500°$_p$C and the V:III ratios indicated. It appeared initially that gallium droplets may have formed. Re-analysis, however, determined that the round features were a condensation of volatile species from the bonding agent used to secure the samples for characterisation.

This was supported by the observed increase in droplet density with decreasing Sb flux and the droplets exhibiting a striking difference in phase to the remainder of the surface. To check this, the analysis was repeated, using previously unprepared portions of each sample.

Upon re-analysis, droplets were also observed on the sample corresponding to a V:III ratio of 5:1, implying that their origin lay not in growth, but in some aspect of sample preparation. The most likely source was the epoxy bonding agent used for substrate fixation. The apparent relationship between droplet density and V:III ratio was coincidental and the result of the order in which the samples were bonded. This had not been noted previously and no definitive cause could be found for the apparently sudden onset of the contamination. Following this discovery, epoxy was replaced by adhesive tabs (Agar). In the subsequent analyses using the adhesive tabs, these surface features were not observed, with the additional benefits that sample preparation could be completed more quickly. Subsequently, AFM characterisation of the remaining samples was undertaken (Figure 4.11).

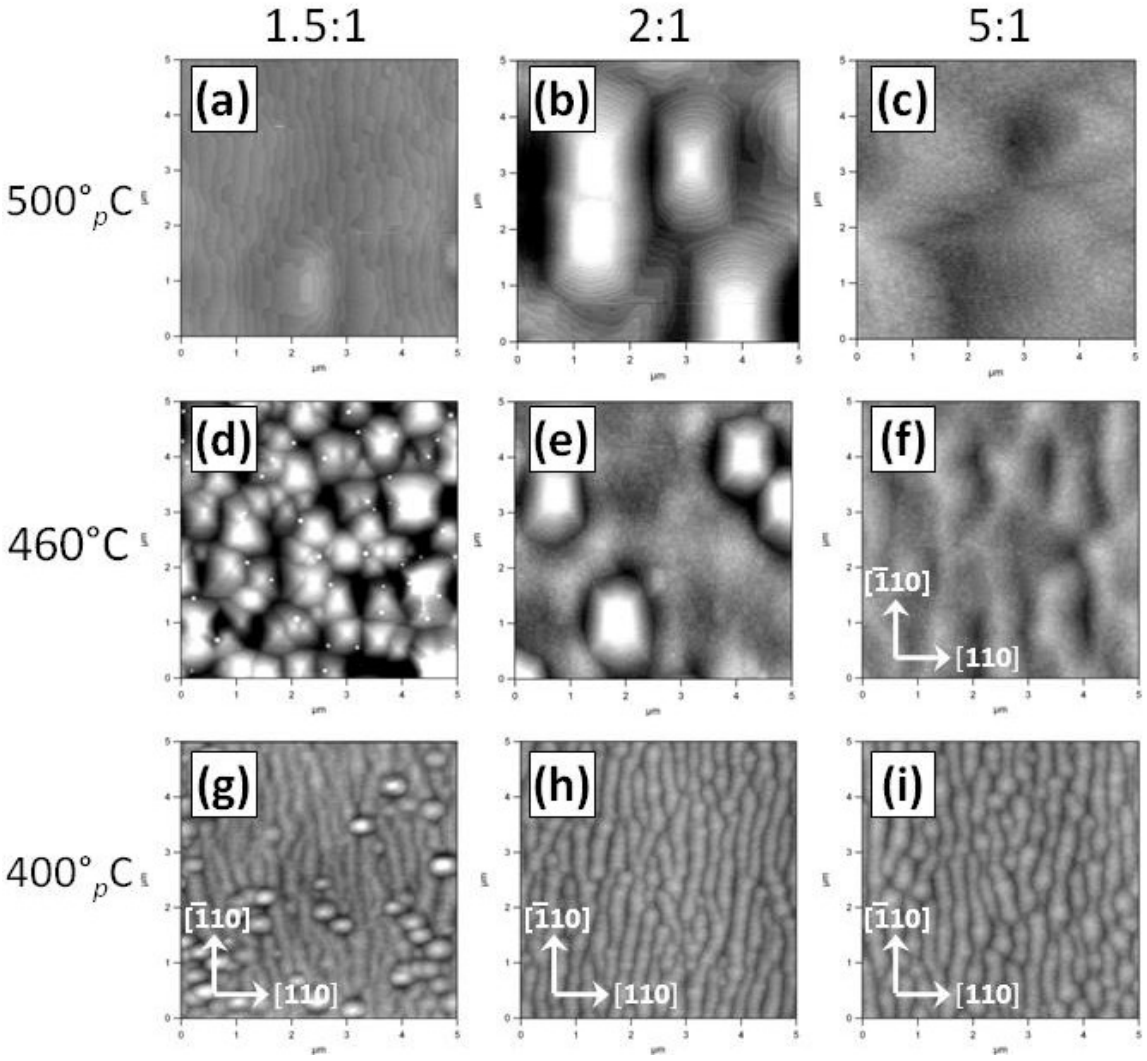

Figure 4.11: 5 µm x 5 µm AFM topographs, collected in tapping mode, of the homoepitaxial GaSb samples produced as a function of V:III ratio and growth temperature. A range of features were observed. These included a flat surface exhibiting monolayer step terraces (V:III = 1.5:1, 500°$_p$C), pyramidal structures (V:III = 2:1, 500°$_p$C) and worm-like structures (400°$_p$C). The RMS roughness values are (a) 0.24 nm, (b) 1.22nm, (c) 0.44 nm, (d) 1.68 nm, (e) 0.91 nm, (f) 0.59 nm, (g) 0.57 nm, (h) 0.43 nm and (i) 0.44 nm. The vertical height is 4 nm in all images. Surface orientation has been assigned where possible.

Examination of the RMS roughness values of the samples did not reveal a clear trend except in the case of the series grown at 460°$_p$C, where an increasing V:III ratio produced a smoother surface, with a decreasing density of mounds as the antimony flux was increased.

The morphology of the samples examined by AFM differed significantly, with the sample of best quality initially appearing to be grown at 500°$_p$C with a V:III ratio of 1.5:1. This showed a relatively flat surface with the presence of wide monolayer step terraces observed to be ~3Å in height. However, AFM analysis over a wider area indicated the presence of pyramidal structures (Figure 4.12), which were also observed under other growth conditions, as were worm-like surfaces and surfaces with a "rippled" appearance.

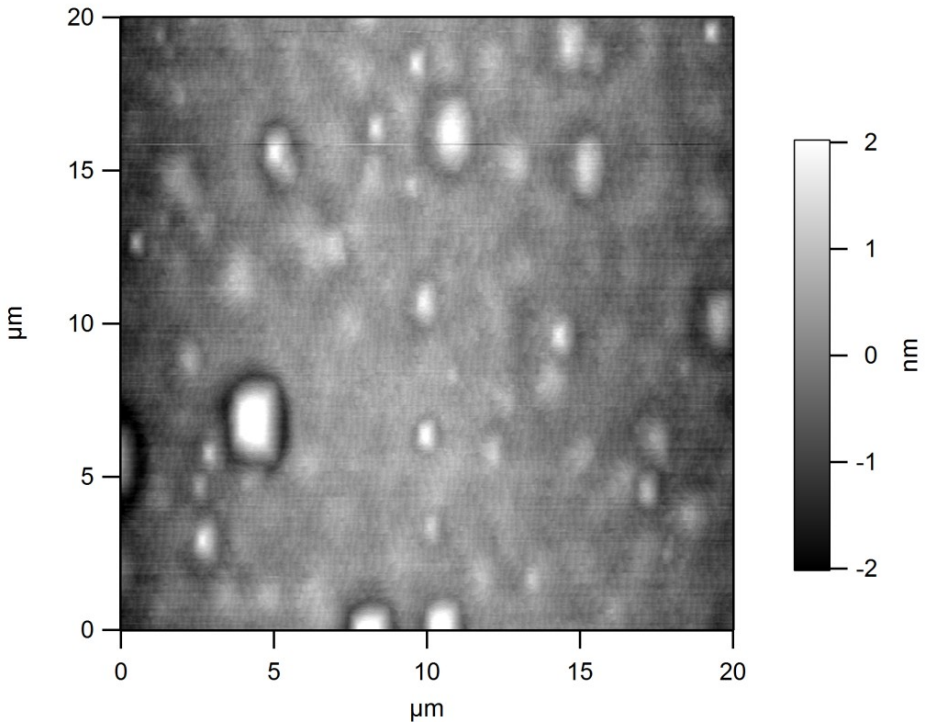

Figure 4.12: A 20µm x 20µm AFM topograph, collected in tapping mode, displaying of pyramidal structures on homoepitaxial GaSb grown at 0.5 µm h^{-1}, 500°$_p$C and a V:III ratio of 1.5:1. The density of these features was observed to be less than at higher flux ratios at the same growth temperature.

4.3.2.2.1 Pyramidal Morphology:

While strain should not be present during homoepitaxial growth, regions of residual oxide, described previously were initially considered as one possible cause of the

mounds recorded. However, closer examination revealed the lack of a spiral defect in any of the pyramidal structures observed (Figure 4.13). This suggested that they were not a manifestation of strain relief as has been observed, for example, in the case of GaSb/GaAs heteroepitaxy.[26] The pyramidal structures were observed to increase in size with increasing growth temperature, as was also seen by Nosho *et al*.[12]

Additionally, pyramidal structures have been observed in the low temperature growth of GaAs, where the underlying mechanism of their formation is reported to be polycrystalline As aggregation which forms a core from which pyramid development subsequently occurs.[45] This seems to be an unlikely cause in this case however, as the substrate temperatures were significantly higher than is required to ensure excess antimony loss from the growing surface.

Such structures may develop as a result of a limited migration of species to lower terraces, which is supported by calculations where energies of activation for step-hopping of adsorbed species are the reason for formation of pyramidal mounds in homoepitaxial growth.[44]

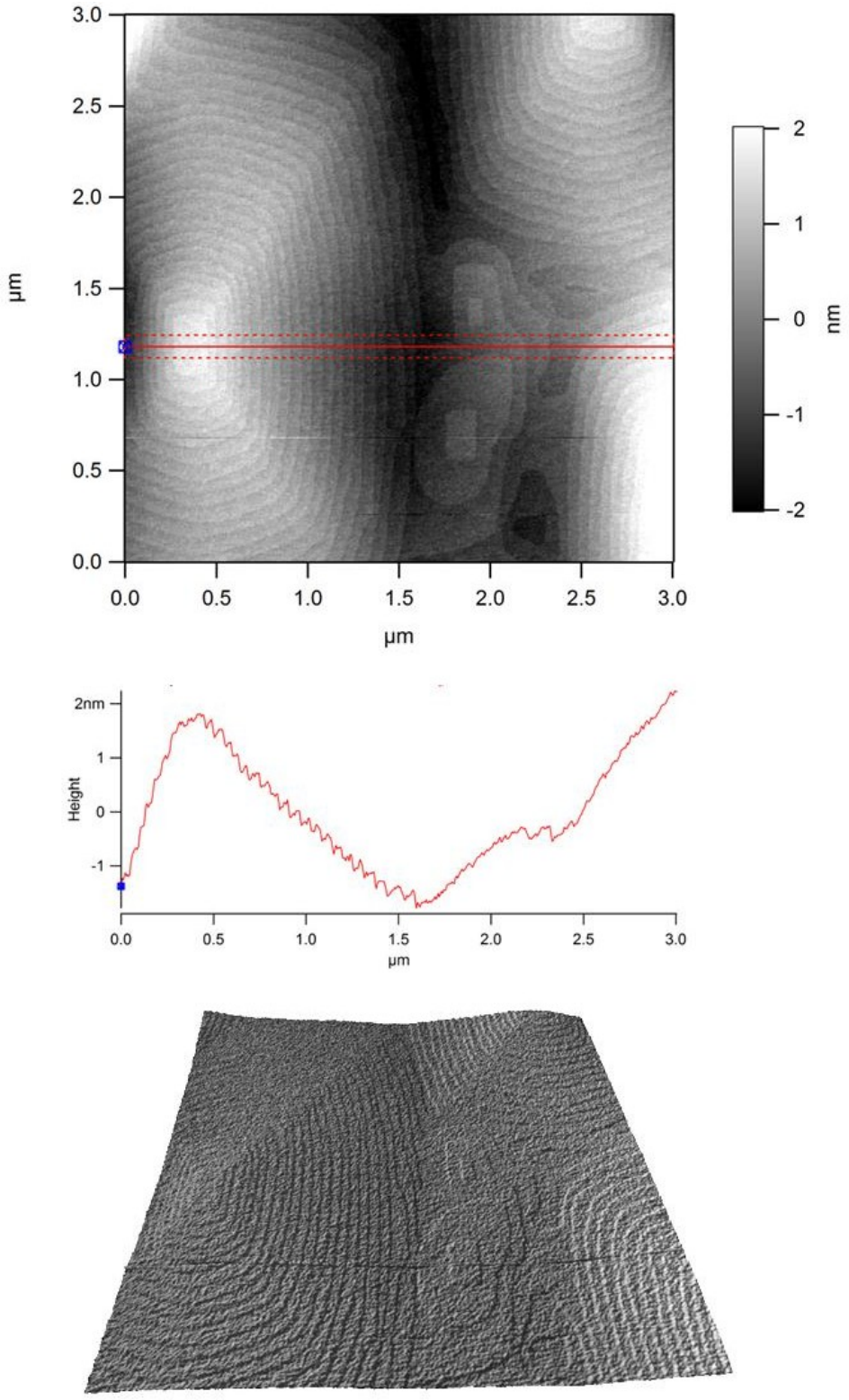

Figure 4.13: An AFM topograph indicating neighbouring pyramidal structures present on a GaSb surface grown at 0.5 µm h^{-1}, 460°$_p$C and with a V:III ratio of 2:1 (top). The data scale is 4µm. A cross-section indicates the step edges of the structure (middle). A 3D representation of the data is also shown, indicating step terraces between the structures (bottom).

In the growth temperature and flux ratio ranges studied here, the formation of pyramidal structures exhibits a strong dependence upon incident Sb flux at 460°$_p$C and 500°$_p$C, with higher antimony fluxes resulting in broader structures. However, at a V:III ratio of 5:1, their density and definition are markedly decreased. An increase of growth temperature had the effect of reducing the density of pyramids and was particularly evident in the series of samples grown at V:III ratios of 1.5:1 and 5:1.

4.3.2.2.2 Rippled Morphology:

Although rippled morphology was also observed by Nosho *et al.*, it was only recorded on vicinal substrates, with the undulating character due to an artefact of the data processing.[12] From experiments conducted in this investigation, it appears that this is not the case on flat substrates, where the rippled character is evident (Figure 4.14).

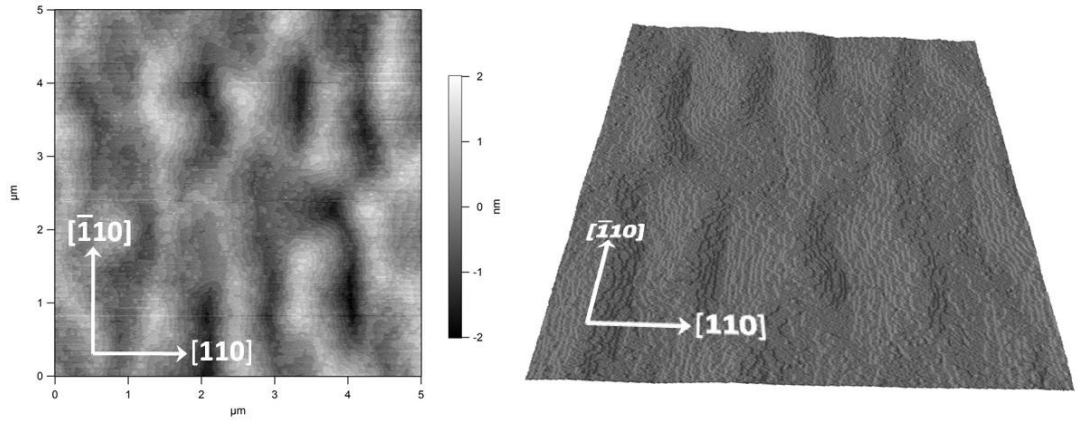

Figure 4.14: A 5 µm x 5 µm AFM topograph, collected in tapping mode, of a GaSb sample grown at 0.5 µm h^{-1}, 460°$_p$C and with a V:III ratio of 5:1 (left). Also presented for clarity is a 3D rendering of the data, in which the sample is seen to exhibit a rippled surface (right).

It is possible that this results from the coalescence of a number of broad pyramidal structures and was not observed by Nosho *et al.* for flat substrates in the flux and growth temperature regime employed in their studies. No mention is made in their paper of the method by which temperature was determined, but assuming the temperatures are similar to those determined on the GEN II, a further increase in substrate temperature will increase surface mobility, which could potentially lead to a step-flow regime. In such a situation, the majority of adatoms will no longer be confined to incorporation at the step edges of the terraces where they adsorbed. This will stop formation of pyramids and result in the formation of a more rippled surface on flat substrates. In the case of this morphology, there appears to be anisotropic broadening, although confirmation of this would require additional investigation through further growth studies.

4.3.2.2.3 Worm-like Morphology:

The worm-like structures observed in the series of samples grown at 400°$_p$C have also been reported by Nosho *et al.*[12] Referred to as exhibiting "cobblestone" morphology, these are suggested to be formed by a high density of comparatively small pyramids, with the rounded appearance resulting from the limiting lateral resolution of the AFM tip. Closer examination, however, reveals that the structures observed in this study are not rounded mounds. Rather, they extend on the order of a few microns and appear preferentially oriented along the same crystallographic direction (Figure 4.15). The measured elongation was confirmed from AFM scans conducted in different scanning directions, by rotating the sample. The scan

direction was not changed. This kept the direction corresponding to the best lateral resolution the same, while the orientation of the structures rotated in the scan view.

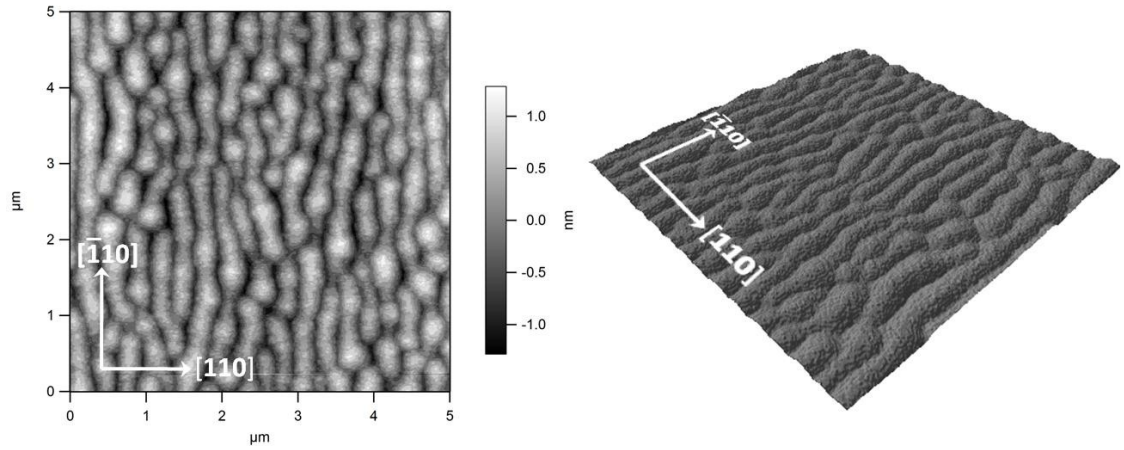

Figure 4.15: A 5 µm x 5 µm AFM topograph, collected in tapping mode, displaying the surface of a homoepitaxial GaSb sample, grown at 0.5 µm h^{-1}, 400°$_p$C and a V:III ratio of 5:1 (left). A 3D rendering of the data is also provided (right).

The AFM topographs of samples grown indicate anisotropic surface structures across the range of temperatures and flux ratios used. For the samples grown at 400°$_p$C, the orientation of the worm-like structures is evident, with anisotropy also visible in the rippled structure (460°$_p$C, V:III = 5:1) and the step edges (500°$_p$C, V:III = 1.5:1). The latter observation has been reported by Koerperick *et al.*, from annealed samples, but cause was given.[11] Surface anisotropy has been observed in the MOVPE growth of GaSb/GaAs and was thought to result from the temperature-dependent reconstruction transitions. Growth was isotropic when carried out on the symmetric (4 x 4) GaAs surface, but was anisotropic if done under conditions where the (2 x 4) or (4 x 2) were seen.[46] The suggestion that the surface reconstruction present may be the cause of the anisotropy observed here is supported by the lack of a fourfold symmetric GaSb reconstruction. Literature reporting STM measurements

of the c(4 x 4) reconstruction suggest that there is asymmetry in the physical arrangement on the surface.[47] In this case, one might still expect gallium to preferentially undergo anisotropic diffusion along the trenches between dimer rows, as theory suggests.[48]

The wide range of morphological features observed suggests that optimum conditions were not sampled in this study, but do provide a basis for two predictions. Firstly, it appears likely that the optimum growth conditions would a temperature of 500°$_p$C, with the minimum antimony flux required to maintain stoichiometric growth. The second prediction is that worm-like surface structures may be observed for growth conditions used for GaN_xSb_{1-x} growth (Tg < 450°$_p$C), where the range of V:III ratios is less important in the determination of surface morphology. XRD analysis has not revealed any correlation between the growth conditions used and the FWHM peak width.

4.3.3 Heteroepitaxial (GaSb/GaAs) Growth:

In many respects, GaAs would be preferable as a substrate, due to its relatively low cost, high quality of production and transmission in the infrared region in which the band gap of materials such as GaN_xSb_{1-x} may be observed. Furthermore, semi-insulating GaAs has a lower carrier concentration than GaSb, giving it a lower absorption profile. Aside from the issue of temperature increase during the deposition of narrow band gap material discussed in chapter 3, one of the main considerations in heteroepitaxial growth is the propagation of dislocations through the film. GaSb/GaAs has a significant lattice mismatch, and dislocations will be

formed to relieve strain in the growing film. When producing material for devices, it is important to consider defect propagation through the deposited GaSb film and its effect upon the final surface morphology and electrical properties. For this reason, careful attention must be paid to buffer layer formation.

Experimental growth was conducted in order to examine the growth of GaSb on GaAs(001) semi-insulating substrates, with a view to ascertaining any phenomena that present from the heteroepitaxial growth of GaSb.

4.3.3.1 Experimental:

Cleaved quarter pieces of GaAs(001) semi-insulating wafer (AXT) were mounted on an indium-free platen and outgassed at 400°$_e$C (> 60 mins), before admission to the growth chamber. Subsequent thermal oxide removal (560-595°$_p$C) under a stabilising antimony flux (~1.6 x 10^{-6} torr) was undertaken under RHEED observation. Following initial analysis of the results from section 4.3.2, the conditions thought to give the optimum GaSb film quality were used for growth (T_g = 500°$_p$C, V:III = 5:1, 0.5 µm h^{-1}). Samples 0.1 µm and 1.0 µm thick were grown in order to assess the effect of material thickness upon surface morphology. Following growth, the samples were cooled under a stabilising antimony flux (~1.6 x 10^{-6} torr), which was stopped when the Eurotherm controller reading reached ca. 300°$_e$C. After stopping the antimony flux, the RHEED pattern was monitored to ensure that the surface was stable.

4.3.3.2 Results and Discussion:

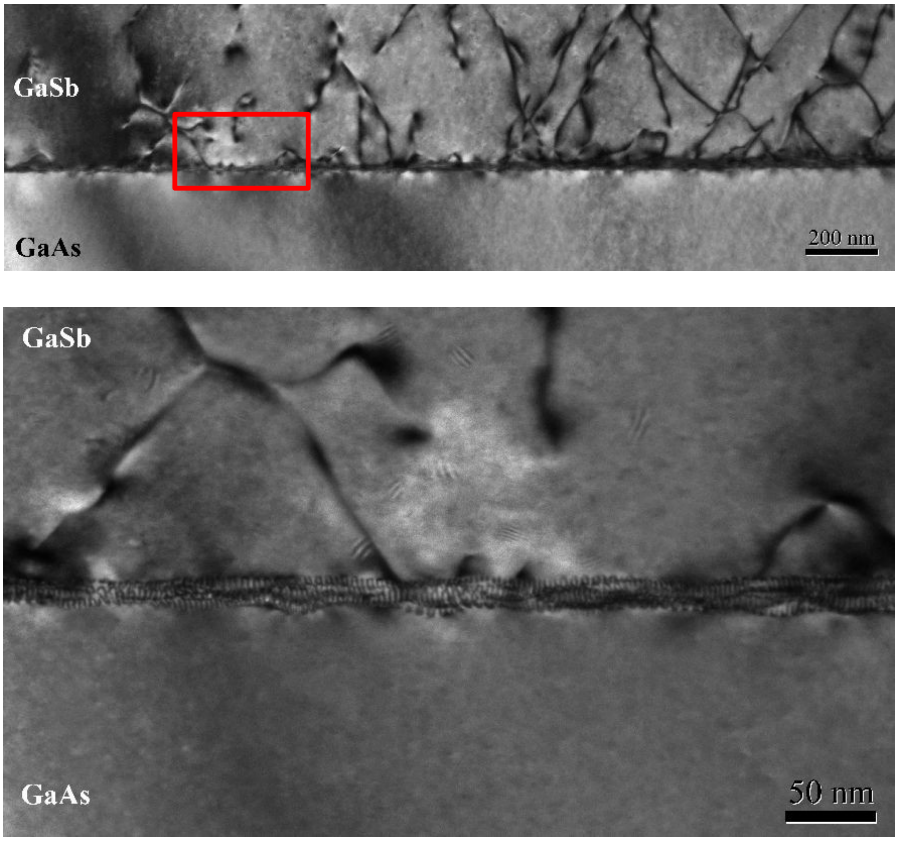

Figure 4.16: TEM images collected under bright field 220 conditions, displaying the GaSb/GaAs interface. The wider-scale view (top) clearly shows threading defects originating at the interface and propagating through the grown film. A higher magnification, indicated by the red box in the top image, indicates misfit dislocations arising from the lattice mismatch, along the rough GaAs surface (bottom).

TEM analysis of the GaSb/GaAs samples indicated a high number of threading defects propagating through the film, with evidence also of misfit dislocations at the interface (Figure 4.16). It was not possible to determine whether the interface contains a residual oxide layer, although the threading defects observed appear to originate from misfit dislocations rather than from the interface itself. Additional TEM analysis shows regions of the sample in which there are no threading dislocations (Figure 4.17). This suggests that, at these places, the strain of lattice

mismatch is accommodated in a misfit array, permitting the overgrowth of higher quality material.

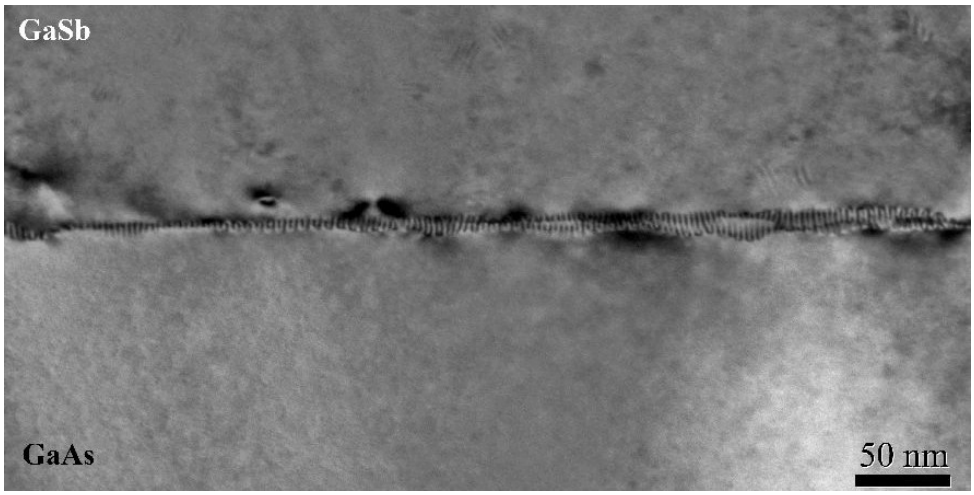

Figure 4.17: A TEM micrograph taken under bright field 220 conditions indicating the misfit dislocations present at the GaSb/GaAs interface. Of particular interest is the lack of threading defects in the region imaged, suggesting the strain resulting from lattice mismatch has been accommodated near the interface.

AFM analysis of the samples produced images demonstrating significant differences in surface morphology (Figure 4.18).

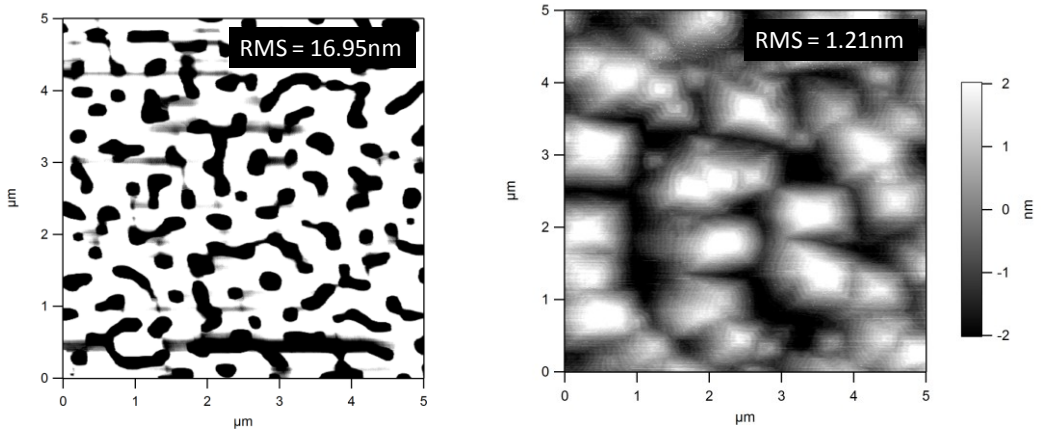

Figure 4.18: 5 µm x 5 µm AFM topographs indicating the difference in observed morphology of GaSb samples grown on GaAs(001) substrates to thicknesses of 0.1µm (left) and 1.0µm (right) at 0.5 µm h^{-1}, 500°$_p$C and with a V:III ratio of 5:1. The 0.1 µm sample indicates the coalescence of islands, consistent with growth involving a large lattice mismatch. The 1.0µm sample exhibits a number of mounds with emerging spiral defects.

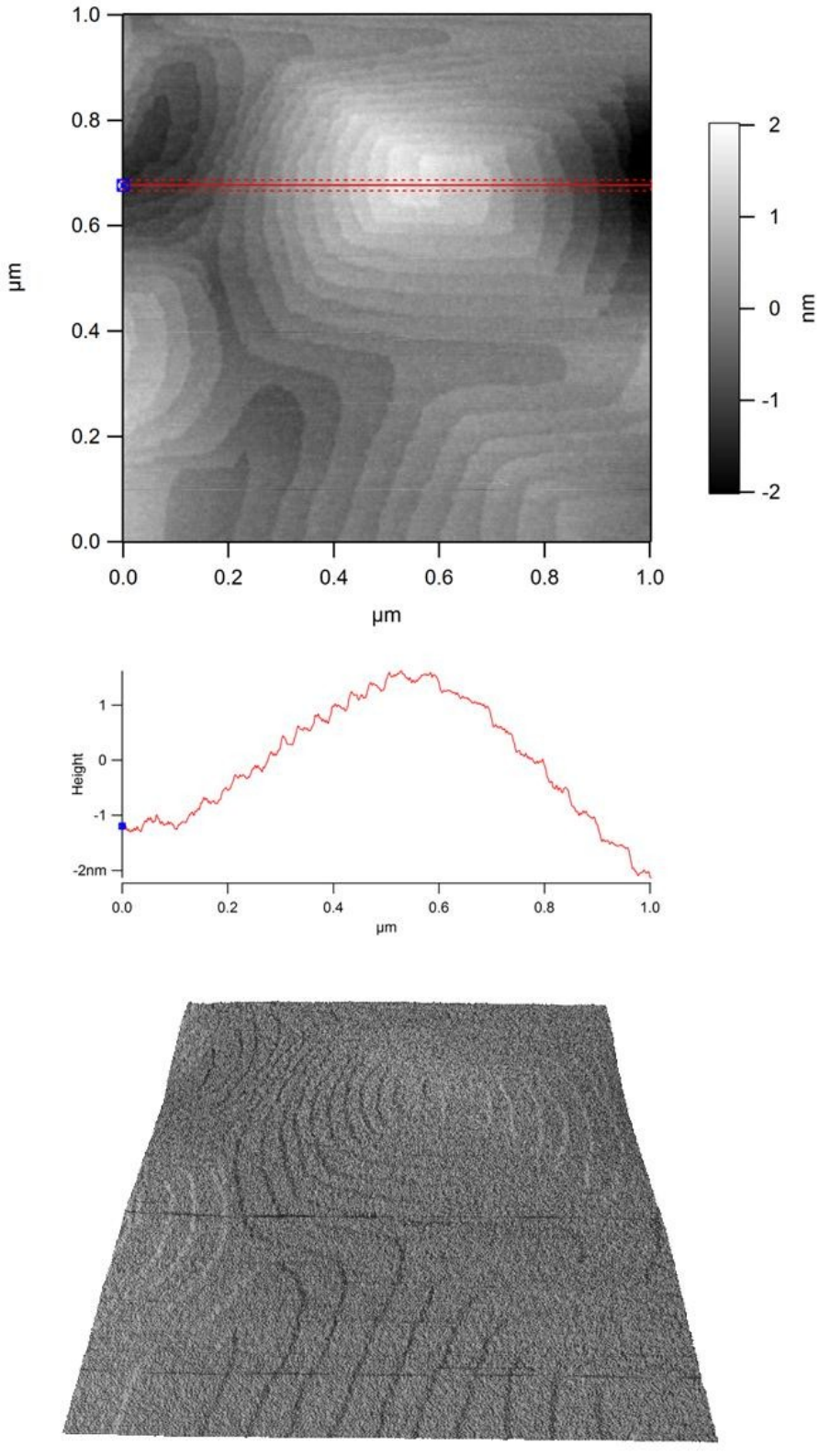

Figure 4.19: A 1 µm x 1 µm AFM topograph, collected in tapping mode, displaying the emergence of a spiral defect from a mound (top). A cross section of the topograph, indicated by the red line (middle) and a 3D rendering of the data (bottom) are also provided. Monolayer steps ca. 3 Å in height are visible.

The 0.1 μm thick sample had a significantly higher RMS roughness (16.95 nm) than that of 1.0 μm deposition (1.21 nm). The morphology in the former sample results from the coalescence of islands, formed in the early stages of growth due to the large lattice mismatch. The sample of 1.0 μm GaSb thickness demonstrates that further growth results in a smoother surface, although the emergence of spirals on the surface has been observed indicating that, even after deposition of 1.0 μm, there are defects that propagate through the grown material (Figure 4.19).

The spirals are superficially similar in appearance to the pyramidal structures observed in the homoepitaxial GaSb growth described. They are indicative of the strain resulting from the GaSb/GaAs lattice mismatch and have been reported previously from STM measurements performed following GaSb/GaAs(001) growth.[26]

Threading defects are common in heteroepitaxy and also seen in InSb/GaAs, where the threading defect density remained approximately constant after an initial decrease by approximately two orders of magnitude in the first 100-200 nm of growth.[49] This suggests that, without a complete misfit array, defects propagate through a significant buffer layer thickness (≥ 1.0 μm).

4.4 Conclusions:

From the preparatory work conducted with respect to the antimony valved source, a method has been found for establishing a relationship between the valve position and antimony BEP. The gallium and antimony sources were calibrated from observation of RHEED intensity oscillations, providing access to accurate V:III ratios from measured BEP values. Due to the lack of observed oscillations over a sufficient range of temperatures, the incorporation kinetics of antimony were not measured during this investigation. The lack of oscillations arises from a transition to step-flow growth where there is no significant change in surface roughness with time.

TEM analysis suggests that thermal oxide desorption from GaSb substrates is not complete, despite samples showing ordered RHEED patterns during cleaning. This has been observed by other researchers, resulting in the supplier from which the substrates were purchased utilising a thinner protective oxide layer than has historically been the case.[*] While the apparatus was not available during the course of this investigation, it would be desirable in the future to try H-atom cleaning, and use AES to determine the composition of the surface *in situ.*

Homoepitaxial GaSb growth has showed a range of morphological characteristics, including pyramidal, rippled and worm-like surfaces, depending on growth temperature and V:III ratio. Of the samples grown, none was observed to exhibit a completely flat surface. For the production of GaN_xSb_{1-x} films, which requires growth temperatures lower than are employed for the binary compound, worm-like morphology will occur if the growth conditions of the ternary are the same as GaSb.

[*] Private communication with Wafertech

In heteroepitaxial GaSb growth on GaAs the quality of the grown film is strongly dependent upon the thickness of deposition and, under the growth conditions used, produces a film with a large density of dislocations at the interface. These dislocations have been observed to propagate through the film and shows that the conditions used are not suited to high quality buffer layer growth. A thick GaSb buffer improves surface flatness, but removes advantages that growth upon GaAs provides, such as infrared characterisation or a low carrier concentration substrate.

There were GaSb/GaAs interfacial regions without threading dislocations. This suggests that misfit dislocations can relieve strain close to the interface, permitting growth of a defect-free GaSb layer or alloy, as has been reported for III-V heteroepitaxy.[50,51] If so, a buffer layer may not be required although, in practice, a planarising layer of some description would be required for reproducible pyrometric temperature determination.

While there is potential for the growth of buffer-free samples using an interfacial misfit (IMF) array, time constraints precluded the investigation and optimisation of this method. In consideration of this and the results of chapter 3 which showed a rise in growth temperature during (In,Ga)Sb deposition on GaAs, the results here indicate that growth of GaN_xSb_{1-x} should initially be tried using GaSb substrates, utilising a thin buffer layer to obtain a planar surface for temperature determination by pyrometry.

[1] Herbert Kroemer, Physica E **20**, 196 - 203 (2004).

[2] P.S. Dutta, H. L. Bhat, Applied Physics Reviews **81**, 5821-5870 (1997).

[3] L. M. Fraas, G. R. Girard, J. E. Avery, B. A. Arau, V. S. Sundaram, A. G. Thompson, J. M. Gee, Journal of applied Physics **66**, 3866 (1989).

[4] T. D. Veal, L. F. J. Piper, S. Jollands, B. R. Bennett, P. H. Jefferson, P. A. Thomas, C. F. McConville, B. N. Murdin, G. W. Smith, L. Buckle, Applied Physics Letters **87**, 132101 (2005).

[5] B. A. Joyce, Rep. Prog. Phys. **48**, 1637-1697 (1985).

[6] T. Ohmi, Journal of the Electrochemical Society **143**, 2957 (1996).

[7] C M Rouleau, R M Park, 4610-4613 (1993).

[8] K. M. Tracy, W. J. Mecouch, R. F. Davis, R. J. Nemanich, Journal of Applied Physics **94**, 3163 (2003).

[9] M. Kodama, A. Ryoji, M. Kimata, Japanese Journal of Applied Physics (n.d.).

[10] M. Kodama, M. Kimata, Journal of Crystal Growth **73**, 641-645 (1985).

[11] E.J. Koerperick, L.M. Murray, D.T. Norton, T.F. Boggess, J.P. Prineas, Journal of Crystal Growth **312**, 185-191 (2010).

[12] B. Nosho, Journal Of Crystal Growth **236**, 155-164 (2002).

[13] P. Thibado, Journal of Crystal Growth **175-176**, 317-322 (1997).

[14] M. Diale, D. Auret, Q. Odendaal, D. Roos, Applied Surface Science **246**, 279-289 (2005).

[15] C. Foxon and B. A. Joyce, Surface Science **50**, 434-450 (1975).

[16] A. Guillén-Cervantes, Z. Rivera-Alvarez, M. López-López, E. López-Luna, and I. Hernández-Calderón, Thin Solid Films **373**, 159-163 (2000).

[17] E. Young, S. Tixier, and T. Tiedje, Journal Of Crystal Growth **279**, 316-320 (2005).

[18] N. Jones, C. Norris, C. L. Nicklin, P. Steadman, J. S. G. Taylor, C. F. McConville, A. D. Johnson, Applied Surface Science **123**, 141–145 (1998).

[19] T. Baba, T Uemura, and M Mizuta, Journal of Crystal Growth **127**, 887–891 (1993).

[20] F. Bastiman, A. G. Cullis, Applied Surface Science **256**, 4269-4271 (2010).

[21] T. D. Veal, C. F. McConville, M. J. Lowe, Surface Science **499**, 251-260 (2002).

[22] E. S. Tok, J. H. Neave, M. R. Fahy, F. E. Allegretti, J. Zhang, T. S. Jones, B. A. Joyce, Microelectronics Journal **28**, 833–839 (1997).

[23] S. Rusponi, G. Costantini, F. Buatier de Mongeot, C. Boragno, U. Valbusa, Applied Physics Letters **75**, 3318 (1999).

[24] S. Rusponi, C. Boragno, U. Valbusa, Physical Review Letters **78**, 2795-2798 (1997).

[25] J. G. C. Labanda, S. a. Barnett, and L. Hultman, Applied Physics Letters **66**, 3114 (1995).

[26] P. M. Thibado, B. R. Bennett, M. E. Twigg, B. V. Shanabrook, L. J. Whitman, **14**, 885-889 (1996).

[27] A. S. Bracker, M. J. Yang, B. R. Bennett, J. C. Culbertson, W. J. Moore, Journal of Crystal Growth **220**, 384–392 (2000).

[28] M. Lee, Dj Nicholas, Ke Singer, B. Hamilton, Journal of Applied Physics **59**, 2895 (1985).

[29] P. M. Thibado, B. R. Bennett, Me Twigg, Journal of Vacuum **14**, 885-889 (1996).

[30] Kf Longenbach, Wi Wang, Applied Physics Letters **59**, 2427 (1991).

[31] J F Chen and A Y Cho, Journal of Applied Physics 277-281 (1991).

[32] M. Kodama and M. Kimata, Journal of Crystal Growth **73**, 641-645 (1985).

[33] Qianghua Xie, J E Van Nostrand, R L Jones, J Sizelove, D C Look, Journal of Crystal Growth **207**, 255-265 (1999).

[34] Fm Mohammedy, M Jamal Deen, Journal of Materials Science: Materials In Electronics 1039-1058 (2009).

[35] Y Rouillard, B Lambert, Y Toudic, M Baudet, M. Gauneau, Journal of Crystal Growth **156**, 30–38 (1995).

[36] Y. Rouillard, B. Jenichen, K. Ploog, C. Gerardi, C. Giannini, L. De Caro, L. Tapfer, Journal of Crystal Growth **204**, 263-269 (1999).

[37] Q. Xie, J. E. V. Nostrand, R. L. Jones, J. Sizelove, D. C. Look, Crystal Growth **207**, 255-265 (1999).

[38] L. Buckle, B. Bennett, S. Jollands, T. D. Veal, N. R. Wilson, B. Murdin, C. F. Mcconville, T. Ashley, Journal of Crystal Growth **278**, 188-192 (2005).

[39] A. Cho, Thin Solid Films **100**, 291-317 (1983).

[40] E. S. Tok, Applied Physics Letters **165**, 345 (1997).

[41] M. Lee, Dj Nicholas, K. E. Singer, B. Hamilton, Journal of Applied Physics **59**, 2895–2900 (1986).

[42] M. Yano, Journal of Crystal Growth **146**, 349-353 (1995).

[43] P. Smilauer, M. Rost, and J. Krug, Physical Review. E, Statistical Physics, Plasmas, Fluids, and Related Interdisciplinary Topics **59**, R6263-6 (1999).

[44] Z. Liliental-Weber, W. Swider, K. M. Yu, J. Kortright, F. W. Smith, A. R. Calawa, Applied Physics Letters **58**, 2153 (1991).

[45] R Graham, Journal Of Crystal Growth **145**, 363-370 (1994).

[46] A. R Avery, D. M. Holmes, J. Sudijono, T. S. Jones, B. A. Joyce, Surface Science **323**, 91-101 (1994).

[47] P. Kratzer, Progress in Surface Science **59**, 135-147 (1998).

[48] V. Ivanov, A. Boudza, N. Kutt, N. Ledentsov, S. Ruvimov, V. Shaposhnikov, S. Kop, Journal of Crystal Growth **156**, 191-205 (1995).

[49] S. H. Huang, G. Balakrishnan, a. Khoshakhlagh, a. Jallipalli, L. R. Dawson, D. L. Huffaker, Applied Physics Letters **88**, 131911 (2006).

[50] M. Mehta, G. Balakrishnan, S. Huang, A. Khoshakhlagh, A. Jallipalli, P. Patel, M. N. Kutty, L. R. Dawson, D. L. Huffaker, Applied Physics Letters **89**, 211110 (2006).

Chapter 5

"They always say time changes things, but you actually have to change them yourself."

Andy Warhol (1928 - 1987)

GaN_xSb_{1-x} samples were grown under systematically varied conditions to determine the relationship between the growth conditions and the N incorporation, as determined by HRXRD.

Changes in nitrogen mole fractions as a function of both temperature and growth rate have been established, allowing nitrogen content to be controlled during growth upon GaSb substrates.

The maximum value of nitrogen incorporation observed was 2.6%. This represents the highest reported value for substitutional nitrogen content at the time of writing.

5.1 Introduction:

The dilute nitride alloy GaN_xSb_{1-x} is of interest, due its applications in the 2-5 μm infrared range.[1,2] Nitrogen incorporation decreases the lattice spacing in a similar manner to arsenic, although its impact on the band gap is different: whereas the inclusion of other group V elements tends to increase E_g, nitrogen causes a decrease, as discussed in chapter 1. This effect has been widely observed for the addition of nitrogen to a number of III-V alloys,[3-6] and is attributed to the differences in electronegativity and atomic radius between the host lattice group V atoms and N species resulting in an interaction of nitrogen and host conduction levels

Dilute nitride antimonides offer the potential for tuneable band gap devices. Indeed, the pairing of nitrogen and antimony results in the largest mismatch in electronegativities and atomic radii amongst the group V elements commonly used for growth, suggesting a larger effect of a given quantity of substitutional nitrogen in GaN_xSb_{1-x} than the same amount of substitutional nitrogen in GaN_xAs_{1-x}, for example.[7] Of further technological interest are quaternary alloys such as $Ga_yIn_{1-y}N_xSb_{1-x}$ where indium increases lattice spacing, giving layers which are both tuneable and lattice matched to GaSb substrates.[8]

One of the most studied of the III-V-N alloys is GaN_xAs_{1-x}, where nitrogen has successfully been incorporated to produce material of both arsenic and nitrogen-rich compositions.[9-17] These can be considered as a binary solid solution mixture of GaN and GaAs. Lattice mismatch of the two compounds (c-GaN ~ 4.5 Å, GaAs = 5.65 Å) leads to a miscibility gap that prevents the production of a single phase over the full range of nitrogen composition, $0 < x < 1$.[18] This results in composition modulation and phase separation, due to the immiscibility of phases.[18,19] Since the

lattice constant for GaSb (6.093 Å) exceeds that of GaAs, it is expected that a a similar effect would occur in GaN_xSb_{1-x}.

The growth of GaN_xAs_{1-x} by PAMBE has shown that nitrogen incorporation is dependent upon growth parameters such as the rate and temperature at which growth is performed.[20,21] In preliminary research, the incorporation of nitrogen into GaSb has also been shown to depend on these factors.[2] Degradation in material quality is reported to occur with nitrogen incorporated in the GaSb lattice,[2] and the findings of chapter 4 suggest that poor GaN_xSb_{1-x} morphology may be expected if the same problems as occur with GaSb are seen.

At the start of this research, detailed studies of GaN_xSb_{1-x} were unavailable and the mode of nitrogen incorporation was unknown. Therefore, experiments were made to determine how nitrogen may be incorporated into GaSb in a reproducible and controllable manner and the results compared with available literature on GaN_xAs_{1-x}, which was thought to represent a suitable analogue.

5.2 Experimental Growth:

Growth was conducted on cleaved quarter-pieces of undoped p-type GaSb(001) wafer (Wafertech), which were outgassed at ca. 300°$_p$C (> 60 minutes) prior to admission to the growth chamber. The protective oxide layer was removed by thermal cleaning, under a stabilising antimony flux (~1.6×10^{-6} torr). A thin planarising layer of GaSb was deposited (0.5 μm h^{-1}, 500°$_p$C, Sb_2:Ga = 5:1) to allow reproducible temperature determination. Substrate temperature was measured directly by the Modline 3V pyrometer, except where the value required was below

450°$_p$C. In such cases, the temperature setpoint was established by linear extrapolation of pyrometer values in the range ca. 460 - 520°$_p$C, as a function of readings provided by the Eurotherm process controller, as described in chapter 3.

For each sample grown, active nitrogen was supplied by an r.f. plasma source (SVTA), operated at a forward power of 500 W and constant 0.2 sccm flow rate of N_2 (> 99.99999% purity). In all cases, the plasma was struck in a separate chamber, isolated from the growth chamber by a gate valve, to avoid unintentional surface nitridation prior to growth and permit the source to stabilise. Due to the large chamber pressure experienced during operation of the plasma source (> $1x10^{-5}$ torr), a turbomolecular pump was used and the ion pumps serving the growth chamber isolated. Throughout sample growth, deflection plates at the nitrogen source aperture were held at 200 V to reduce the flux of ionic species emanating from the plasma source upon the surface.[22,23]

A period of ca. 15 minutes was allowed for each sample to achieve thermal equilibrium at the target setpoint prior to growth commencing. Immediately following growth, the gallium shutter and nitrogen shutters were closed simultaneously, followed by the plasma source gate valve. This sequence was performed as quickly as possible, in order to limit the potential for plasma damage to the sample and to reduce the pressure in growth chamber, so that ion pumps could be re-engaged.

Immediately after growth, the sample was cooled, removed from the growth chamber and cleaved for analysis. As shown in chapter 3, care was taken to select a region of the wafer sampled by the pyrometer. Nitrogen content was established by

HRXRD performed on a Philips diffractometer. Characterisation of the surface morphology was undertaken using AFM. Experiments to find nitrogen content as a function of the growth conditions are described below.

5.2.1 Probing the temperature dependence of nitrogen content in GaSb:

Samples were grown at a constant rate of 0.5 μm h^{-1}, and the growth temperature systematically varied in the range 285 - 400°$_p$C. The Sb_2:Ga ratio employed was varied between 1.2:1 to 2:1 to ensure that excessive antimony sublimation was avoided.

Sb_2:Ga flux ratios were determined in terms of the limiting growth rates, as established by the RHEED intensity oscillation experiments described in chapter 4, and set at 2:1 ($T_g \geq 350°_pC$) to prevent Sb loss from the surface. For $T_g < 350°_pC$, an Sb_2:Ga ratio of 1.2:1 was employed to maintain a small excess of Sb_2 over Ga.

5.2.2 Probing the growth rate dependence of nitrogen content in GaSb:

The samples grown to establish any correlation between the growth rate and resulting nitrogen content were made at nominal growth rates in the range 0.125 – 1.6 μm h^{-1}. Growth was conducted at 325°$_p$C and 400°$_p$C to determine the effects of growth at different temperatures, based upon temperatures reported by Buckle *et al.*[2] The values selected are thought to lie within a region in which the nitrogen content is a maximum and in another region where nitrogen incorporation is decreasing rapidly with increasing temperature respectively. Using the same methodology described

above, the Sb_2:Ga ratio for the growth series were set at 1.2:1 (325°$_p$C) and 2:1 (400°$_p$C).

5.2.3 Additional Growth:

It appeared from initial XRD measurements that growth conducted at low temperatures and low growth rates resulted in films with higher nitrogen content. Tjherefore, further growth was conducted to find the maximum level of incorporated nitrogen and whether increasing the range of temperatures and flux ratios employed would result in any changes in material quality.

Limited material resources permitted only a limited number of additional samples to be grown, so sample growths were restricted to the growth rate and temperature combinations shown in table 5.1.

T_g [°$_p$C]	Growth Rate [μm h^{-1}]	Sb_2:Ga Ratio
275	0.5	1.2:1
310	0.5	1.2:1
300	0.125	1.2:1

Table 5.1: A table of the growth parameters used for the production of additional GaN_xSb_{1-x} films.

These samples were grown and prepared in the same manner as described previously.

5.3 Results and discussion:

From initial examination of the grown samples by C-DIC microscopy, largely flat surfaces were observed, revealing no trend in morphology as a function of growth parameters.

For the samples grown, analysis indicated that the concentration of incorporated nitrogen varied over the range of parameters sampled. The maximum value obtained in these experiments was measured by HRXRD to be 2.6% which, at the time of writing, represents the highest reported substitutional nitrogen incorporation into GaSb. For the majority of samples, AFM analysis revealed worm-like structures that are aligned preferentially along the direction, in common with GaSb growth described in chapter 4 (Figure 5.1).

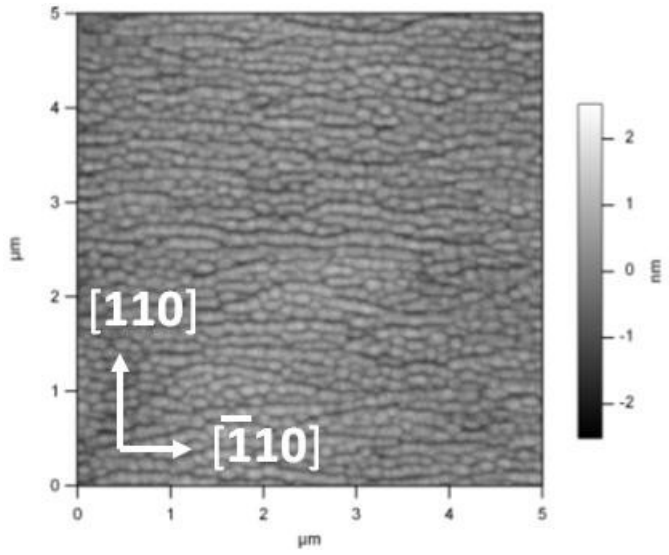

Figure 5.1: An AFM topograph of a $GaN_{0.0132}Sb_{0.968}$ sample, grown at 0.5µm h^{-1}, Sb_2:Ga = 1.2:1 and T_g = 350°$_p$C. The worm-like structures can be seen to extend from left to right, along the direction.

Similar aligned features have previously been observed in the MOMBE growth of GaNAs, with the formation of faceted surfaces along "wire-like" structures. Suemune *et al.* have attributed this as being due to strain relief due to compositional modulation,[24] but in chapter 4 the same morphology was observed in the growth of GaSb below 450°$_p$C where it is a feature of the binary compound, when grown at low temperatures.

As discussed in chapter 4, a small number of GaN_xSb_{1-x} samples exhibited some antimony capping or gallium droplet formation (Figure 5.2). The former is thought to arise when the Sb_2 supply is terminated too late during post-growth cooling, in agreement with the conclusions of Koerperick *et al*.[25] The difficulty in determining this point is attributed to the uncertainty in substrate temperature during cooling. Although this has hindered AFM analysis of a minority of samples, it does not have any effect upon the nitrogen content in the bulk.

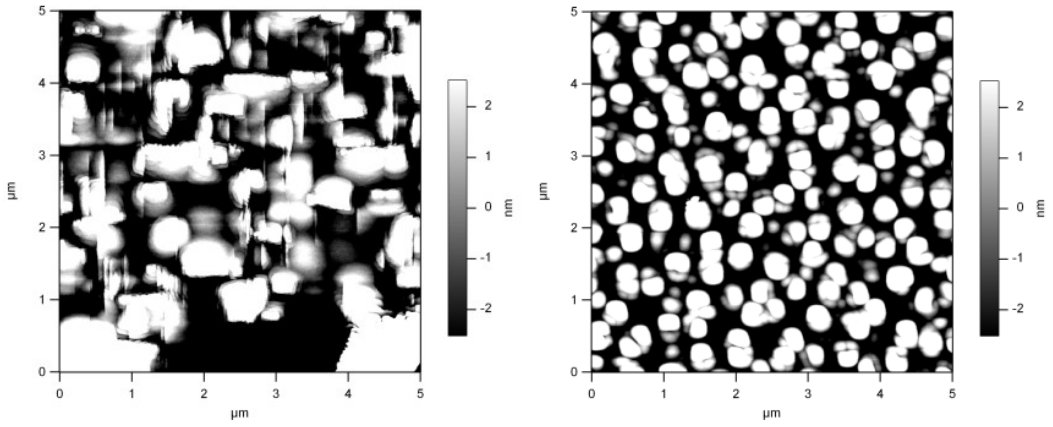

Figure 5.2: Left: An AFM topograph of a surface showing an accumulation of antimony.[25] The most likely cause is the supply of antimony below the temperature at which Sb capping commences. Right: Where antimony flux was removed in a temperature regime in which significant desorption occurs, gallium droplets are observed to form. While both situations are detrimental to the quality of the uppermost part of the layer, this has no bearing on the bulk nitrogen content.

This illustrates that, while AFM provides a useful insight into the final surface quality, it may not be relied upon as an indication of the underlying crystal quality.

In order to determine the stability of growth parameters, a GaN_xSb_{1-x} film grown on GaSb(001) was submitted for SIMS analysis. The results revealed a uniform level of nitrogen throughout the grown layer (Figure 5.3).

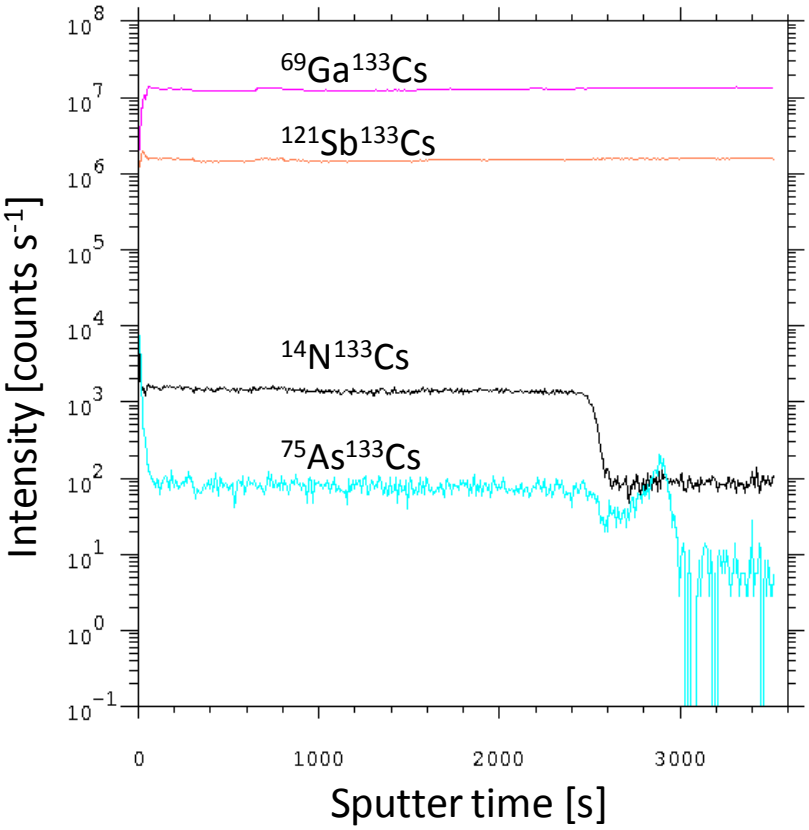

Figure 5.3: A SIMS profile of $GaN_{0.0036}Sb_{0.9964}$, grown on GaSb(001) with a 100 nm GaSb buffer layer. The uniformity of the nitrogen signal throughout the grown layer indicates that no significant changes to growth conditions occurred during material deposition. The peak resulting from arsenic is thought to originate from inadvertent contamination, resulting from residual arsenic background pressure in the growth chamber.

The variation in temperature across the substrate observed in chapter 3 was found to result in antimony condensation close to the edges of the wafer for some samples grown. This appeared as a milky haze near the edges of the sample that gave way to

a mirror-like finish in the centre of the wafer. The characteristics observed bear striking similarity to thermal images reported by Jackson *et al.* for cleaved quarter-pieces of p-type GaAs wafer.[26]

To assess the uniformity of nitrogen content in the plane of the wafer, spatially-resolved XRD studies were conducted on a sample exhibiting the behaviour described above. Rocking curve measurements were performed with the beam incident upon different points of the sample, along the diagonal joining the edge and centre of the sample (Figure 5.4). The results indicated that the nitrogen content was affected, with a step decrease occurring within a distance of < 1mm (Figure 5.5). This demonstrates that, under certain conditions, antimony can prevent nitrogen uptake in the growing film. However, the results also show that nitrogen content is uniform across the majority of the wafer.

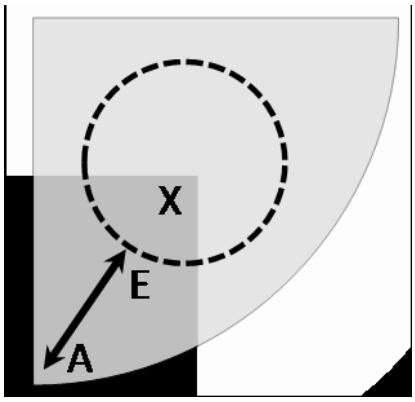

Figure 5.4: A schematic demonstrating the method by which the spatially-resolved XRD investigation was conducted upon the cleaved quarter wafer. The sample had a dull, milky finish at the edges, with a mirror-like surface in the centre. The region denoted by the dotted circle indicates the approximate region sampled by the pyrometer. The point marked "X" approximately denotes the preferred area for analysis.

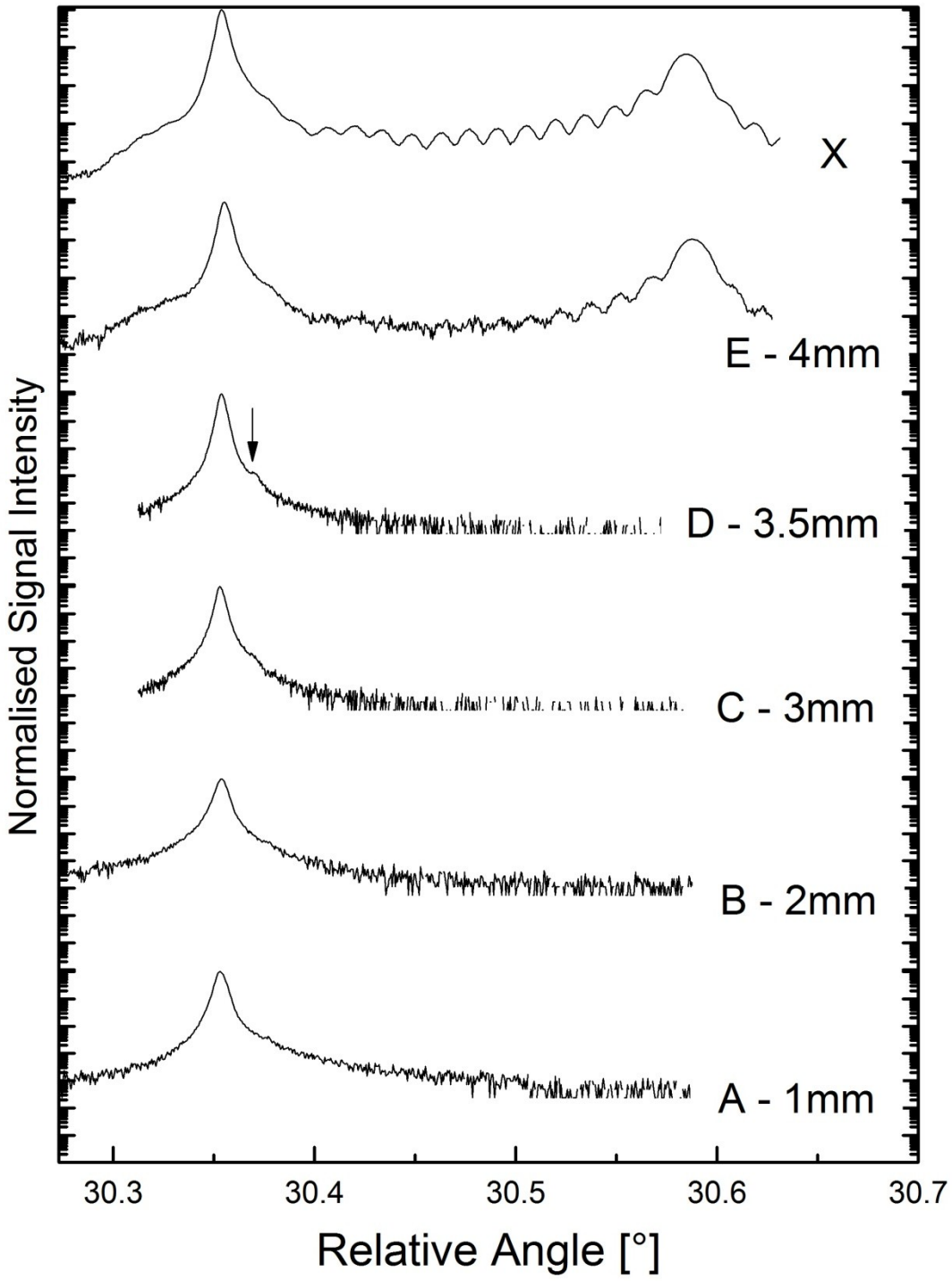

Figure 5.5: A plot of XRD rocking curves taken from the same sample, at the labelled distances along the line AE, as shown in Figure 5.4. The peak centred at ca. 30.35° is the substrate peak in each instance. A possible shoulder (indicated by an arrow) was recorded in the scan corresponding to the point D, suggesting a small degree of nitrogen incorporation. The nitrogen content recorded at point E is in agreement with the value recorded from the centre of the quarter wafer (X), implying good uniformity of nitrogen content in the central region of the sample.

Lack of available time on the diffractometer meant that it was not possible to conduct this type of measurement on other samples, although it is believed that these results are consistent with the findings of chapter 3. Since measurements were routinely conducted on a region corresponding to the centre of the grown sample, it is unlikely that any of the XRD measurements conducted would have been affected by this effect.

5.3.1 Nitrogen content as a function of growth temperature:

The incorporation of nitrogen depended on growth temperature, as has been reported for GaN_xAs_{1-x},[21,27]. An initial plateau at low growth temperature leads, with increasing temperature, to a sharp decline in the quantity of nitrogen incorporated into the film (Figure 5.6). In GaN_xAs_{1-x}, this is attributed to a decrease in nitrogen incorporation factor by Odnoblyudov *et al*.[20] The observations for GaN_xSb_{1-x} are qualitatively similar to GaN_xAs_{1-x}, suggesting that the incorporation of active nitrogen species does not differ significantly with temperature between GaAs and GaSb alloys.

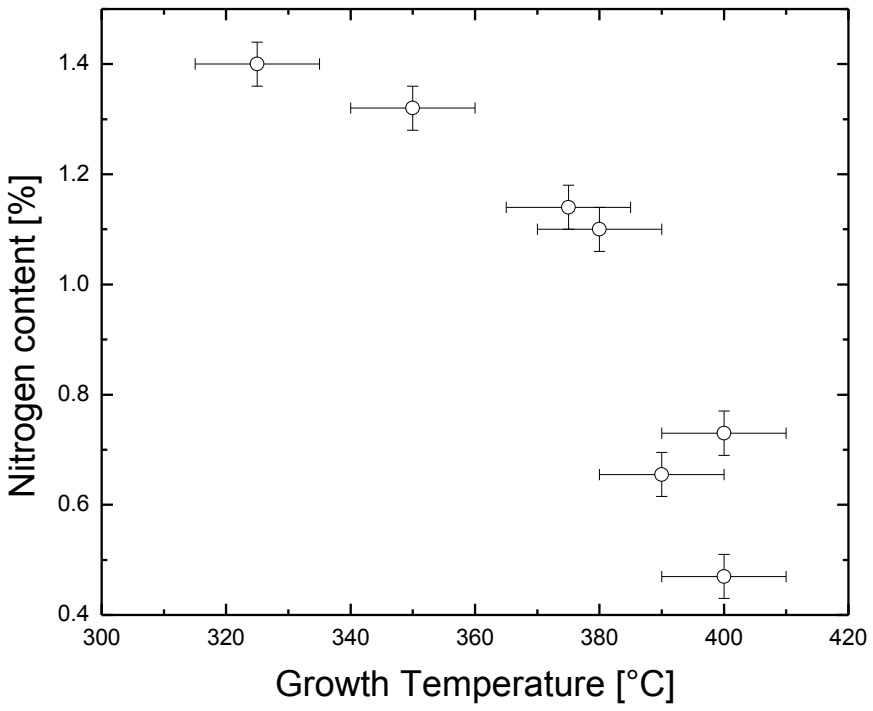

Figure 5.6: A graph depicting the nitrogen content, as determined by XRD, and the growth temperature. The upper bounds of uncertainty in T_g is thought to be ± 10°$_p$C, and 0.04% for the nitrogen content. The data demonstrate a trend consistent with calculations and experimental results detailed in the literature.[20,21]

The slight deviation in the correlation between nitrogen content and substrate temperature data in the region where a decrease in N incorporation was recorded is within the error of temperature measurement. In this region, a difference between real and measured growth temperature would have a larger effect on the incorporated nitrogen than on the plateau, where the nitrogen concentration differs only slightly across a comparatively large range of temperatures.

AFM analysis conducted on samples indicated droplet-like features for the sample grown at 310°$_p$C, with the worm-like morphology dominating at 325°$_p$C (Figure 5.7).

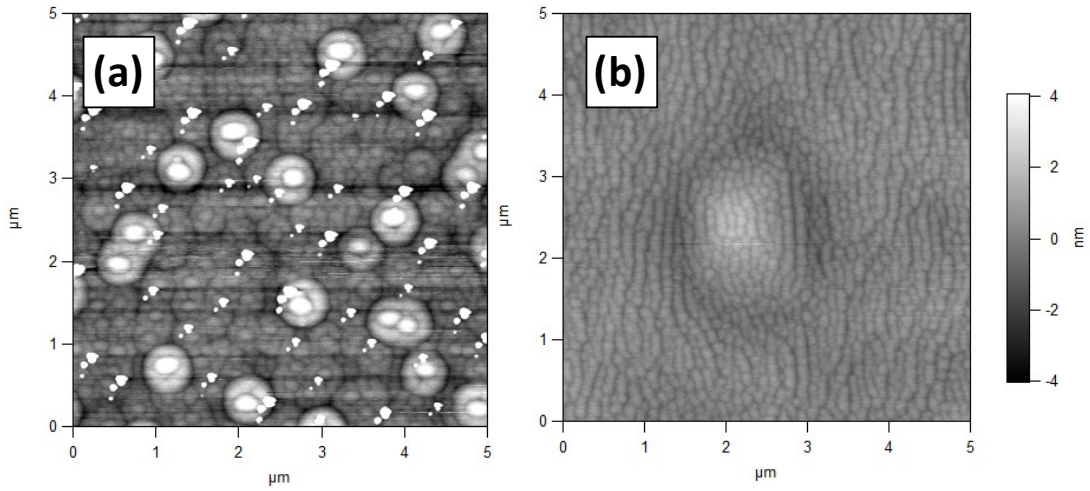

Figure 5.7: 5 µm x 5 µm AFM topographs displaying the surface morphology of samples grown at (a) 310°$_p$C and (b) 325°$_p$C, the nitrogen contents of which are shown in Figure 5.6. Droplet-like morphology was observed replaced by a surface dominated by worm-like surface structure with the increase in growth temperature.

This is a large change in morphology over a growth temperature range of only 15°$_p$C, implying that the onset of material degradation as a function of decreasing temperature occurs abruptly.

5.3.2 Nitrogen content as a function of growth rate:

The growth rate dependence of dilute nitride materials has been the subject of few publications. Where a trend has been established, it is generally considered that N incorporation is inversely proportional to the growth rate employed,[3,15] although results have been published that suggest the nitrogen content in GaN_xSb_{1-x} increases as a function of growth rate.[2] From the data gathered in this study, it can be seen that the inverse growth rate dependence is found in GaN_xSb_{1-x}, before levelling off at sufficiently low growth rates (Figure 5.8).

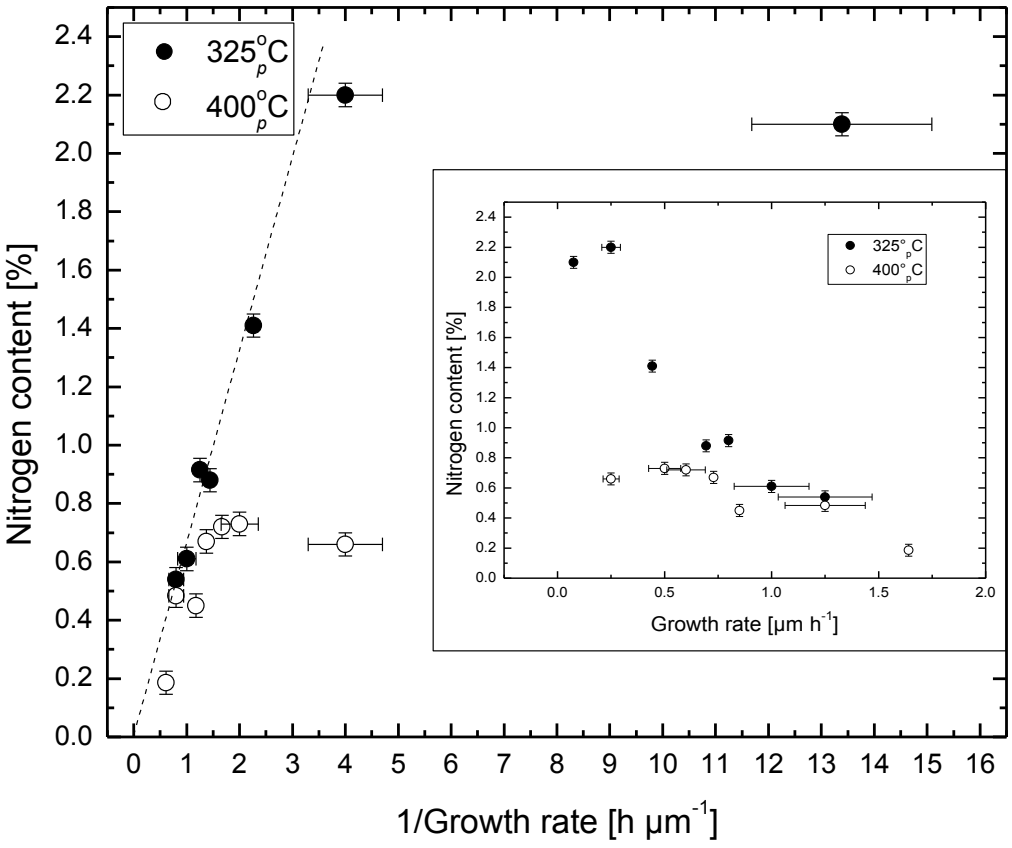

Figure 5.8: There was initially observed to be an inverse dependency of nitrogen content on growth rate. The point at which the nitrogen content deviates from this behaviour increases as a function of decreasing temperature. Uncertainties, representing the largest measured deviation from the nominal growth rate, have been applied to those data for which thickness measurements were not available.

Interestingly, a similar observation has been reported by Odnoblyudov *et al.* in relation to the nitrogen flow rate employed for growth. Here a limit of incorporation is reached after an initial increase as a function of increasing nitrogen flux.[19]

In GaNAs, particularly low growth rates (~0.125 μm h^{-1}) appear to have been largely unexplored. One of the challenges present in using very low growth rates is in obtaining constant antimony fluxes, due to the inherent instability in the valve of the antimony source. While a drift over the course of growth in the order of 10^{-7} torr is relatively insignificant at high growth rates, where the required antimony flux is large, at low growth rates the effect on the Sb_2:Ga ratio is large. As a result,

consistent growth at rates of 0.125 µm h^{-1} and below was not accessible in this investigation. As described previously, due to the construction of the equipment, it was not possible to monitor the beam equivalent pressure during sample growth.

AFM analysis of the samples on the plateaux displayed in Figure 5.8 indicate that the droplet features that were absent in the sample grown at 325°$_p$C and 0.5µm h^{-1} were observed upon a reduction of growth rate to 0.25 µm h^{-1} under otherwise nominally identical growth conditions (Figure 5.9). The sample grown at 0.25 µm h^{-1}, 400°$_p$C and with a Sb_2:Ga ratio of 2:1 did not exhibit these features. Considering the temperature dependence of these features (Figure 5.7), it is unlikely that the difference in Sb_2:Ga ratio is the primary cause in this instance.

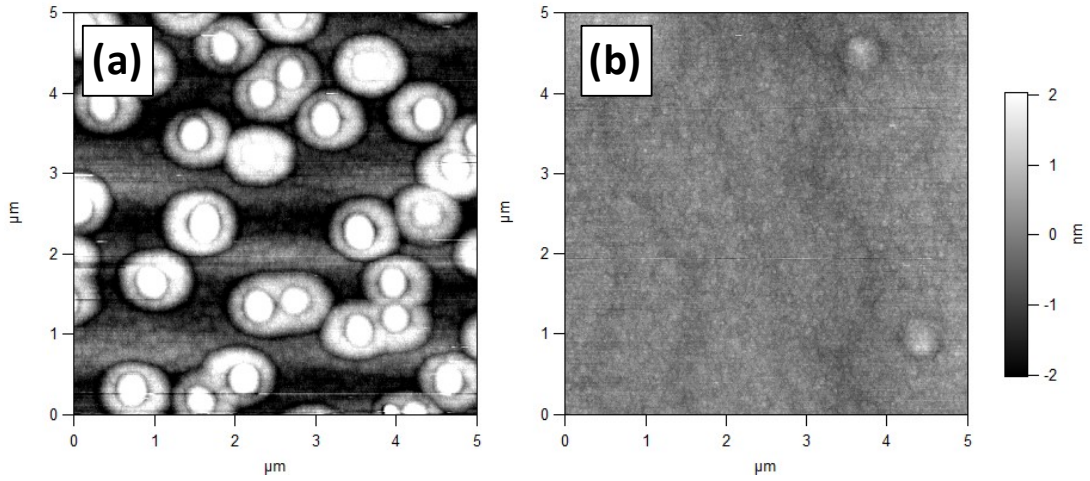

Figure 5.9: 5µm x 5µm AFM topographs of two samples grown at (a) 325°$_p$C and (b) 400°$_p$C, 0.25µm h^{-1} and Sb_2:Ga ratio of (a) 1.2:1 and (b) 2:1. The droplet features that were observed to be absent in Figure 5.7b appear to have presented due to a reduction in growth rate.

As discussed previously, SIMS and XRD analysis of GaN_xAs_{1-x} have shown different degree of nitrogen content in the same sample, due to the species to which each method is sensitive. While the plateaus for substitutional nitrogen content

observed as a function of growth rate are consistent with the observations of Zhao *et al.* for GaN_xAs_{1-x}, SIMS shows an inversely proportional increase in total nitrogen content to a level higher than that for substitutional nitrogen.[28]

5.3.3 Additional Growth:

Analysis of the additional samples grown indicated that nitrogen had been incorporated in each of the films. Of these, the highest nitrogen substitutional content (2.6%) resulted from growth at 300°$_p$C, 0.125 µm h^{-1} and an Sb_2:Ga ratio of 1.2:1 (Figure 5.10).

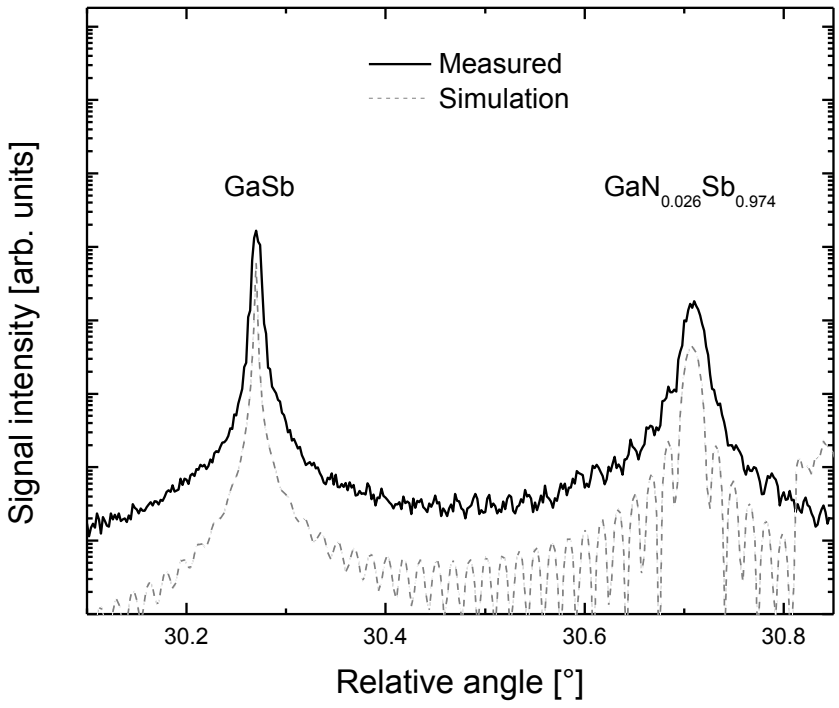

Figure 5.10: An XRD 004 rocking curve depicting the difference in diffraction maxima between the GaSb substrate and the $GaN_{0.026}Sb_{0.974}$ film, resulting from growth at 300°$_p$C, 0.125µm h^{-1} and an Sb_2:Ga ratio of 1.2:1.

This supports the findings that reduced temperature and lower growth rates allow a higher degree of substitutional nitrogen incorporation. Furthermore, it shows that there is no detrimental effect upon nitrogen content of reducing both parameters simultaneously. Such a level of nitrogen incorporation into GaSb has not previously been reported.

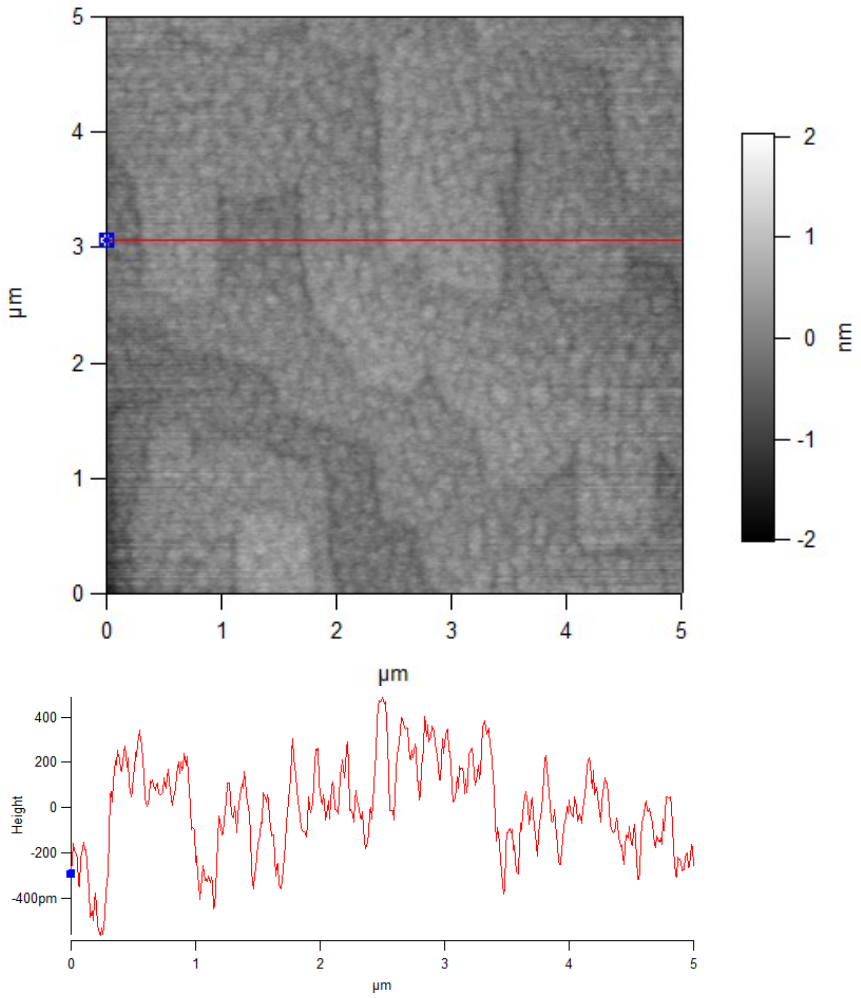

Figure 5.11: A 5 µm x 5 µm AFM topograph and corresponding cross-section of the sample grown at 0.125µm h^{-1}, 300°$_p$C and with Sb_2:Ga = 1.2:1. From the cross section, the plate structures appear to be two monolayers high.

AFM analysis indicated that the surface morphology is similar to other low temperature GaSb and GaN_xSb_{1-x} samples grown, with remnants of worm-like

character persisting (Figure 5.11). Plate-like structures were observed, although like the sample grown at 0.125 µm h^{-1} and T_g = 325°$_p$C, the droplet structures observed for samples grown at 0.25 µm h^{-1} (Figure 5.9) were absent. The RMS roughness was determined to be 0.226 nm.

It may be the case that the droplets have not formed, as a result of the lower growth rate, permitting more uniform growth.

The samples grown to explore further the temperature dependence of nitrogen content showed particularly interesting results, with a decrease in nitrogen content measured by XRD with decreasing temperature (Figure 5.12).

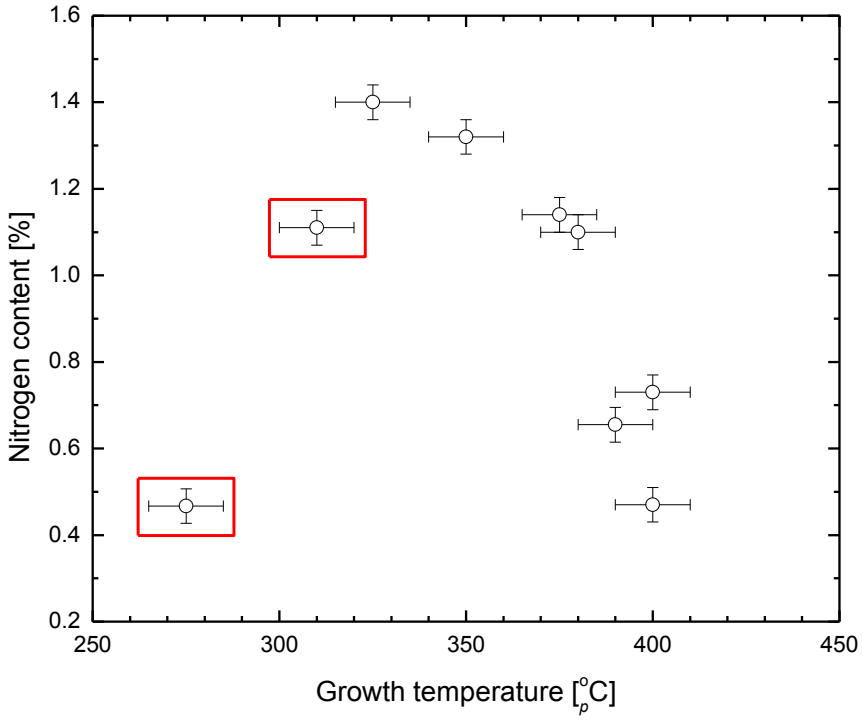

Figure 5.12: The samples grown to further probe the effect of growth temperature upon nitrogen content are enclosed in red. While the nitrogen content values were expected to lie on a plateau (~1.4%), there was found to be a marked decrease.

Samples grown at the lowest temperatures have a nitrogen content that is smaller than would be expected, according to the model proposed by Odnoblyudov *et al*. Possibly, nitrogen incorporated at very low temperatures is interstitial, rather than substitutional. At low temperatures, one would expect a decrease in the nitrogen content measured by XRD and could be attributed to a lower surface mobility of N and Ga species upon the surface. AFM analyses of the samples grown at 275°$_p$C and 310°$_p$C indicate the presence of surface features consistent with gallium droplets.[29] This suggests that the surface mobility of antimony at this temperature was too low to achieve optimum growth (Figure 5.13).[30,31]

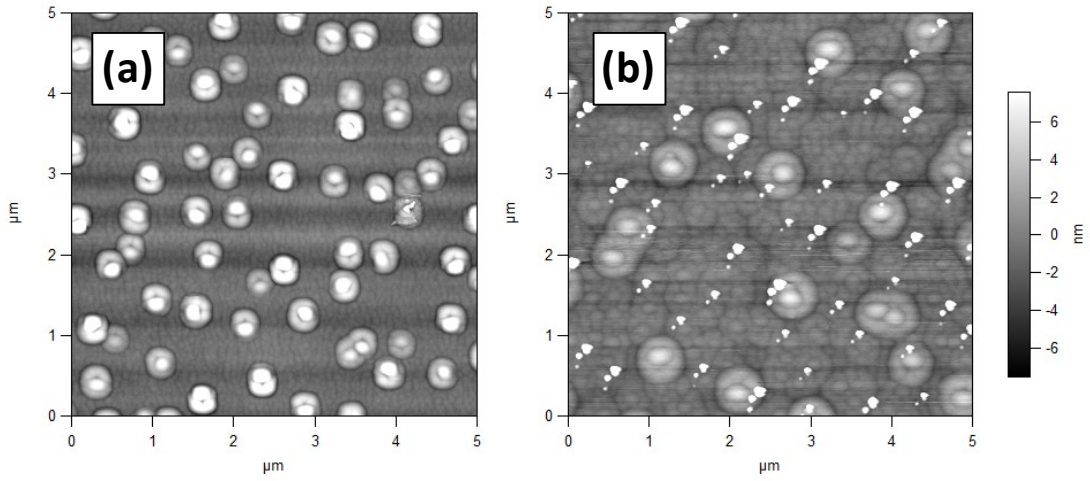

Figure 5.13: 5 µm x 5 µm AFM topographs, depicting the surface morphology of samples grown at 0.5µm h^{-1}, Sb_2:Ga ratio of 1.2:1 and (a) 275°$_p$C (b) 310°$_p$C. The surface between the droplet features of (a) was observed to have a worm-like morphology, consistent with observations for the low temperature growth of GaSb. The surface of (b) demonstrates a lower density of comparatively larger droplet features.

This agrees partially with measurements made using TEM. In the case of the sample grown at 275°$_p$C, degradation of material quality coincides with a decrease in nitrogen content. TEM analysis shows a rough surface (Figure 5.14), as well as voids and threading defects in the grown material (Figure 5.15).

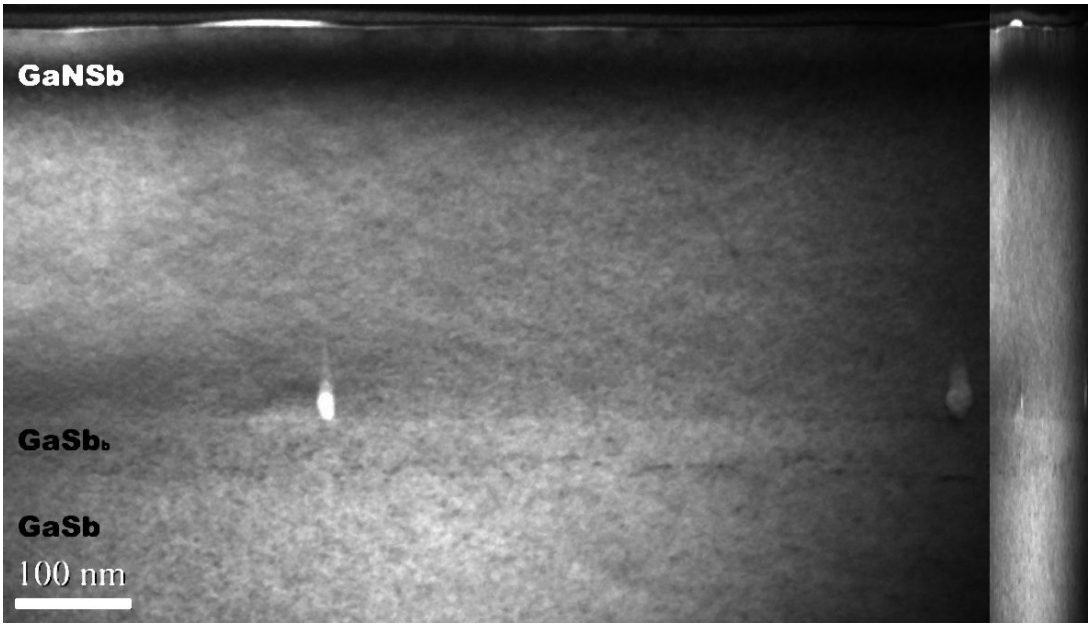

Figure 5.14: A cross-sectional TEM micrograph, taken under 002 dark field conditions, of the $GaN_{0.00467}Sb_{0.99533}$ sample grown at 0.5 µm h^{-1}, 275°$_p$C and Sb_2:Ga ratio of 1.2:1. While the interface between the substrate and buffer layer is clean, suggesting effective oxide removal, the digitally compressed image to the right demonstrates a rough and relatively inhomogeneous surface.

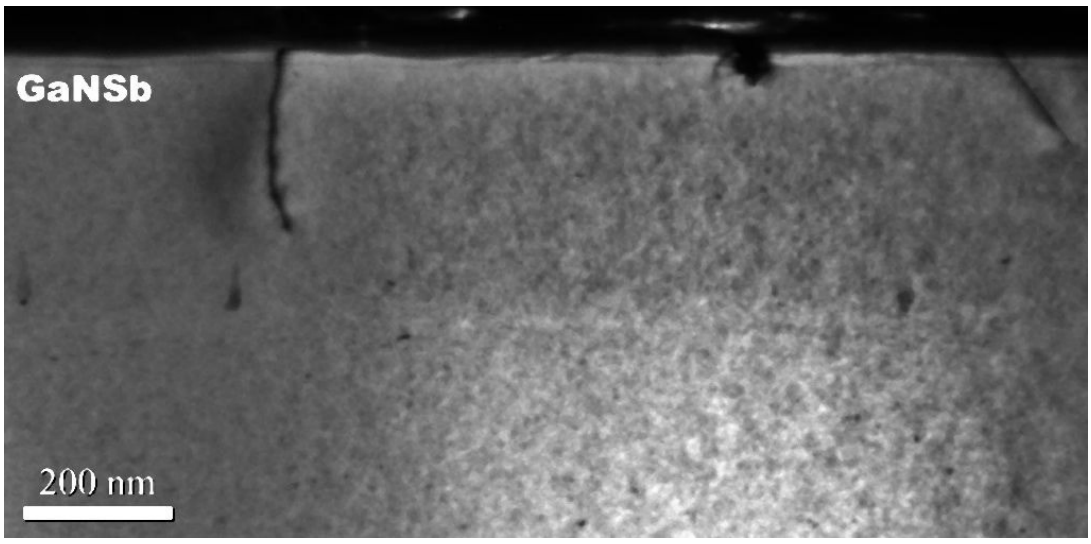

Figure 5.15: A cross-sectional TEM micrograph, taken under 220 bright field conditions, of the same sample as imaged in Figure 5.14. Significant morphological defects were observed, as well as the "tear-drop" defects near the GaNSb/GaSb interface.

These defects were absent in TEM analysis of the sample grown at 310°$_p$C, suggesting that the lower limit for good quality growth lies in the range 275-310°$_p$C and that a decrease in substitutional nitrogen content may be noted before the observation of reduced material quality by TEM.

However, an alternative explanation may be found in equipment malfunction. The thickness measurements determined by HRXRD, which were approximately -25% from the target value, indicated a problem with a material source. If the Ga source had been obstructed, a lower nitrogen content could be caused by a low group III flux changing the Sb_2:Ga ratio, and increasing antimony competition with active N species for the available gallium atoms or group V sites. An increased V:III ratio causes a lower nitrogen content in the growing layer for GaNAs.[19] However, an excess of antimony will not produce gallium droplets on the surface. This suggests that the antimony source drifted, resulting in a group V limited growth regime, thus giving a smaller material thickness and the observed droplets.

In consideration of the latter scenario and, in the absence of further corroborating data for the first hypothesis, further experiments would be required in order to reach a definitive conclusion.

5.4 Modelling N incorporation as a function of growth parameters:

Models have been proposed to explain observations of experimental MBE growth, both for binary compounds and III-V alloys.[20,21,27,32-35] Based on either thermodynamic or kinetic principles, the primary motivation is to gain understanding of the processes at work and their effects upon the growth conditions.

This section covers approaches made to rationalise nitrogen incorporation as a function of growth parameters, both thermodynamic and kinetic, with a discussion of their respective merits and limitations with respect to describing the nitrogen content of III-V-N films.

5.4.1 Kinetic Approach:

Kinetic models have been constructed to rationalise the composition of polynary films.[21,32,36] They are based upon the consideration of the rates of material gain and loss, and good agreement with experimental findings has been provided by this approach. Of the kinetic methods applied to determine film composition, arguably one of the most simple is described by Wood *et al,*[36] which was originally developed to describe the incorporation into III-V materials of Mg and Ca. It was successfully adopted by Pan *et al*. to describe the effects of growth rate and substrate temperature upon the nitrogen content of $Ga_xIn_{1-x}N_yAs_{1-y}$.[21]

In each case, the model is based upon the factors affecting the concentration of a given surface species (Mg, Ca, N). Taking nitrogen as the species of interest, the processes governing the rate of change of surface nitrogen concentration (dC_N/dt) are the rates of arrival (J_N), desorption (D_N) and incorporation (K_N). Combined, these result in

— (5.1)

The incorporation rate constant, K_N, is defined as being proportional to the gallium flux, J_{Ga}, in the form

$$K_N = K'J_{Ga}, \tag{5.2}$$

where K' is a constant of proportionality. The desorption rate constant, D_N, is temperature-dependent, and is given as

$$-\quad\overline{\quad}, \tag{5.3}$$

where τ is the surface residency time for an N atom, E_d denotes the energy required for N atom desorption, k_B is the Boltzmann constant and T is the surface temperature in Kelvin. To avoid the complexities of non-steady state growth, Wood *et al.* and Pan *et al*. have treated the growth occurring under equilibrium conditions; that is to say $dC_N/dt = 0$. With the substitution of (5.2) and (5.3) into (5.1), C_N may be expressed as

$$\frac{\qquad\qquad}{-\quad\overline{\quad}} \tag{5.4}$$

The product of the concentration (5.4) and the rate constant, $K'J_{Ga}$, thus gives the rate of incorporation as

$$\frac{\qquad\qquad}{-\quad\overline{\quad}} \tag{5.5}$$

N_{Ga} is the number density of gallium in the III-V lattice and dividing (5.5) by the growth rate, $J_{Ga}/N_{Ga,}$ the density of incorporated N atoms, ρ_N is given by

$$\frac{\qquad\qquad}{\quad\overline{\quad}} \tag{5.6}$$

From inspection of eq. 5.6, the reciprocal dependence of nitrogen content upon the growth rate is apparent, with the gallium flux featuring in the denominator, which gives the rate at which overgrowth occurs. This factor also relates to the length of time that each monolayer is exposed to the incident nitrogen flux. The exponential loss term in the denominator describes the rate at which nitrogen desorbs from the surface as a function of temperature. Together, they explain the plateau regions that are observed for nitrogen content with respect to both temperature and growth rate. In the former case, and at a constant growth rate, a rise in substrate temperature increases the significance of the desorption term, leading to a sharp decrease in nitrogen content (Figure 5.16). The parameters used are displayed in Table 5.2.

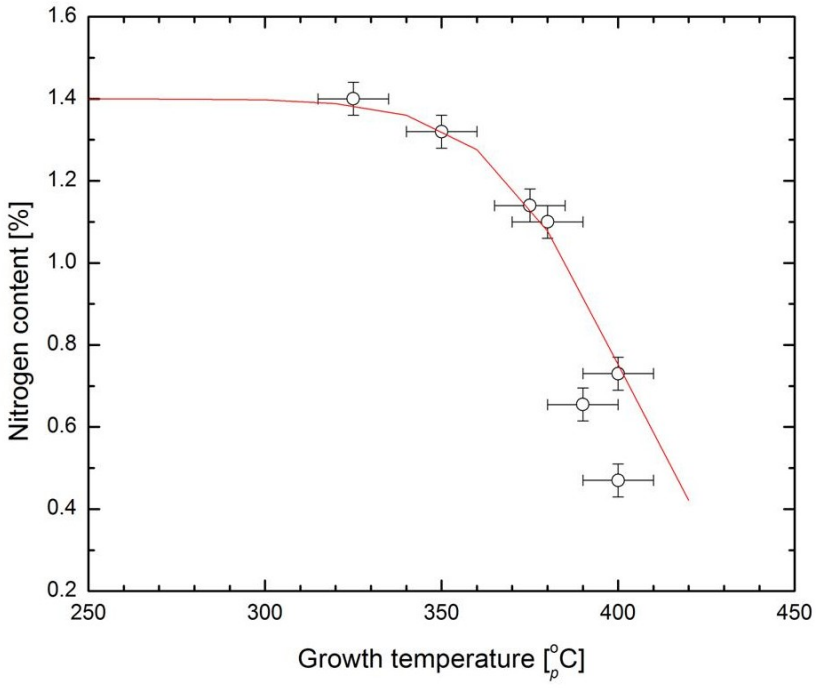

Figure 5.16: A comparison between experimental data gathered in this study and a simulation performed using the equation of Wood *et al.*

Parameter	Value
N_{Ga}	1.77 x 10^{28} atoms m^{-3}
J_N	3.43 x 10^{16} atoms m^{-2} s^{-1}
J_{Ga}	1.77 x 10^{18} atoms m^{-2} s^{-1}
τ	5.00 x 10^{-6} s
K'	1.00 x 10^{-28} m^2 $atom^{-1}$
E_d	2.0 eV

Table 5.2: The parameters used in the simulation shown in Figure 5.16. Of these, τ, K' and E_d were free for fitting. The value for E_d is in close agreement to the desorption energy of 2.1 eV used by Pan *et al.*

Examination of eq. 5.6, with two fixed temperatures and a range of values for the growth rate, demonstrates a similar effect. With an initially low gallium flux, corresponding to a long exposure time of each monolayer, the desorption term is more significant (Figure 5.17).

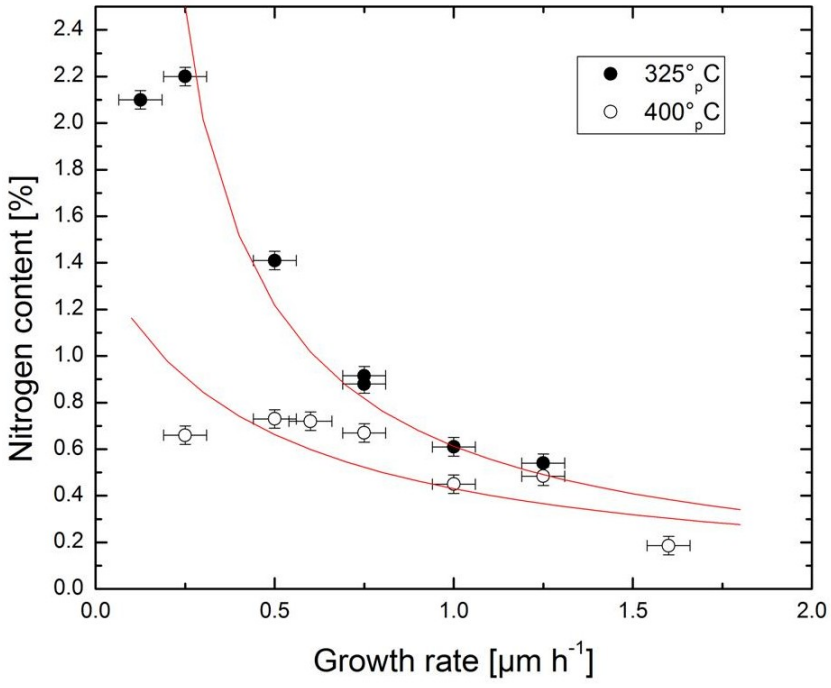

Figure 5.17: A comparison of the experimental data gathered from GaN_xSb_{1-x} growth and a simulation performed using the equation of Wood *et al.* and the parameters in Table 5.3.

Parameter	Value
N_{Ga}	1.77×10^{28} atoms m^{-3}
J_N	3.43×10^{16} atoms m^{-2} s^{-1}
T	325°C, 400°C
τ	5.00×10^{-6} s
K'	1.00×10^{-28} m^2 $atom^{-1}$
E_d	2.0 eV

Table 5.3: The parameters used in the simulation shown in Figure 5.17. Of these, τ, K' and E_d were free for fitting. It can be seen that, aside from the change from temperature to growth rate as the independent variable, the other parameters match those displayed in Table 5.2.

At a fixed substrate temperature, this term is constant, causing the nitrogen content to drop below the straight line. As the gallium flux increases, the nitrogen desorption rate becomes smaller than the rate of overgrowth, resulting in the nitrogen content being proportional to exposure time.

Many parameters used for fitting are well-defined, with the gallium flux, growth temperatures and atom number density having been taken from physical material data and instrumental calibration. An estimate has been made for the nitrogen desorption energy, E_d, leaving K' and τ as free parameters. Eq. 5.6 reveals that the free parameters K' and τ are combined, effectively limiting the total number of free parameters to 3. A comparison of the simulations in Figure 5.16 and Figure 5.17, along with the consistency in the parameters used for each, demonstrates generally good agreement with the experimental data.

A plot of nitrogen content as a function of both temperature and gallium flux provides a good visual guide to the combined effects of each parameter (Figure 5.18).

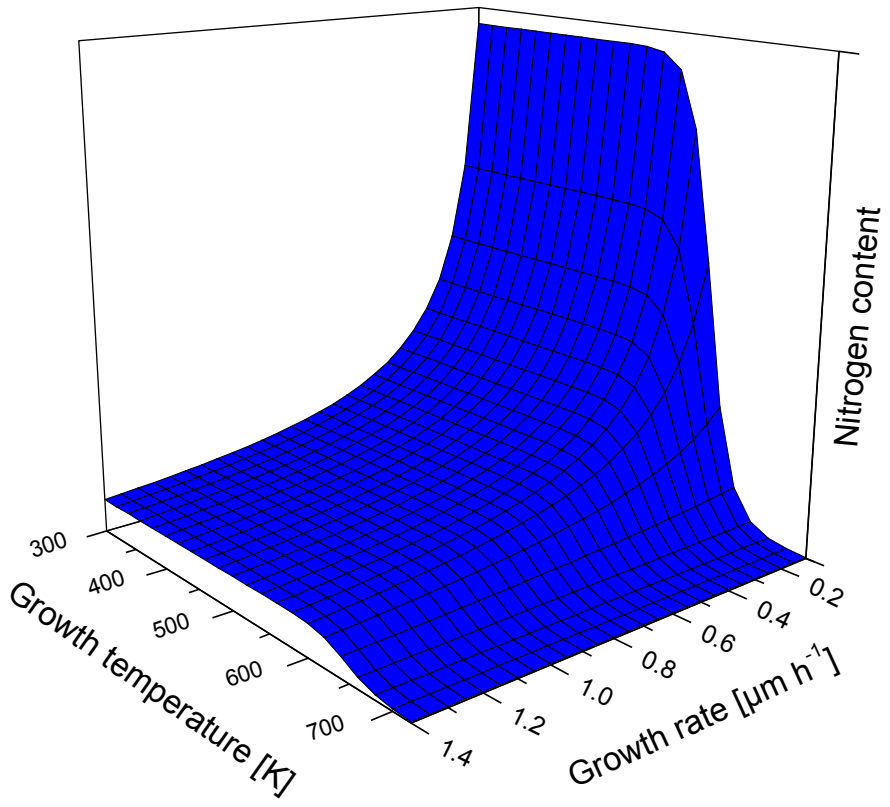

Figure 5.18: A surface plot indicating the effects of both growth temperature and rate of material deposition exert upon nitrogen content, according to eq. 5.6.

Although plateaux have been found in the experimental data discussed previously, this model does not produce flat plateau regions as a function of growth rate. This suggests that there may be additional factors not considered by the model. The primary limitation with respect to GaN_xSb_{1-x} is the lack of of competition between Sb and N. The previous results show that increasing the V:III ratio can decrease the nitrogen content. However, there is no V:III dependence for nitrogen content observed for GaN_xSb_{1-x},[2] GaP_xAs_{1-x},[37] or GaN_xAs_{1-x} and their alloys grown by either MOVPE or MBE.[11,21] This is in contrast to data presented by Odnoblyudov *et al.*, which shows x in GaN_xAs_{1-x} is a function of the As:N ratio.[27]

A fundamental issue with the models utilised by Wood *et al.* and Pan *et al.* is that they imply growth under equilibrium conditions, whereas MBE growth is widely regarded as being a non-equilibrium process. So, they do not accurately describe the systems under investigation.

Pan *et al.* state that, for GaN_xAs_{1-x}, the desorption term (eq. 5.3) alone is insufficient to describe the sharp reduction in nitrogen content with increasing temperature,[21] and suggest thermally activated surface segregation as an additional loss process. In common with Wood *et al.*[36] and Bandić *et al.* in their kinetic treatment of a GaN_xAs_{1-x}/GaAs superlattice,[32] nitrogen atoms are thought to be resident for a period greater than the monolayer formation time. In the latter publication, the suggestion is made that, given enough thermal energy, nitrogen atoms can migrate from one monolayer to the one above. It is stated that this additional term produces better agreement with experimental data, although no results have been published in support of this. It is not surprising that the addition of a further loss term provides a better fit to experimental data, although it need not refer specifically to surface segregation. Indeed, Bandić *et al.* and Pan *et al.* state that model incorporating surface segregation, produces a gradient in the nitrogen content throughout the grown layer. This was not observed in any of the SIMS profiles taken in this study. However, a comparison of SIMS and XRD results for GaN_xAs_{1-x} indicate a significant proportion of non-substitutional nitrogen,[15] so it is possible that this segregation term applies to activated migration of nitrogen from substitutional centres to interstitial locations.

5.4.2 Thermodynamic Approach:

For the proper thermodynamic treatment, the system should be at equilibrium. However, this requirement is not strictly observed in the case of MBE growth, due to the ongoing accumulation of a solid product,[34] as well as the anisothermal nature of the system.[38] Furthermore, in the Gen II system, re-evaporated species are trapped by the cryoshroud and thus take no further part in any process. MBE is often treated instead as a quasiequilibrium process,[33] and Heckingbottom demonstrated that a thermodynamic model for GaAs growth agreed well with experimental data.[34] Therefore, a thermodynamic model may provide a useful description of film growth by MBE.

From the work of Heckingbottom, it is shown that the growth rate of GaAs exhibits a strong temperature dependence, with a sharp decrease occurring in the temperature range over which the re-evaporated gallium flux becomes significant. It is the difference between the equilibrium pressure of Ga over the surface and the applied overpressure which determines the rate of Ga deposition.[34] Qualitatively, temperature dependence of normalised GaAs growth rate is similar to that observed for the incorporation of nitrogen into GaSb in this study (Figure 5.6), as well as those reported in the available literature for GaN_xAs_{1-x}.[27] This is not a surprise as, in the case of III-V-N alloys, it is expected that physisorbed nitrogen is the most volatile species. The general assumption is that atomic nitrogen is the active species,[27,39] rather than metastable dinitrogen, as has been suggested by other researchers.[40,41]

There are different approaches in applying thermodynamic treatments to III-V-N materials. One model considers the growth process to be one of equilibrium,[20] whereas Egorov *et al.* describe material formation as a stationary irreversible

process.[42] The choice between these two approaches results in different nitrogen content dependencies with respect to V:N ratio, so there is a great degree of flexibility to fit a model to experimental findings.[42]

One significant difference between the models proposed for describing the nitrogen content in GaN_xAs_{1-x} films and the approach published by Heckingbottom for $Al_xGa_{1-x}As$ is that, in the latter, there is no miscibility gap. This permits the mixture of the binary AlAs and GaAs compounds to be approximated as an ideal solution and the corresponding activity coefficients are unity. This is not the case for a binary solution of GaAs and GaN, where the large lattice mismatch prevents the growth of single-phase material over the full compositional range,[7] with phase separation in GaN_xAs_{1-x} for $x \sim 0.1$.[19] It is expected that, due to a similar mismatch between GaN and GaSb, immiscibility will be present in the GaN_xSb_{1-x} system. This alloy may be approximated by the regular solution model,[43] where the activity coefficients describe the degree to which the properties of the binary components deviate from ideal behaviour.[33]

The results presented by Odnoblyudov *et al*. are in qualitative agreement with the trends provided by the model proposed by Wood *et al.*[20,36] As with the kinetic treatment, the thermodynamic model does not produce flat plateau regions as a function of growth rate. The thermodynamic model presented is also incomplete, as it too includes only substitutional nitrogen and makes no provision for N occupancy of other sites or the interchange between them. However, an advantage of this approach over the kinetic model is that it considers the incident fluxes of each growth species, giving a nitrogen content dependence upon the V:N ratio employed.

As discussed previously, there are reports suggesting that the nitrogen content is independent of the V:N ratio used during growth.[2,21] Also, Pan *et al*. report that similar observations were made over a range of As-cracker temperatures, implying that changing fluxes of both dimeric and tetrameric species had no effect upon the level of nitrogen incorporated. This is in contrast to the thermodynamic model and experimental data presented by Odnoblyudov *et al.* for GaN_xAs_{1-x} in which increasing the dimeric arsenic flux employed decreases the nitrogen content. The most likely explanation for this arises from the ranges over which the experimental data were collected. In the study by Pan *et al.*, the As BEP was varied over a range of less than a decade, whereas Odnoblyudov *et al*. used As:N flux ratios over a range of almost two orders of magnitude. Where anion exchange on the surface is the dominant mechanism through which nitrogen is incorporated, large V:N flux ratios will result in arsenic species outcompeting nitrogen, giving a lower degree of N incorporation. Given the reports discussed above, further investigation is needed into the V:N dependence of the incorporation of substitutional nitrogen, such that a definitive conclusion may be reached.

Antimony nitride species, SbN_x can be formed. While the formation of AsN_x has not been reported in epitaxial growth, antimony nitride has been synthesised through sputtering with an RF nitrogen source,[28] with additional evidence of SbN formation on InSb reported in MBE.[44] Because of the high activity of N species produced in RF plasma,[41] the possibility of V-nitride formation must be considered.

V-nitride material formation is absent from all thermodynamic and kinetic models and treatment should include all products of any significance. However, the qualitative agreement observed suggests that this product, if present, has not

dramatically changed the behaviour of the GaN_xSb_{1-x} system with respect to GaN_xAs_{1-x}.

5.5 Conclusion:

The control of substitutional nitrogen content of GaN_xSb_{1-x} films has been demonstrated, through variation of the rate of deposition and temperature used for growth. The results show qualitative agreement with previous studies describing both experimental results and models of GaN_xAs_{1-x} growth. The largest quantity of substitutional nitrogen incorporated was 2.6 %, which is the largest value at the time of writing. Samples produced at a low growth rate have highlighted the need for greater stability of the antimony source for the reliable growth of dilute antimonide material with a high N-content, as well as for any future GaN_xSb_{1-x} quantum dot production.[20]

Spatially-resolved XRD measurements show that, where the temperature gradients across a sample are sufficient to induce antimony condensation, nitrogen incorporation is inhibited. It was also determined, however, that the distance over which this effect occurs is of the order of 1 mm, suggesting that compositional uniformity away from the edges of the sample was otherwise good.

In absence of a standardised SIMS study of nitrogen incorporation, it is important to consider the limitations of XRD as an analysis technique. While the substitutional nitrogen content of the layers may be determined using X-ray diffraction, it does not measure the total quantity of nitrogen present. In GaN_xAs_{1-x} there can be a difference between the levels of nitrogen as determined by SIMS and XRD.[15] SIMS

measures the total nitrogen content, including both substitutional and interstitial species. Therefore a calibration series should be taken and compared with XRD analyses, to find the fraction of N species that are not substitutional.

Sample degradation has been observed for GaN_xSb_{1-x} samples grown < 310°$_p$C, with the appearance of voids and threading defects throughout the grown film observed by TEM for the sample grown at 275°$_p$C. The surface became rougher, with an accompanying decrease in nitrogen content. In light of this, it is proposed that the plateau region of nitrogen content observed does not remain constant with decreasing temperature. Instead, there is a lower limit, below which the level of substitutional nitrogen diminishes as a result of poor quality growth. In order to better characterise this region and the causes and characteristics of the observed change in material quality, further growth in combination with full TEM, SIMS and XRD analyses is needed.

As nitrogen incorporation into GaSb shows similarities with GaN_xAs_{1-x}, it is likely that a degree of interstitial nitrogen incorporation into GaSb has also occurred, especially in those samples grown at lower growth rates. To determine the effect of growth parameters upon material quality and the different ways that nitrogen may be incorporated, PL and SIMS should be made respectively.

[1] T. D. Veal, L. F. J. Piper, S. Jollands, B. R. Bennett, P. H. Jefferson, P. A. Thomas, C. F. McConville, B. N. Murdin, G. W. Smith, L. Buckle, Applied Physics Letters **87**, 132101 (2005).

[2] L. Buckle, B. Bennett, S. Jollands, T. D. Veal, N. R. Wilson, B. Murdin, C. F. Mcconville, T. Ashley, Journal of Crystal Growth **278**, 188-192 (2005).

[3] S. Spruytte, Journal of Crystal Growth **227-228**, 506-515 (2001).

[4] P. H. Jefferson, L. Buckle, D. Walker, T. D. Veal, S. Coomber, P. A. Thomas, T. Ashley, C. F. McConville, Physica Status Solidi (RRL) – Rapid Research Letters **1**, 104-106 (2007).

[5] P. H. Jefferson, T. D. Veal, L. F. J. Piper, B. R. Bennett, C. F. McConville, B. N. Murdin, L. Buckle, G. W. Smith, T. Ashley, Applied Physics Letters **89**, 111921 (2006).

[6] W. G. Bi, C. W. Tu, Journal of Crystal Growth **0248**, (1997).

[7] Y. Qui, S. A. Nikishin, H. Temkin, V. A. Elyukhin, Y.A. Kudriavtsev, Appl. Phys. Lett **70**, 2831–2833 (1997).

[8] P. H. Jefferson, B. R. Bennett, L. Buckle, T. D. Veal, D. Walker, N. R. Wilson, L. F. J. Piper, P. A. Thomas, T. Ashley, C. F. McConville, Journal of Crystal Growth **304**, 338–341 (2007).

[9] A. Kimura, H.F Tang, T.F Kuech, Journal of Crystal Growth **265**, 71-77 (2004).

[10] Y. Lin, Thin Solid Films **368**, 249-252 (2000).

[11] A. Moto, S. Tanaka, N. Ikoma, T. Tanabe, S. Takagishi, M. Takahashi, T. Katsuyama, Jpn. J. Appl. Phys **38**, 1015–1018 (1999).

[12] Y. Sun, M. Yamamori, T. Egawa, H. Ishikawa, Japanese Journal of Applied Physics **43**, 2409-2413 (2004).

[13] M. Kondow, K. Uomi, A. Niwa, T. Kitatani, S. Watahiki, Y. Yazawa, K. Hosomi, T. Mozume, Solid-State Electronics **41**, 209–212 (1997).

[14] A. Takata, R. Oshima, H. Shigekawa, Y.A Okada, Journal of Crystal Growth **310**, 3710-3713 (2008).

[15] Q. X. Zhao, S. M. Wang, M. Sadeghi, A. Larsson, M. Friesel, M. Willander, Applied Physics Letters **89**, 031907 (2006).

[16] M. Uchiyama, F. Ishikawa, and M. Kondow, Japanese Journal of Applied Physics **48**, 081102 (2009).

[17] M. Kondow, T. Kitatani, Semiconductor Science and Technology **17**, 746-754 (2002).

[18] H. Dumont, L. Auvray, Y. Monteil, O. Marty, G. Patriarche, Physica Status Solidi (C) **2752**, 2749-2752 (2003).

[19] S. Thomas, S. White, P. R. Chalker, T. J. Bullough, T. B. Joyce, Journal of Materials Science: Materials in Electronics **13**, 525–529 (2002).

[20] V. A. Odnoblyudov, A. R. Kovsh, A. E. Zhukov, N. A. Maleev, Semiconductors **35**, 554-559 (2001).

[21] Z. Pan, L. H. Li, W. Zhang, Y. W. Lin, R. H. Wu, Applied Physics Letters **77**, 214 (2000).

[22] H. Kiinzel, R. Bochnia, P. Harde, A. Hase, U. Griebenow, Journal of Crystal Growth **150**, 18-22 (1995).

[23] H. P. Bae, S. R. Bank, H. B. Yuen, T. Sarmiento, E. R. Pickett, M. A. Wistey, J. S. Harris, Applied Physics Letters **90**, 231119 (2007).

[24] I. Suemune, K. Uesugi, T. Seong, Semiconductor Science and Technology **17**, 755-761 (2002).

[25] E.J. Koerperick, L.M. Murray, D.T. Norton, T.F. Boggess, J.P. Prineas, Journal of Crystal Growth **312**, 185-191 (2010).

[26] A. W Jackson, A. C. Gossard, Journal of Crystal Growth **301-302**, 105-108 (2007).

[27] V. A. Odnoblyudov, A.Y. Egorov, A. R. Kovsh, A. E. Zhukov, N. A Maleev, E. S. Semenova, V. M. Ustinov, Semiconductor Science and Technology **16**, 831 (2001).

[28] Qian Sun, Wen-Jing Li, Zheng-Wen Fu, Solid State Sciences **12**, 397-403 (2010).

[29] T. E. Lamas, A. A. Quivy, Brazillian Journal of Physics **32**, 399-401 (2002).

[30] P.S. Dutta, H. L. Bhat, Applied Physics Reviews **81**, 5821-5870 (1997).

[31] K. F. Longenbach, W. I. Wang, Symposium A Quarterly Journal in Modern Foreign Literatures **59**, 2427-2429 (1991).

[32] , R. J. Hauenstein, M. L. O'Steen, T. C. McGill, Applied Physics Letters **68**, 1510 (1996).

[33] A. Y. Egorov, A. R. Kovsh, A. E. Zhukov, V. M. Ustinov, P. S. Kop'ev, Semiconductors **31**, 989–993 (1997).

[34] R. Heckingbottom, Journal of Vacuum Science & Technology B: Microelectronics and Nanometer Structures **3**, 572–575 (1985).

[35] H. Seki, A. Koukitu, Journal of Crystal Growth **74**, 172–180 (1986).

[36] C. E. C. Wood, D. Desimone, K. Singer, G. W. Wicks, Journal of Applied Physics **53**, 4230–4235 (1982).

[37] H. Q. Hou, B. W. Liang, T. P. Chin, C. W. Tu, Applied Physics Letters **59**, 292 (1991).

[38] B. A. Joyce, Rep. Prog. Phys. **48**, 1637-1697 (1985).

[39] R. Vaudo, J. Cook Jr., J. Schetzina, Journal of Crystal Growth **138**, 430-436 (1994).

[40] N. Newman, Journal of Crystal Growth **178**, 102-112 (1997).

[41] J. C. Harmand, G. Ungaro, L. Largeau, G. Le Roux, Applied Physics Letters **77**, 2482 (2000).

[42] A. Y Egorov, A. R. Kovsh, V. M. Ustinov, A. E. Zhukov, P. S. Kop'ev, C. W. Tu, Journal of Crystal Growth **188**, 69-74 (1998).

[43] A Jordan, Journal of Physics and Chemistry Of Solids **36**, 329-342 (1975).

[44] L. Haworth, Journal of Vacuum Science & Technology B: Microelectronics and Nanometer Structures **16**, 2254 (1998).

Chapter 6

"One finds limits by pushing them."

Herbert Simon (1916 - 2001)

This chapter covers the growth of InSb(001), including observed diffraction patterns and their transitions. Results from experiments conducted into the optimisation of In(N)Sb are also discussed.

6.1 Introduction

Indium antimonide has applications in the mid- to far-IR region, due to its small band gap (0.175 eV)[1] and the further reduction in band gap produced by the incorporation of N. In common with GaSb, there are quaternaries such as $Ga_xIn_{1-x}N_ySb_{1-y}$, $InAs_xN_ySb_{1-(x+y)}$ and $Ga_xIn_{1-x}As_yN_zSb_{1-(y+z)}$ that are lattice-matched with a tuneable range of band gaps.

This chapter is concerned with the growth and characterisation of InSb films. There then follows a description of the growth and analysis of InN_xSb_{1-x} films as a function of growth rate and substrate temperature. A rationale is then proposed to account for the difference in the ease of N incorporation with respect to GaN_xAs_{1-x}, GaN_xSb_{1-x}, and InN_xSb_{1-x}.

6.2 InSb

Due to the interest in mid- and far-IR applications of InSb and its alloys, there are a number of reports describing its growth and properties.[2,3-6]

InSb has a lattice constant of ~6.48 Å, and growth suffers from a large lattice mismatch on many commonly used substrates (ca. 14% and 19% for GaAs and Si respectively).[7-9] While CdTe substrates offer a very small mismatch (0.04%), the quality of commercially available substrates remains poor.[10] Like other antimonides such as GaSb, antisite defects are a concern when attempting to produce high-quality films and, in order to minimise such imperfections, an excess antimony flux is generally necessary. However, in contrast to the Ga_{Sb} and Sb vacancy defects which are present in GaSb,[11-14] in InSb it is the indium interstitial and Sb_{In} antisite defects

which cause the unintentional n-type doping of InSb.[15] This suggests that while an excess of antimony may be required for growth, only the smallest excess should be practically used.

In addition to having the smallest band gap of any of the III-V binary alloys, InSb also possesses a comparatively low melting temperature (527°C).[16] As such, it has been reported that reproducibility of good quality InSb films has been difficult to achieve.[17*] In addition, thermal oxide removal is problematic, with evidence of incomplete oxide removal and a rough surface.[7] This is due to the oxide desorption temperature being in excess of the temperature of non-congruent evaporation (~350°C)[19] and relatively close to the melting point of InSb.[19,20] These factors indicate that InSb should be expected to be more sensitive to thermal processing than GaAs, for example.[18,19]

Various surface reconstructions have been reported for the InSb(001) surface, with (1 x 1), c(4 x 4), asymmetric (1 x 3), c(8 x 2), (4 x 3) and (7 x 5) structures observed by RHEED and STM.[20] The last two reconstructions are of particular note, with the (4 x 3) thought to comprise intermixed (1 x 3) and c(8 x 2) unit cells.[20,21] The observation of the (7 x 5) reconstruction contradicts the suggestion by Thibado *et al*. that (*n* x 5) reconstructions are unique to GaSb.[22]

6.2.1 Calibration of Material Sources:

To stop platen obstructing the RHEED beam, a 2" wafer was used for these measurements. A GaAs(001) semi-insulating wafer (AXT), chosen for ease of

[*] Private communication with Wafertech

thermal cleaning, was outgassed at 400°$_e$C (> 60 minutes), prior to thermal oxide desorption (580-600°$_p$C) under a stabilising antimony flux (~1.6 x 10^{-6} torr) and observation by RHEED. A 0.5 μm layer of GaSb was deposited (0.5 μm h^{-1}, T_g = 500°$_p$C, Sb_2:Ga = 5:1), followed by a 0.5 μm InSb film (0.5 μm h^{-1}, T_g = 400°$_p$C, Sb_2:In = 2:1), forming a relaxed InSb surface. The substrate temperature was reduced to 340°$_e$C and, with the antimony valve at a fixed setting, the nominal In growth rate was set and the cell temperature allowed to equilibrate.

The substrate was oriented such that the two-fold periodicity of the c(4 x 4) reconstruction was visible on the RHEED screen. The fringe intensity of the specular diffraction spot was recorded using the KSA 400 RHEED software (*k*-Space Associates). The In shutter was then opened until either the oscillation intensity damped or, in the case where the incident Sb_2 flux was too low to support an Sb-stabilised surface, a reconstruction consistent with an In-rich surface was observed. This was repeated at least twice, before the nominal In growth rate was changed and the process repeated. The Sb_2 flux was changed and the entire measurement procedure repeated after determining the group V limited growth rate.

This process gave information about the measured group III and group V incorporation rates. An initial linear relationship in measured growth rate as a function of nominal In flux provided a calibration factor for the In source. The plateau regions gave the group V-limited growth rates for the Sb_2 flux values employed (Figure 6.1).

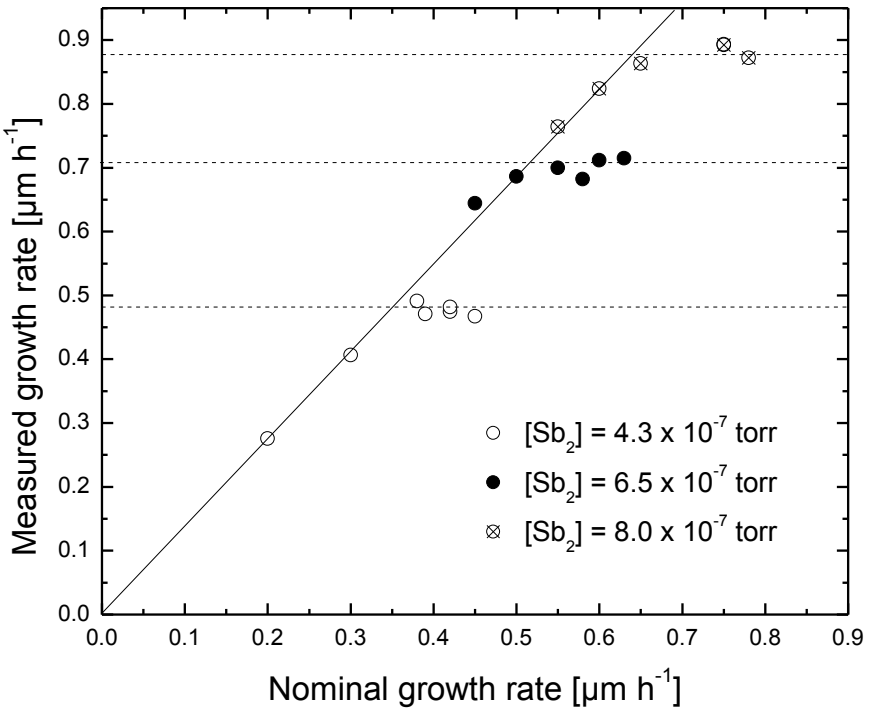

Figure 6.1: Plot of the measured growth rate of InSb as a function of the nominal growth rate described by a previous calibration of the In source. The solid black line indicates the group III-limited regime and the plateau regions indicate a growth regime limited by group V supply are marked with dashed lines.

To calibrate the group V-limited growth rate as a function of Sb_2 BEP, a plot was produced, with a linear trend similar to that observed for the GaSb calibration described in chapter 4 (Figure 6.2).

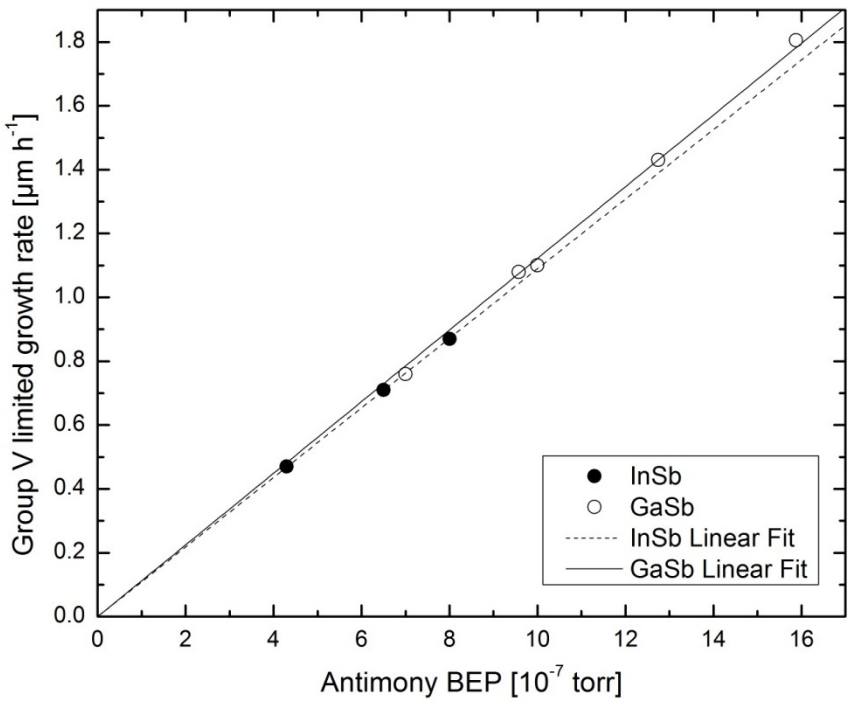

Figure 6.2: Comparison between the group V limited growth rates for GaSb (T_g = 440°$_e$C) and InSb (T_g = 340°$_e$C). The growth rates determined show agreement, suggesting that there is not a significant change in the incorporation of antimony between InSb and GaSb under these conditions.

A comparison of the group V-limited growth rates as a function of Sb_2 BEP obtained for InSb (T_g = 340°$_e$C) and GaSb (T_g = 440°$_e$C) in chapter 4 demonstrates a striking similarity. Since the group V-limited rates were calculated as the rate of change of absolute thickness, rather than in terms of MLs^{-1}, one might expect a slightly higher measured growth rate for InSb than GaSb for the same Sb flux, due to the difference in lattice parameters and the corresponding lower atomic density for InSb. This was not observed in the linear fitting of the data, where the growth rate of GaSb was marginally higher. This may be due to the uncertainty in determination of the Sb_2 BEP, which was limited to two significant figures by the ion gauge controller.

Group III-rich surfaces were observed at higher In fluxes, due to insufficient incident Sb_2 flux to maintain an Sb-stabilised surface. A transition from the two-fold periodicity of the c(4 x 4) reconstruction to a four-fold periodicity (Figure 6.3) in the [010] azimuth. It is thought that the latter reconstruction corresponds to the c(8 x 2) surface structure, consistent with growth of InSb(001) in a group III-rich regime.[20,23]

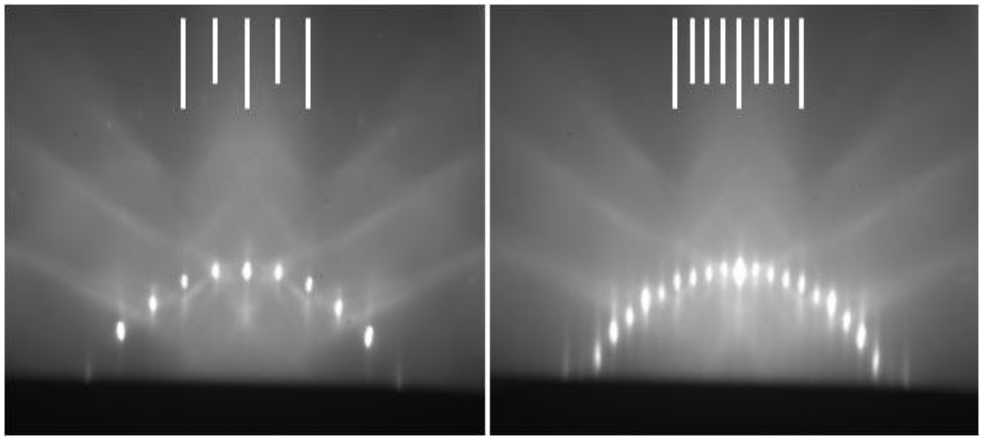

Figure 6.3: ~13 kV RHEED images with the electron beam incident in the [100] direction, showing the change in reconstruction observed as group V-limiting flux was exceeded by increasing the In flux. The two-fold periodicity (left) of the c(4 x 4) exhibited a sharp transition to a reconstruction with four-fold periodicity (right). After stopping the indium supply, the c(4 x 4) was recovered.

Upon closing the In shutter, the reverse transition was sharp, occurring over a span of ~2s, with no visible degradation of the diffraction pattern following repeated cycling between each reconstruction.

6.2.2 Experimental Growth

In chapter 4, growth temperature was found to determine the surface morphology for GaSb. GaSb also requires a minimum Sb excess to reduce defects. In a similar manner, InSb growth was performed over a range of temperatures.

Cleaved quarter-pieces of unintentionally *n*-type InSb(001) (Wafertech) were mounted on indium-free platens and outgassed at 200°$_e$C (> 60 minutes), prior to admission to the growth chamber. Oxide removal was conducted under a stabilising antimony flux (~1.6x10^{-6} torr) and the efficacy determined by RHEED. A planarising layer (0.2 μm) was grown at 380°$_e$C and an Sb_2:In ratio of 2:1, after which pyrometer measurements were made as a function of Eurotherm controller readings to provide extrapolated temperature values. In an effort to prevent damage to the InSb wafer, the extrapolation was conducted to a maximum temperature of 500°$_p$C.

0.4 μm thick samples were grown at 300°$_p$C, 350°$_p$C and 400°$_p$C, with a fixed Sb_2:In ratio of 1.2:1.

Following completion of growth, the samples were cooled and removed from the growth system. For the samples grown at 350°$_p$C and 400°$_p$C, the Sb_2 flux was terminated at T_g ~ 320°$_p$C to avoid degradation of the surface. The samples were cleaved and mounted for analysis in the same manner as described in chapter 5.

6.2.3 Results and discussion:

Upon removal of the samples from the indium-free platen, it was observed that each had adhered to the molybdenum mounting plate. This varied in severity from a mild adhesion to cases in which the wafer was effectively soldered to the platen. Following removal, the area of the wafer that was in contact with the platen exhibited a rough surface with a silver lustre. A metallic deposit was also noted over the region of the platen which had been on contact with the sample. There appeared

to be no correlation between growth temperature and the degree to which samples had become affixed.

There are two possible causes, one of which is that the wafer could have undergone thermal decomposition where the incident antimony flux was masked by the edge of the platen, resulting in indium metal from the InSb wafer through incongruent evaporation. This seems unlikely, however, as the reverse face of the wafer that was directly exposed to the heater was not observed to have been affected for any of the samples. It would be possible though, if the platen achieved a temperature significantly higher than the wafer at any point, so that conductive heating to the wafer occurred.

An alternative explanation is that indium used during growth or liberated from the face of the platen was sufficiently mobile that droplet formation could occur at the edges of the wafer. Physisorbed indium has a large surface migration length, although quantitative values have not been published.[23] Wafer fusion between InSb and GaAs has been demonstrated through diffusion of interfacial species,[24] supporting the suggestion that the observed metallic deposit originated from within the wafer.

These effects were confined to the edge of the wafer, which suggests that surface uniformity was not affected. However, this may not have been the case, as solder-induced strain has previously been reported to have a detrimental effect upon the crystal quality of material.[10] A full analysis must consider the thermal expansion coefficients of both the molybdenum platen and the InSb wafer and the level of mechanical strain produced by the adhesion.

Examination of the samples by C-DIC microscopy revealed a rough surface in all cases (Figure 6.4).

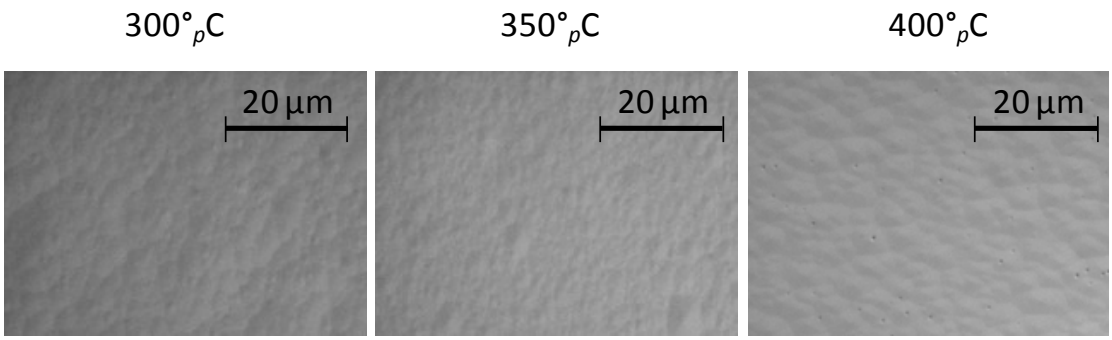

Figure 6.4: C-DIC images of InSb samples grown at 0.5 µm h^{-1} and with an Sb_2:In ratio of 1.2:1. The growth temperature is indicated in each instance. For all samples, the rough surface is due to roughening caused by thermal oxide removal.

The observation of rough sample surfaces was confirmed by AFM analysis (Figure 6.5). This is thought to result from thermal pitting of the substrate during oxide removal.

The measured RMS roughness values were 1.505 nm (T_g = 300°$_p$C), 1.735 nm (T_g = 350°$_p$C) and 1.328 nm (T_g = 400°$_p$C). Each sample surface also had monolayer terraces, measured from analysis of the cross sections to be ca. 3.5 Å high, with a width of ~50-200 nm. These terraces were markedly broader for the film grown at 400°$_p$C. This implies that the optimum growth temperature for the binary material is likely to lie above the region in which N incorporation is expected to be at a maximum, which Zhang *et al.* estimate to occur at T_g < 300°C.[25]

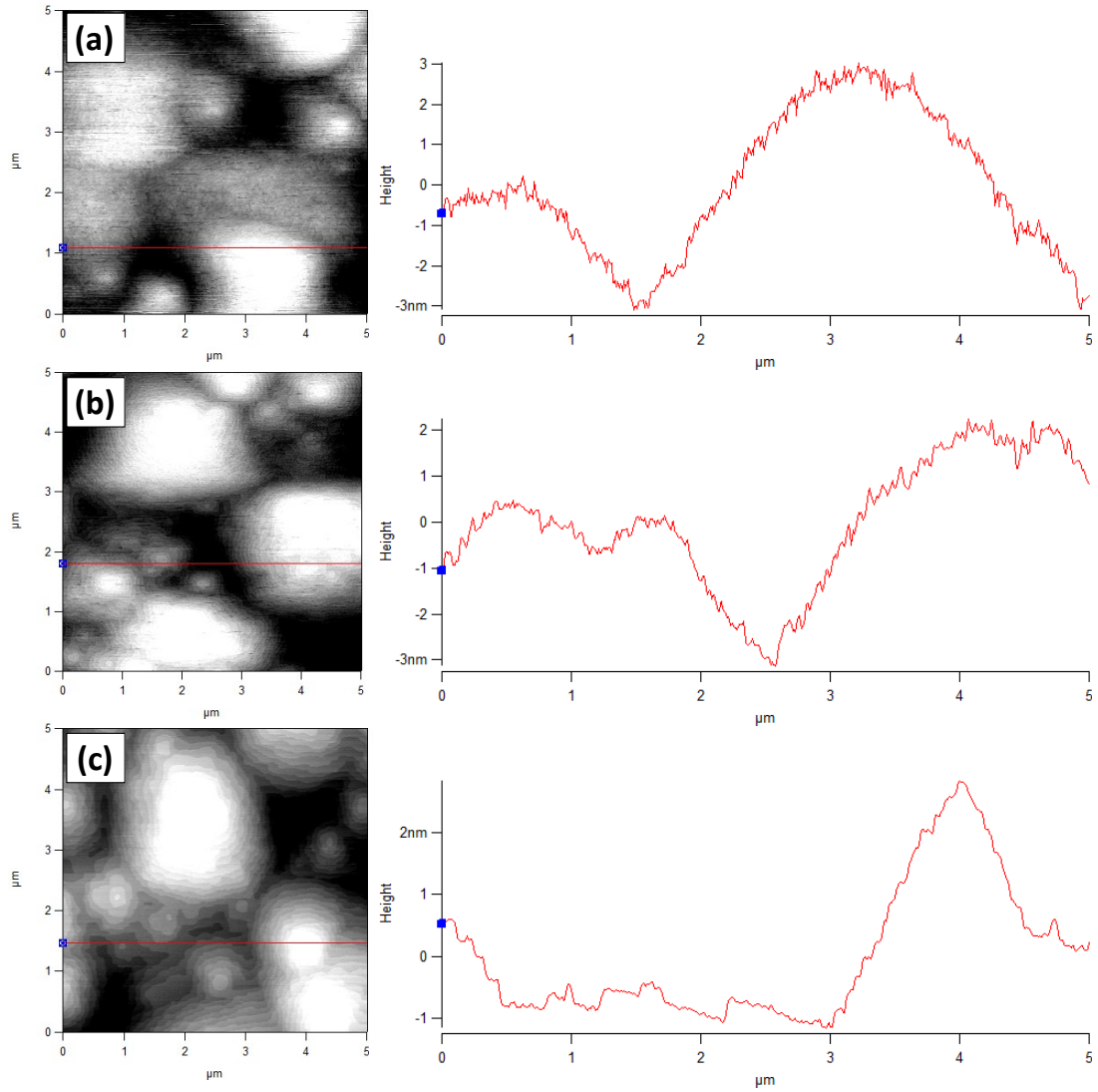

Figure 6.5: 5 µm x 5 µm AFM topographs and their respective cross sections of the surfaces resulting from InSb growth at (a) 300°$_p$C (b) 350°$_p$C and (c) 400°$_p$C. In each instance the surface is rough, with monolayer steps visible. An appreciable broadening of the terraces was observed for the sample grown in (c), with comparatively large flat areas. The data range in each image is 4 nm.

No evidence of indium droplet formation or antimony condensation was observed, suggesting that the V:III ratio employed was within acceptable bounds, the Sb_2 flux was stopped at the correct point during cooling, and that no surface degradation occurred during post-growth cooling.

6.3 InN_xSb_{1-x}:

The interest in InN_xSb_{1-x} alloys results from the opportunity to reduce the already narrow bandgap of InSb still further, to access a range of energies coinciding with the atmospheric transmission window (87 - 155 meV).[26] Further addition of N was predicted to reduce the bandgap causing a transition from semiconductor to semi-metal for $x \sim 0.02$.[27]

Potential difficulties with the growth of InN_xSb_{1-x} films include the issues described for the binary alloy, and also the determination of the correct temperature for N incorporation. Temperature determination requires extrapolating pyrometer data as a function of Eurotherm controller, as described in chapter 5 for GaN_xSb_{1-x} samples, to even lower temperatures for InN_xSb_{1-x} growth.[25] Other researchers have previously encountered difficulties with reproducible temperature determination, resulting in the report of a very narrow temperature region for N incorporation,[26] contrary to the findings of Zhang *et al.*[25]

Less nitrogen has been incorporated into InSb than GaSb, which is in turn less than for GaAs. However, an N content of ~6% has been achieved by low energy ion implantation.[28] From the results in chapter 5 and previous work on InN_xSb_{1-x},[25] as well as GaN_xAs_{1-x} and GaN_xSb_{1-x}, a decrease in growth temperature probably increases substitutional N incorporation. From the results of chapter 5 and previous work on GaN_xAs_{1-x} films,[29-31] lower growth rates probably increase N mole fraction, although one published report for InN_xSb_{1-x} growth suggest that this may not the case.[26] Also, unlike GaN_xAs_{1-x},[32] the level of substitutional N probably depends upon the V:III ratio.[25]

6.3.1 Experimental Growth

As in chapter 5, experiments were performed to determine the variation of N incorporation with growth rate and growth temperature. Cleaved quarter-pieces of unintentionally n-type doped InSb(001) (Wafertech) were mounted, prepared and an InSb buffer layer grown in the same manner described previously for the growth of the binary compound. Growth was conducted in the range 270-365°$_p$C, overlapping the temperature range used by Zhang *et al*.[25] To establish any temperature dependence of the substitutional N content, growth was conducted at 0.5 μm h^{-1}. The effect of varying the growth rate upon nitrogen incorporation was examined over the range 0.125 μm h^{-1} - 1.0 μm h^{-1}, which extends the range studied by Jefferson *et al.* to lower values.[26] These experiments were conducted at 270°$_p$C and 340°$_p$C, in order to determine the plateau concentrations as a function of temperature, as was done for GaN_xSb_{1-x} growth in chapter 5. The temperatures were chosen as the best estimate of the onset of the plateau region and being within the region where a sharp fall-off in N content is observed. The choice of temperatures was based upon initial results from samples grown to determine the temperature dependence.

For each sample grown, the nitrogen plasma conditions were the same as those used for growth of GaN_xSb_{1-x} (500 W and a 0.2 sccm flow rate), so that direct comparisons could be drawn as a function of growth temperature and rate.

6.3.2 Results and discussion:

The substitutional N content, as determined by XRD, decreased with increasing growth temperature, similar to GaN_xSb_{1-x} and reported for GaN_xAs_{1-x} (Figure 6.6).[30,33] A plateau in N content was reached which corresponds to ~1.1%.

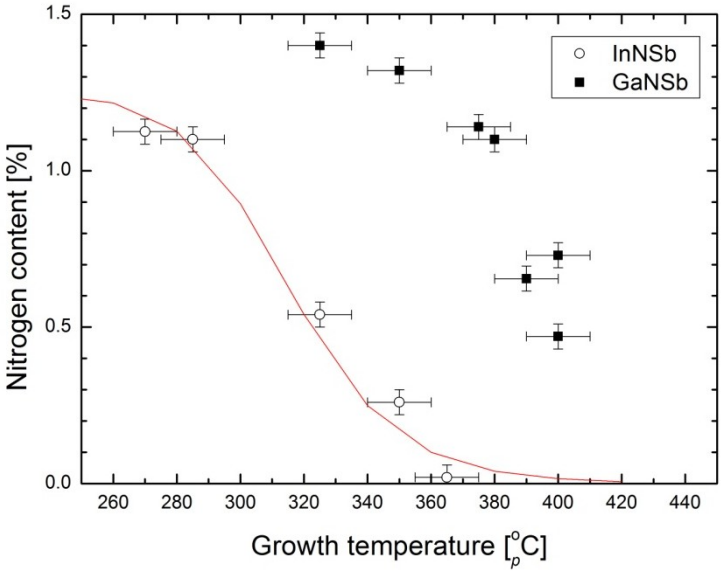

Figure 6.6: Plot of substitutional nitrogen content as a function of growth temperature for InN_xSb_{1-x} and GaN_xSb_{1-x} films. The temperature at which the nitrogen content of the InN_xSb_{1-x} samples starts to decrease is ca. 80°$_p$C lower than for GaN_xSb_{1-x}. The red line indicates a simulation made using the equation of Wood *et al.*, using *E*d = 1.75 eV and the In atom density for InSb. Other parameters remain unchanged from those used for GaN_xSb_{1-x} in chapter 5.

The rate at which N content decreased as a function of increasing growth temperature was lower for InN_xSb_{1-x} than for the GaN_xSb_{1-x} samples grown in chapter 5. The relatively gradual decrease observed was also different from the sharp falloff reported from both calculation and experiment for GaN_xAs_{1-x}.[30,31,33] A good fit to the equation of Wood *et al.* is achieved by changing the value for E_d to 1,75 eV. However, although the decrease with temperature is definite, it is unknown whether the gradient is accurate. Since temperatures were extrapolated from measurements taken ca. 80-180°$_p$C above the growth temperature, it is possible that

non-linearity in the relationship between the pyrometer and Eurotherm controller distorted the temperature scale.[34] In terms of reproducible InN_xSb_{1-x} growth, assuming that this non-linearity is constant, this is not thought to be important.

As seen in previous studies of InN_xSb_{1-x} growth,[25,35] the maximum level of substitutional N incorporated was less than in GaN_xSb_{1-x} and much less than in GaN_xAs_{1-x},[29,36,37] with similar decrease in the onset of the plateau regions.

Assuming that the surface roughness results from thermal oxide removal, it is expected that the surfaces of the InN_xSb_{1-x} films will be similar to InSb. Furthermore, higher growth temperatures should yield surfaces with wider terraces and a lower RMS roughness. Indeed, AFM analysis of the InN_xSb_{1-x} samples indicated similar changes in surface morphology to those seen in InSb (Figure 6.7, Figure 6.8). Low growth temperatures resulted in a rough surface with indistinct and densely-packed step edges, with samples grown at $T_g \geq 350°_pC$ having wider terraces and generally flatter surfaces. Surface roughness generally decreased with increasing growth temperature, but anomalous RMS values were observed (Table 6.1), suggesting that the roughness from the oxide removal process persisted on some samples (Figure 6.9).

Growth Temperature [$°_pC$]	RMS Roughness [nm]
270	1.805
285	0.530
325	3.015
350	0.471
365	0.448

Table 6.1: Roughness values recorded for the InN_xSb_{1-x} samples grown at 0.5 μm h^{-1} and the temperatures indicated.

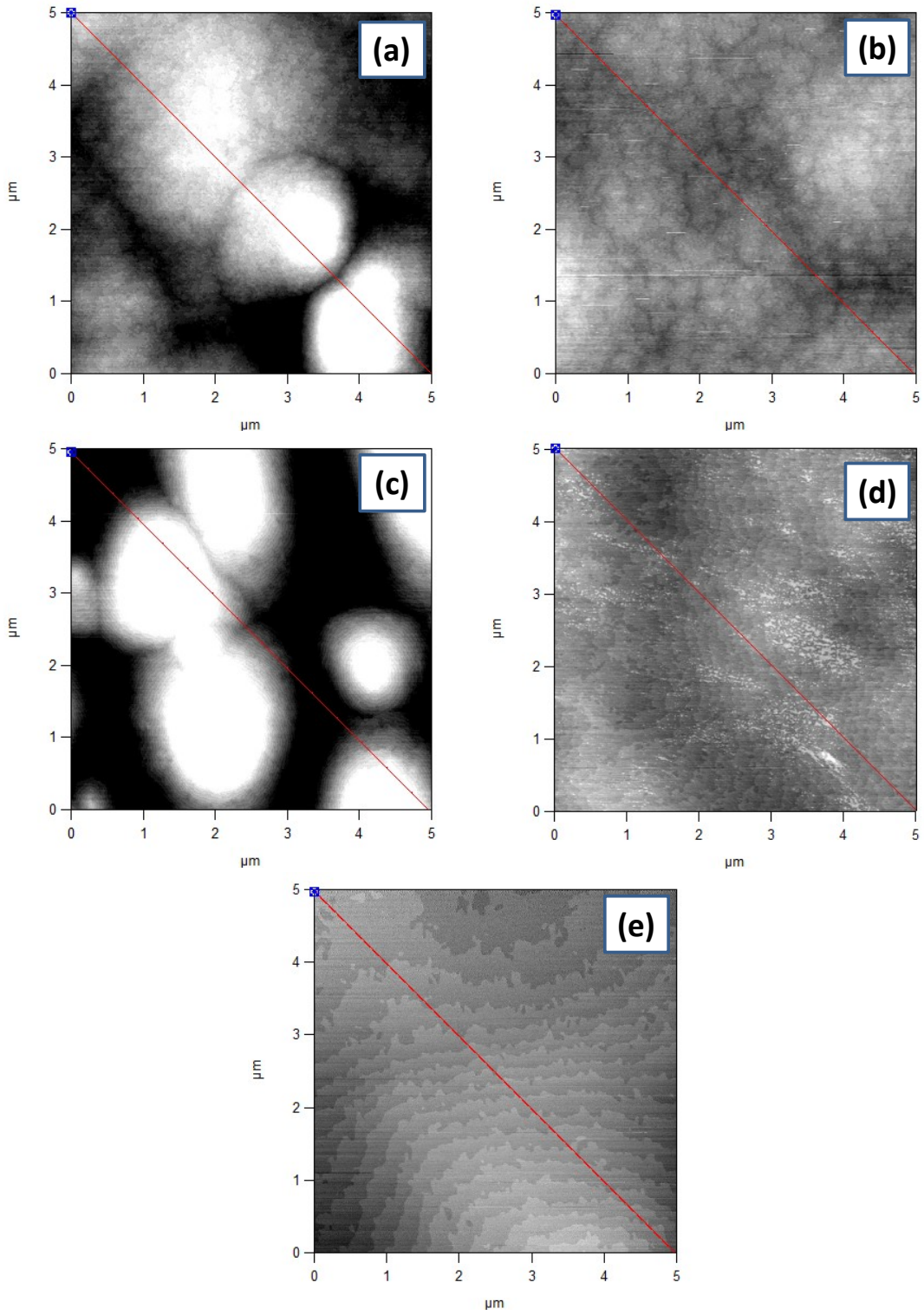

Figure 6.7: 5 µm x 5 µm AFM topographs showing the surface morphology of the InN_xSb_{1-x} samples grown at 0.5 µm h^{-1} and (a) 270°$_p$C, (c) 325°$_p$C, (d) 350°$_p$C and (e) 365°$_p$C. The substitutional nitrogen content values are (a) 1.125%, (b) 0.54%, (c) 0.26% and (d) 0.02%. The red lines indicate the source of the cross section profiles (Figure 6.8). The vertical height for each image is 4 nm.

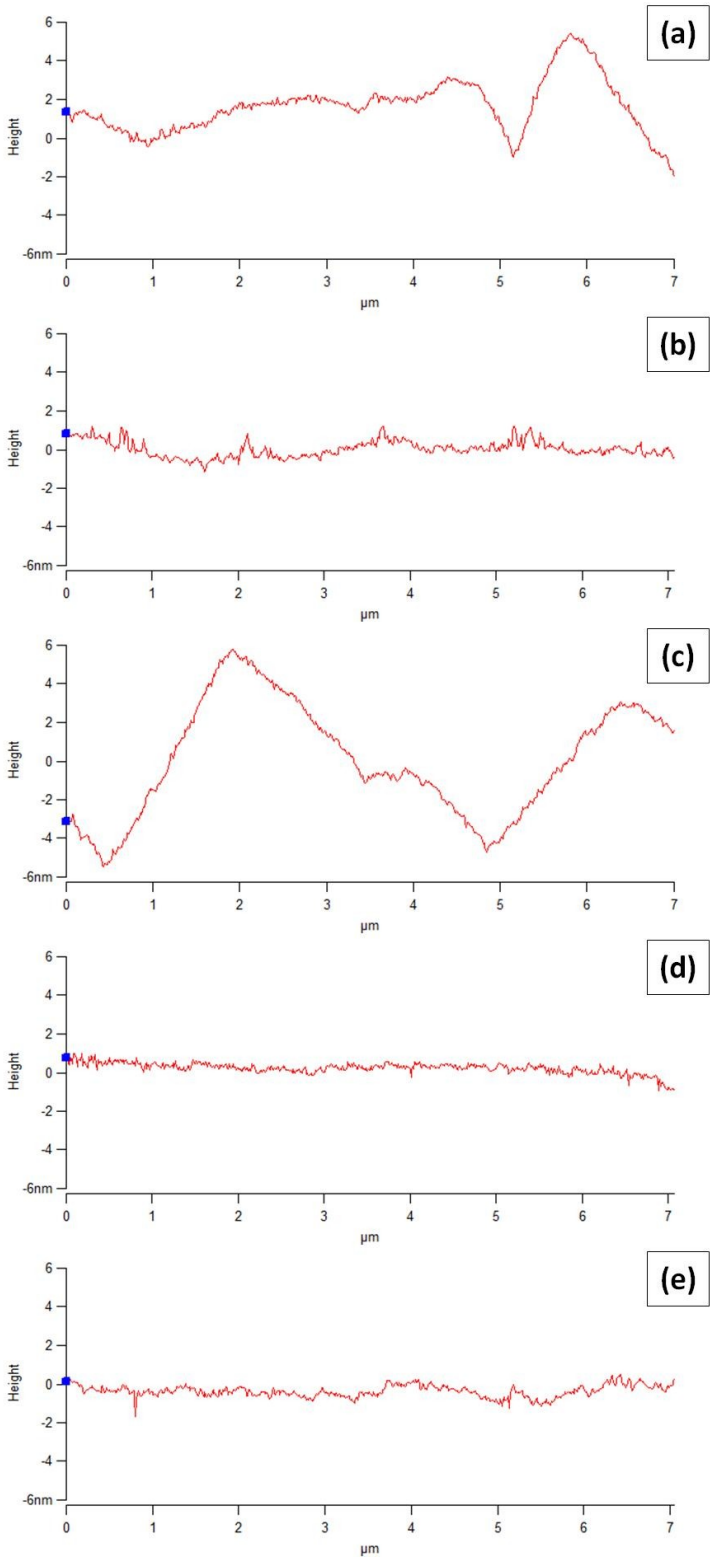

Figure 6.8: AFM height cross sections indicated by the red lines in Figure 6.7 and corresponding to growth at (a) 270°$_p$C, (b) 285°$_p$C, (c) 325°$_p$C, (d) 350°$_p$C and (e) 365°$_p$C,. Sections (a) and (c) exhibit a large height range, whereas (b), (d) and (e) are observed to be comparatively smooth. It is thought that the anomalously large range in (c) is due to variability in the surface quality, following thermal oxide removal.

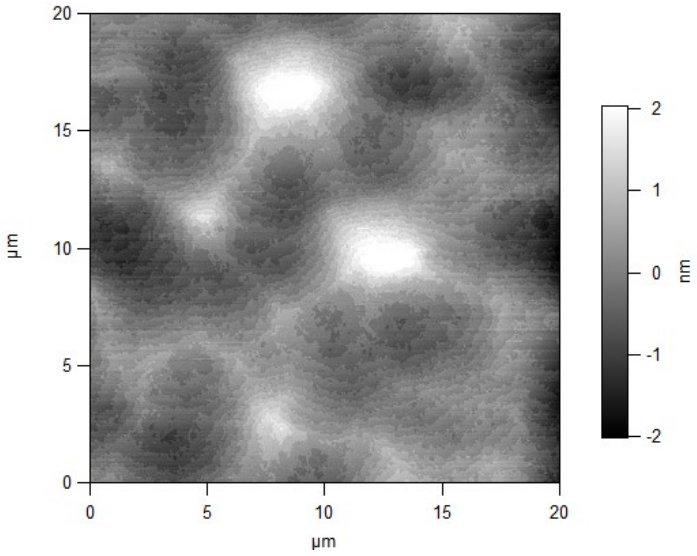

Figure 6.9: A 20 µm x 20 µm AFM topograph of an InN_xSb_{1-x} sample grown at 0.5µm h^{-1} and 365°$_p$C. Despite the wide terraces, the sample surface is observed to remain relatively rough.

The feature observed on the surface of the sample grown at 350°$_p$C (Figure 6.7e) is thought to result from indium droplets, resulting from non-congruent evaporation of InSb (Figure 6.10). This suggests that the Sb_2 flux was terminated at too high a temperature during cooling, although the other samples were unaffected.

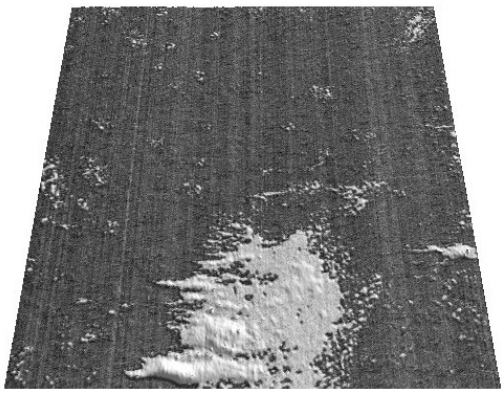

Figure 6.10: A 3D rendering of a 5 µm x 5 µm region of the InN_xSb_{1-x} sample grown at 350°$_p$C. The image is shown with phase contrast, indicating that the composition of the material shown in white differs from the remainder of the surface. This suggests indium aggregation as a result of insufficient Sb_2 flux during the cooling of the sample.

AFM data presented by Zhang *et al.* indicates that flat surfaces with sub-nanometer RMS roughness values for InN_xSb_{1-x} films may be achieved through MBE growth, following deposition of a 0.15 µm InSb buffer layer.[25] However, it appears that these values were obtained from 1 µm x 1 µm scans, which may have been sufficiently small to avoid sampling roughness of the magnitude observed in Figure 6.7. Performing roughness measurements over a smaller region can significantly affect the RMS roughness values determined, as illustrated by data gathered from both 5 µm x 5 µm (1.735 nm) and 1 µm x 1 µm (0.661 nm) regions of the same AFM scan of the InSb sample grown at 350°$_p$C (Figure 6.11).

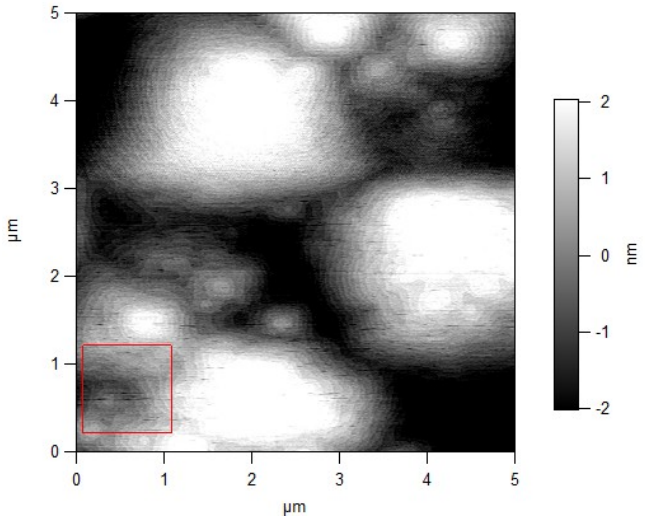

Figure 6.11: A 5 µm x 5 µm AFM topograph indicating the effect that the size and choice of sampling region may exert upon rms roughness measurements. The global rms roughness value of the scan was determined to be 1.735 nm, with the 1 µm x 1 µm region (red box) giving a value of 0.671 nm.

Experiments to determine the growth rate dependence of N content gave unexpected results. In contrast to the data collected as a function of temperature, where a clear trend was evident, there was no such correlation as a function of growth rate for the samples grown at 270°$_p$C (Figure 6.12). Closer examination of the XRD data

indicated that the composition in two of the samples varied throughout growth. A systematic change was not seen, as the N content rose during the growth of one sample and decreased in the other.

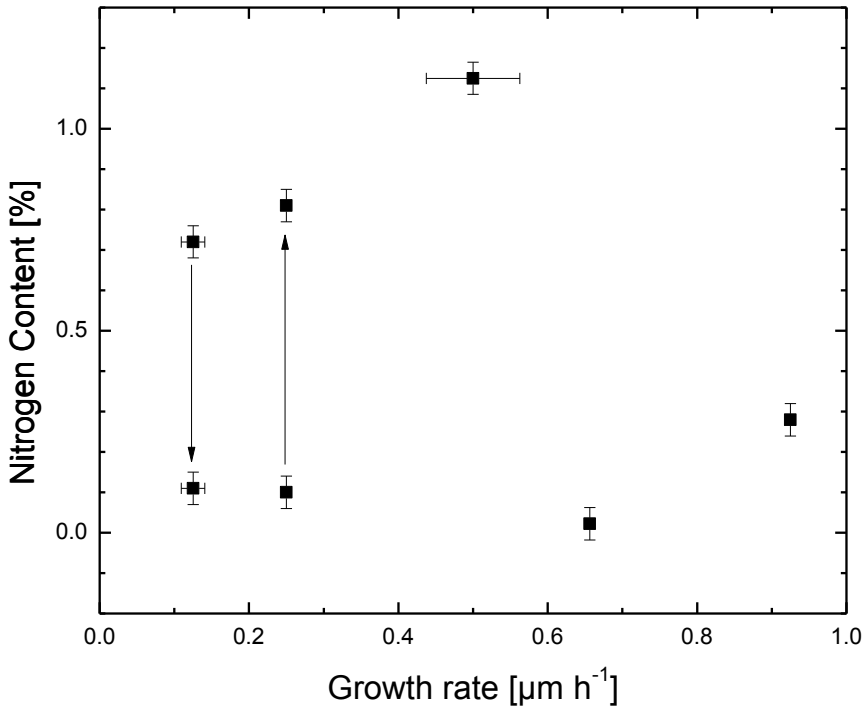

Figure 6.12: A plot of N content as a function of growth rate for InN_xSb_{1-x} films grown at 270°$_p$C. For the samples grown at 0.125µm h^{-1} and 0.25µm h^{-1}, the arrows indicate the change of composition as a function of deposition time. Where growth rates could not be corrected, due to lack of thickness measurements, uncertainties are indicated as the largest observed deviation between nominal and observed growth rates.

Although these results are not particularly useful in determining composition as a function of growth rate, one conclusion may be drawn, which is that the growth must take place under conditions where nitrogen may be reproducibly incorporated into InSb.

C-DIC microscopy showed most samples had a rough surface, similar to that observed for InSb (Figure 6.4). However, the samples grown at nominal rates of

0.125 µm h^{-1} and 0.25 µm h^{-1} feature metallic droplets for both growth temperatures employed (Figure 6.13).

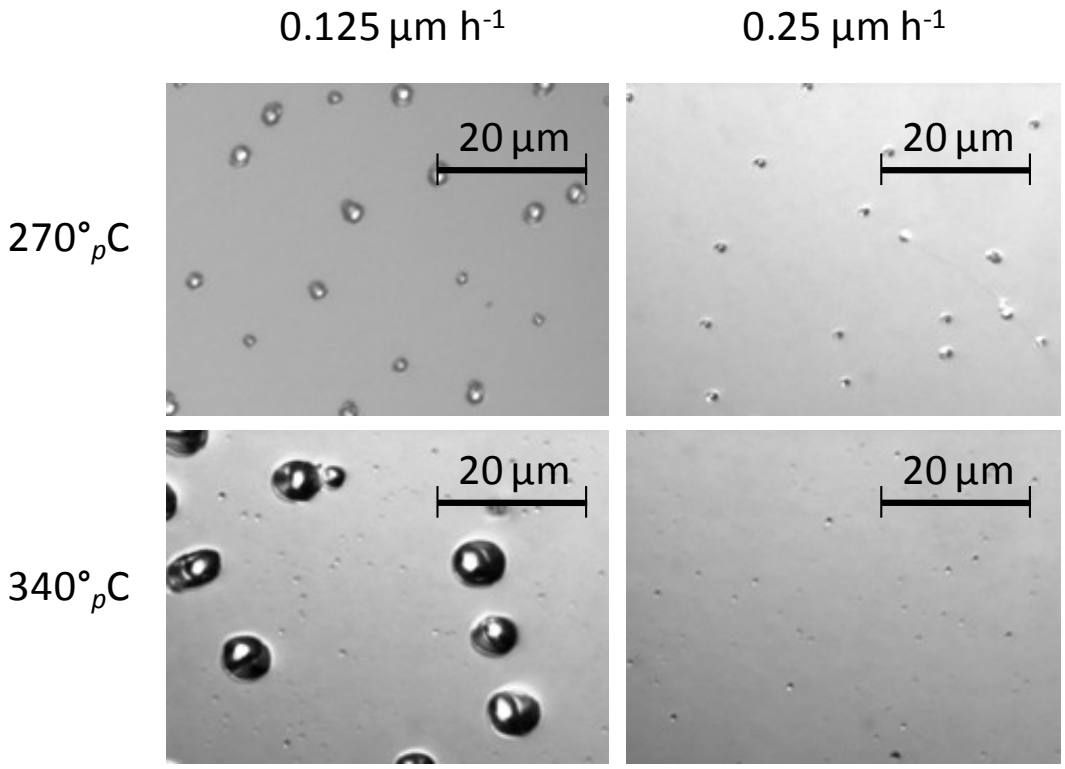

Figure 6.13: C-DIC images of InN_xSb_{1-x} samples grown at the temperature values and rates indicated. The droplets are larger for samples grown at the lowest growth rate, with the largest droplets on the sample grown at the lowest rate and highest temperature. This supports the suggestion that instability in the Sb valved source caused the V:III ratio to drop and formed corresponding In droplets.

It is thought that, as was observed for the growth of GaN_xSb_{1-x} films at low growth rates, an unintentional reduction in Sb_2 flux may have occurred due to valve drift, resulting in In droplet formation.

AFM analysis showed a range of morphologies in the series of samples grown at 270°$_p$C, with a mosaic-like morphology for samples grown at nominal group III rates of 0.125 µm h^{-1} and 0.25 µm h^{-1} (Figure 6.14). For these samples, each of the surface tiles had a relatively flat upper face. These decreased slightly in size with

increasing growth rate. The sample grown at 0.5 μm h^{-1} had a relatively rough surface, although a number of step edges were visible. Increasing the growth rate to 1.0 μm h^{-1} improved the surface quality, with the appearance of well-defined terraces. The roughness values obtained are indicated in Table 6.2.

The tile features are of comparable size to the InSb nanocrystals described by Watanabe *et al*.[38] In this publication, the nanocrystal formation appears to have been the result of growth nucleation at indium droplets on a Se-terminated GaAs surface. Clearly, the growth described here differs from that described by Watanabe *et al*., but it may indicate that some phase separation occurred at low growth rates, with long surface exposure times leading to a larger nitrogen incorporation. Also, samples exhibiting this morphology are those with N composition varying as a function of deposition time (Figure 6.12). Given the observed metallic droplets, the tile features may have a high concentration of InN on the surface resulting from an Sb_2 deficit during growth.

Growth Rate [μm h^{-1}]	RMS Roughness [nm]
0.125	2.925
0.25	3.357
0.5	0.394
0.75	0.394
1.0	0.507

Table 6.2: RMS roughness values obtained from the InN_xSb_{1-x} samples grown at 270°$_p$C and the growth rates indicated.

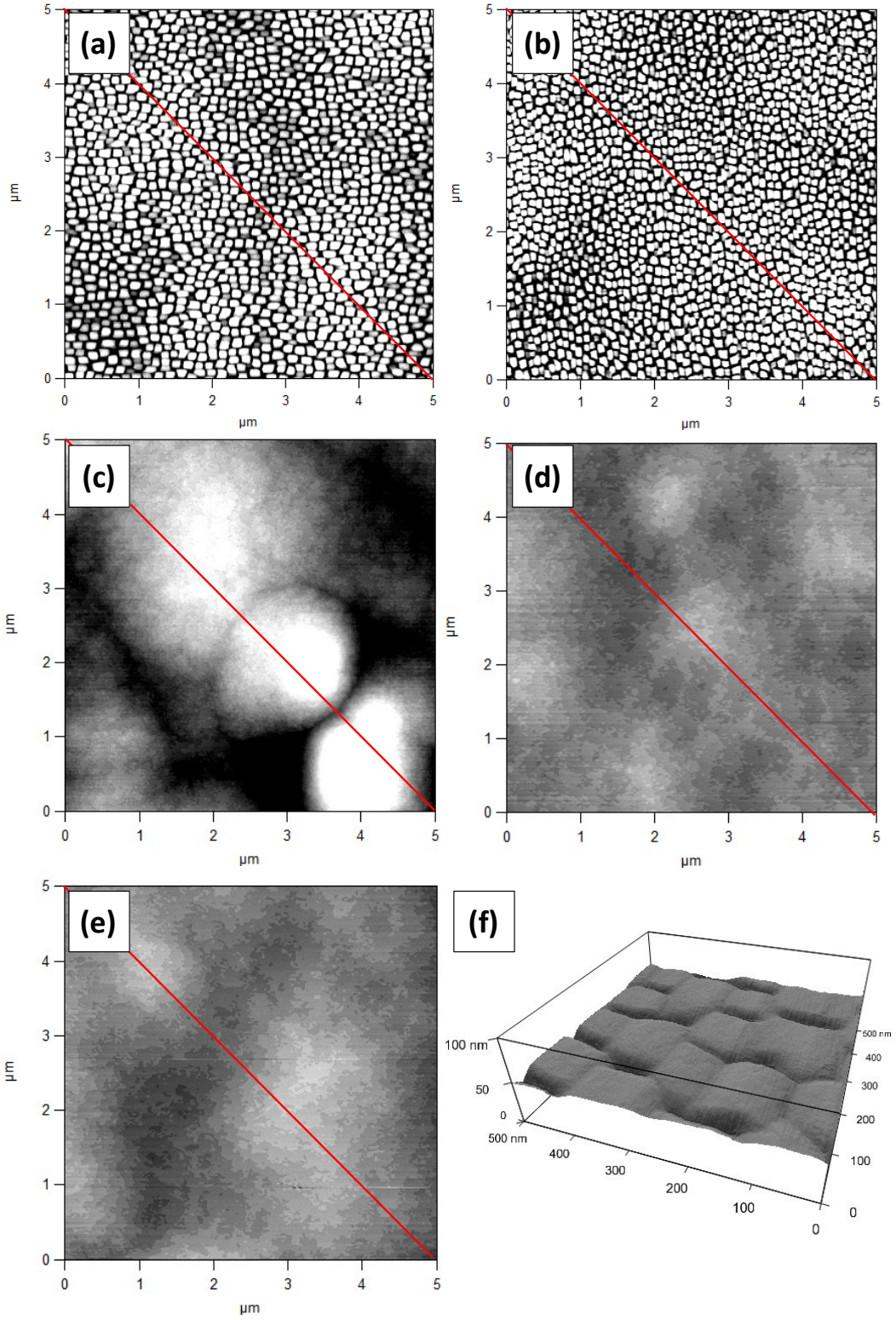

Figure 6.14: 5µm x 5µm AFM topographs from InN_xSb_{1-x} films grown at 270°$_p$C and (a) 0.125 µm h^{-1}, (b) 0.25 µm h^{-1}, (c) 0.5 µm h^{-1}, (d) 0.75 µm h^{-1} and (e) 1.0 µm h^{-1}. The substitutional nitrogen contents are (a) 0.11-0.72%, (b) 0.1-0.81%, (c) 1.13%, (d) 0.02% and (e) 0.28%. The vertical height in each image is 4 nm, with each red line denoting the orientation of the cross section profiles (Figure 6.15). A 3D rendering of a 500 nm x 500 nm scan from the sample depicted in (a) is also shown (f).

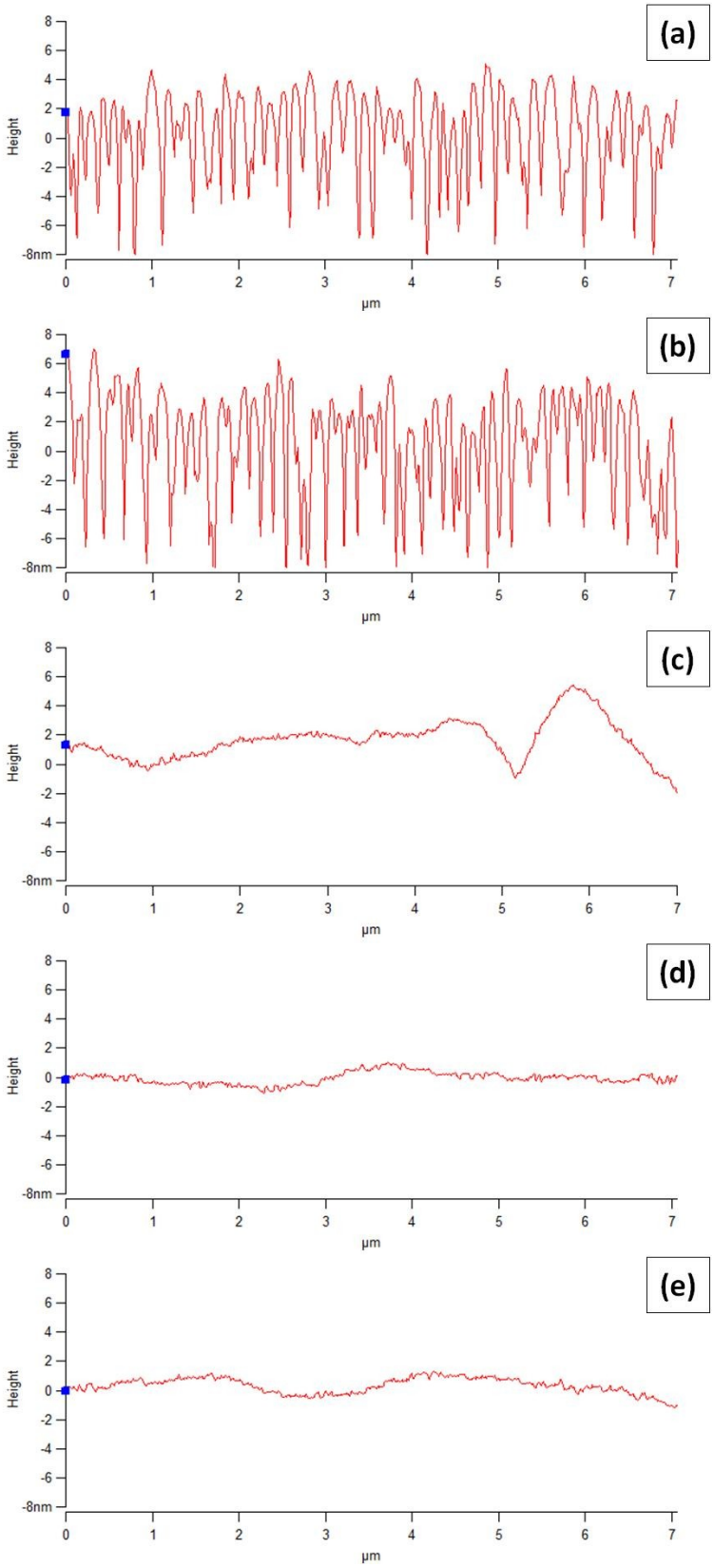

Figure 6.15: AFM height cross section profiles, indicated by the red lines in Figure 6.14. The significant roughness caused by the mosaic-like morphology in (a) and (b) is apparent. The smaller roughness is visible in (d) and (e).

Analysis of samples grown at 340°$_p$C indicated an increase in N content with increasing growth rate (Figure 6.16), in contrast to the results from GaN_xSb_{1-x} and those published for GaN_xAs_{1-x} and $Ga_xIn_{1-x}N_yAs_{1-y}$.[29-31] However, Jefferson *et al.* suggest that N incorporation in InN_xSb_{1-x} initially increases as a function of growth rate, before a subsequent decrease is observed.[26]

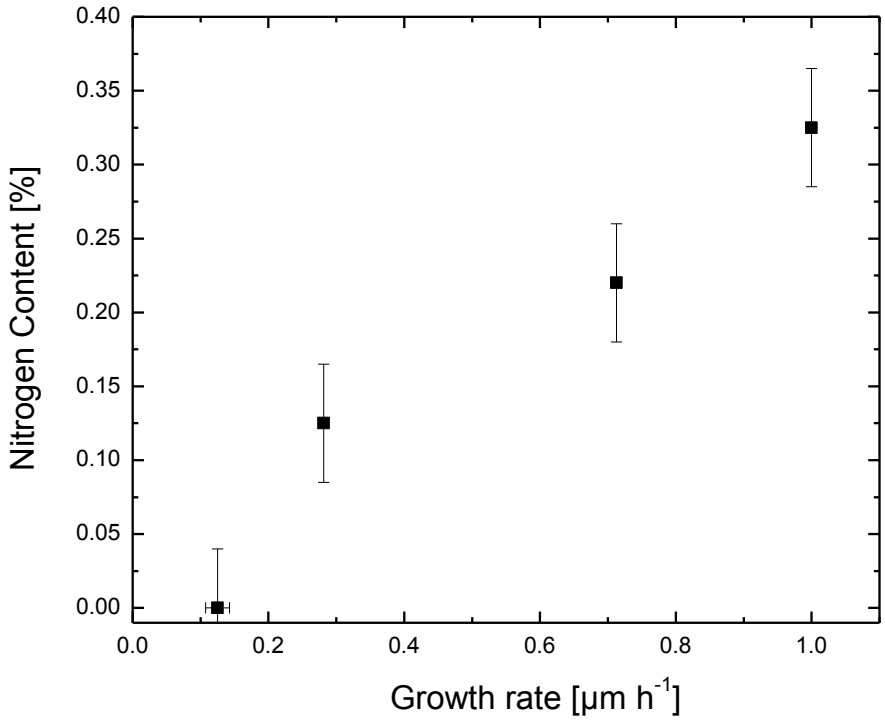

Figure 6.16: A plot of nitrogen content as a function of growth rate for InN_xSb_{1-x} films grown at 340°$_p$C. The nitrogen content is low, as the temperature lies within the fall-off region (Figure 6.6). For all samples except that nominally grown at 0.125µm h^{-1}, growth rates have been corrected, according to thickness determination by XRD. For this point, an uncertainty corresponding to the largest deviation from nominal growth rate has been applied.

AFM analysis revealed an improvement in surface morphology for the series grown at 340°$_p$C as a function of increasing growth rate (Figure 6.17), like the samples grown at 270°$_p$C. The RMS roughness values obtained are indicated in Table 6.3.

Growth Rate [µm h^{-1}]	RMS Roughness [nm]
0.125	0.878
0.25	0.482
0.75	0.285
1.0	0.283

Table 6.3: RMS roughness values obtained from the InN_xSb_{1-x} samples grown at 340°$_p$C and the growth rates indicated.

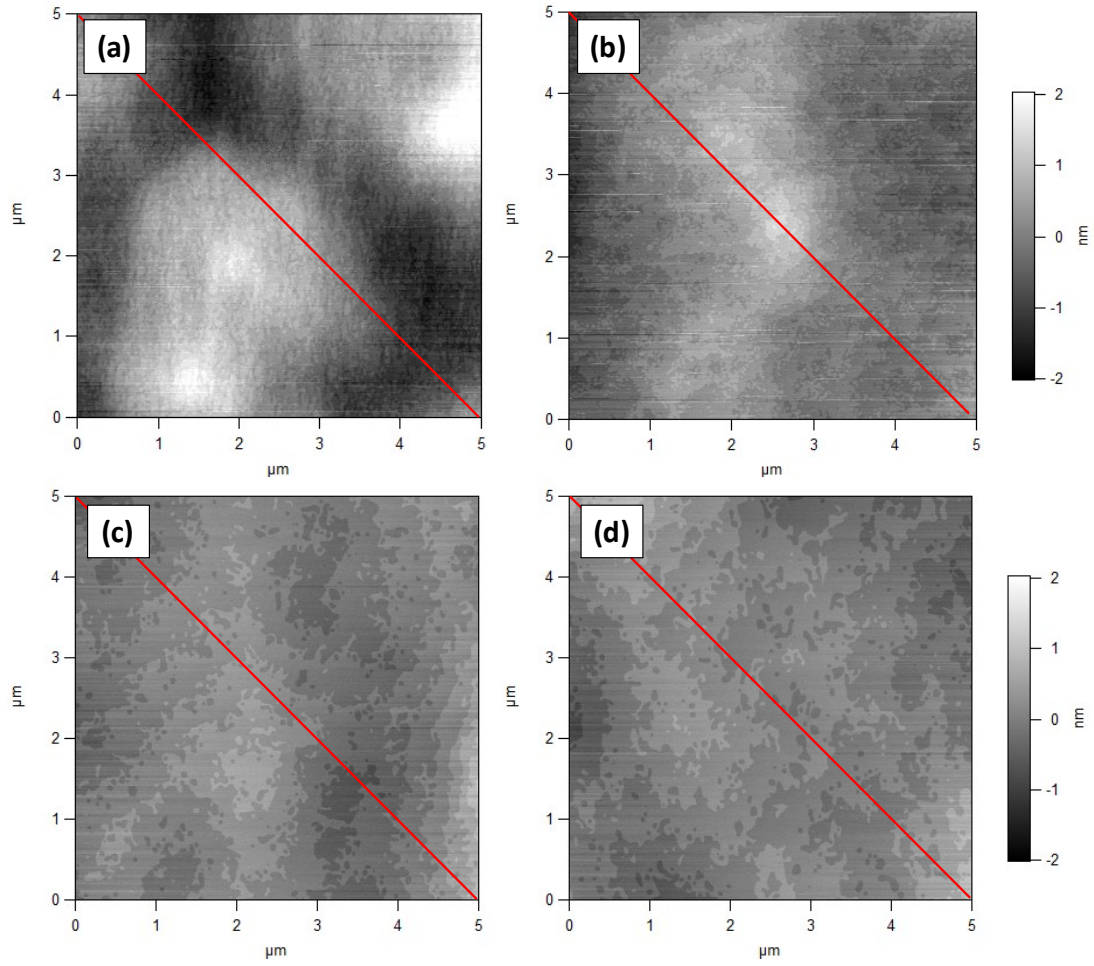

Figure 6.17: 5µm x 5µm AFM topographs showing the surface morphology of InN_xSb_{1-x} films grown at 340°$_p$C with nominal growth rates of (a) 0.125 µm h^{-1}, (b) 0.25 µm h^{-1}, (c) 0.75 µm h^{-1} and (d) 1.0 µm h^{-1}. The substitutional nitrogen content values are (a) 0%, (b) 0.125%, (c) 0.22% and (d) 0.325%. The quality of the surface improved as a function of increasing growth rate, with a corresponding decrease in RMS roughness. The red lines indicate the orientation of the cross-section profiles recorded (Figure 6.18).

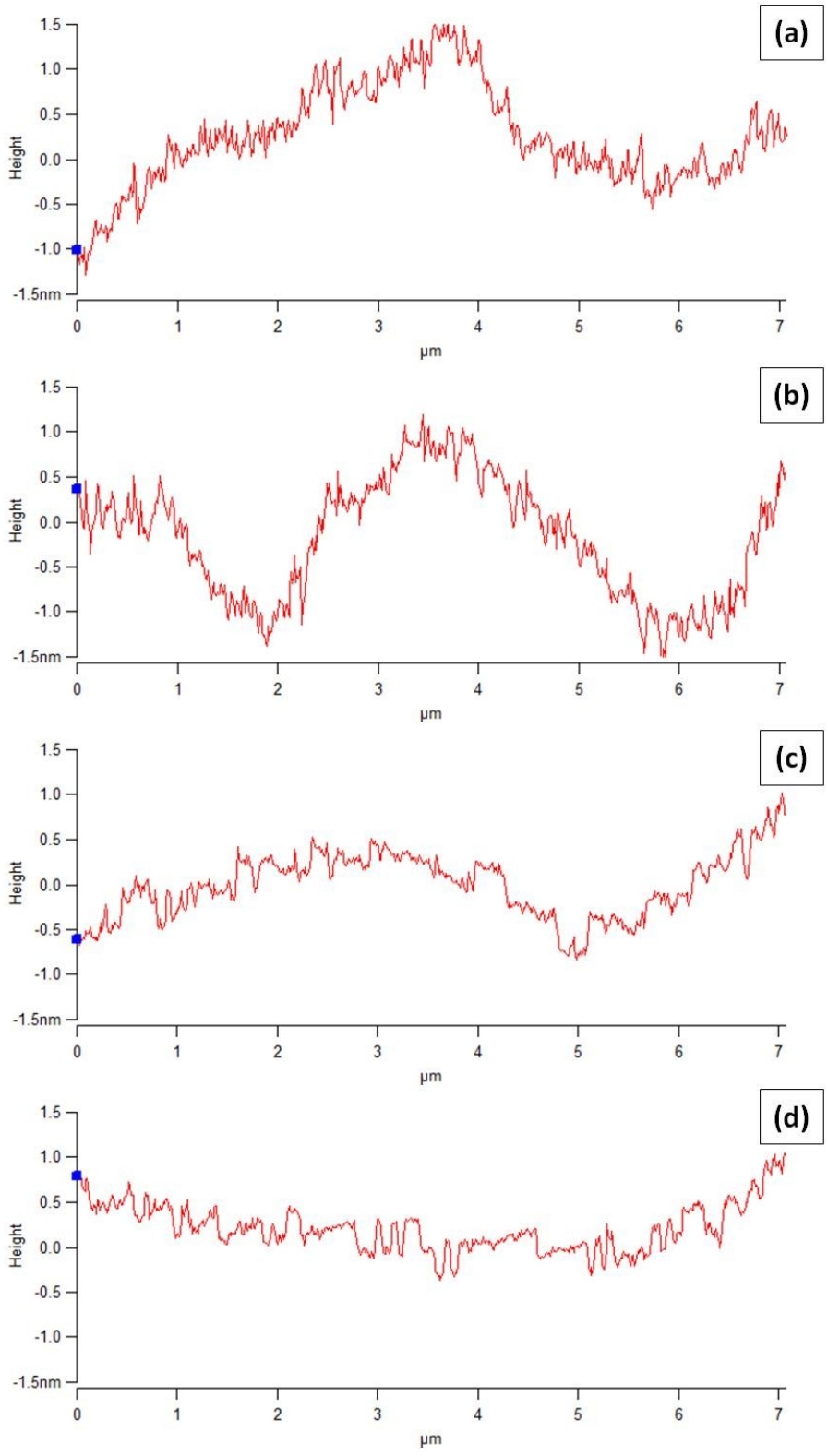

Figure 6.18: AFM height cross-sectional profiles of the samples in Figure 6.17. While there is some variation in the surface roughness, it is less than that observed for the series of samples grown at 270°$_p$C. Considering the rough surface that persisted for the InSb sample grown at 400°$_p$C (Figure 6.5c), this is not thought necessarily thought to result from growth at a higher temperature, however.

For the samples grown at 340°$_p$C, there was no evidence of the strange morphology observed for the samples grown at 270°$_p$C with low growth rates. If the mosaic tile features arise from phase separation, it is likely that temperature contributes to their disappearance. It is normally expected that phase separation would occur to a greater degree at lower temperatures and faster at higher temperatures. However, as the nitrogen content decreases with increasing temperature, the possibility of phase separation is smaller.

Apart from the mosaic-like morphology, it is difficult to see whether N incorporation results in significant morphological change, as the parameter space of growth conditions was larger in the case of InN_xSb_{1-x} growth than InSb. However, the results indicate that an increase in the incorporated N content and improved surface quality result from increased growth rates, in contrast to the findings of chapter 5.

6.3.3 The variation in nitrogen content of III-V-N alloys:

From the results of this investigation and previous studies, it is more difficult to incorporate significant quantities of N into epitaxially-grown InSb than GaSb which, in turn, is incorporates less than GaAs. Since GaN_xAs_{1-x} films were not grown in this study, the methods of production will necessarily differ from the samples grown here. A model of alloy growth which incorporates pseudomorphic strain has been devised. This shows a difference in calculated GaP_xAs_{1-x}/GaAs and InP_xAs_{1-x}/InP film compositions for calculations made with and without strain.[32] In the case of GaP_xAs_{1-x} growth on GaAs, the strain acts against an decrease in bond length from GaAs to GaP, whereas the strain present in the growth of InP_xAs_{1-x} on InP causes the

pseudomorphic layer to be commensurate with the larger InP lattice parameter, thus accommodating the InP component to a greater degree. These factors suggest that, where strain is present, it acts to lower the free energy of one binary product with respect to the other. Bond distortion and a change in the effective bond energy has been calculated for a number of III-III-V materials.[39] Extending this to III-V-N films, for GaN_xAs_{1-x}, the lattice parameter of GaAs is larger than that of GaN; a difference that is larger still in the case of GaSb and GaN. Where InN and InSb are compared, there is a smaller mismatch between the respective lattice parameters, although the bond energy of InN is ca. ~13% less than that of GaN,[40] which could account for a lower degree of bond distortion having a greater net effect on the bond energy.

6.4 Conclusions:

InN_xSb_{1-x} films were grown and found to have $0 \leq x \leq 0.0125$. Measurements of the relationship between N content and growth rate yielded mixed results, with growth conducted at 270°$_p$C hampered by instrumental issues. Samples produced at 340°$_p$C, however, showed an increase in substitutional nitrogen as a function of increasing growth rate. This is in contrast to both GaN_xAs_{1-x} and the results obtained in this thesis for GaN_xSb_{1-x}. This implies that a different mechanism may dominate in the growth of InN_xSb_{1-x} films, with the rate of overgrowth playing a crucial role in nitrogen incorporation.

The temperature dependency of the level of substitutional N followed a similar trend to that observed in both GaN_xAs_{1-x} and GaN_xSb_{1-x}, although there was a more

gradual decrease in N content as a function of temperature. While this potentially corresponds to a lower energy of nitrogen desorption from the surface, further experiments are required to determine the accuracy of temperature measurements.

Considering the effects of bond distortion, an explanation has been given for the lower N levels in InSb than GaN_xSb_{1-x} and GaN_xAs_{1-x}.

Growth and characterisation of InSb and InN_xSb_{1-x} films have highlighted a number of challenges. In particular, InSb as a substrate material is prone to adhere to the mounting assembly unlike GaSb or GaAs. Furthermore, thermal oxide removal is thought to have resulted in a rough surface which was still measureable by AFM after 0.4 μm of growth. However, the surface morphology, as characterised by AFM, did not reveal any characteristics associated with an excess of group III or group V and exhibited monolayer step terraces for all growth temperatures. This suggests that the V:III ratio employed was satisfactory, with wider terraces indicating a better quality of growth at a higher temperature. An increase in surface quality was also observed with an increase in growth rate.

Extrapolation from pyrometer readings as a function of measurements from the Eurotherm controller was thought to provide the most consistent basis for temperature determination. However, there may be distortion in the temperature scale due to non-linearity at lower temperatures. Future investigation to determine both consistency and accuracy of this temperature method is desirable.

[1] V. Ivanov, A. Boudza, N. Kutt, N. Ledentsov, S. Ruvimov, V. Shaposhnikov, S. Kop, Journal of Crystal Growth **156**, 191-205 (1995).

[2] E. Michel, G. Singh, S. Slivken, C. Besikci, P. Bove, I. Ferguson, M. Razeghi, Applied Physics Letters **65**, 3338 (1994).

[3] B. V. Shanabrook, L. J. Whitman, Journal of Crystal Growth **176**, 888-893 (1997).

[4] G. M. Williams, C. R. Whitehouse, C. F. McConville, A. G. Cullis, T. Ashley, S. J. Courtney, C. T. Elliott, Applied Physics Letters **53**, 1189 (1988).

[5] A. J. Noreika, M. H. Francombe, C. E. C. Wood, Journal of Applied Physics **52**, 7416–7420 (1981).

[6] A. J. Noreika, J. Greggi Jr, W. J. Takei, and M. H. Francombe, Journal of Vacuum Science Technology **1**, 558–561 (1983).

[7] A. J. Noreika, J. Greggi Jr., W. J. Takei, M. H. Francombe, Journal of Vacuum Science Technology **1**, 558–561 (1983).

[8] A. J. Noreika, M. H. Francombe, C. E. C. Wood, Journal of Applied Physics **52**, 7416 (1981).

[9] J. I. Chyi, D. Biswas, S. V. Iyer, N. S. Kumar, Applied Physics Letters **54**, 1016-1018 (1989).

[10] G. M. Williams, I. M. Young, Journal of Crystal Growth **62**, 219–224 (1983).

[11] P.S. Dutta, H. L. Bhat, Applied Physics Reviews **81**, 5821-5870 (1997).

[12] T. D. Veal, C. F. McConville, M. J. Lowe, Surface Science **499**, 251-260 (2002).

[13] K. F. Longenbach, W. I. Wang, Symposium A Quarterly Journal in Modern Foreign Literatures **59**, 2427-2429 (1991).

[14] F. M. Mohammedy, J. Deen, Journal of Materials Science: Materials in Electronics, 1039-1058 (2009).

[15] Y. J. Jin, D. H. Zhang, X. Z. Chen, X. H. Tang, Journal of Crystal Growth **318**, 356-359 (2011).

[16] P. Liu, J. Maan, Physical Review B **47**, 16274-16278 (1993).

[17] H. T. Pham, S. F. Yoon, D. Boning, S. Wicaksono, Journal of Vacuum Science & Technology B: Microelectronics and Nanometer Structures **25**, 11 (2007).

[18] N. Jones, C. Norris, C. L. Nicklin, P. Steadman, J. S. G. Taylor, C. F. McConville, A. D. Johnson, Applied Surface Science **123**, 141–145 (1998).

[19] O. Tereshchenko, Applied Surface Science **252**, 7684-7690 (2006).

[20] C. F. McConville, T. S. Jones, F. M. Leibsle, S. M. Driver, T. C. Q. Noakes, M. O. Schweitzer, N. V. Richardson, Physical Review B **50**, 14965 (1994).

[21] P. John, T. Miller, and T. C. Chiang, Physical Review B **39**, 1730 (1989).

[22] P. Thibado, Journal of Crystal Growth **175-176**, 317-322 (1997).

[23] R. Droopad, R. L. Williams, S. D. Parker, Semiconductor Science and Technology **4**, 111 (1989).

[24] D. Ban, H. Luo, H. C. Liu, Z. R. Wasilewski, Y. Paltiel, A. Raizman, A. Sher, Applied Physics Letters **86**, 201103 (2005).

[25] Y. H. Zhang, P. P. Chen, H. Yin, T. X. Li, W. Lu, Journal of Physics D: Applied Physics **43**, 305405 (2010).

[26] P. H. Jefferson, L. Buckle, D. Walker, T. D. Veal, S. Coomber, P. A. Thomas, T. Ashley, C. F. McConville, Physica Status Solidi (RRL) – Rapid Research Letters **1**, 104-106 (2007).

[27] L. Bhusal, A. Freundlich, Applied Surface Science **255**, 703-705 (2008).

[28] T. Veal, I. Mahboob, C. McConville, Physical Review Letters **92**, 92-95 (2004).

[29] Q. X. Zhao, S. M. Wang, M. Sadeghi, A. Larsson, M. Friesel, M. Willander, Applied Physics Letters **89**, 031907 (2006).

[30] Z. Pan, L. H. Li, W. Zhang, Y. W. Lin, R. H. Wu, Applied Physics Letters **77**, 214 (2000).

[31] V. A. Odnoblyudov, A. R. Kovsh, A. E. Zhukov, N. A. Maleev, Semiconductors **35**, 554-559 (2001).

[32] A. Y Egorov, A. R. Kovsh, V. M. Ustinov, A. E. Zhukov, P. S. Kop'ev, C. W. Tu, Journal of Crystal Growth **188**, 69-74 (1998).

[33] , R. J. Hauenstein, M. L. O'Steen, T. C. McGill, Applied Physics Letters **68**, 1510 (1996).

[34] H. Yao, P. G. Snyder, J. A. Woollam, Journal of Applied Physics **70**, 3261-3267 (1991).

[35] L. Buckle, S. D. Coomber, T. Ashley, P. H. Jefferson, D. Walker, T. D. Veal, C. F. McConville, P. A. Thomas, Microelectronics Journal **40**, 399-402 (2009).

[36] Y. Lin, Thin Solid Films **368**, 249-252 (2000).

[37] S. Thomas, S. White, P. R. Chalker, T. J. Bullough, T. B. Joyce, Journal of Materials Science: Materials in Electronics **13**, 525–529 (2002).

[38] Y. Watanabe, F. Maeda, and M. Oshima, Applied Surface Science **82-83**, 136-140 (1994).

[39] D. Talwar, D. Sofranko, C. Mooney, S. Tallo, Materials Science and Engineering B **90**, 269-277 (2002).

[40] R. Shul, Solid-State Electronics **42**, 2269-2276 (1998).

Chapter 7

"The best preparation for good work tomorrow is to do good work today."

Elbert Hubbard (1856 - 1915)

Results are presented of preliminary experiments that were conducted to probe the. growth of $In_xGa_{1-x}N_ySb_{1-y}$ films. Preliminary results are also presented from temperature determination of an InSb surface, using a pyrometer operating at 1.6 µm.

7.1 Introduction

Initial results are presented for the growth of the quaternary $Ga_xIn_{1-x}N_ySb_{1-y}$ alloy, demonstrating the potential for tuneable band gap films, lattice-matched to GaSb. Further experiments are proposed to map the N content as a function of growth rate, substrate temperature and material flux ratios.

Measurements utilising a pyrometer operating at 1.6 μm are reported, and discussed in relation to temperature determination for narrow band gap materials.

7.2 Preliminary Results from $Ga_xIn_{1-x}N_ySb_{1-y}$ Growth:

Preliminary experimental growth has been conducted with respect to $Ga_xIn_{1-x}N_ySb_{1-y}$ films, as the first step towards production of a quaternary alloy exhibiting a tuneable bandgap material lattice matched to GaSb. The primary objective was to establish under which conditions N may be incorporated and to probe any dependency upon growth temperature.

7.2.1 Experimental:

Growth was conducted on cleaved quarter-pieces of unintentionally p-type 2" GaSb(001) wafers (Wafertech). In each case, the wafer was outgassed (300°$_p$C, > 60 minutes) and admitted to the growth chamber. Following thermal oxide desorption, $Ga_xIn_{1-x}Sb$ was grown to a thickness of 0.2 μm at 275-350°$_p$C and an Sb_2:III ratio of 1.2:1. The Ga:In ratio employed was 9:1. In addition to providing a planar surface for a temperature extrapolation to be made, this layer also served as a marker layer

from which the N content could be established. As such, the In, Ga and Sb source parameters were unchanged for the growth of the nitrogen-containing layer. Upon opening the gate valve separating the plasma source from the growth chamber, deposition of $Ga_xIn_{1-x}N_ySb_{1-y}$ (0.4 μm) commenced immediately. After growth, the samples were removed from the system and cleaved for AFM and XRD analyses.

7.2.2 Results and Discussion:

XRD analysis indicated that, for each of the $Ga_xIn_{1-x}N_ySb_{1-y}$ samples, a level of N had been incorporated into the ternary system over the range 0.35-1.97%. The initial series of samples grown alluded to a trend of decreasing substitutional N content as a function of increasing growth temperature (Figure 7.1).

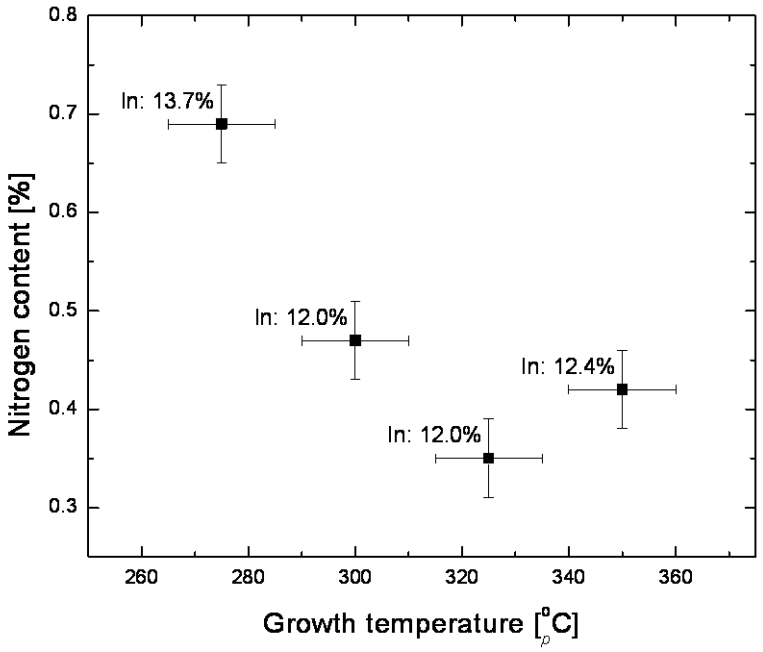

Figure 7.1: A plot displaying the substitutional N content of $Ga_xIn_{1-x}N_ySb_{1-y}$ films produced as a function of growth temperature. The indium content of each sample is shown next to the corresponding datum.

Although the source settings were fixed through the growth of the samples, the varying degree of indium content observed is indicative that growth was not as consistent between samples as would be desired. There is disagreement in the literature pertaining to $Ga_xIn_{1-x}N_yAs_{1-y}$ on the effect of In content upon N content, with assertions made that the proportion of In does influence the level of substitutional N,[1] and that In content does not affect N uptake.[2,3] In either case, a change in the level of Ga flux would necessarily change the V:III:N ratio for growth and could potentially introduce effects associated with a change in growth rate. As such, it is thought that there was a degree of deviation from ideal growth conditions and the possibility of a corresponding effect upon N content.

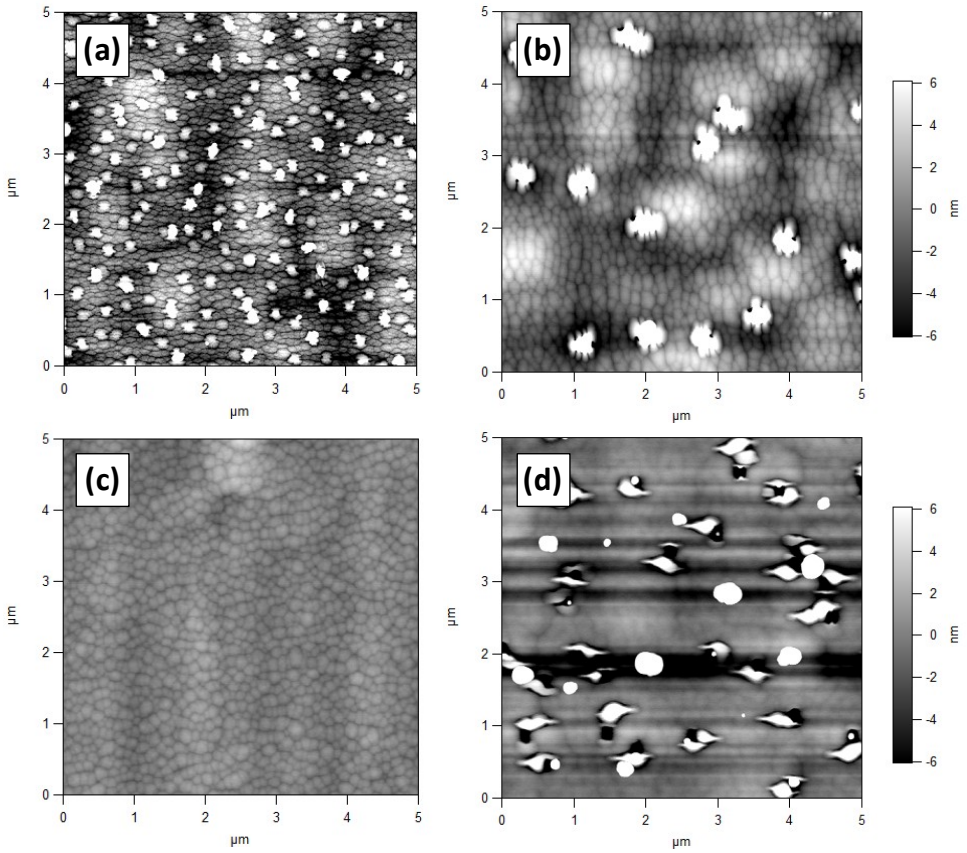

Figure 7.2: 5 µm x 5 µm AFM topographs of $GaxIn_{1-x}N_ySb_{1-y}$ samples grown at 0.5 µm h^{-1} and (a) 275°$_p$C, (b) 300°$_p$C, (c) 325°$_p$C and (d) 350°$_p$C. The data scale for each image is 12 nm.

AFM analysis of the samples revealed surfaces similar to the cobblestone/worm morphology (Figure 7.2), as described previously in chapters 4 and 5. It was observed that there was generally a trend of improving surface morphology with increased growth temperature. For the samples grown at 275°$_p$C, 300°$_p$C and 350°$_p$C, structures were observed on the surface.

For the sample grown at 350°$_p$C, the features appear to be different to those observed for the films produced at lower growth temperatures, which exhibited similarities in height (~20 – 40 nm) and shape (Figure 7.3). For the features arising from lower temperature growth, it appears that they may be formed as a result overgrowth of metallic droplets, due to the differences in probe phase recorded for some of the features.

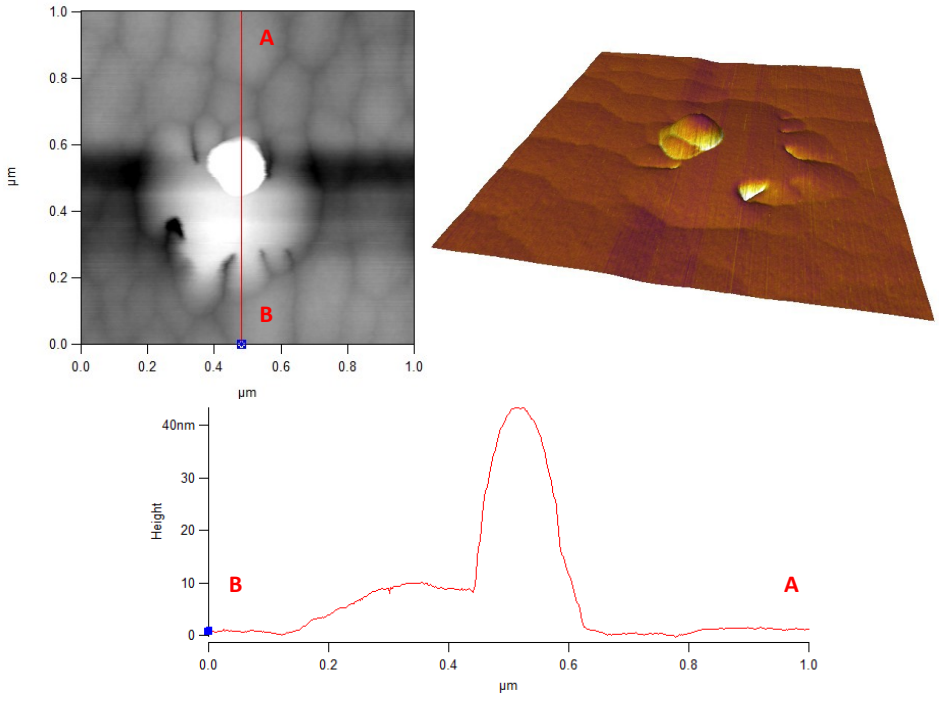

Figure 7.3: A 1 µm x 1 µm AFM topograph with a 20 nm data scale, showing cobblestone morphology and one of the surface features from the sample grown at 300°$_p$C (top left). A 3D rendering has been provided for clarity, with the colour map indicating a difference in the measured phase of the probe (top right). A line profile indicating the height and distribution of the observed feature is also shown (bottom).

An increase of growth temperature from 275°$_p$C to 300°$_p$C lead to enlargement of the lateral dimensions of the features and a decrease in number density from ~1 x 10^9 cm^{-2} to ~5.6 x 10^7 cm^{-2}. These structures were not observed in the sample grown at 325°$_p$C. At this stage, it is unclear why structures should be present on the film grown at 350°$_p$C and further investigation is planned to determine their composition and internal structure.

Of particular interest was the last sample grown of this preliminary investigation. Nominally a repeat of the sample at 325°$_p$C, the In content (12.6%) was observed to be within the range exhibited by the samples produced previously. Upon XRD analysis, however, the N content was determined to be 1.97% (Figure 7.4).

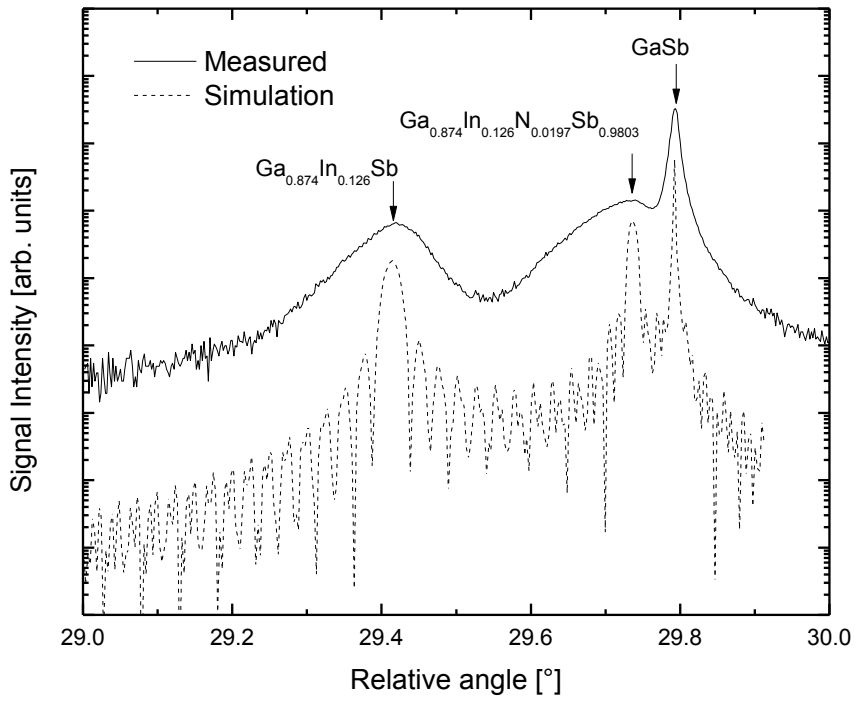

Figure 7.4: A plot showing an XRD 004 rocking curve of the $Ga_{0.874}In_{0.126}N_{0.0197}Sb_{0.9803}$ sample grown and the corresponding simulation. The measured peaks exhibit significant broadening, which may be indicative of poor material quality and are consistent with rocking curves of ternary and polynary films in the available literature.[4-7]

Although the cause of the variation remains unclear, it can be seen from the rocking curve of the $Ga_{0.874}In_{0.126}N_{0.0197}Sb_{0.9803}$ film that peak corresponding to the nitrogen-containing layer has shifted significantly from the ternary layer, almost coinciding with the GaSb substrate peak. It is envisaged that, with further research into the dependency of nitrogen upon factors such as In content, growth temperature and the rate of deposition, lattice-matched materials exhibiting a tuneable bandgap are readily accessible.

7.3 Pyrometric temperature determination (1.6 μm):

Following the discussion of pyrometry as a temperature determination technique in previous chapters, initial measurements have been conducted using a pyrometer sensitive in the 1.6 μm IR region. Undertaken to probe the suitability of such a device for temperature measurements performed during the growth of narrow band gap materials, the objective was to establish the lower bounds of sample temperatures that could be measured, with a view to the potential for extrapolation to lower temperature values.

7.3.1 Experimental:*

A cleaved quarter-piece of unintentionally p-type doped 2" GaSb(001) wafer (Wafertech) was outgassed (300°$_p$C, > 60 minutes) and admitted to the growth chamber. Following thermal oxide desorption under a stabilising Sb_2 flux, a

* Procedure undertaken by Mark Ashwin (Department of Chemistry, University of Warwick)

planarising layer of GaSb was grown, onto which an InSb layer (~ 0.5 μm) was deposited at 0.5 μm h^{-1} and 400°$_p$C.

Following layer deposition, the substrate temperature was set to 325°$_p$C and the sample permitted to attain thermal equilibrium. Data were collected using a Marathon Series 2ML pyrometer (Raytek) while the substrate temperature was ramped to 350°$_p$C at a rate of 1.5°$_e$C min^{-1} and under an overpressure of Sb_2, in order to prevent material degradation.

7.3.2 Results and Discussion:

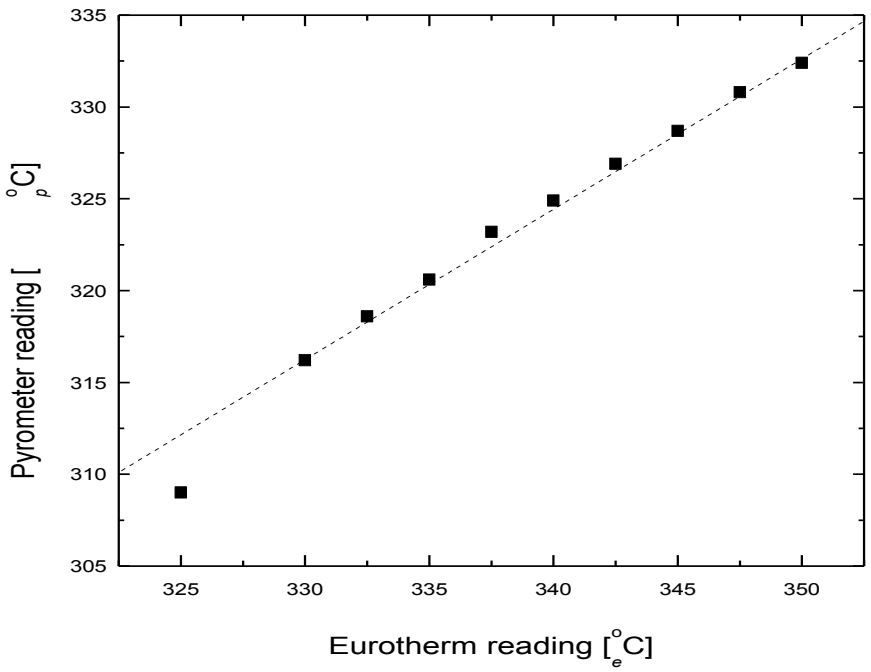

Figure 7.5: Plot of pyrometer reading as a function of the Eurotherm reading. In common with the measurements undertaken using the Modline 3V pyrometer for higher temperatures, the initial datum is lower than the remainder of the points. This may be indicative of the period of time required for the thermocouple feedback control to stabilise.

The data gathered from the pyrometer demonstrate fair linearity in a region inaccessible with the Modline 3V device available throughout this study (Figure 7.5). As with measurements conducted with the Modline 3V apparatus described in chapter 3, the beginning of the ramp demonstrates non-linearity. This is thought to be related to the time over which the feedback loop of the Eurotherm controller stabilises the power output of the heater control unit.

Extending the lower limit of pyrometric temperature determination by > 125°$_p$C, the preliminary measurements demonstrate promise for the low temperature growth of narrow band gap films by direct measurements. Furthermore, the linearity implies that, using the same extrapolation method employed with the Modline 3V instrument for the growth below 450°$_p$C described previously, still lower temperatures may be accessed.

In addition to the benefits with respect particularly to future InN_xSb_{1-x}/InSb growth, there is scope to map phase transitions as a function of surface temperature in a manner not previously possible with the GEN II system. However, prior to application of the pyrometer in growth, further experiments of the type described in chapter 3 are required to ascertain the consistency of measurements and any difference in the susceptibility of the instrument to stray radiation to the Modline 3V apparatus, for example.

7.4 Conclusions:

The results of preliminary experiments demonstrate the growth of N-containing films based on the $In_xGa_{1-x}N_ySb_{1-y}$ ternary alloy, up to an N content of 1.97%.

Furthermore, results allude to the feasibility of lattice-matching the quaternary alloy to a GaSb substrate. Additional investigation has been proposed to elucidate the dependencies of N content and film quality as a function of growth parameters, including material flux ratios. Proposed experiments also include $In_xGa_{1-x}N_ySb_{1-x}$ growth on GaAs substrates and the exploratory research into utilising interfacial misfit arrays which could produce material of low defect density, suitable for IR characterisation and device applications.

Initial results gathered from a pyrometer operating at 1.6 μm indicate that surface temperatures as low as 325°$_p$C may be directly measured for InSb substrates. With the use of such equipment, it is thought that temperature extrapolations of greater reliability are accessible, thus extending further the lower bound of temperatures used for narrow band gap material growth.

[1] D Friedman, Journal Of Crystal Growth **195**, 438-443 (1998).

[2] Z. Pan, L. H. Li, W. Zhang, Y. W. Lin, and R. H. Wu, Applied Physics Letters **77**, 214 (2000).

[3] Masahiko Kondow and Takeshi Kitatani, Semiconductor Science and Technology **17**, 746-754 (2002).

[4] T.J. Garrod, J. Kirch, P. Dudley, S. Kim, L.J. Mawst, and T.F. Kuech, Journal Of Crystal Growth 1-6 (2010).

[5] H. F. Liu, N. Xiang, and S. J. Chua, Applied Physics Letters **89**, 071905 (2006).

[6] P. H. Jefferson, B. R. Bennett, L. Buckle, T. D. Veal, D. Walker, N. R. Wilson, L. F. J. Piper, P. A. Thomas, T. Ashley, and C. F. McConville, Journal Of Crystal Growth **304**, 338–341 (2007).

[7] L. Buckle, S. D. Coomber, T. Ashley, P. H. Jefferson, D. Walker, T. D. Veal, C. F. McConville, and P. A. Thomas, Microelectronics Journal **40**, 399-402 (2009).

Chapter 8

"Now this is not the end. It is not even the beginning of the end. But it is, perhaps, the end of the beginning.

Winston Churchill (1874 - 1965)

Experiments are proposed to provide further insight into the production of high quality dilute nitride material. A discussion of the results obtained in this study is also provided, summarising the achievements of this investigation.

8.1 Proposed Experiments:

Analyses of the experimental growth undertaken in this thesis and literature research have provided the starting points for a number of different future investigations. These arise from ideas that could not be pursued, but could improve our understanding of dilute nitride production.

8.1.1 Temperature Determination:

As described in chapters 3, during the growth of InSb on GaAs, there was observed to be an increase in the growth temperature determined by band-edge thermometry as a function of deposition time. This is consistent with reported observations made both by band-edge thermometry and pyrometer measurements during the growth of InN and GaSb on GaAs. In addition to available literature, chapters 5 and 6 describe the temperature dependency of substitutional N content. As such, the growth of dilute nitrides using GaAs substrates may present the additional problem of compositional variation throughout growth to those encountered in this study, such as the propagation of defects through grown films.

In consideration of the temperature variation, it is proposed equipment be employed in which the substrate temperature may be changed through feedback to minimise temperature variation during film growth. The obvious candidate for this would be a system such as BandiT, as a pyrometer featuring a detection band extending to a sufficiently long wavelength to measure InN_xSb_{1-x} film temperature, for example, would be likely to suffer interference from transmitted radiation through the GaAs

substrate. However, band-edge thermometry applied in this manner would be prone to extinction of the transmitted signal as a function of film thickness.

The pyrometer operating at 1.6 μm has demonstrated that lower growth temperatures are likely to be reproducibly achievable, although further investigation of the type described in chapter 3 is required to ascertain the reliability of the equipment before it is used for growth.

8.1.2 Further Investigation of GaSb:

The heteroepitaxial GaSb/GaAs growth conducted has demonstrated defect-free regions of material, appearing to result from the strain due to mismatch having been dissipated at the interface by an array of misfit dislocations. It is desirable to investigate this further with respect to the growth conditions under which this may be achieved over larger area, particularly with respect to the flux ratios employed and the state of the surface prior to growth.

Some difficulty has been observed with respect to thermal cleaning, with TEM analysis suggesting incomplete oxide removal and a rough interface. While not as severe as was observed in the growth of InSb, it is proposed that alternative methods of wafer processing should be investigated. It is thought that atomic hydrogen cleaning represents a potential solution and should be examined first.

8.1.3 Further Investigation of GaN_xSb_{1-x}:

The results presented earlier demonstrate the way in which substitutional N can be incorporated reproducibly into GaSb. Although fulfilling the primary objective of correlating substitutional N content with the rate and temperature employed for growth, these data do not give an indication of the optical quality of the material produced. It may be the case, for example, that the conditions under which a large degree of N is incorporated may result in a lower material quality. Indeed, it has been reported that an increasing amount of N leads to a decrease in optical quality for GaN_xAs_{1-x}.[1]

The literature disagrees on the effect of V:III ratios on the uptake of N in a growing GaN_xAs_{1-x} film, thus it would be desirable to ascertain how this parameter affects the substitutional N content for GaN_xSb_{1-x} films. To this end, it is envisaged that growth of samples should occur at two temperatures and with the Sb_2:Ga ratio varied from 0.9:1 to 10:1. The temperature was chosen to be ca. 325°$_p$C and 400°$_p$C, values that should fall within (i) the plateau region; and (ii) the region in which N has been observed to decline sharply with an increase in growth temperature. In this way, should a decrease in N content be observed, it may be correlated with regimes in which a varying degree of Sb loss from the surface is likely.

8.1.4 Further Investigation of InSb:

The InSb growth described in chapter 6 was limited by material constraints and could not extend to an investigation of binary compound growth of the type conducted for GaSb. It is proposed that further experiments should be undertaken to

examine a wider set of growth parameters to assess any variation in quality and/or morphology that may result.

The InSb films grown suggest that thermal processing of the InSb wafer prior to growth has resulted in pitting that persists after a 0.4 μm film deposition. Further work to investigate alternative methods of oxide removal, principally the use of atomic hydrogen in conjunction with a surface spectroscopy technique in order to determine the efficacy of oxide removal.

8.1.5 Further Investigation of InN_xSb_{1-x}:

The incorporation of N at substitutional lattice sites has been seen to follow a downward trend with increasing temperature. While this is qualitatively consistent with reports for GaN_xAs_{1-x} and the observations made for GaN_xSb_{1-x}, the fall-off observed was not as sharp, with the theoretical relationship provided by Wood *et al.* and Pan *et al*. providing a fair fit. It is thought that, at low temperatures, the pyrometer extrapolation values utilised throughout this investigation may have become non-linear, thus distorting the data along the temperature axis. To ascertain whether the origins of this phenomenon lie in instrumental or material factors, it is desirable to conduct further growth with an alternate means of establishing temperature. The use of BandiT for such measurements is unlikely to present a solution, as the spectrometers available for such use do not encompass the region in which the InSb band edge is expected to lie.[*] As described in chapter 3, the blackbody operating mode requires calibration at temperatures in excess of that at

[*] Private communication with Jeff Harris, *k*-Space Associates.

which material InSb degradation is expected. Furthermore, deposition of a nitrogen-containing film may further inhibit accurate measurements, due to the difference in band gap between the binary and ternary alloys. Instead, it is proposed that measurements are undertaken using an IR pyrometer with a sufficiently long operating wavelength that the lower bound of accurate temperature measurement may be decreased. The preliminary results from the 1.6μm pyrometer, discussed in chapter 7 suggest that it provides a feasible means of achieving this.

The experiments conducted to investigate the dependency of N content upon growth rate yielded mixed results. While one dataset permitted no firm conclusion to be drawn, another indicated that the substitutional N content was enhanced by increasing the growth rate, in agreement with reported data by Jefferson *et al*.[2] Contrary to the results reported for GaN_xAs_{1-x} and observed for the GaN_xSb_{1-x} films in this study, this poses the question of whether or not there is a significant difference in the behaviour of InN_xSb_{1-x}. Furthermore, it is uncertain at this stage whether there may be a change in the mode of incorporation, as a function of growth temperature. It is thought that different surface reconstructions present at the growth temperatures employed could contribute to such an effect. This hypothesis is supported by the work of Zhang and Zunger, who report a dependency of dopant solubility in III-V materials on the surface reconstruction.[3]

To better understand the system and its dependencies upon growth parameters, it is proposed that further growth be conducted at several different temperatures established by a longwave IR pyrometer and as a function of growth rate at each value. It would also be desirable to ascertain the effects upon substitutional nitrogen content of the plasma settings and V:N:III ratios. To elucidate the relative quantity

of substitutional N, as opposed to N-species incorporated at any other sites, SIMS results should also be conducted to compliment analysis by HRXRD.

Analysis by TEM was unavailable for the InN_xSb_{1-x} films grown during this investigation, partially due to the relative difficulty in preparation of high quality specimens.* As such, no information was available as to the quality of the substrate/buffer interface and the efficacy of thermal oxide desorption. It is suggested that cross-sectional TEM analysis would yield information pertaining to this, as well as providing an insight into how growth parameters affect the quality of the grown film.

8.1.6 Further Investigation of $In_xGa_{1-x}N_ySb_{1-y}$:

The variation of In content observed in the data presented in chapter 7 is indicative that there may be instability in one or more material sources, which requires investigation prior to further experimental growth.

It is proposed that the investigation of $Ga_xIn_{1-x}N_ySb_{1-y}$ films proceed initially as a function of growth rate and temperature, as has been demonstrated with GaN_xSb_{1-x} and InN_xSb_{1-x} films. Given the lack of consensus in the literature pertaining to the effect that In content may exert upon nitrogen content, it is desirable to attempt growth in the range $0 \leq (x,y) \leq 1$ to probe the full compositional range and to examine the scope for phase separation that may arise due to the mismatches between the four binary compounds. To this end, and to assess the dependencies of

* Private communication with Ana Sanchez (Department of Physics, University of Warwick)

morphology on growth parameters, a systematic study involving variation of growth temperature, the rate of deposition and the V:III ratio would also be desirable.

Cross-sectional TEM studies should be performed to determine the nature and composition of the features observed for lower growth temperatures.

8.1.7 Additional Further Work:

The formation of SbN has been reported, resulting from the exposure of InSb to a flux of active nitrogen species.[4] The proportion of incident N that contributes to the SbN, as opposed to InN, is unclear. However, should the former constitute a product of any significant proportion, further analysis of the way in which N is incorporated would have to be undertaken. This is particularly desirable with respect to adaptation of models for GaN_xAs_{1-x} composition which currently take no account of the potential for V-N products.

It is likely that destructive techniques such as SIMS would be unsuitable for determination of the presence of Sb-N, as there is distinct potential that it would dissociate during sputtering, whereas laser desorption ionisation (LDI) mass spectrometry may induce the formation of such species.

8.2 Conclusions:

There follows a summary of the observations made and aims achieved during this investigation.

8.2.1 Temperature Determination:

The investigation into methods of temperature determination has established best practice with the available equipment, through which growth has been achieved below the specified minimum of the pyrometer. Experiments have demonstrated areas in which care must be taken, particularly with respect to temperature measurements differing between various sample/platen arrangements. Additionally, the results obtained indicate that, without a method of feedback control linked to the surface temperature, growth of narrow bandgap material may suffer from compositional variation resulting from increased infrared absorption by the growing film.

Preliminary results from a pyrometer operating at 1.6 μm, described in chapter 7, suggest that growth temperatures lower than those reproducibly accessed in this investigation are likely to be possible with new equipment.

8.2.2 Growth of GaSb:

The homoepitaxial growth of GaSb has highlighted a range of surface morphologies arising from different sets of growth parameters. These have been of particular use in rationalising the morphologies observed in the GaN_xSb_{1-x} samples grown and suggest that compromise is required in the growth of the dilute nitride alloy, to permit nitrogen incorporation whilst maintaining a good surface morphology.

Heteroepitaxial GaSb/GaAs growth has demonstrated the strain-induced problems that can be encountered and indicate that, while a thick buffer layer may reduce the

propagation of defects through the grown material, a significant density are observable at the surface after ~1.0 μm of deposition.

TEM analysis has indicated regions of the grown material that is defect-free, with the strain arising from lattice mismatch appearing to have been accommodated by an array of misfit dislocations at the interface. Further investigation of this has been proposed to examine the feasibility of optimising this to produce buffer-free III-Sb material on GaAs substrates.

8.2.3 Growth of GaN_xSb_{1-x}:

The data gathered in this study have demonstrated a substitutional N content of 2.6%, representing the highest reported value at the time of writing.

The nitrogen content of grown films has been rationalised in terms of the growth rate and substrate temperature. Nitrogen content has been observed to increase as a function of decreasing temperature and decreasing growth rate. This provides good qualitative agreement with previous studies on GaN_xAs_{1-x}. A kinetic model has been found to provide a good fit to experimental data, but does not adequately describe the plateau regions observed as a function of growth rate. A rationale for this has been presented, in which the uptake of nitrogen in the growing film may change from occurring primarily at substitutional sites to interstitial locations.

Morphologies consistent with GaSb grown at low temperatures have been observed, suggesting that some of the growth conditions under which significant nitrogen incorporation can occur are detrimental to the surface quality.

8.2.4 Growth of InSb:

The homoepitaxial growth of InSb conducted has shown that thermal cleaning can result in a rough surface that persists after 0.4 μm of deposition, suggesting that an alternative method of processing should be employed. No unusual morphologies were observed for the films grown under the growth conditions used and experiments have been proposed for further investigation of the type conducted with respect to GaSb.

The transition between c(4 x 4) and a(1 x 3) surface reconstructions has been established as a function of thermocouple readings and provides an opportunity to probe InN_xSb_{1-x} growth across the phase boundary to establish whether the surface reconstruction has a significant effect on nitrogen incorporation.

8.2.5 Growth of InN_xSb_{1-x}:

Nitrogen has been incorporated into InSb, which required lower growth temperatures than those used for GaN_xSb_{1-x}. It was observed that the amount of substitutional nitrogen was less than that seen in the GaN_xSb_{1-x} grown, which is less than that reported for GaN_xAs_{1-x}. A rationale has been proposed for this, taking into account the differences in lattice parameter of the host matrix and relative energies of the III-N bonds.

The kinetic model proposed by Wood *et al.* has shown reasonable agreement with experimental data, although further experiments to determine the reliability of the temperature determination and the effect on nitrogen content of the growth rate used have been proposed.

8.2.6 Growth of $In_xGa_{1-x}N_ySb_{1-y}$:

Preliminary growth of $In_xGa_{1-x}N_ySb_{1-y}$ has demonstrated the successful incorporation of nitrogen, up to 1.97%. A film was grown which proves the feasibility of a quaternary film that is lattice-matched to GaSb.

Experiments have been proposed to extend the investigation of $(In,Ga)N_xSb_{1-x}$ ternary alloys, in order to establish growth conditions under which high quality films with a controllable and reproducible composition may be produced.

[1] Q. X. Zhao, S. M. Wang, M. Sadeghi, a. Larsson, M. Friesel, and M. Willander, Applied Physics Letters **89**, 031907 (2006).

[2] P. H. Jefferson, L. Buckle, D. Walker, T. D. Veal, S. Coomber, P. A. Thomas, T. Ashley, and C. F. McConville, Physica Status Solidi (RRL) – Rapid Research Letters **1**, 104-106 (2007).

[3] S. B. Zhang and Alex Zunger, Applied Physics Letters **71**, 677 (1997).

[4] L. Haworth, Journal Of Vacuum Science & Technology B: Microelectronics and Nanometer Structures **16**, 2254 (1998).